



HAL
open science

Sol-gel/ALD low temperature process: study of Al₂O₃ and codoped TiO₂ nanostructures for photovoltaic applications

Fatma Trabelsi

► To cite this version:

Fatma Trabelsi. Sol-gel/ALD low temperature process: study of Al₂O₃ and codoped TiO₂ nanostructures for photovoltaic applications. Materials Science [cond-mat.mtrl-sci]. Université Grenoble Alpes [2020-..]; Université de Sfax. Faculté des sciences, 2021. English. NNT : 2021GRALI059 . tel-03355479

HAL Id: tel-03355479

<https://theses.hal.science/tel-03355479>

Submitted on 27 Sep 2021

HAL is a multi-disciplinary open access archive for the deposit and dissemination of scientific research documents, whether they are published or not. The documents may come from teaching and research institutions in France or abroad, or from public or private research centers.

L'archive ouverte pluridisciplinaire **HAL**, est destinée au dépôt et à la diffusion de documents scientifiques de niveau recherche, publiés ou non, émanant des établissements d'enseignement et de recherche français ou étrangers, des laboratoires publics ou privés.



THÈSE

Pour obtenir le grade de

DOCTEUR DE L'UNIVERSITE GRENOBLE ALPES

**préparée dans le cadre d'une cotutelle entre la Communauté
Université Grenoble Alpes et l'Université de Sfax**

Spécialités :

Matériaux, Mécanique, Génie Civil, Electrochimie

Matériaux et environnement

Arrêté ministériel : le 6 janvier 2005 – 25 mai 2016

Présentée par

Fatma TRABELSI

Thèse dirigée par **Elisabeth BLANQUET**, Directrice de Recherches, CNRS, SIMaP et **Rached SALHI**, Maître de conférence, HDR, ISSIG-Tunisie
Codirigée par **Frédéric MERCIER**, Chargé de Recherches, CNRS, SIMaP

préparée au sein du **Laboratoire SIMaP-Sciences et Ingénierie des matériaux et Procédés** et **Laboratoire des matériaux avancés (LMA)**
dans l'**Ecole Doctorale I-MEP2- Ingénierie – Matériaux, Mécanique, Environnement, Energétique, Procédés, Production et sciences** et l'**Ecole Doctorale Sciences et technologies**

Sol-gel/ALD low temperature process: the study of Al₂O₃ and TiO₂ nanostructures for photovoltaic applications

Thèse soutenue publiquement le « **01 juillet 2021** »,
devant le jury composé de :

M, Michel LANGLET

Directeur de Recherches, CNRS, LMGP, Président du jury

M, Jamel BOUAZIZ

Professeur des Universités, LMA-ENIS, Examineur

M^{me}, Genevieve CHADEYRON

Professeur des Universités, SIGMA Clermont, Rapporteur

M, Radhouane CHTOUROU

Professeur des Universités, Centre de Recherches et des Technologies
de l'Energie-Borj Cedria, Rapporteur

M^{me}, Elisabeth BLANQUET

Directrice de Recherches, CNRS, SIMaP, Directrice de thèse

M, Rached SALHI

Maître de conférence, HDR, ISSIG-Tunisie, Directeur de thèse

M, Frédéric MERCIER

Chargé de Recherches, CNRS, SIMaP, Co-encadrant de thèse

M, Jean-Luc DESCHANVRES

Chargé de Recherches, CNRS, LMGP, Invité



Abstract

Solar energy remains one of the most common renewable energy sources. Using photovoltaic cells, the energy of sunlight can be converted into electricity. Unfortunately, one of the main drawbacks of Si solar cells is their limited efficiency absorption of long wavelength sunlight. To address this issue, special attention is given to the upconversion luminescence process in which the sequential absorption of two or more photons leads to the emission of light at shorter wavelength (Visible) than the excitation wavelength (Near Infra Red) that can be reabsorbed by the cell. In this context, the work of this PhD thesis aims to develop coated upconversion nanopowder based thin films to extend the spectral sensitivity of solar cells to the NIR (Near Infra Red) spectrum.

The idea is to investigate the efficiency of a low temperature procedure to get an efficient upconversion emission that can be used to improve the performance of Si solar cells. The structural, morphological and composition properties after every step of the proposed approach are examined in details. For the nanopowder based thin film, TiO_2 is chosen as host material and $\text{Er}^{3+}/\text{Yb}^{3+}$, embedded as activator/sensitizer, to play the role of spectrum modifier. This nanopowder based thin film is formed through an optimization of the dispersion (pH, ultrasonication) and deposition (spin coating parameters) steps of the elaborated upconversion nanopowder. The Atomic Layer Deposition (ALD) layer of Al_2O_3 material followed by thermal treatment is used as an important tool for Si passivation through defects reducing. In addition, its potential application as a barrier from the surrounding environment helps to avoid the suppressing of luminescence. The influence of thickness layer and thermal treatment on upconversion luminescence and structural properties of the nanopowder-based films are studied. It is concluded that ALD reinforced nanopowder thin films retained the original functionality of the nanopowder related to upconversion phenomenon. Interestingly, by tuning the thickness of the coating layer, enhancement by 98% of the green upconversion emission can be obtained, it is proved that Al_2O_3 acts as a barrier to decrease the quenching of luminescence and promote the light absorption. Furthermore, the effect of ALD coating and thermal treatment on adhesion and hardness of the coated nanopowder based films is investigated. The combination of the common steps used for enhancing electrical properties with good luminescence and mechanical properties makes these films more attractive.

Keywords: upconversion; Erbium; Ytterbium; sol-gel; ALD

Résumé

L'énergie solaire reste l'une des sources d'énergie renouvelables les plus courantes. En utilisant des cellules photovoltaïques, l'énergie solaire peut être convertie en électricité. Malheureusement, l'un des principaux inconvénients des cellules solaires en Si est leur efficacité limitée d'absorption de la lumière solaire à longueur d'onde élevée. Pour résoudre ce problème, une attention particulière est accordée aux processus de luminescence par upconversion dans lequel l'absorption séquentielle de deux photons ou plus conduit à l'émission de lumière à une longueur d'onde plus faible que la longueur d'onde d'excitation. Dans ce contexte, afin de faire face à cette perte spécifique d'absorption des photons de longueur d'onde au-dessus de la bande interdite de Si, les travaux de cette thèse visent à développer des couches minces à base de nanopoudres photoluminescentes enrobées pour étendre la sensibilité spectrale des cellules solaires au spectre proche infrarouge.

L'idée est d'étudier l'efficacité d'un procédé à basse température pour obtenir une émission efficace par phénomène d'upconversion (UC) qui peut être utile pour améliorer l'efficacité des cellules solaires à base de Si. Les propriétés structurales, morphologiques et de composition après chaque étape de l'approche hybride proposée sont détaillées. Pour le film mince à base de nanopoudres, TiO_2 est choisi comme matériau hôte et $\text{Er}^{3+}/\text{Yb}^{3+}$ est intégré comme activateur/sensibilisateur pour jouer le rôle de modificateur de spectre. Ce film mince à base de nanopoudre est formé grâce à une optimisation des étapes de dispersion (pH, ultrasons) et de dépôt (paramètres de spin coating) de la nanopoudre élaborée. Le revêtement de dépôt de couche atomique (ALD pour Atomic Layer Deposition) en utilisant l' Al_2O_3 suivi d'un traitement thermique est un outil important pour la passivation du Si afin de réduire les défauts, et ainsi son application potentielle en tant que barrière contre l'environnement environnant pour éviter la suppression de la luminescence. L'influence de l'épaisseur de la couche déposée et du traitement thermique sur la luminescence et les propriétés structurales du film à base de nanopoudres est étudiée. Il est conclu que les couches minces de nanopoudres renforcées par un dépôt d'ALD ont conservé la fonctionnalité originale de la nanopoudre liée au phénomène d'upconversion. En réglant l'épaisseur de la couche de revêtement, une amélioration de l'émission par upconversion dans le vert (98%) peut être obtenue, qui montre que le revêtement d' Al_2O_3 agit comme une barrière pour diminuer l'extinction de l'UC et également pour favoriser l'absorption de la lumière. En outre, l'effet du revêtement ALD et du traitement thermique sur

l'adhérence et la dureté des films à base de nanopoudre revêtus est étudié. La combinaison d'étapes couramment utilisées pour améliorer les propriétés électriques avec une luminescence et des propriétés mécaniques élevées obtenues dans ce travail est optimisée afin d'obtenir un film aux propriétés améliorées.

Mots-clés: upconversion; Erbium; Ytterbium; sol-gel; ALD

Acknowledgement

The present work would never have been possible without the support of a great number of people who have cordially given their help and supported me intellectually as well as personally throughout the last three years of my PhD thesis.

No words can express my profound and deep sense of gratitude to my supervisors: Elisabeth Blanquet, Rached Salhi and Frédéric Mercier for their help, support and encouragement in all stages of this work. They always gave me constant encouragements and advices, despite their busy agenda. They were always available for me what made the thesis writing and correction very fast and efficient. In addition, without their constant guidance and illuminating instruction, this thesis would not have reached its present form. It was a great pleasure for me to work with them.

I would like to thank all the professors, engineers, researchers and technicians in the group TOP where I spent three exciting years. I would like to thank Alexandre Crisci, Roman Reboud, Laurent Artaud, Raphael Boichot, for their technical and scientific support. I would dedicate these lines to Michel Pons. Unfortunately, he is not anymore with us but we do remember him each time, he was such an amazing person. I would also to thank Marc Fivel (GPM2) for his availability each time I contact him for mechanical characterization and all the discussions we had.

Special thanks to CMTC team for materials characterization. Thanks to Rachel Martin, Gilles Renou, Frédéric Charlot, Joelle Clabaro, Francine Roussel, Thierry Encinas and Stéphane Coindeau for SEM and XRD analysis. I also thank Laetitia Rapenne from LMGP for TEM analysis. I am also thankful to Laure Cointeaux (LEPMI) and Cecile Sillard (LGP2) for providing me with the dispersion tools, without you I would not be able to realize this part.

I would like to expand my thanks to all PhD students and postdoctoral researchers for all their help, advices, as well as moments and interesting conversations that we share it at the platform, coffee break and out of the laboratory: Jorge Sanchez, Elise Garel, Erwan Gicquel, Manoel Jacquemin, Solène Iruela, Vincent Tabouret, Adrien Moll, and all others. Thank's for my wonderful office colleagues: Juan Su and Danying Chen. Thank's Juan for your help and for the great moments that we share it specially during our trip to Madrid. Danying Chen, thank you for your help and unfortunately we never did a sport together. From PM group, I would

like to thank Mohamed Allam for his help and Chayma Boujrourf for her kindness and support, thank you for the great moments that we share it specially in your office talking about everything.

I should give also special thanks to my friends in Sfax: Ahlem Ben Daoud, Ikram Ben Ammar and also Ms. Mouna Messaoud Salhi for their help support and encouragement. Dhouha Abid, we had pass a great time together in Grenoble, do not try to lose weight, you are just perfect my friend. I would Like to thank my housemates at 60 boulevard joseph Vallier that kept encourage me and provide me with good vibes. I really had such a good company, thank you: Ingrid Hernandez, Camille Bert (Noah also) and Anna Gorina.

These lines will be dedicated for Mohammed Ali Lakhdari, the algerian, calm guy from PM group. Thank you for everything, your support, help, encouragement (which you can do it very well by the way, unlike me) and handling my stress. I appreciate what you did for me specially the last six months of my PhD. You can put it on the list.

Last but not least, my thanks go to my parents: Mohamed Ali Trabelsi and Samia Gharbi who supported me throughout this thesis by providing continuous support and guidance in all events. Thanks for your confidence and your love during all these years of my life. I would like also to express my gratitude for my little brothers Ali and Mohammed. I'm really thankful to have such a lovely family like you.

With my deepest grateful

Fatma

Table of Contents

Chapter I

I. Photovoltaic solar cells	21
I.1 Introduction	21
I.2 Limitations	22
I.3 Solutions for solar cell efficiency improvement	26
I.3.1 Spectral conversion.....	26
I.3.2 Surface passivation	27
II. Lanthanide UC nanoparticles	29
II.1 UC phenomenon	29
II.1.1 UC mechanisms.....	29
II.2 Lanthanide ions as upconvertors.....	31
II.2.1 Introduction	31
II.2.2 Erbium-Ytterbium couple	34
II.2.3 Parameters influencing the UC luminescence.....	36
II.3 TiO ₂ as host matrice	39
II.3.1 Crystal structure	39
II.3.2 Stability of crystalline phases.....	41
II.3.3 Potential applications of TiO ₂ nanoparticles in PV.....	42
II.4 Synthesis methods.....	42
II.4.1 Spray pyrolysis	43
II.4.2 Co-precipitation.....	44
II.4.3 Microwave.....	44
II.4.4 Sol-gel	45
III. Colloidal dispersion of UC nanoparticles	46
III.1 Stabilization of colloidal dispersion	46
III.1.1 Steric stabilization.....	47
III.1.2 Electrostatic stabilization	47
IV. Nanoparticles wet thin film deposition techniques	47
IV.1 Doctor-blade technique	48
IV.2 Dip-coating technique	48
IV.3 Spin-coating technique	48
V. Atomic Layer Deposition	49
V.1 Principle of ALD	50
V.2 Al ₂ O ₃ as a Model ALD System	52
V.3 Post-deposition annealing.....	53

VI. Conclusions and motivation of this thesis.....	54
<u>Chapter II</u>	
I. Low temperature procedure proposed in this study	67
I.1 Nanopowder synthesis using Sol-gel method	67
I.1.1 Hydrolysis.....	67
I.1.2 Condensation	67
I.1.3 Aging	68
I.1.4 Drying.....	68
I.1.4.1 Supercritical drying	69
I.1.5 Thermal treatment.....	70
I.1.6 Parameters	70
I.1.7 Synthesis of undoped and codoped TiO ₂ nanopowders	71
I.2 Nanopowders dispersion	73
I.3 Spin-coating	75
I.3.1 cleaning process.....	75
I.3.2 Influence of spin-coating operative parameters.....	79
I.4 Al ₂ O ₃ -ALD coating on Si substrate	84
II.4.1 ALD growth window.....	84
II.4.2 Optimization of TMA pulse time	85
II.4.3 Film thickness vs ALD cycle numbers	86
II. Characterization.....	87
II.1 Structural Characterization	87
II.1.1 X-ray diffraction (XRD).....	87
II.1.2 BET analysis	87
II.1.3 Electron microscopy.....	87
II.1.4 Dynamic and electrophoretic light scattering.....	89
II.1.2 Chemical characterization	91
II.1.3 Thermal analysis (TG-DTA).....	92
II.1.4 Optical analysis	92
II.1.5 Mechanical analysis	92
<u>Chapter III</u>	
I. Structural and spectroscopic studies of TiO ₂ nanopowders	99
I.1 Thermal analysis (TG-DTA).....	99
I.2 Structural analysis	101
I.3 Spectroscopic analysis.....	103
I.4 Morphological and surface analysis	106
II. Dispersion and stability optimization of TiO ₂ nanoparticles in ethanol.....	110

II.1 Effect of the sonicator type	110
II.2 Effect of pH.....	113
II.2.1 Fixed concentration of additives	113
II.2.2 Variation of additives concentration	114
II.3 Ultrasonic duration and doping effect.....	116
III. Deep investigation of structure and composition of the optimized dispersion of the codoped TiO ₂	119

Chapter Conclusion

Chapter IV

I. Deposition of dispersed nanopowders on Si wafer	131
I.1 Deposition quality and adhesion tests	131
I.2 Spin-coating	133
I.2.1 Study of optimization conditions for spin-coating process	134
I.2.2 Spin coating cycles influence on PL response.....	139
II. ALD-Al ₂ O ₃ coating on codoped TiO ₂ nanopowder deposited on Si wafer	144
II.1 Morphological analysis	144
II.2 Compositional investigations of ALD-Al ₂ O ₃ coating on codoped TiO ₂ nanopowder deposited on Si.....	150
II.3 Structural investigation of ALD-Al ₂ O ₃ coating on codoped TiO ₂ nanopowder deposited on Si.....	157

Chapter Conclusion

Chapter V

I. UC luminescence study.....	170
II. Mechanical properties.....	178
II.1. Adhesion measurements	178
II.2 Hardness.....	186
<i>Annex</i>	198

Chapter Conclusion

Annex 1: Williamson –Hall method for crystallite size and strain calculation	198
Annex 2: Comparison between the TMA amounts injected to the exposed surface of nanoparticles based film	202

List of figures

Figure I.1 : PV Cell Working Principle [2].	21
Figure I.2: The three generations of solar photovoltaic (PV) cells [2].	22
Figure I.3 : Spectral distribution of the AM1.5G solar irradiance and the total power density for PV technologies based on the absorption of the semiconductor layer [8].	23
Figure I.4: Loss mechanisms in a solar cell: high energy photons ($E > E_g$) are absorbed with a part of the energy lost as heat (blue), low energy photons ($E < E_g$) are not absorbed (red). Only photons with an energy matching exactly the band gap can be converted (green) [9].	24
Figure I.5 : Solar power distribution [13].	24
Figure I.6: The possible recombination mechanisms of photo-generated charge carriers: (a) radiative recombination, (b) recombination via defects and (c) Auger recombination [16].	26
Figure I.7: Energy diagrams showing photon adsorption and subsequent DC, DS and UC processes from [18].	27
Figure I.8: Schematic illustration of the different mechanisms mainly contributing to the UC process according to ref. [31].	31
Figure I.9: Classification of RE elements in the periodic table.	32
Figure I.10 : Partial energy level diagram of Ln^{3+} ions and the corresponding radiative emissions [33].	33
Figure I.11: Schematic energy level diagram of the sensitization of Er^{3+} by Yb^{3+} according to [49].	35
Figure I.12: Log-log plot of the pump power 980 nm laser dependence of UC emissions centered at 525, 550 and 655 nm emission intensity of the Er^{3+} - Yb^{3+} codoped TiO_2 ions as reported in [53].	38
Figure I.13 : Steps involved in sol-gel process as reported in [92].	45
Figure I.14: Different shapes of materials synthesis by sol-gel method [93-95].	45
Figure I.15 : Schematic representation of the two mechanisms of particles stabilization [104].	47
Figure I. 16: Typical stages of spin-coating process as reported in [118].	49
Figure I.17: The coverage metrics of ALD-film on a substrate with 3D features as reported in [122].	50
Figure I.18: Schematic representation of different steps of ALD process consisting of two half-reactions [122].	51
Figure I.19: The temperature window of the ALD process, indicated by the growth per cycle as a function of temperature [124].	52
Figure I.20: The low temperature procedure used in this study for the synthesis, deposition and coating of the UC TiO_2 nanopowder.	56
Figure II.1: Phase diagram of a pure substance presenting different thermal drying routes [1].	69
Figure II.2: Schematic illustration of the nanopowders synthesis procedure.	72
Figure II.3: Sol-gel under supercritical drying conditions equipment.	72
Figure II.4: the synthesized nanopowders: (a) undoped and (b) codoped TiO_2 .	73
Figure II.5: The different sonicators used in this study (a) bath and (b) probe.	74
Figure II.6: Surface wetting property of n-type and p-type Si before and after RCA process [18].	76
Figure II.7: Optical microscope observations of the different substrates S1, S2 and S3 in two areas (center and border).	78
Figure II.8: Substrate cleaning process adapted in this study.	79
Figure II.9: Si/ codoped TiO_2 nanopowder under different operation parameter (1) using a spin-coater jacket, (2) without jacket and (3) without jacket changing the chuck.	83
Figure II.10: Spin coating steps used in this study.	83

Figure II.11: The growth rate of ALD-Al ₂ O ₃ deposited on silicon substrates as a function of deposition temperature.	85
Figure II.12: The growth rate evolution as function of TMA pulse time.....	86
Figure II.13: Thickness evolution with ALD cycles.....	86
Figure II.14: Schematic representation of the ACOM-TEM method [45].....	88
Figure II.17: Schematic diagram of the principle of the PZ technique [51].	91
Figure III.1: TG-DTA curves of as-prepared undoped and codoped TiO ₂ nanopowders.....	100
Figure III.2: FT-IR spectra of codoped TiO ₂ nanopowders (a) as-prepared and (b) calcined at 300°C-2h.....	102
Figure III.3: XRD patterns of: (a, b) as-prepared undoped and codoped TiO ₂ , respectively.....	101
Figure III.4: XPS spectra of TiO ₂ (a) Survey Scan, (b) Ti2p, (c) O1s (d) C1s, (e) Er 4d _{5/2} and (f) Yb 4d _{5/2} . Black line undoped TiO ₂ and red line codoped nanopowders calcined at 300°C-2h.....	105
Figure III.5: SEM images of (a-c) undoped and (d-f) codoped TiO ₂ nanopowders calcined at 300°C-2h at different magnifications.....	106
Figure III.6: Different types of adsorption isotherms as classified by IUPAC, showing both the adsorption and desorption pathways [31].....	107
Figure III.7: (a) N ₂ adsorption-desorption isotherms and (b) Barrett-Joyner-Halenda (BJH) pore size distributions as determined from the adsorption branche of the isotherm for N ₂ gas on both undoped and codoped TiO ₂ calcined at 300°C-2h.	109
Figure III.8: (a) TEM image and (b) selected area electron diffraction patterns (SAED) where diffraction planes corresponding to anatase structure of co-doped TiO ₂ nanoparticles.	110
Figure III.9: (a, b) Examination of temperature evolution of pure TiO ₂ suspensions in ethanol without adjusting pH of the solution using different ultrasonication methodologies under two different modes.	112
Figure III.10: SEM images of undoped TiO ₂ suspensions after 10 min of ultrasonication with different magnifications using: (a-b) bath and (c-d) probe sonicators under the second mode (changing the water bath every 5 min).	112
Figure III.11 : Zeta potential as function of operational pH and evolution of suspensions with time in stationary state of undoped and codoped TiO ₂	114
Figure III.12: (a, b) Zeta potential as function of operational pH and additives concentration of undoped and codoped TiO ₂ suspensions.....	115
Figure III.13: evolution of suspensions with time in stationary state of (a) undoped and (b) codoped TiO ₂ using 0.001 M of additives.....	116
Figure III.14: Evolution of size dispersion of (a) undoped, (b) codoped TiO ₂ nanopowders and (c) polydispersity index (PDI) of the codoped TiO ₂ nanopowders in ethanol as a function of ultrasonication time (operational pH = 3 with 0.1M of additives, C _{solution} = 0.24 M, 24 h of magnetic stirring).	118
Figure III.15: SEM images of a grid after being soaked in the codoped TiO ₂ suspension (operational pH = 3 with 0.1M of additives, C _{solution} = 0.24 M, 24 h of magnetic stirring) for 60 s. (b, d) and (c, e) are the same image with different magnifications.....	120
Figure III.16: ACOM-TEM on the codoped TiO ₂ nanopowders: (a) orientation map along z-axis, (b) the matching index, (c) phase reliability.	121
Figure III.17: a, b and c outputs of ACOM-TEM on the codoped TiO ₂ nanopowders showing phase maps of anatase plotted with rutile, Er ₂ O ₃ and Yb ₂ O ₃ respectively.	121
Figure III.18: outputs of ACOM-TEM on the codoped TiO ₂ nanopowders showing (a) grain boundaries map and (b) grain size distribution deduced from (a).	122
Figure III.19: HAADF-STEM image and representative STEM-EDS line.....	123

Figure IV.1 : SEM images of deposited colloidal suspension of undoped and codoped TiO ₂ under different time of ultrasonication (t = 0 min, 10 min, 20 min and 30 min) on n-type (100) Si wafer using a spin coating process (depositing phase: 1000 rpm - 30 s and drying phase: 1 min at 200°C on a hotplate).....	132
Figure IV.2 : SEM images of adhesion tests: (a) rinsed with water and (b) blown with N ₂ gas of codoped TiO ₂ film deposited on n-type (100) Si wafer using a spin coating process (depositing phase: 1000 rpm – 30 s, US = 20 min and drying phase: 200°C - 1 min on a hotplate).	133
Figure IV.3 : Schematic view of the process	133
Figure IV.4: Hadamard matrix H4.	133
Figure IV.5: The three different areas of SEM observations for DOE.....	136
Figure IV.6: SEM top view images of the DOE experiments in every area.	137
Figure IV.7: Level of impact of parameters on responses.	138
Figure IV.8: SEM Top view images of Si/ codoped TiO ₂ nanopowder with different spin-coating cycle numbers (2, 4 and 8).	140
Figure IV.9: Thickness comparison with other reports and cross-sectional SEM images of Si/ codoped TiO ₂ nanopowder with different spin-coating cycle numbers (2, 4 and 8), (bar errors are included in the dot size).	141
Figure IV.10: Identification Raman peaks from PL emissions of Er ³⁺ under excitation wavelength $\lambda=514$ nm of undoped and codoped TiO ₂ nanopowders.	142
Figure IV.11: (a) PL emission under excitation wavelength $\lambda=514$ nm of all the different samples from powder to film and (b) the corresponding integrated intensity of the peaks. The green emissions are shown in dotted rectangle.	143
Figure IV.12: PL emission of different samples under excitation wavelength $\lambda=514$ nm (a) green emissions of Er ³⁺ ($^2H_{11/2} + ^4S_{3/2} \rightarrow ^4I_{15/2}$) enlarged and presented in order to get a clear view and (b) blue shift of the peaks.....	144
Figure IV.13: SEM top view images of (a-b) Np/62 and (c-d) Np/62 + FGA.....	146
Figure IV.14: SEM top view images of (a-b) Np/620 and (c-d) Np/62 + FGA.....	146
Figure IV.15: SEM images of a pore on the surface of Np/620 +FGA film.	147
Figure IV.16: ALD –TiO ₂ layer on TiO ₂ nanoparticles to enhance interparticles connection as reported in [26].....	148
Figure IV.17: Cross-sectional SEM images of (a-c) Np/62, (d-f) Np/62 + FGA films.....	149
Figure IV.18: Cross-sectional SEM images of (a-b) Np/620, (c-d) Np/620+FGA films.....	149
Figure IV.19: HR-TEM images showing the thickness of (a, b) Np/62+FGA, (c, d) Np/620 +FGA films and (e) ACOM-TEM on the Np/ 62 film showing phase map of anatase plotted with Er ₂ O ₃ , Yb ₂ O ₃ , Al ₂ TiO ₅ and amorphous Al ₂ O ₃ respectively.	150
Figure IV.20: STEM-EDS elemental mapping of Np/ 62+ FGA film.	152
Figure IV.21: STEM-EDS elemental mapping of (a-d) Np/620 and (e-h) Np/620+FGA.	153
Figure IV.22: Depth profile of the different elements for (a) Np/ 62+FGA, (b) Np/ 620 and (c) Np/ 620 + FGA. The white arrows give the direction of the scan, from the tail (0 μ m) to the head (between 0.7 and 0.95 μ m)	155
Figure IV.23: The possible explanation for Al and O elements diffusion after FGA.	156
Figure IV.24: XRD patterns of: (a) Np, (b) Np/ 62 +FGA and (c) Np/620+FGA films.	158
Figure IV.25: Acquired pattern fitted with anatase, Al ₂ TiO ₅ , Er ₂ O ₃ and Yb ₂ O ₃ templates.....	159
Figure IV.26: ACOM-TEM on the Np/ 62 exhibited on two different areas showing phase maps of anatase plotted with Er ₂ O ₃ , Yb ₂ O ₃ and Al ₂ TiO ₅ respectively: (a, e) phase map, (b, f) the matching index, (c, g) combined phase-index maps and (d, h) combined phase-index-reliability.	161

Figure IV.27: ACOM-TEM on the Np/ 620 exhibited on two different areas showing phase maps of anatase plotted with Er ₂ O ₃ , Yb ₂ O ₃ and Al ₂ TiO ₅ respectively: (a, e) phase map, (b, f) the matching index, (c, g) combined phase-index maps and (d, h) combined phase-index-reliability.	162
Figure IV.28: ACOM-TEM on the Np/ 620 + FGA exhibited on two different areas showing phase maps of anatase plotted with Er ₂ O ₃ , Yb ₂ O ₃ and Al ₂ TiO ₅ respectively: (a, e) phase map, (b, f) the matching index, (c, g) combined phase-index maps and (d, h) combined phase-index-reliability.	163
Figure V.1: UC luminescence spectra and histogram from the integrated intensities from powder phase to coated nanopowder based films.	171
Figure V.2: Schematic energy level diagram of Er ³⁺ and Yb ³⁺ showing the possible mechanism....	172
Figure V.3: Protection behavior of the coating of luminescent nanoparticles from OH group to insure better luminescence response as reported in [10]......	174
Figure V.4: (a) SEM image of Np/620 +FGA combined with line profile graph for Al and O elements presence along the film and (b) The probably mechanism for the indirect excitation of Er ³⁺ ions by ALD-Al ₂ O ₃ layer.	177
Figure V.5: Optical images of the resulting scratch channel after the test being applied on Np.	179
Figure V.6: Optical images of the resulting scratch channel after the test being applied on (a) 62, (b) 620, (c) Np / 62 and (d) Np/ 620.	182
Figure V.7: Optical images of the resulting scratch channel after the test being applied Np/620+FGA.	183
Figure V.8: Optical images of the resulting scratch channel after the test being applied on (a) Np /62 +FGA and (b) Np/620+FGA.	184
Figure V.9: The critical loads Lc1 and Lc2 of different films as average value of 10 measurements.	185
Figure V.10: Frictional force (F _T) evolution with the detected normal force (F _n) at the failure point of Np/ 62 and Np/ 620 before and after the FGA treatment.	185
Figure V.11: HR-TEM images of Np/62+FGA showing the porosities among the film.	188
Figure V.12: HR-TEM images of Np/620+FGA showing the porosities among the film.	189
Figure V.13: Optical images of Berkovich indent print on different films.	190
Figure A.1.1: Williamson-Hall plot of $\beta_{hkl} \cos \theta$ vs $4 \sin \theta$	199
Figure A.2.2: Schematic representation of the amount of TMA precursor injected and the exposed surface of nanopowders.	203

List of tables

Table I.1: Band gap and absorption threshold for different photovoltaic technologies.	25
Table I.2: The most studied UC couples based on Yb ³⁺ as a sensitizer.....	34
Table I.3: Summarize of the integration of Er ³⁺ -Yb ³⁺ couple in various fields.....	35
Table I.4: The RE elements listed with common properties [50].....	35
Table I.5: Phonon energy of the most frequently used matrices for rare-earth ions.....	39
Table I.6: Crystallographic data of the anatase, rutile and brookite phases of TiO ₂ [68].....	41
Table I.7: Er ³⁺ -Yb ³⁺ percents annealing temperature and luminescence UC emissions for codoped TiO ₂ films as reported in literature.	55
Table II.1: Critical Points of Various Substances.	70
Table II.2: Properties of ethanol.	73
Table II.3: Area coverage percents of the nanoparticles deposited on Si substrate deduced using ImageJ software.....	78
Table II.4: Spin Coating process troubleshooting [41].	82
Table III.1: Microstructural parameters of undoped and codoped TiO ₂ as-prepared and calcined at 300°C for 2 h obtained from XRD patterns.....	103
Table IV.1: Levels of the factors used in the experimental design following Hadamard matrix of order 4.	135
Table IV.2: Experiments designed by the DOE approach following Hadamard matrix of order 4 ...	136
Table IV.3: Level of impact of parameters on responses.	138
Table IV.4: Films attribution name.	145
Table IV.5: Microstructural parameters of the films uncoated and coated with different thickness of ALD-Al ₂ O ₃ layer from XRD patterns.	158
Table V.1: Hardness values of different films.....	186
Table A.1.1: Elastic compliances values of anatase and rutile phases.	200
Table A.1.2: The stress calculated for each plane (hkl) of the four samples.....	201

List of abbreviations

ALD: Atomic Layer Deposition
BET: Brunauer-Emmett-Teller
CR: Cross relaxation
DC: downconversion
DS: downshifting
DSSCs: Dye sensitized solar cells
ET: energy transfer
FGA: forming gas annealing
GPC: growth per cycle
IR: Infrared
NIR: near-infrared
PL : photoluminescence
PV: Photovoltaic
PIE: Isoelectric point
RCA: Radio Corporation of America
RE: rare earth
UC: upconversion
UV : Ultraviolet
Vis : Visible

Introduction

In PV field, Si solar cells have been the dominant driving force for the past several decades due to the relative abundance and environmentally friendly nature as no toxic heavy metals (such as Cd or Pb) are involved in their elaboration [1]. Nevertheless, one of the main drawbacks of Si solar cells is the limited efficiency absorption of long wavelength sunlight. To overcome this issue, many efforts are carried out to improve cells absorption especially in Infra-Red (IR) region. In this context, application of Up Conversion (UC) luminescent nanopowder composed of lanthanide ions doped inorganic host material as spectrum modifier have attracted great interest due to their outstanding luminescent properties. Up Conversion (UC) luminescence is a nonlinear optical phenomenon that can convert low energy incident photons (NIR) to high energy (Vis) via the absorption two or more photons [2]. This high-energy photon is then returned to the host solar cell where it can be absorbed [3].

It has been proved that nanopowders of codoped TiO₂ with Rare Earth (RE) ions are promising candidates for the usage in optoelectronics by extending the spectral range from the near-UV to the infrared region. TiO₂ is widely used due to its low cost, non-toxicity, photo-stability, biological and chemical inertness [4]. Additionally, in its anatase phase, TiO₂ has lower local symmetry than the rutile phase that is beneficial for UC luminescence. Moreover, TiO₂ codoped with Er³⁺-Yb³⁺ is a transparent material with a high refractive index ($n = 2.4$) in Vis wavelength, which makes it widely desired for application in the solar cells field [5-6].

RE ions have been extensively studied due to their specific 4f electronic structure and unique properties. For the lanthanides ions, Er³⁺ shows green and red UC luminescence, but its weak absorption at the NIR wavelength gives low luminescence efficiency, which limits its applications. This problem is improved by adding Yb³⁺ ion that acts as a sensitizer. Yb³⁺ exhibits high absorption at 850 – 1050 nm, which enhances the emission of Er³⁺ by transferring its energy to Er³⁺. Deposition of nanoparticles as thin films to extend their application to optoelectronics field is necessary and different methods can be used (dip-coating, spin-coating).

Although UC nanoparticles are an attractive wavelength converter, the luminescence is not very stable because of the large sensitive surface area. Even exposure to ambient air can cause a degradation of luminescence due to the surface defects that creates non-radiative trap states and leads to the quenching of UC emission which influences the device performance. To improve and stabilize luminescence efficiency, surface encapsulation is an effective way. Surface

passivation using dielectric Al₂O₃ layer deposited by atomic layer deposition process is known to provide an outstanding effect of surface passivation of PV cells. The dielectric material Al₂O₃ is used to reduce the defects (passivation-Si) which is beneficial for electrical properties but also to insure the long-term stability of the device [7]. It is reported that effective passivation by ALD-Al₂O₃ requires an activating annealing [8]. Therefore, we will keep the same structure and process provided for the enhancement of electrical properties for PV cells and we will introduce the UC film between Si and the ALD- Al₂O₃ layer.

Although UC TiO₂ codoped Er³⁺-Yb³⁺ thin films have been already investigated by several research groups for different applications, the preparation of films with a good crystallinity, high surface area and efficient UC luminescence at temperature below 500°C still remains challenging. Till now, the annealing temperature that has been used in most of the studies is above 500°C, in order to achieve high crystallinity and consequently an efficient luminescence. But, at high annealing temperatures: size, shape, phase and luminescence properties (specially the profile of the emissions) are changed. Moreover, the poor mechanical reliability and durability of these UC thin films limit their industrial and commercial applications.

Therefore, this thesis is concerned with the improvement of UC phenomena efficiency combined with good mechanical properties using a simple and low temperature process (< 500°C). The proposed multi-step process consists first on the synthesis of RE (Erbium and Ytterbium) codoped TiO₂ nanopowder elaborated by hydrothermal-assisted sol-gel method, followed by their dispersion and deposition as thin films at the surface of Si substrates using a spin-coating process. Finally, Er³⁺-Yb³⁺codoped TiO₂ nanopowder assembled as a film is coated with an amorphous Al₂O₃ layer using ALD, followed by Forming Gas Annealing (FGA) (N₂:H₂) at 430°C for 30 min.

The thesis is structured as follows:

- **Chapter 1** presents an introduction to Si-based PV cells, the main losses and the different existing solutions provided in literature. Next, a detailed description of the upconversion phenomenon, the chosen matrix and the RE ions is provided. Then, the basics of the different processes (sol-gel, spin-coating, ALD) used during this thesis are briefly presented.
- **Chapter 2** refers to the synthesis of undoped and lanthanides codoped TiO₂ nanopowder. Then it presents the optimization of the nanopowder dispersion before their deposition on the Si substrate. In addition, optimization of the atomic layer deposition of Al₂O₃ parameters

is performed. It describes also the characterizing methods used in this work involving structural, thermal, chemical, optical and mechanical analysis.

- **Chapter 3** is devoted to discuss the structural and spectroscopic properties of the elaborated material.
- **Chapter 4** discusses the DOE approach with the Hadamard matrix conducted for spin coating step in order to optimize the deposition conditions. Next, it treats the impact of different ALD-Al₂O₃ thicknesses and FGA treatment on the structural and compositional properties of codoped TiO₂ nanopowders assembled on n-type (100) Si substrate.
- **Chapter 5** provides a detailed discussion on the improvement of the UC luminescence and mechanical properties of the uncoated and coated nanopowder based thin films.

References

- [1] A. Khare, "A critical review on the efficiency improvement of upconversion assisted solar cells," *Journal of Alloys and Compounds*, vol. 821, pp. 153214, 2020.
- [2] Z. Yang, K. Zhu, Z. Song, D. Zhou, Z. Yin, and J. Qiu, "Preparation and upconversion emission properties of TiO₂:Yb, Er inverse opals," *Solid State Communications*, vol. 151, pp. 364–367, 2011.
- [3] D. G. Sellers, J. Zhang, E. Y. Chen, Y. Zhong, M. F. D. N, and J. M. O. Zide, "Novel nanostructures for efficient photon upconversion and highefficiency photovoltaics," *Solar Energy Materials and Solar Cells*, vol. 155, pp. 446–453, 2016.
- [4] B. Tryba, S. Jafari, M. Sillanpää, A. Nitta, B. Ohtani, A. W. Morawski, "Influence of TiO₂ structure on its photocatalytic activity towards acetaldehyde decomposition," *Applied Surface Science*, vol. 470, pp. 376–385, 2019.
- [5] RE. Rojas-Hernandez RE, NP. Barradas, E. Alves, LF. Santos, RM. Almeida RM, "Up-conversion emission of aluminosilicate and titania films doped with Er³⁺/Yb³⁺ by ion implantation and sol-gel solution doping," *Surface and Coatings Technology*, vol. 355, pp. 162–168, 2018.
- [6] R. Y. S. Zampiva *et al.*, "Luminescent anti-reflection coatings based on Er³⁺ doped forsterite for commercial silicon solar cells applications," *Solar Energy*, vol. 170, no. May, pp. 752–761, 2018.
- [7] B. Hoex, J. Schmidt, P. Pohl, M. C. M. Van De Sanden, W. M. M. Kessels, "Silicon surface passivation by atomic layer deposited Al₂O₃," *Journal of Applied Physics*, vol. 104, pp. 044903, 2008.
- [8] F. Kersten, A. Schmid, S. Bordhim, J. W. Muller, J. Heitmann, "Role of Annealing Conditions on Surface Passivation Properties of ALD Al₂O₃ Films," *Energy Procedia*, vol. 38, pp. 843–848, 2013.

The best that most of us can hope to achieve in physics is simply to misunderstand at a deeper level.

Wolfgang Pauli

Chapter I

Literature Review

I. Photovoltaic solar cells

I.1 Introduction

Solar cells generate directly electrical power from incident solar radiation through the PV effect. It is discovered by the French physicist Edmond Becquerel in 1839 and is first used in industrial applications in 1954 [1]. A PV cell is in a form of a sandwich of n-type semiconductor, doped with atoms of phosphorus (abundance of electrons), and p-type semiconductor doped with atoms of boron (abundance of holes), which is exposed to the sun light. When these two doped silicon materials are put next to each other, they form a semiconducting junction named the depletion zone that creates an electric field. No electrons can cross the barrier. When the cell is exposed to sun light, a remarkable phenomenon called photoelectric effect takes place. The photons can be absorbed by the cell and so, the electrons get sufficient energy to move to the conduction band and leaves a “hole” in the valence band. These electrons and holes are called photo-generated charge carriers. The electrons jump out of the lower, p-type layer across the barrier to the n-type layer above and flow out around the circuit while the holes drift to the p-side (**Figure I.1**). The electrons and holes are directed to the electrical contacts applied to both sides before flowing to the external circuit in the form of electrical energy that produces direct current [2].

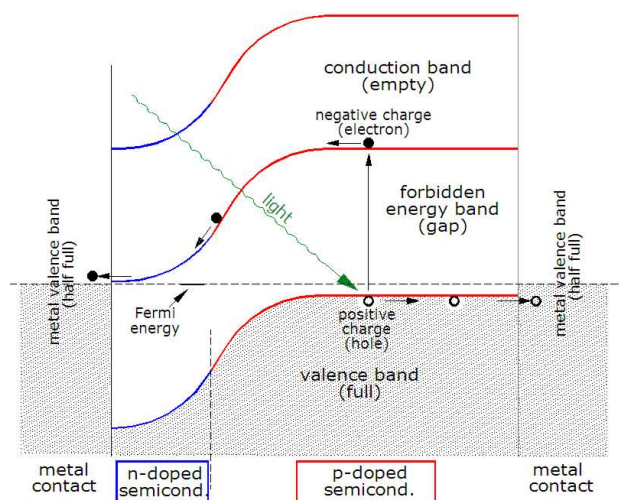


Figure I.1 : PV Cell Working Principle [2].

As presented in **Figure I.2**, the existing PV cells can be classified into three generations according to time and categories of materials which are used for their fabrication [3]. First generation PV cells are based on Si wafer technology. These cells are currently the most used amongst all the three generations and this generation occupies approximately 80% of the PV market. Generally, it presents the longer and higher efficiency but unfortunately suffers from

high costs in terms of energy consumption and work, and their performance easily degrades at higher temperature and under aggressive environment conditions. The second generation is based on very thin films of semiconductor materials. Compared to the first generation, since the manufacturing processes of these cells are simpler and consume fewer material amount, the cost are lower. However, these cells suffer from low efficiency. This generation represents approximately 20% of the total PV market. The third generation is the evolution of the second one with the goal to produce more efficient and less expensive cells by using a variety of new material structures such as organic dyes and nanotubes. Research and development work on third generation PV technology are being conducted in research laboratories. Therefore, most of these technologies are still commercially unavailable [2].



Figure I.2: The three generations of solar photovoltaic (PV) cells [2].

I.2 Limitations

Solar cell efficiency is fundamentally impacted by the following parameters:

- Spectral or optical losses, which are caused by the inefficient absorption of light. It can first be related to:
 - The refractive index mismatch between silicon and the environment, that gives rise to reflection losses from the front surface of the cell. Consequently, the photons that do enter the silicon semiconducting layer may escape before being absorbed. The reflection losses can be reduced by covering the top of the solar cell surface by antireflective coatings. Single or double layers such as silicon nitride $\text{SiN}_x\text{:H}$, boron nitride (BN_x), TiO_2 , ZnO , SiO_2 and ZnO/TiO_2 are proved to be good anti-reflective coatings for solar cells because of their spectral stability, high strength and sufficiently wide bandgap [4–7].

- The second major loss limiting the conversion efficiency of PV cells is the insensitivity to a full solar spectrum. As presented in **Figure I.3**, the spectral distribution of sunlight at Air Mass 1.5 global (AM 1.5G) consists of photons with wide wavelengths ranging from UV to IR (280 – 2500 nm). Meanwhile, the majority of PV cells can absorb a relatively small fraction of the solar photons. This is attributed to that each PV semiconductor material responds to a narrow range of solar photons which energy matches the characteristic bandgap, noted E_G , of the semiconductor [8].

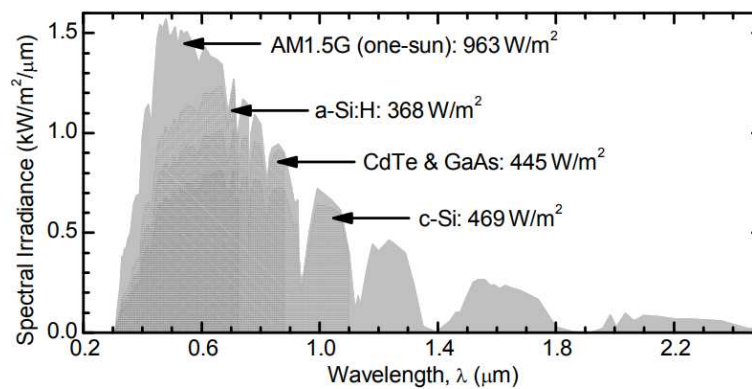


Figure I.3 : Spectral distribution of the AM1.5G solar irradiance and the total power density for PV technologies based on the absorption of the semiconductor layer [8].

These spectral mismatch losses are called thermalization and sub-bandgap loss (or transmission loss). Together, they account for over 55% of the total absorbed solar energy [9]. Photons with $E > E_G$ contribute to thermalization losses due to the fact that when they get absorbed they possess higher energy than required to generate photocurrent. As a result, electrons are promoted into the conduction band with additional kinetic energy that is wasted as heat within the lattice of the semiconductor, whereas photons with $E < E_G$ will be transmitted through the cell without adding to the output load [10–12] (**Figure I.4**).

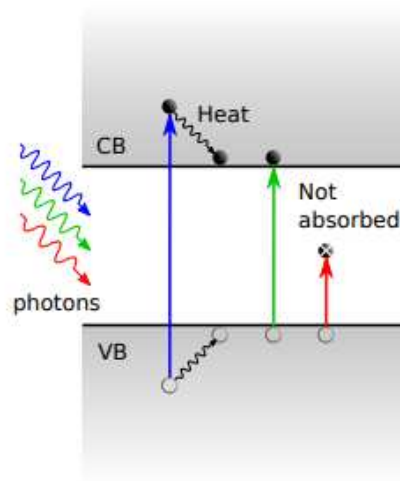


Figure I.4: Loss mechanisms in a solar cell: high energy photons ($E > E_g$) are absorbed with a part of the energy lost as heat (blue), low energy photons ($E < E_g$) are not absorbed (red). Only photons with an energy matching exactly the band gap can be converted (green) [9].

The inability to absorb IR light (700 – 2500 nm), which constitutes 52% of the energy of the totality of solar spectrum as shown in **Figure I.5**, forms the major energy loss mechanism of the conventional solar cells [13]. This fundamental issue is governed by the sizable bandgap of light-absorbing materials in PV cells (**Table I.1**). For single crystalline Si PV cells presenting a small semiconductor band-gap (1.12 eV) that correspond to a wavelength of ~ 1100 nm, the transmission loss of sub-band-gap photons can still reach to about 20% of the sun’s energy. The PV cells with a larger band-gap, such as amorphous Si solar cells, which are limited to absorb sunlight with wavelengths below 730 nm, show higher NIR transmission losses [14].

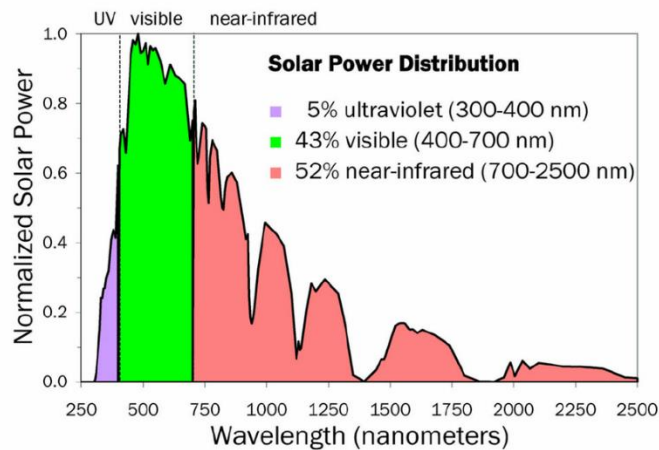


Figure I.5 : Solar power distribution [13].

Table I.1: Band gap and absorption threshold for different photovoltaic technologies.

Solar cell type	Band gap (eV)	Absorption threshold (nm)
Crystalline silicon	1.12	1110
Perovskites	1.5	827
Dye sensitized	1.65	750
Amorphous silicon	1.7	730
Gallium Arsenide	1.42	873
Organic, e.g., P ₃ HT:PCBM	1.77-1.91	650-700

- Another energy loss mechanism is the recombination of photo-generated charge carriers or the annihilation of photo-excited electron-hole pairs (**Figure I.6**). This recombination can be classified as either intrinsic or extrinsic.
 - The extrinsic recombination is associated to the recombination via defects, commonly referred to as Shockley Read Hall (SRH) recombination. Defects and impurities can form discrete energy levels within the forbidden energy gap of the semi-conductor that provide states for charge carriers to be trapped. As a consequence, the energy is lost as heat [15].
 - The intrinsic recombination is attributed to Auger and radiative recombinations. Auger recombination implies that electron and a hole recombine, but rather than emitting the energy as heat or as a photon, the energy is given to a third charge carrier and converted into heat during the subsequent thermalization back to the band edge. In the radiative recombination process, an electron in the conduction band relaxes to the valence band, recombining with a hole, emitting energy as a photon ($h\nu = E_g$) [16,17].

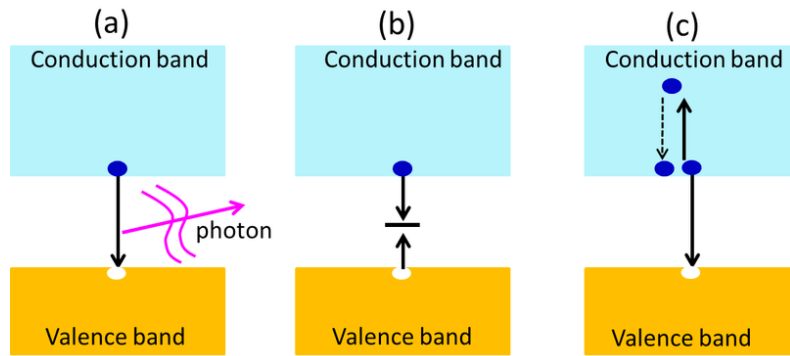


Figure I.6: The possible recombination mechanisms of photo-generated charge carriers: (a) radiative recombination, (b) recombination via defects and (c) Auger recombination [16].

Improvement by either enhancing the light absorption or avoiding recombination has attracted great interest. Recently, new advances in luminescent nanomaterials and material synthesis methods have resulted in introducing lanthanide-based nanostructures to manipulate light in order to overcome the optical losses. Moreover, the reduction of surface recombination can be achieved by surface passivation, which combines the reduction in the trap states present at the surface via a chemical component, and the reduction in the charge carriers available for a recombination process, via a field effect component.

I.3 Solutions for solar cell efficiency improvement

I.3.1 Spectral conversion

Various routes are proposed to address spectral or optical losses, and all of these methods obviously concentrate on a better exploitation of the solar spectrum. An alternative approach to overcome the optical losses is spectral or photon conversion which aims at converting via luminescence phenomenon the incident solar spectrum to match the absorption properties of the semi-conductor device. This process is in contrast to the other concepts, which focus on developing a semiconductor able to match the polychromatic solar spectrum. One advantage of spectral conversion is the possibility to add it to existing solar cells, since the optimization of the solar cell and spectral converter can be achieved separately, photon conversion being treated as an optical process alone [8,10]. Different types of spectral conversion processes can be distinguished as illustrated in **Figure I.7**:

- Down Conversion (DC) or quantum cutting, in which a single absorbed high-energy photon is transformed into two lower energy photons.

- Down Shifting (DS), which is similar to down-conversion, with however, one high-energy photon transformed into one lower energy photon. Energy is lost due to non-radiative relaxation.
- Up Conversion (UC), in which two low-energy (sub-bandgap) photons are combined to give one high-energy photon.

The downconversion and downshifting processes consist in converting the UV part of the solar spectrum into visible light. As a result, the energy loss caused by thermalization is minimized. Meanwhile, the UC process consists in converting the sub-band gap IR part of the spectrum into visible light by photon addition to reduce non-absorption energy losses.

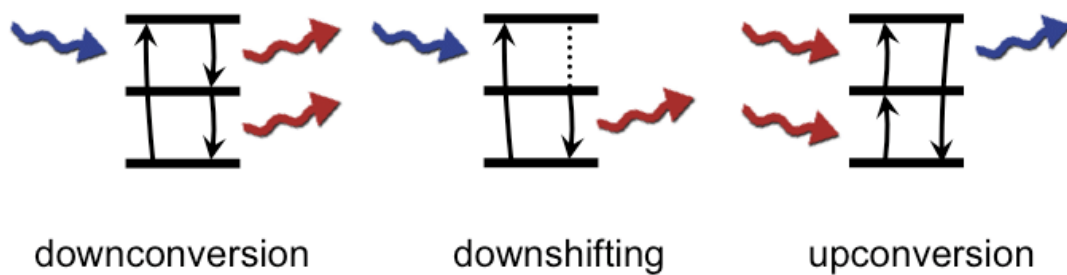


Figure I.7: Energy diagrams showing photon adsorption and subsequent DC, DS and UC processes from [18].

These spectral conversion processes can be achieved using luminescent materials as spectral converters. One family of the materials that are extensively studied for this purpose are the lanthanides or rare-earth systems, due to the suitability of their discrete energy levels for photon conversion inside a wide variety of host materials [19-20]. As presented in **Figure I.5**, UC process is a promising approach to overcome the major energy loss (IR photons not absorbed). For this reason, UC luminescence is the subject of this work and will be described in details in the next section.

I.3.2 Surface passivation

As commonly used in metallurgy, surface passivation aims to avoid degradation mechanism of the material properties from the aggressive environment and provide long-term protection [21]. In photovoltaics and microelectronics applications, this passivation is becoming increasingly important. It includes the protection from aggressive conditions but mainly concerns the inhibition of recombination mechanisms in order to preserve its electronic properties. As intrinsic recombination processes are unavoidable, the objective of silicon surface passivation is to reduce extrinsic recombination. The passivation can be performed by two fundamentally different strategies. Due to the fact that recombination rate is proportional with the interface

defect density (D_{it}), the first strategy is labelled as the chemical passivation which consists in the reduction of the number of defects states at the semiconductor surface such as SiO_x and silicon dangling bonds. The latter defect is associated to electronic orbitals of silicon atom that are not participating in bonding and create trap levels distributed over the band gap leading to non-radiative recombination [22]. This surface defect density can be reduced for example by atomic hydrogen [23]. The second passivation strategy is named as the field effect passivation that consists in the reduction of either majority or minority carrier (electrons or holes) concentration located near the semiconductor-oxide interface [24]. In this approach, surface recombination processes include both electrons and holes. This field can be created by silicon doping or by fixed charges present in a dielectric deposited on its surface. The second way is the most popular and includes the application of an internal electric field below the silicon surface that can be established by an equivalent oxide charge density (Q_{ox}) with the appropriate polarity in the passivation layer. So, either the electron or hole concentration can be dramatically reduced by repelling the carriers away from the surface. Consequently, surface recombination rate is significantly suppressed. Both surface passivation strategies can be achieved by the deposition of thin films on the silicon surface. Nowadays, several deposition techniques, such as PECVD or ALD, allow the deposition of passivation materials at low temperature ($< 450\text{ }^\circ\text{C}$). Many dielectric passivation layers have been extensively studied, including silicon oxide (SiO_2), amorphous hydrogenated silicon nitride ($\text{a-SiN}_x\text{:H}$) and amorphous aluminium oxide (Al_2O_3) [23], [25-26].

Recently, improved passivation has been reported when Al_2O_3 surface passivation layer is deposited by ALD which have attracted much interest because of the excellent conformality and step coverage of the thin films, low defect density and low deposition temperatures. In addition, the impressive performance of passivation using Al_2O_3 is related to the combination of chemical and field-effect passivation induced by the fixed negative charge close to the semiconductor-oxide interface [27]. Furthermore, it is demonstrated that the chemical inertness, high step coverage, and pinhole-free structure of the conformal Al_2O_3 layer can also provide effective anticorrosion protection for the structures against harmful environments [28-29]. It is worth noting that annealing is always necessary to get high level of surface passivation [30]. Within this context, ALD deposited then annealed Al_2O_3 passivated layers are used for this study.

II. Lanthanide UC nanoparticles

UC nanoparticles mostly consist of lanthanide-doped nanomaterials whereby lanthanide ions are diluted in an appropriate inorganic host lattice. Dopants (sensitizers and activators) provide a luminescence center, while host matrices supply a platform for energy transfer between the dopants, and drive them into optimal positions.

II.1 UC phenomenon

The UC phenomenon, as described for the first time in the 1960s, belongs to the Anti-Stokes processes and refers to a non-linear optical process, where a sequential absorption of two or more low energy photons usually at NIR or IR wavelengths leads to the emission of photons with higher energy range from UV to visible wavelengths. This process can be performed by low-power and incoherent excitation sources, such as continuous-wave (CW) lasers, standard xenon or halogen lamps, or even focused sunlight.

Efficient UC is achieved with two ions: one plays the role of sensitizer and the second as activator. Activator ions act as the centers of luminescence, while sensitizing ions increase the intensity of UC luminescence.

II.1.1 UC mechanisms

Various mechanisms can lead to UC phenomenon, which can be either alone or in combination. The three basic mechanisms are excited-state absorption (ESA), energy transfer UC (ETU) and photon avalanche (PA) (**Figure I.8**) [31].

- In the ESA process, a single ion with multiple energy levels absorbs two or more photons. The electron is excited from the ground state to intermediate metastable energy level, and finally populates at excited state, from which UC luminescence takes place [32].
- For PA, it could happen in some circumstances. It is produced only above a certain threshold of the excitation power. Below that threshold, negligible luminescence is observed. This mechanism is not common in nanostructured Lanthanide based UC materials [33].
- The most efficient mechanism for upconversion: energy transfer UC (ETU), is independent of the pump power. This process requires at least two ions in proximity, one being the sensitizer and other acting as the activator. It can be categorized as follows [33-34]:
 - ETU followed by ESA: the sensitizer absorbs the first photon and undergoes a transition to the metastable excited state. After that, the energy is transferred to the activator to promote it to its metastable intermediate state that absorbs a second

photon to generate a final excited state. A radiative relaxation of the final excited state of the activator emits an upconverted photon.

- Successive energy transfer: this process differs from the previous one in a way that the absorption of both photons successively takes place by the sensitizer ion only. The energy is transferred to the activator ion via two successive energy transfer steps, as suggested by the name of the process itself. The activator in its metastable excited state emits an upconverted photon and relaxes back to its ground state.
- Cross Relaxation: this process occurs when a first ion is initially in a higher excited state and exchanges energy with a second ion that is initially in a lower state, resulting in both ions simultaneously changing to intermediate energy states between the two initial states.
- Cooperative sensitization: two ions individually absorb two excitation photons to reach to their excited states and then transfer the energy to the third ion, which first undergoes an excitation and then radiatively de-excites to emit an upconverted photon.
- Cooperative luminescence: two ions individually absorb two incoming photons and then interact to emit a higher energy photon, without involvement of another ion.
- Energy migration upconversion: this process takes place in core-shell type NPs containing four types of ions, named sensitizer, accumulator, migrator and activator. The sensitizer transfers its energy to an accumulator, which from its high-lying excited state, delivers the energy to a migrator ion. Finally, the energy is released to the activator ion that emits an upconverted photon.

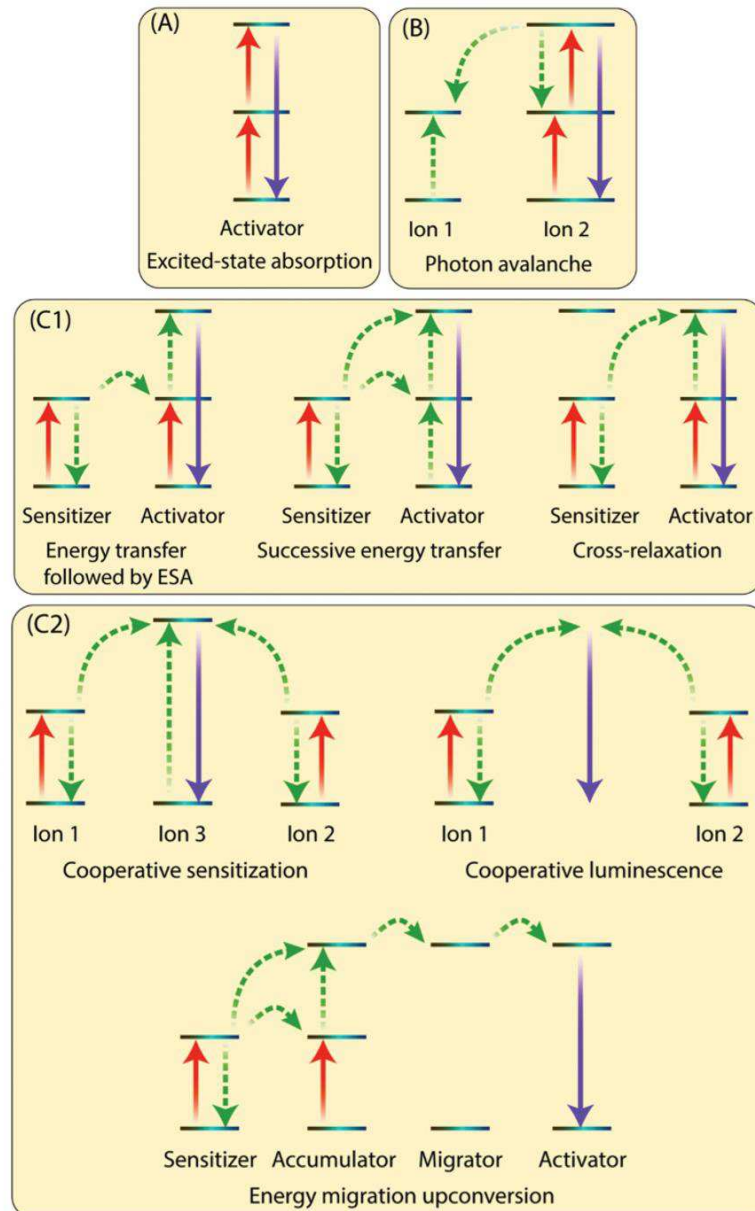


Figure I.8: Schematic illustration of the different mechanisms mainly contributing to the UC process according to ref. [31]

The UC phenomenon is observed in transition metals, actinides, but mainly in the RE elements family, which contain the lanthanide (Ln) series, yttrium, and scandium [32].

II.2 Lanthanide ions as upconvertors

II.2.1 Introduction

The lanthanides family contains 15 chemical elements with atomic number ranging from 57 to 71 (La, Ce, Pr, Nd, Pm, Sm, Eu, Gd, Tb, Dy, Ho, Er, Tm, Yb, Lu). Together with the elements scandium (Sc, number 21) and yttrium (Y, number 39), they are categorized as RE elements. Although once called the rare earths, most lanthanides are not particularly rare in the earth's

crust. Except Promethium, the lanthanides are known to have abundances comparable to many other elements. Thulium, one of the scarcest lanthanides, has an abundance of 0.2 parts per million (ppm), and is more abundant than arsenic or mercury. They are named RE elements since their appearance is limited to relatively rare mines. They do not appear in pure form in nature but together as compounds in minerals and their similar properties make them extremely difficult to isolate.

The discovery of the lanthanides spanned more than a century of work, beginning in the late 1700s. The first lanthanide containing mineral to be identified, which is called first ytterbite is found in 1787 by Carl Axel Arrhenius, in a small Swedish village called Ytterby. The elements ytterbium, yttrium, erbium and terbium are named after this village later on. With time, various lanthanide elements were separated from this mineral. During the 19th century, the discovery of individual lanthanide elements is handicapped by the similarity of neighbouring elements in their chemical properties. Later on, with the invention of the spectroscope, the English physicist Henry Moseley demonstrates the existence of 15 lanthanide elements in total, from lanthanum to lutetium. Lanthanides are divided according to their weight into light and heavy lanthanides (**Figure I.9**).

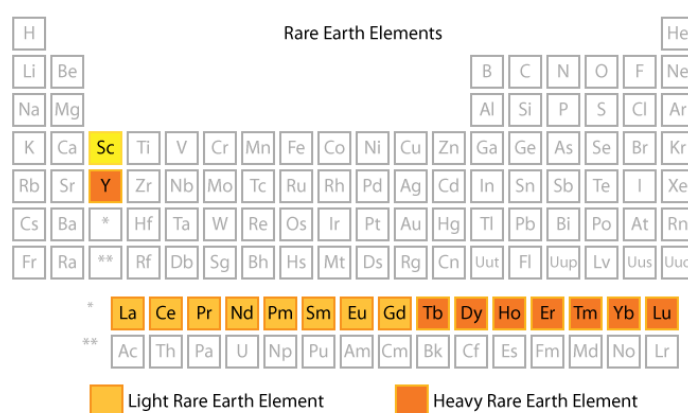


Figure I.9: Classification of RE elements in the periodic table.

All these elements can form trivalent cations and the +3 oxidation state is dominating. Ln^{3+} ions have special $4f^n 5d^{0-1}$ inner shell configurations, which are well-shielded by outer shells that isolated them from forming chemical bonding. That makes these elements relatively stable providing them small interaction with environmental crystal fields and unique energy level structures. UC luminescence results from $4f - 4f$ transitions. All lanthanides have an electron configuration starting from Xenon with additional electrons in the 6s, 5d, and 4f orbitals. They can be represented as $[\text{Xe}] 4f^x 5d^y 6s^2$ where x ranges from 0 to 14, and y ranges from 0 to 1.

As a result, the PL emission profiles of 4f orbitals are very sharp. Their position depend on the specific symmetry of the nearest environment of the rare-earth ion. In fact, PL is not a property for all lanthanide elements, as shown by the partial energy diagram of the lanthanides in **Figure I.10**. The lanthanide elements, Yb^{3+} , Ce^{3+} and Gd^{3+} have simple energy level structure, and elements: Pr^{3+} , Nd^{3+} , Sm^{3+} , Eu^{3+} , Tb^{3+} , Dy^{3+} , Ho^{3+} , Er^{3+} and Tm^{3+} are luminescent.

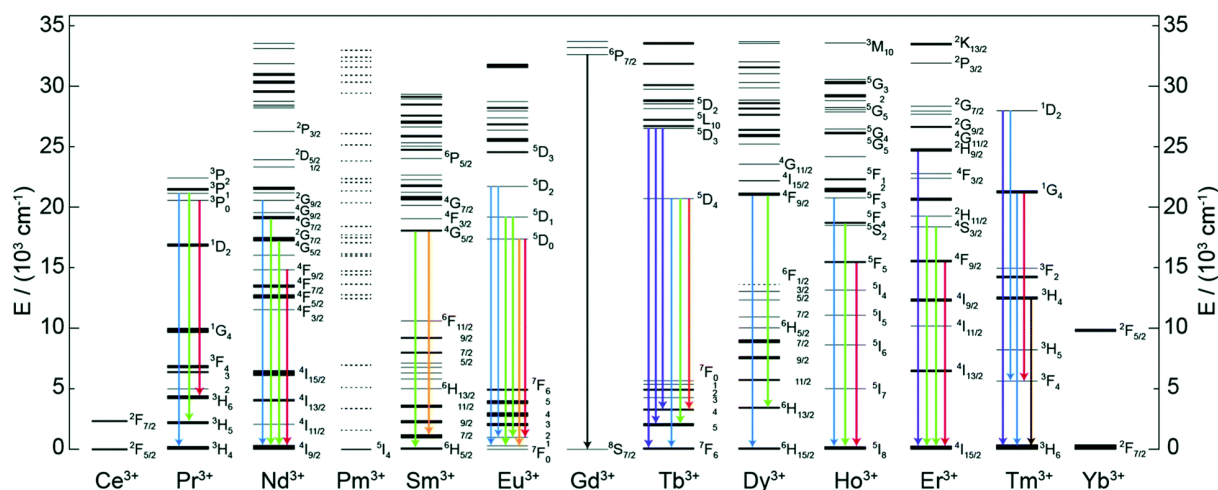


Figure I.10 : Partial energy level diagram of Ln^{3+} ions and the corresponding radiative emissions [33].

UC luminescent nanoparticles composed of lanthanide ions doped inorganic host material as spectrum modifier have attracted great interest due to their outstanding luminescent properties, which are widely used for biomedical applications, including biosensing, imaging, and theranostics [34-36], wastewater treatment [37], also to improve the efficiency of solar cells [38-39].

Theoretically, most lanthanide ions can undergo the NIR to visible UC process. However, relatively efficient UC is only possible with few trivalent lanthanide ions. Emission of different colors can be obtained in a material with different activators and their combinations. The most RE element used as a sensitizer is Yb^{3+} . This ion has a simple energy level structure with two levels ($^2\text{F}_{7/2}$ and $^2\text{F}_{5/2}$) and a larger absorption cross section compared to other trivalent rare-earth ions. Absorption can take place over a wide range of wavelengths between 910 nm and 980 nm. The energy separation of Yb^{3+} $^2\text{F}_{7/2}$ ground state and $^2\text{F}_{5/2}$ excited state must match up well the transitions of an activator dopant ion, which lead to easy charge transfer between its excited state and the activator states. For visible emission, Er^{3+} , Tm^{3+} , Ho^{3+} , Tb^{3+} and Pr^{3+} are frequently selected as activator dopants. UC emissions of the listed elements are reported in **Table I.2**.

Table I.2: The most studied UC couples based on Yb³⁺ as a sensitizer.

Sensitizer	Activators	UC emissions (nm)	Ref.
Yb ³⁺	Ho ³⁺	540, 642, 749	[40]
	Tm ³⁺	290, 345, 474, 362, 450, 576, 643, 807	[41]
	Tb ³⁺	412, 436, 487, 541, 584, 620	[42]
	Er ³⁺	525, 548, 670	[43]
	Pr ³⁺	457, 486, 510, 550	[31]

II.2.2 Erbium-Ytterbium couple

Out of the different ions, Er³⁺ and Yb³⁺ are recognized as an ideal couple for integration in many fields (**Table I.3**). The choice of this couple is based on the strong energy level matching between them. When irradiated, the Yb³⁺ ion absorbs a photon, as a result of which a transition to the excited state of ²F_{5/2} occurs. Then it relaxes to the ground state of ²F_{7/2}, non-radiatively transferring energy to the nearest ion of the acceptor, which then passes into the ⁴I_{11/2} state. In addition to energy transfer, the Er³⁺ acceptor ion can absorb a quantum of exciting radiation directly and go to the ⁴I_{11/2} state, but the probability of such a process is much lower.

From the energy transfer between the two levels: ²F_{5/2} (Yb³⁺) → ⁴F_{7/2} (Er³⁺), then the ⁴F_{7/2} level relaxes rapidly and non-radiatively to the next lower ²H_{11/2} and ⁴S_{3/2} levels in Er³⁺ because of the short lifetime of the ⁴F_{7/2} level. The radiative transitions of ²H_{11/2} ⇒ ⁴I_{15/2} and ⁴S_{3/2} ⇒ ⁴I_{15/2} lead to green emission in the region 510–570 nm. For the red emission, the ⁴F_{9/2} level is generated from two possible pathways: population of the ⁴F_{9/2} level by non-radiative relaxation from the ⁴S_{3/2} to the ⁴F_{9/2} level and CR transition: ⁴F_{7/2} + ⁴I_{11/2} → ⁴F_{9/2} + ⁴F_{9/2}. Finally, the ⁴F_{9/2} level relaxes radiatively to the ground state, and releases red emission observed in the 610–670 nm region. The green emission is always intense at the expense of red luminescence due to weak absorption cross relaxation. The Energy level diagrams describe the photons absorption and energy transfer in Er³⁺-Yb³⁺ and their common properties are presented in **Figure I.11** and **Table I.4**. Furthermore, the positions of the energy level for Er³⁺ and Yb³⁺ dopants in different hosts remain almost the same because of the shielding effect of their outer closed 5s² and 5p⁶ shields.

Table I.3: Summarize of the integration of Er³⁺-Yb³⁺ couple in various fields.

Sensitizer/Activator	Hosts	Application	Ref.
Er ³⁺ / Yb ³⁺	CeO ₂	Dye sensitized solar cells	[44]
	Lu ₂ MoO ₆ phosphors	Fiber optical temperature sensor.	[45]
	KLu ₂ F ₇ nanocrystals	Solar cells, multicolor display and bioimaging.	[46]
	TiO ₂ Nanorod Arrays	Perovskite Solar Cells	[39]
	NaYF ₄	Drug delivery system	[47-48]

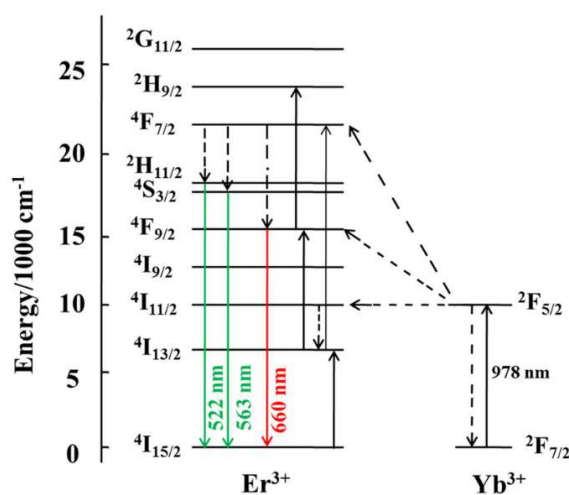


Figure I.11: Schematic energy level diagram of the sensitization of Er³⁺ by Yb³⁺ according to [49].

Table I.4: The RE elements listed with common properties [50].

Property	Erbium	Ytterbium
Atomic Mass (g/mol)	167.26	173.04
Electronegativity	1.24	1.1
Melting Point (°C)	1529	824
Boiling Point (°C)	2868	1196
Density (g/cm ³)	9.066	9.321

II.2.3 Parameters influencing the UC luminescence

The properties of UC luminescence are strongly influenced by several factors including: the synthesis method, particle size, concentration and spatial arrangement of dopant ions, surface chemistry, and the excitation power density (P).

- An increase in the dopant concentration is accompanied by an increase in the emitted light intensity due to the high absorption efficiency, which is possibly due to strong energy transfer between the dopant ions. However, above a certain concentration, the luminescence intensity starts to decrease due to the concentration quenching. The quenching starts when there is a sufficient reduction in the average distance between luminescent centres that leads to non-radiative energy transfer [51]. One of the most studied UC nanoparticles converters is β -NaYF₄:Er³⁺-Yb³⁺ excitable at 976 nm. The optimum dopant concentration of β -NaYF₄ is assumed to be 17% – 20% of the sensitizer Yb³⁺ and 2% – 3% of the activator Er³⁺ [52]. Bian et al. reported an investigation of KLu₃F₁₀ samples codoped with Yb³⁺ and Er³⁺ [12]. For a fixed Yb³⁺ doping of 16%, an optimum Er³⁺ doping of approximately 2% is obtained. The optimized Er³⁺-Yb³⁺ percents incorporated into TiO₂ is found to be 5 mol%Er³⁺– 5 mol%Yb³⁺ better than codoped TiO₂ with 5 mol%Er³⁺–10 mol%Yb³⁺ [53]. For LaSr₂AlO₅:Er³⁺-Yb³⁺ phosphors, the intensity of green and red emissions increases as the Er³⁺ concentration increases up to 1 mol.%, reaching a maximum at this concentration, and then is quenched for higher Er³⁺ concentrations. The smallest upconverted emission is observed for 6 mol.% of Er³⁺ [54]. In conclusion, the optimal doping concentrations are dependent on the host matrix. Lanthanide ion doping concentrations can also affect the emission intensities, at low dopant concentration, the CR process negligibly populates the red emission level. Thus, the green emission is stronger than the red emission. The rate of CR process is inversely proportional to the distance between two neighbouring ions. It occurs when the distance between ions is small. With increasing the ions concentration, the distance between the neighboring ions decreases resulting in the higher possibility of CR process. Some researchers [45-55] reported that the intensity of red emission could be increased with increasing the dopants concentration by improving the CR process (${}^4F_{7/2} + {}^4I_{11/2} \rightarrow {}^4F_{9/2} + {}^4F_{9/2}$). The doubling of the ions in ${}^4F_{9/2}$ offers a reason for increasing the red emission. From the energy level diagram of Er³⁺, the energy gap between ${}^4F_{7/2}$ and ${}^4F_{9/2}$ (approximately 5200 cm⁻¹) matches well with the energy gap between ${}^4F_{9/2}$ and ${}^4I_{11/2}$ (approximately 5100 cm⁻¹). Moreover, both ${}^4F_{7/2}$ and ${}^4I_{11/2}$ could be

directly filled by the ET process, which guarantees major populations in the two energy levels [56].

- For the synthesis method and the calcination step, the non-radiative transitions can occur by quenching centers (traps) randomly distributed in the material. Surface states related with some anionic groups such as OH⁻ originate from two aspects: on one hand, the synthesis is conducted in aqueous solution, and thus OH⁻ ions come from H₂O, and on the other hand the sample is annealed in air, and thus OH⁻ ions come from air [57]. OH⁻ group have high-energy vibrational modes (3200– 3600 cm⁻¹) that could be situated between ⁴I_{15/2} and ⁴I_{13/2} levels of Er³⁺. These high-energy vibrations would strongly quench the excited states of Er³⁺ by multi-phonon relaxation, thus leading to a great influence on the UC processes. It has been reported that OH⁻ group quench the luminescence of NaYF₄:Er³⁺-Yb³⁺ by facilitating multiphonon relaxation of ²H_{11/2} and ⁴S_{3/2} to ⁴F_{9/2} also ⁴I_{11/2} to ⁴I_{13/2}. Both of these relaxation mechanisms favor the population of the ⁴F_{9/2} state (either directly or via ⁴I_{13/2} → ⁴F_{9/2} transition, respectively), from which the red luminescence occurs at the expense of green luminescence [56], [58-59].
- The UC emission intensity is dependent on the pump power density. The relationship between an unsaturated UC luminescence emission intensity and the pump power can be represented by the following equation [52,60] :

$$I \propto P^n$$

Where I is the emitted intensity, P is the pump power and n represents the number of incident photons required to excite the Er³⁺ ions from the ground state to the emitting excited state. The UC emission intensities increase when the laser pump power is increased. The number of pumping photons n can be estimated from the slope of the UC intensity versus the laser excitation power in a log–log plot. **Figure I.12** shows the dependence of the intensities of UC peaks on the excitation intensity of the 980 nm laser. The slopes of the three curves are 1.481, 1.877, and 1.435 at emission peaks of 525, 550, and 655 nm, respectively. These results explain that the UC mechanism of green and red emissions occurs as a result of a two-photon UC process. Hence, the decrease in the slope of an UC luminescence is also expected with increasing laser pump power [61].

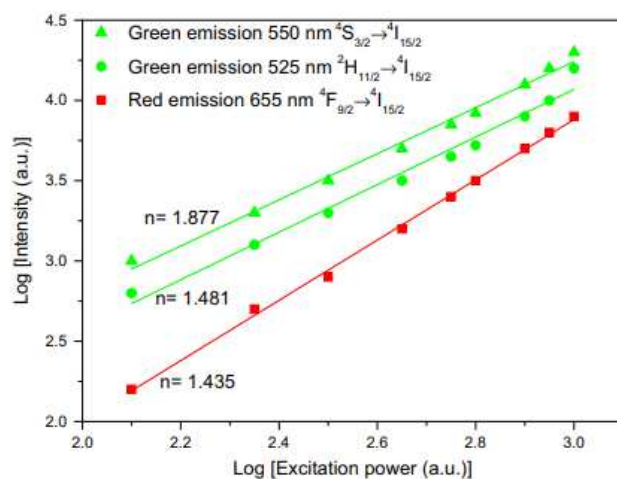


Figure I.12: Log-log plot of the pump power 980 nm laser dependence of UC emissions centered at 525, 550 and 655 nm emission intensity of the Er^{3+} - Yb^{3+} codoped TiO_2 ions as reported in [53].

- The host material is the parent material, which accepts a foreign element that leads to the enhancement in optical properties of a system. It is demonstrated in other studies that the structure of the host lattice and its interaction with the sensitizer and activator ions have a strong influence on the UC process [62]. Lanthanide are generally incorporated in an inorganic host. To date, the UC process has been widely studied in various nanoscale host matrices, such as fluorides and other halides (chlorides, bromides, and iodides), oxides, oxysulfides, phosphates, vanadates, among others. Since the energy of the phonon greatly affects the efficiency of the UC process, it must be low in the ideal host materials. Phonon energy is the resonant energy caused by lattice vibrations so it must be low in order to minimize non-radiative loss and maximize the radiative emission. The phonon energy values for some matrix materials are presented in **Table I.5**. It is important to select properly the composition of the host matrix because it has a high impact on the UC luminescence efficiency and emission peak ratios. Its critical role lies on the distance between the lanthanide ions, their spatial position, their coordination numbers, and the crystal fields around them [63]. The most important quality of the host matrix is that the host lattice needs to be transparent in the visible and NIR regions with low phonon energy to prevent non-radiative multiphoton relaxations that can lower the UC efficiency. Additionally, chemical and thermal stabilities are required in order to use UC material in various applications. Heavy halides, such as chloride, bromide and iodide-based materials, have phonon energies lower than 300 cm^{-1} but are hygroscopic, so cannot be widely used in applications. Many studies in recent years are focused on fluorides because they exhibit low phonon energies (between 300 and 500 cm^{-1}) [64]. The most investigated fluoride is NaYF_4 . Meanwhile,

fluorides have poor chemical stability and may cause environmental issues due to the toxicity, which may limit its applications in some situations [65]. Despite their relatively high phonon frequencies ($\sim 500 \text{ cm}^{-1}$), oxide host materials are desirable due to their high chemical and thermal stabilities, low cost and high mechanical strength [66]. Therefore, more intention is focused on the fabrication of Ln^{3+} ions embedded in inorganic oxide matrix. Among the wide range of oxides such as ZrO_2 , Y_2O_3 , TiO_2 drew much attention. For instance, Er^{3+} - Yb^{3+} codoped Y_2O_3 presents higher phonon energy (597 cm^{-1}), but a heat treatment above 750°C is required to have yttrium oxide crystallized in the cubic system with good crystallinity. Similarly, for Er^{3+} - Yb^{3+} codoped ZrO_2 , the heat treatment mostly used reported is 1000°C to have the cubic phase. However, a crystallized phase can be obtained at relatively low temperatures. Indeed, properties such as biological and chemical inertness, stability toward corrosion, low cost due to abundant reserves, high natural abundance and no toxicity make TiO_2 a suitable semiconductor for different applications.

Table I.5: Phonon energy of the most frequently used matrices for rare-earth ions.

Host	Phonon energy (cm^{-1})
Phosphate glass	1200
Fluoride glass	550
Chalcogenide glass	400
Y_2O_3	597
ZrO_2	470
NaYF_4	350
LaF_3	300
TiO_2	450

II.3 TiO_2 as host matrix

II.3.1 Crystal structure

Titanium (Ti) is a transition metal (atomic number 22). It is a light, strong and corrosion-resistant metal. Titanium dioxide (TiO_2) is the most commonly used compound of titanium. Since its commercial production in the early twentieth century, TiO_2 has been widely used as a pigment in sunscreens, paints, cements and photocatalyst. TiO_2 powder is chemically inert and stable under sunlight. It occurs in three different crystalline phases, namely, rutile, anatase, and brookite. While rutile is the stable phase, both anatase and brookite are metastable [67]. Anatase

and rutile are the forms more frequently studied because pure brookite is quite difficult to synthesize. These three crystalline forms are (**Table I.6**):

- Anatase structure is formed from a three-dimensional arrangement of TiO_6 octahedra linked together by edges to form a chain zigzagging along axis [100]. Anatase crystallizes in the $I4_1/amd$ space group, with titanium occupying site 4a and oxygen occupying site 8e. TiO_2 -anatase is n-type semiconductor, which has a band gap $\sim 3.2\text{eV}$. This phase is preferred from a kinetic point of view for temperatures below 600°C .
- Rutile crystallizes in the $P4_2/mnm$ space group in which the titanium occupies site 2a and oxygen site 4f. The octahedral TiO_6 are ordered parallel to the c axis. Each octahedron shares an edge with his neighbor in this chain. Each chain is connected to four neighboring chains by pooling of summits thus leaving tunnels with a square section. TiO_2 -rutile is an n-type semiconductor, which has a band gap $\sim 3.0\text{ eV}$. Rutile phase begins to appear at $\sim 600^\circ\text{C}$. The kinetics of anatase to rutile transition is dependent on various factors such as impurities, synthesis method and heat flow conditions.
- Brookite crystallizes in the $Pbca$ space group, along with titanium and oxygen on the 8e site. The brookite structure results from a three-dimensional arrangement deformed octahedra connected to each other by edges and vertices. The octahedral TiO_6 forms, by pooling edges, a zigzag chain of octahedra according to [001] direction. These chains sharing edges according to [010] direction, constitute a layer of double chains in the plane (100). These layers combine along [100] direction by setting in common summits. TiO_2 -brookite is an n-type semiconductor which has a band gap equal to anatase one ($\sim 3\text{eV}$).

The anatase to rutile transformation is reconstructive, which means that the transformation involves the breaking and reforming of bonds. This transformation involves a contraction of the c-axis and an overall volume contraction of 8%. This volume contraction explains the higher density of rutile compared to anatase. The c-axis of anatase appears to be significantly longer than that of rutile only because anatase has more atoms per unit cell than rutile [67].

Table I.6: Crystallographic data of the anatase, rutile and brookite phases of TiO₂ [68].

	Rutile	Anatase	Brookite
Weight (g/mol)		79.89	
Z	2	4	8
Crystal system	Tetragonal	Tetragonal	Orthorhombic
Point group	4/mmm	4/mmm	mmm
Space group	P4 ₂ /mm	I4 ₁ /amd	Pbca
Unit cell : a	4.5845	3.7842	9.184
Unit cell : b	-	-	5.447
Unit cell: c	2.9533	9.5146	5.145
Volume	62.07	136.25	257.38
Density (g/cm ³)	4.2743	3.895	4.123
Refraction index	2.48-2.56	2.61-2.89	2.58-2.70

II.3.2 Stability of crystalline phases

The Gibbs free energy (G) of a nanoparticle system comprises the bulk free energy (G_b) and the surface free energy (G_s). Inequality in the specific surface energies of two polymorphs can lead to a reversal in the relative magnitudes of their Gibbs free energies under a specific size and hence can affect their relative phase stabilities. Phase stability reversal in nanocrystalline TiO₂ as a function of particle size is reported by Gribb et al. [69], also proven by the thermodynamic analysis and calorimetric determination conducted by Zhang et al. [70] and Ranade et al.[71], respectively. In other words, the smaller the particle size, the higher the surface/volume ratio, the higher the surface free energies and surface stresses. Therefore, anatase polymorph for sizes below roughly 14 nm whereas rutile for sizes larger than 35 nm and brookite for particle sizes from 14 to 35 nm are the most thermodynamically stable, respectively [72-73]. Anatase is thus the stable nanophase of TiO₂, whereas rutile is the stable bulk phase of TiO₂ at high temperature and pressure.

Many researches demonstrate that lower symmetric symmetry is favourable for higher UC efficiency. So, the UC property of TiO₂-anatase phase is better than that of rutile (lower symmetry) [74].

II.3.3 Potential applications of TiO₂ nanoparticles in PV

Over the past decades, TiO₂ nanomaterials have been intensively studied for their application in solar to electricity conversion because of their compatibility with modern technologies [75]. These steady progresses have demonstrated that TiO₂ nanomaterials play an important role in the search for efficient and low cost photovoltaic technologies.

TiO₂ based PV devices provide optimal results. One important application of TiO₂ nanomaterials in PV fields is Dye-sensitized solar cell- DSSCs [75-76]. UC luminescent Er³⁺-Yb³⁺ codoped TiO₂ nanoparticles spin-coated on Ti-mesh supported TiO₂ nanowire arrays are used as photoanode for fully flexible dye sensitized solar cell. The photoelectrical conversion efficiency of the device is enhanced to about 52% compared when using the codoped matrix [77]. In addition, Chi-Hwan et al. [78] show that the performance of dye-sensitized solar cell increases by 15% when Er³⁺-Yb³⁺ codoped TiO₂ is used as scattering layer.

Xiaoli et al. [79] reported an enhancement by 20.8% in power conversion efficiency in perovskite solar cells based on Er³⁺-Yb³⁺ co-doped TiO₂ as an electron transfer material compared to the undoped TiO₂.

GeO₂-PbO glasses containing Eu³⁺ ions and TiO₂ nanoparticles are explored by Gunji and co-authors [80] in order to enhance the efficiency of polycrystalline silicon solar cells. Results reveal a maximum efficiency enhancement of 16% for the silicon solar cell covered with GeO₂-PbO glass doped with 1% of Eu₂O₃ and 0.5% of TiO₂ heat-treated for 24 h. This efficiency enhancement is attributed to the location of the Eu³⁺ ions in sites of low symmetry of anatase-TiO₂ nanoparticles.

II.4 Synthesis methods

Luminescence properties of Er³⁺-Yb³⁺ codoped TiO₂ depend on the synthesis method, that greatly influences the size, shape, crystal phase, crystallinity (crystal size) and distribution of dopants in the particles. In order to have excellent luminescence properties, the dopants need to be uniformly distributed into the host particle, and the crystallinity of the host matrix should be high without forming any impurity phase [81]. Therefore, it is important to use a suitable synthesis method for the production of UC TiO₂ nanoparticles having excellent light emission characteristics.

For instance, it is reported that at high calcination temperatures (~ 700°C), the UC luminescence intensity can decrease because Yb³⁺ is no longer well-substituted in the host crystal lattice and

involved in the formation of $\text{Yb}_2\text{Ti}_2\text{O}_7$ crystals (Er^{3+} - Yb^{3+} codoped TiO_2). This means that Yb^{3+} no longer serves as a sensitizer in TiO_2 : Er^{3+} - Yb^{3+} .

II.4.1 Spray pyrolysis

Spray pyrolysis is an effective, low-cost and quite versatile method for the synthesis of submicron and nano-sized materials, especially oxides. It is considered intermediate to both gas-phase and liquid-phase methods [82]. It is based on the formation of an aerosol from various precursor solutions, which can be a solution of metallic salts or a colloidal solution.

The fabrication steps include [83]:

- Dissolution of the inorganic precursors in a suitable solvent to get the liquid source
- Generation of droplets from this liquid source using two-fluid atomization or ultrasonic atomizer
- Transport of the droplets into a preheated chamber using a carrier gas
- Vaporization of the droplets in the chamber and trapping with a filter, promoting their decomposition to give the respective oxide materials
- Selective reduction of the metal oxides to produce the respective metallic materials

The use of two-fluid atomization has the advantage of high throughput but the disadvantage of broad droplet size distribution that leads to broad particle size distribution. Ultrasonic atomization has the disadvantage of low throughput, but on the other hand, narrow droplet size distribution and therefore, narrow particle size distribution is obtained. The size and morphology of the particles are dependent on the concentration of reactants in the precursor solution, nature of additives, flow rate of droplets, and the temperature of the furnace [84]. However, the nanoparticles are arranged in aggregates (whose shape appears to reflect the droplet from which they formed) which may be difficult to separate. However, as every other method, a spray pyrolysis technique has some disadvantages, including that it is not easy to scale-up (yield is very low) and there are difficulties with the determination of the growth temperature. Serdar et al. [85] have reported the synthesis of 0.5% Er^{3+} doped TiO_2 using spray pyrolysis method with a post heat treatment at 550°C - 2h. They obtained a mixture of anatase, rutile and pyrochlore ($\text{Er}/\text{Yb}_2\text{Ti}_2\text{O}_7$) with an average particle size about 135 nm (XRD). With this method, Er^{3+} - Yb^{3+} codoped anatase TiO_2 submicron sized spherical particles (680 nm-SEM) are obtained after a post heat treatment at 700°C [81].

II.4.2 Co-precipitation

The co-precipitation is a simple, economical and industrially viable technique that includes the separation of a solid containing various ionic species from a solution phase. The precipitation usually starts within an acidic solution and subsequently added with alkaline solution to attain a neutralized precipitate. Ammonia or sodium bicarbonate are commonly used as a precipitating agent. Then, the precipitate is washed several times and dried. This is followed by calcination in a furnace at appropriate temperatures that results in the formation of the final powder [86]. For the synthesizing route, the optimization of operating conditions such as concentration of solution, pH, temperature, and stirring speed of the mixture is required in order to obtain the final product with required properties. The pH of the co-precipitation mixture has a crucial effect on the chemical, structural, and textural properties of the final material. The co-precipitation method is often preferred to other processes because it involves simple steps and the composition is easy to control. Nevertheless, the problem of this method is that undesired impurities co-precipitate. In addition, this procedure usually produces poor crystalline nanoparticles, and for this reason a post heat treatment is required. Ramachari et al have synthesized UCe^{3+} - Yb^{3+} codoped ZrO_2 nanoparticles with a size range from 30 to 35 nm. Also, spherical shaped (0.2-1%) Dy^{3+} doped TiO_2 nanoparticles annealed at 600°C for 2h have been synthesized with wide size distribution ranging from 12 to 30 nm [87].

II.4.3 Microwave

Microwave-assisted synthesis is a green and effective method for preparation of different assemblies. It have been widely used to elaborate oxide, hydroxide and sulfide nanoparticles [88]. The microwaves are electromagnetic radiations between the infrared region and radio waves with wavelength ranges from 0.01 to 1 m, which are significant to induce nucleation or growth of material. Generally, microwaves interact with polar molecules in solution. This interaction leads to the rotation and vibrational motion of polar molecules and generates heat within the material. The major advantages of this process are: uniform heating of the material and shorter synthesis time, no selective heating of the surface, energy saving process, lower processing cost, small narrow particle size distribution, and high purity. Hai-Qiao et al. [89] reported that a microwave assisted approach allows the synthesis of monodisperse, luminescent upconverting nanocrystals Er^{3+} - $\text{Yb}^{3+}/\text{Li}^+$ codoped NaYF_4 within 5 min.

II.4.4 Sol-gel

This technique provides efficient routes for synthesizing highly homogeneous, cost-effective nanomaterials with high purity at low temperatures. It insures the preparation of inorganic polymers or ceramics from solution through a transformation from liquid precursors to a sol and finally to a gel [90]. This method has excellent control over the texture and surface properties of the materials. In general, sol-gel method can be described in five key steps described below: formation of clear colloidal solution by hydrolysis and partial condensation of molecular precursors, condensation of sol particles into a three-dimensional network producing a gel material, aging, drying and thermal annealing (**Figure I.13**) [91- 92]. This method will be detailed in **chapter II**.

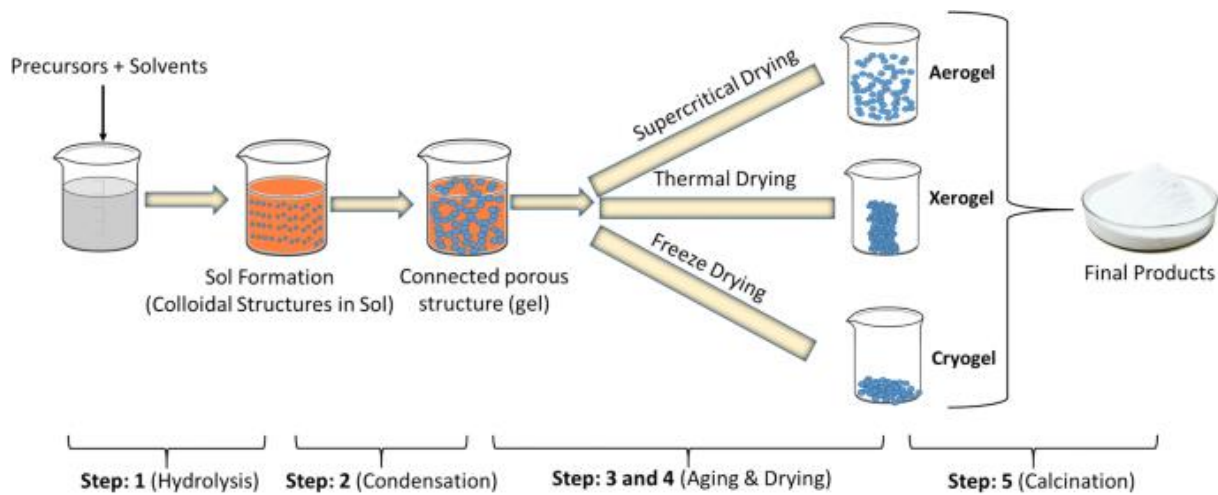


Figure I.13 : Steps involved in sol-gel process as reported in [92].

Different morphologies (particles, rods, wires) at the nanometer scale can be obtained using sol-gel method as shown in **Figure I.14**.

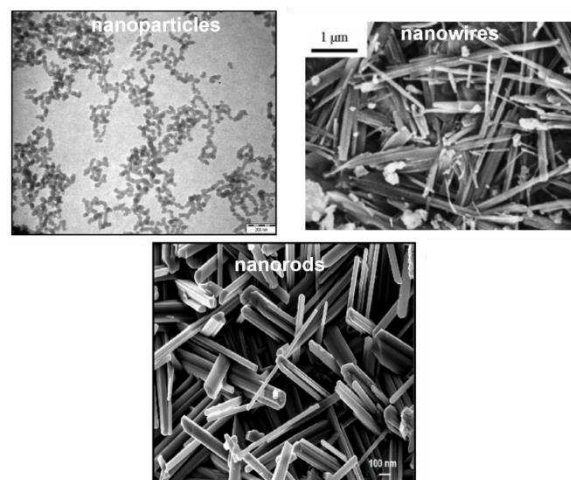


Figure I.14: Different shapes of materials synthesis by sol-gel method [93-95].

For the preparation of lanthanides doped nanomaterials, this offers the easy incorporation of functional ions in the suitable host materials such as TiO_2 , $\text{B}_2\text{Ti}_2\text{O}_7$, $\text{BaGd}_2(\text{MoO}_4)_4$ [96]–[99]. The main disadvantages of this process that could be cited are the long processing time, the use of organic solutions that can be toxic and the residual hydroxyl and/or carbon groups [100].

III. Colloidal dispersion of UC nanoparticles

Colloidal dispersion (also referred to colloidal suspension) are suspensions of particles in a liquid phase. For solar cell applications, the dispersion and stability of UC nanoparticles in a liquid medium are important steps in coating preparation, requiring the control of nanoparticles aggregation to obtain a good dispersion [101].

When particles dimension is low, typically in micrometers or less, and when they are dispersed in a solvent, Van der Waals attraction forces and Brownian motion play important roles, whereas the influence of gravity becomes negligible [102]. Van der Waals force is a weak force and becomes significant only at a very short distance. Brownian motion ensures the particles colliding with each other all the time. When particles dimension reduces, typically in micrometers or less, and are dispersed in a solvent, van der Waals attraction force and Brownian motion play important roles and their combination would result in the formation of aggregation of the nanoparticles [103]. This process occurs when colloidal particles interact attractively. They stick to each other, forming progressively larger aggregates to reduce this interfacial energy. The aggregates then grow until they reach a critical size and sediment. For this reason, repulsive interactions between the particles are required to insure the stability of a colloidal suspension by making the particles repel each other. This can be performed by exploiting electrostatic forces, in charge stabilisation, or by modifying the interfaces by attaching polymer chains to them, in steric stabilisation

III.1 Stabilization of colloidal dispersion

There are two primary methods to stabilize a colloidal dispersion against Van der Waals force: steric stabilization and electrostatic stabilization (**Figure I.15**).

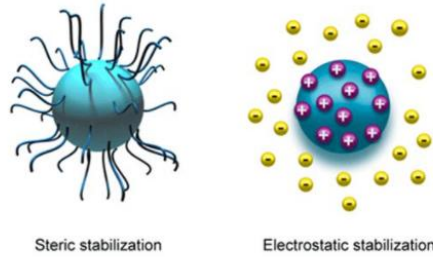


Figure I.15 : Schematic representation of the two mechanisms of particles stabilization [104].

III.1.1 Steric stabilization

Layers of large molecules, such as long chain polymers, are adsorbed onto a particle surface. The steric stability depends on polymer concentration, temperature, solubility of the polymer, and average chain length. The coating may be physically adsorbed on the particle or chemically bonded to it. The physical mechanism underlying steric stabilization is strongly related to the thermodynamic behavior of polymers in solutions. However, the use of steric stabilization will require a heat treatment to eliminate polymers ($< 400^{\circ}\text{C}$) is undesirable for the application.

III.1.2 Electrostatic stabilization

In electrostatic stabilization, when the particles are dispersed in a polar liquid such as water the particle surface an electric charge appears. The counter-ions discharged into the liquid move away from the surface of particles in Brownian motion but nevertheless remain in its field of force. The result is an electrical double layer surrounding the particle, composed of the counterions and the ions [105-106]. When two particles approach each other, overlap of their double layers creates a repulsive force, which can stabilise the particles against aggregation. Electrostatic stability depends on pH, additives and concentration of solution. The surface potential and the ionic strength in the solution are the two most important parameters controlling electrostatic stabilization in aqueous as well as non-aqueous solvent [107].

Contrarily to steric stabilisation, electrostatic stability does not need any further heat treatment, and therefore is an effective solution.

IV. Nanoparticles wet thin film deposition techniques

When it comes to deposit highly uniform wet thin films, there are many different wet-processing techniques capable of producing high-quality films at low cost. Each processing technique has its own unique advantages and disadvantages, as well as critical parameters that must be monitored carefully to achieve desired coatings with a good quality.

IV.1 Doctor-blade technique

Doctor blade or tape casting is one of the extremely used techniques for producing thin uniform films over large surface areas on an industrial scale [108-109]. In this process, a slurry containing a suspension of ceramic particles along with other additives (such as binders, dispersants or plasticizers) is placed on a substrate beyond the doctor blade. It involves either moving linearly a blade over the substrate or moving a substrate underneath the blade at a relative movement. A drying step is essential at the end of the process. This process is suitable to coat substrate with a very wide range of wet film thicknesses ranging from 20 to several hundred microns [110]. However, the produced wet film thickness has poor reproducibility, also this method cannot offer the nanoscale uniformity or extremely thin films that other techniques can offer [111-112].

IV.2 Dip-coating technique

This process could be defined as producing films by the deposition of liquid phase solutions containing hydrolysable metal compounds or readily formed particles into the surface of a substrate [113]. Films with the thickness of a few microns to hundreds of microns can be produced. An alternative way of dip-coating is to keep a substrate horizontally, while moving it downward until one of the substrate faces comes into contact with the liquid surface. Dipping may be manual or automatic.

The advantage of this process is that no stress and no damage or distortion may occur. Nevertheless, the main disadvantages are that the produced film may not be of good quality and has non-uniform thickness. In addition, there is a probability to create defects due to the instabilities in the dip coater or the variation of withdrawal speed [114-115].

IV.3 Spin-coating technique

Spin-coating technique is one of the fastest, low temperature and low cost methods employed to produce uniform thin films with a full surface coverage with thickness of the order of micrometers and nanometers [116-117]. This process is based on centrifugal forces created by a spinning substrate to spread a coating solution over a surface of the substrate that is fixed to a plate by an aspirator.

Four stages can describe the spin coating process: solution deposition, spin-up, spin-off and solvent evaporation as presented in **Figure I.16**.

- **Solution deposition:** it is a simple step where either a manually (pipette or syringe) or an automated pumping system and programmable arm on hydrophilic substrate dispenses a

known volume of the solution. Dispensing of the liquid occurs as the substrate is stationary (static dispense) or when it is spinning at a low speed (dynamic dispense) [116].

- **Acceleration (spin-up):** the second stage is the acceleration of the substrate up to its final and desired rotation speed. The substrate starts to rotate to induce a centrifugal force, which helps to spread the solution all over the wafer or substrate. This acceleration will influence the final coating coverage. A high acceleration will lead to a lower coating coverage.
- **Constant speed (spin-off):** the third stage is the spin of the substrate at a constant rate. Fluid viscous forces predominantly define the film thickness. This stage is also known as flow controlled stage.
- **Solvent evaporation:** in this stage, the substrate is rotating at a persistent rate and solvent evaporation controls the film thickness. When the evaporation of the entire solvent is completed, a solid film is produced. This stage is also known as evaporation controlled stage. However, solvent should evaporate at room temperature otherwise a separate annealing process should be added as a fifth stage.

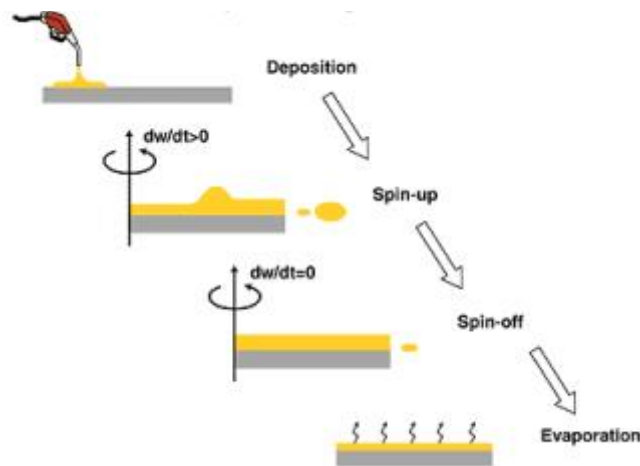


Figure I. 16: Typical stages of spin-coating process as reported in [118].

V. Atomic Layer Deposition

Although UC luminescent nanoparticles are an attractive wavelength converter, the luminescence is not very stable because of the large sensitive surface area. Even exposure to ambient air can cause degradation of PL. In addition, with a large amount of activators doped at the surface, quenching of UC luminescence is inevitable, leading to a decrease of the UC efficiency. Therefore, luminescent stabilization or enhancement is necessary. Consequently, a passivation layer that can be deposited through a dry deposition technique such as ALD (Atomic layer deposition) to protect these photoluminescent nanoparticles is needed.

V.1 Principle of ALD

ALD is a chemical gas-phase technique developed to deposit a variety of materials including oxides, metals, sulfides, and fluorides, with a wide range of properties, depending on the application [119]. As device requirements especially in the electronics field push toward smaller and more spatially demanding structures, ALD has demonstrated potential advantages over other thin films deposition methods such as chemical vapor deposition (CVD) and various physical vapor deposition (PVD) techniques. As shown in **Figure I.17**, this is due to [120-121]:

- Excellent conformality for surface features including trenches, pores, surface roughness
- Uniformity on large substrates such as large wafers, sheet materials and foils
- Atomic scale thickness control
- Low growth temperature to deposit high-quality materials with a high purity and a high density (no voids or pinholes)

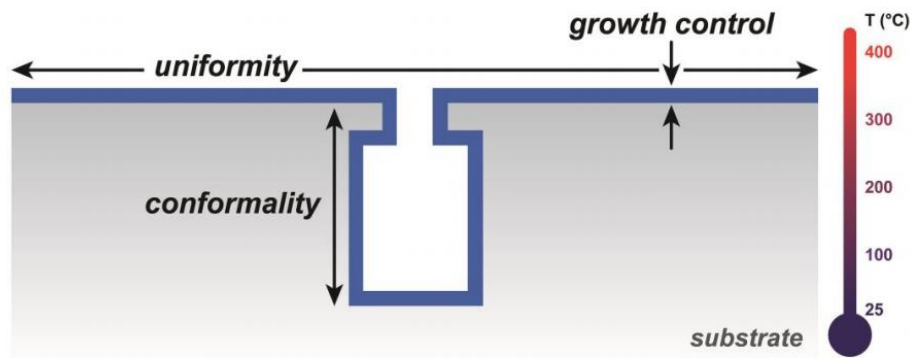
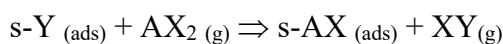
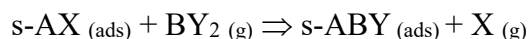


Figure I.17: The coverage metrics of ALD-film on a substrate with 3D features as reported in [122].

These desirable characteristics originate from the cyclic, self-saturating nature of ALD processes. A schematic representation of ALD process is illustrated in **Figure I.18**. It consists of sequential alternating pulses of gaseous chemical precursors that react with the substrate. These individual gas-surface reactions are called ‘half-cycles’ (in the first half-cycle the precursor is dosed and in the second half-cycle the co-reactant) and appropriately make only part of the materials synthesis. During each half-cycle, the precursor is pulsed into a chamber under vacuum (<1 Torr) for a designated amount of time to allow the precursor to fully react with the substrate surface through a self-limiting process that leaves no more than one monolayer at the surface. Subsequently, the reactor chamber is purged with an inert carrier gas (typically N₂ or Ar) to remove any unreacted precursor or reaction by-products. The reaction during the first half-cycle is of the form:



Where s indicates the surface with surface groups Y , AX_2 is the precursor, with A the first element to be deposited, X the ligand, and XY is the reaction product. This is followed by the counter-reactant precursor pulse and purge, creating up to one layer of the desired material. The reaction during the second half-cycle is of the form:



where BY_2 is the formula for the co-reactant, with B the second element to be deposited and Y the ligand, and XY is again the reaction product. This process is then repeated in an $\text{ABAB}\dots$ fashion until the appropriate film thickness is achieved [123].

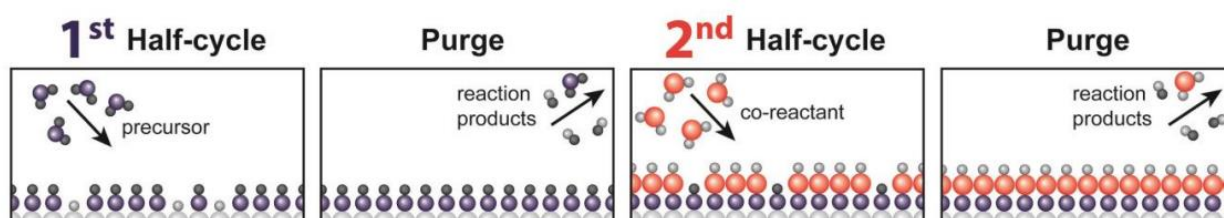


Figure I.18: Schematic representation of different steps of ALD process consisting of two half-reactions [122].

The saturation of both half-cycles leads to a characteristic amount of growth per cycle, which is abbreviated to GPC. Each process is deemed to have a specific temperature window in which ALD behavior is obtained. For ideal ALD growth, the temperature window represents the temperature range over which the GPC shows a weak or no temperature dependence, as indicated by the horizontal line in **Figure I.19**. Outside the temperature window, several chemical and physical processes can disrupt the ALD behavior [124].

- At low temperature, some precursors and co-reactants can condense on the surface. In addition, the reactivity of the molecules with the surface sites can be too low because of limited thermal energy at low temperatures, which prevents saturation of the reaction.
- At high temperatures, the precursors or co-reactants can decompose, leading to a CVD component and an increase in growth. Furthermore, the film itself or the reactive surface groups involved may desorb, above a certain temperature, leading to a decrease in growth.

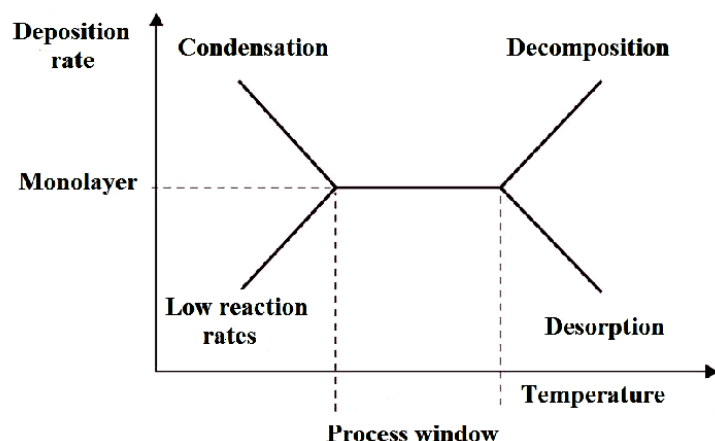
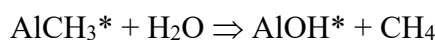
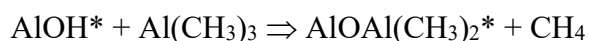


Figure I.19: The temperature window of the ALD process, indicated by the growth per cycle as a function of temperature [124].

The field of ALD is growing fastly and expanding into many applications. Al₂O₃ layer deposited by ALD can serve to optical waveguides [125], it also can be applied as evanescent waveguide for biomedical sensor applications [126]. Protective and insulating coatings can also be deposited by ALD on particles to prevent particle oxidation and to modify the optical or mechanical properties of the particles [127].

V.2 Al₂O₃ as a Model ALD System

The ALD of Al₂O₃ has been developed as a model ALD system because the surface reactions are very efficient and self-limiting. An earlier extensive review by Puurunen [128] has previously discussed the details of Al₂O₃-ALD. Aluminium oxide grown from trimethylaluminum (TMA) and H₂O is the most studied from the late 1980s and early 1990s. This couple allows the deposition of a layer with a very low residual hydrogen and carbon composition. In addition, with these two precursors it is possible to achieve excellent surface coverage with very good conformity even on deep 3D structures. It should also be noted that as-deposited ALD-Al₂O₃ is typically amorphous with a density of 2.5 - 3.2 g/cm³, a refractive index between 1.50 and 1.65 eV and a bandgap 6.1 – 7.0 eV. The surface chemistry during Al₂O₃ ALD can be described as [127]:



The main reason for the efficient reactions is the formation of a very strong Al-O bond. The overall reaction for Al₂O₃ ALD is:



This reaction has an extremely high reaction enthalpy. This is one of the highest reaction enthalpies encountered for any ALD reaction.

ALD- Al_2O_3 is considered a promising coating agent to passivate, enhance the optical properties and the resistance of the coated materials. It exhibits a good level of surface passivation on both p- and n-type silicon. The passivation properties of Al_2O_3 are associated with the combination of a low interface defect density and an enhanced field-effect passivation attributed to a high negative fixed charge density in the Al_2O_3 that consequently increase the minority carrier lifetimes [23,26]. It is also reported that nanotextured black silicon (NBSi) solar cells efficiency increased from 15.4 % to 16.6% after ALD- Al_2O_3 deposition [29].

It is shown that ALD- Al_2O_3 coating with precisely controlled thickness can obviously improve the luminescence intensity and greatly enhances the thermal stability of the YAG:Ce phosphor [129]. In this study it is reported that ALD- Al_2O_3 coating act like a barrier to decrease the thermal quenching and help to promote the light absorption and transfer. It is also used to improve the ambient stability of quantum dot films [130] and organic–inorganic perovskite solar cells [131]. Results demonstrate that the stability of the solar cell against humidity is greatly enhanced without an obvious reduction in cell efficiency.

V.3 Post-deposition annealing

Optoelectronic devices coated by ALD- Al_2O_3 present a lack of chemical passivation in as-deposited state. The post deposition annealing is mandatory to enhance the performance and especially for the activation of the Al_2O_3 surface passivation as reported in literature [30]. For that purpose, an annealing treatment is required to activate the Al_2O_3 -ALD layer. After annealing, the Al_2O_3 film remains amorphous at temperature $< 800^\circ\text{C}$. Thus, the improvement of the passivation does not happen due to crystallization of Al_2O_3 . The post-annealing temperature, duration and atmosphere are the main factors to carefully select during this step. Usually, the ALD- Al_2O_3 annealing process is performed at temperature ranging from 300 to 600°C , duration from 10 min to 30 min and in atmospheres such as oxygen (O_2), nitrogen (N_2), hydrogen (H_2) and forming gas N_2 or $\text{Ar}:\text{H}_2$ (95%:5%).

PL intensity enhancement (by 689%) is observed for porous SiC after ALD- Al_2O_3 deposition followed by an annealing for 5 min at 350°C in N_2 environment is reported in [132]. This behaviour is explained by the reduction of Al-OH bonds during the annealing step. These bonds exist in the film after the ALD process and are easily broken and released within Al_2O_3 layer.

The released H atoms play an important role for the passivation performance in this porous layer. H atoms diffuse and reach the Al₂O₃/SiC interface to neutralize the dangling bonds.

It is reported that the main requirement for hydrogen release by the Al₂O₃ films is the application of an annealing temperature higher than the deposition one. As an example, for a low deposition temperature of 100°C, a significant reduction of defects (D_{it}) is observed after annealing at 250 °C [22].

Among the different studied atmospheres, FGA is seen to provide an effective passivation. It suggests a complex mechanism involving hydrogen and hydroxyl groups in the dielectric. Residual incorporation of –OH groups as previously explained in ALD-Al₂O₃ layer when H₂O is used as the oxidant are presented. H₂ annealing induces the oxidation of interface layer between ALD-Al₂O₃ layer and the surface of substrate (less defective) with residual –OH groups in the Al₂O₃ layer by H₂O formation. That can significantly reduce the interface state density and ensure high film quality of several stacks. In that case, vacuum or inert gas annealing do not produce the large D_{it} reduction that is observed after FGA [133]. High-efficiency (18.1%) of nanotextured black silicon (NBSi) solar cell is achieved by the application of FGA on ALD-Al₂O₃ layer compared to untreated stack (16.6%) [29].

Forming gas annealing (FGA) on n-type and p-type In_{0.53}Ga_{0.47} as Metal-Oxide-Semiconductor capacitors with atomic layer deposition (ALD) Al₂O₃ is demonstrated to improve the gate stack interface properties and increase the on-current by 25% at 350°C for 30 min [134].

Vladimir et al. [135] show that FGA at 300°C for 30 min significantly improves the source- or drain-to-substrate junction isolation, with a reduction of two orders of magnitude in the reverse bias leakage exhibited by the Si-implanted In_{0.53}Ga_{0.47} as n⁺/p junctions, which is consistent with passivation of mid gap defects in In_{0.53}Ga_{0.47} by the FGA process. In addition, Manuel et al. [136] explain that the passivation of p-type poly-Si/SiO_x that contacts to n-type c-Si can be improved by applying an Al₂O₃ layer, followed by a post-deposition annealing in FGA at 400°C for 1 h due to chemical passivation of SiO_x and its interfaces to Si with hydrogen reducing the defects.

VI. Conclusions and motivation of this thesis

Although UC TiO₂ codoped Er³⁺-Yb³⁺ thin films have been already investigated by several research groups for different applications, the preparation of films with a good crystallinity, high surface area and efficient green and red luminescence at temperature below 500°C still remains challenging. As illustrated in **Table I.7**, till now, the annealing temperature that has

been used in most of the studies is above 500°C, in order to achieve high crystallinity and consequently an efficient luminescence. At high annealing temperatures, the size, shape, phase and luminescence properties (specially the profile of the emissions) can be strongly modified.

Table I.7: Er³⁺-Yb³⁺ percents annealing temperature and luminescence UC emissions for codoped TiO₂ films as reported in literature.

	Dopant percents	Annealing temperature	Luminescence emission	Ref.
Up-conversion emission of aluminosilicate and titania films doped with Er ³⁺ -Yb ³⁺ by ion implantation and sol-gel solution doping	1% Er ³⁺ - 10% Yb ³⁺	1100°C- 30s	Red	[137]
Enhanced Photovoltaic Performance of Perovskite Solar Cells Based on Er ³⁺ -Yb ³⁺ codoped TiO ₂ Nanorod Arrays	13% Er ³⁺ - 6% Yb ³⁺	500°C- 1h	Green + Red	[138]
Efficient up-conversion red emission from TiO ₂ : Er ³⁺ -Yb ³⁺ nanocrystals	2% Er ³⁺ - 10% Yb ³⁺	700°C	no luminescence	[74]
		800°C	Green + Red	
		900°C	Green + Red	
		1000°C	Green + Red	
Preparation and UC emission properties of TiO ₂ :Er ³⁺ -Yb ³⁺ inverse opals	10% Er ³⁺ - 10% Yb ³⁺	650°C- 8h	Green + Red	[139]

So, the purpose of our work is to investigate a simple, low temperature (T < 500°C) process that can enhance many devices efficiency based on UC phenomena and also could be used for temperature-sensitive devices.

It is based on multi-steps (**Figure I.20**):

First, hydrothermal-assisted sol-gel method as a soft chemistry route is used to synthesize UC nanoparticles with a low RE ions concentration, a controllable phase (anatase), size (diameter < 50 nm), morphology (spherical shape), a good crystallinity and high surface area in order to increase the reactivity of the material vs photons absorption and get an efficient UC luminescence. Then, nanoparticles deposition on silicon substrate using spin coating process as a fast and easy method to produce homogenous thin films is conducted. Finally, encapsulation of the structure with an ultra-thin ALD- Al_2O_3 layer followed by a forming gas annealing, as a protective film to prevent cell degradation and luminescence quenching from environmental attack (O_2 , H_2O) is investigated while maintaining (or even improving) the optical properties.

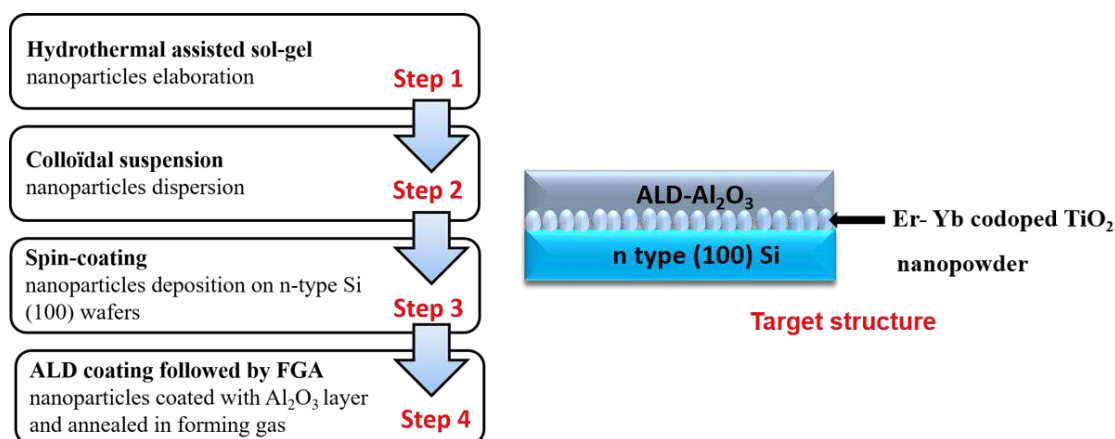


Figure I.20: The low temperature procedure used in this study for the synthesis, deposition and coating of the UC TiO_2 nanopowder in order to obtain the desired structure.

References

- [1] Panel Elvira Fortunato *et al.*, “Chapter 11 - Optoelectronic Devices from Bacterial NanoCellulose”, in *Bacterial Nanocellulose*, 2016, pp. 179–197.
- [2] T. Zhang, M. Wang, and H. Yang, “A review of the energy performance and life-cycle assessment of building-integrated photovoltaic (BIPV) systems”, *Energies*, vol. 11, no. 11, 2018.
- [3] S. O.K, P. R. Nair, and A. M.Ashok, “Chapter 41 - Engineered Nanomaterials for Energy Applications”, in *Handbook of Nanomaterials for Industrial Applications*, 2018, pp. 751–767.
- [4] O. V. Semenova, V. A. Yuzova, T. N. Patrusheva, F. F. Merkushev, M. Y. Railko, S. A. Podorozhnyak, “Antireflection and protective films for silicon solar cells” *Materials Science and Engineering*, vol. 66, no. 1, 2014.
- [5] V. Kumar, “Anti-Reflection coatings for highly efficient solar cells”, 2016, pp.1-2.
- [6] N. Sahouane, A. Zerga, “Optimization of antireflection multilayer for industrial crystalline silicon solar cells,” *Energy procedia*, vol. 44, pp. 118–125, 2014.
- [7] B. Swatowska, T. Stapinski, K. Drabczyk, and P. Panek, “The role of antireflective coatings in silicon solar cells - The influence on their electrical parameters”, *Optica Applicata*, vol. 41, pp. 487–492, 2011.
- [8] A. Shalav, B. S. Richards, M. A. Green, “Luminescent layers for enhanced silicon solar cell performance: Up-conversion”, *Solar Energy Materials and Solar Cells*, vol. 91, pp. 829–842, 2007.
- [9] H. Heidarzadeh, A. Rostami, and M. Dolatyari, “Management of losses (thermalization-transmission) in the Si-QDs inside 3C–SiC to design an ultra-high-efficiency solar cell”, *Materials Science in Semiconductor Processing*, vol. 109, pp. 104936, 2020.
- [10] J. De Wild, A. Meijerink, J. K. Rath, W. G. J. H. M. Van Sark, R. E. I. Schropp, “Upconverter solar cells: Materials and applications”, *Energy and Environmental Science*, vol. 4, pp. 4835–4848, 2011.
- [11] J. DayS., Senthilarasu, T. K. Mallick, “Improving spectral modification for applications in solar cells: Areview”, *renewable nergy*, vol. 132, pp. 186–205, 2019.
- [12] A. Le Bris, “Feasibility study of a hot carrier photovoltaic device”, 2012.
- [13] C. Stanley, A. Mojiri, G. Rosengarten, “Spectral light management for solar energy conversion systems”, *Nanophotonics*, vol. 5, pp. 161–179, 2016.
- [14] Y. Shang, S. Hao, C. Yang, G. Chen, “Enhancing solar cell efficiency using photon upconversion materials,” *Nanomaterials*, vol. 5, pp. 1782–1809, 2015.
- [15] I. Masiot, “Design and fabrication of nanostructures for light-trapping in ultra-thin solar cells” es Massiot To cite this version”, 2014.
- [16] N. Tucher, “Analysis of Photonic Structures for Silicon Solar Cells”, 2017.
- [17] A. Abass, “Light Absorption Enhancement and Electronic Properties of Thin-Film Solar Cells”, 2014..
- [18] W. G. J. H. M. van, A. Meijerink, R. E. I. Schropp, “Solar Spectrum Conversion for Photovoltaics Using Nanoparticles”, Chapter in *Third Generation Photovoltaics*, 2012.
- [19] X. Ren, J. Gao, H. Shi, L. Huang, S. Zhao, S. Xu, “A highly sensitive all-fiber temperature sensor based on the enhanced green upconversion luminescence in $\text{Lu}_2\text{MoO}_6:\text{Er}^{3+}/\text{Yb}^{3+}$ ”

- phosphors by co-doping Li⁺ ions”, *Optik*, vol. 227, pp. 166084, 2020.
- [20] M. Yan, L. Guo, P. Cai, Y. Huang, Q. Zhang, Q. Lue, “Hydrothermal synthesis of NaYF₄:Yb³⁺,Tm³⁺ upconversion microparticles and their effects on polymerization for stereolithography”, *Optical Materials*, vol. 109, pp. 110311, 2020.
- [21] L. Ma, E. M. Pascalidou, F. Wiame, S. Zanna, V. Maurice, P. Marcus, “Passivation mechanisms and pre-oxidation effects on model surfaces of FeCrNi austenitic stainless steel,” *Corrosion Science*, vol. 167, 2020.
- [22] F. Lebreton, “Silicon surface passivation properties of aluminum oxide grown by atomic layer deposition for low temperature solar cells processes”, 2018.
- [23] B. Hoex, J. Schmidt, P. Pohl, M. C. M. Van De Sanden, W. M. M. Kessels, “Silicon surface passivation by atomic layer deposited Al₂O₃,” *Journal of Applied Physics*, vol. 104, 2008.
- [24] A.J.A.Töfflinger, A. Laades, C. Leendertz, L. Margarita, L. Korte, S. Uta, H-P. Sperlich, B. Rech, “PECVD-AlO_x/SiN_x passivation stacks on silicon: Effective charge dynamics and interface defect state spectroscopy,” *Energy Procedia*, vol. 55, pp. 845–854, 2014.
- [25] B. Vermang, H. Coverde, A. Uruena, A. Lorenz, E. Cornagliotti, A. Rothschild, J. John, J. Poortmans, R. Mertens, “Blistering in ALD Al₂O₃ passivation layers as rear contacting for local Al BSF Si solar cells”, *Solar Energy Materials and Solar Cells*, vol. 101, pp. 204–209, 2012.
- [26] D. Suh, D. Y. Choi, K. J. Weber, “Al₂O₃/TiO₂ stack layers for effective surface passivation of crystalline silicon,” *Journal of Applied Physics*, vol. 114, 2013.
- [27] P. Repo, H. Talvitie, S. Li, J. Skarp, H. Savin, “Silicon surface passivation by Al₂O₃: Effect of ALD reactants”, *Energy Procedia*, vol. 8, pp. 681–687, 2011.
- [28] M.-J. C, W-Ch. Wang, M-Ch. Tsai, J. Yang, C. Hsu, “Efficiency Enhancement of Nanotextured Black Silicon Solar Cells Using Al₂O₃/TiO₂ Dual-Layer Passivation Stack Prepared by Atomic Layer Deposition,” *applied materials and interfaces*, vol. 7, pp. 10228–10237, 2015.
- [29] W. C. Wang, M. C. Tsai, J. Yang, C. Hsu, M. J. Chen, “Efficiency enhancement of nanotextured black silicon solar cells using Al₂O₃/TiO₂ dual-layer passivation stack prepared by atomic layer deposition,” *ACS Applied Materials and Interfaces*, vol. 7, pp. 10228–10237, 2015.
- [30] J. Frascaroli, G. Seguini, E. Cianci, D. Saynova, J. Van Roosmalen, M. Perego, “Surface passivation for ultrathin Al₂O₃ Layers grown at low temperature by thermal atomic layer deposition”, *Physica status solidi A*, pp. 732-736, 2013.
- [31] C. B. Zheng, Y.Q. Xia, F. Qin, Y. Yu, J.P. Miao, Z.G. Zhang, W.W. Cao, “Femtosecond pulsed laser induced synthesis of ultrafine Y₂O₃: Pr, Yb nanoparticles with improved upconversion efficiency,” *Chemical Physics Letters*, vol. 496, pp. 316–320, 2010.
- [32] J. Chen, J. X. Zhao, “Upconversion nanomaterials: Synthesis, mechanism, and applications in sensing,” *Sensors*, vol. 12, pp. 2414–2435, 2012.
- [33] M. Safdar, A. Ghazy, M. Lastusaari, M. Karppinen, “Lanthanide-based inorganic-organic hybrid materials for photon-upconversion,” *Journal of Materials Chemistry C*, vol. 8, pp. 6946–6965, 2020.
- [34] M. Kraft, “Spectroscopic characterization of upconversion nanomaterials with systematically varied material composition and surface chemistry Dissertation,” 2018.
- [35] Z. Wang, D. C. Thang, Q. Han, X. Zhao, X. Xie, Z. Wang, J. Lin, B. Xing, “Near-infrared photocontrolled therapeutic release via upconversion nanocomposites,” *Journal of Controlled Release*, vol. 324, pp. 104–123, 2020.

- [36] M. Mohan, R. Poddar, “Ex-vivo molecular imaging with Upconversion Nanoparticles (UCNPs) using Photo Thermal Optical Coherence Tomography (PTOCT)”, *Photodiagnosis and Photodynamic Therapy*, 2020.
- [37] S. Duo, J. Zhang, H. Zhang, Z. Chen, C. Zhong, T. Liu, “Synthesis of NaYF₄: Yb³⁺, Tm³⁺@TiO₂ and β-NaYF₄: Yb³⁺, Tm³⁺@TiO₂@Au nanocomposites and effective upconversion driven photocatalytic properties,” *Optical Materials*, vol. 62, pp. 240–249, 2016.
- [38] J. Christiansen, J. V. Petersen, S. Roesgaard, S. H. Moller, R. E. Christiansen, O. Sigmund, S. P. Madsen, P. Balling, B. Julsgaard, “Strongly enhanced upconversion in trivalent erbium ions by tailored gold nanostructures: Toward high-efficient silicon-based photovoltaics”, *Solar Energy Materials and Solar Cells*, vol. 208, pp. 110406, 2020.
- [39] X. Guo, W. Wu, Y. Li, J. Zhang, Li Wang, H. Agren, “recent research progress for upconversion assisted dye-sensitized solar cells,” *chinese chemical letters*, vol. 4, pp. 64–75, 2020.
- [40] Xuejiao Wang, Z. Hu, M. Sun, P. Du, W. Liu, S. Huang, J-G. Li, “Phase-conversion synthesis of LaF₃:Yb/RE (RE = Ho, Er) nanocrystals with Ln₂(OH)₄SO₄·2H₂O type layered compound as a new template, phase/morphology evolution, and upconversion luminescence”, *journal of materials research and technology*, vol. 9, pp. 10659–10668, 2020.
- [41] J. Tang, M. Yu, E. Wang, C. Ge, Z. Chen, “Intense ultraviolet upconversion luminescence from YF₃: Yb/Tm submicrorice,” *Materials Chemistry and Physics*, vol. 207, pp. 530–533, 2018.
- [42] P. Deshmukh, R. Deo, A. Ahlawat, A. A. Khan, R. Singh, A.K. Karnal, S. Satapathy, “Spectroscopic investigation of upconversion and downshifting properties LaF₃:Tb³⁺, Yb³⁺: A dual mode green emitter nanophosphor,” *Journal of Alloys and Compounds*, vol. 4, no. 1, pp. 64–75, 2020.
- [43] H. Zhang, X. Dong, L. Jiang, Y. Yang, X. Cheng, H. Zhao, “Comparative analysis of upconversion emission of LaF₃:Er/Yb and LaOF:Er/Yb for temperature sensing”, *Journal of Molecular Structure*, vol. 1206, pp. 127665, 2020.
- [44] G. Han, M. Wang, D. Li, J. Bai, G. Diao, “Novel upconversion Er, Yb-CeO₂ hollow spheres as scattering layer materials for efficient dye-sensitized solar cells”, *Solar Energy Materials and Solar Cells*, vol. 160, pp. 54–59, 2017.
- [45] X. Q, T. Lin, “Multicolor Emission Tuning and Red/Green Ratio Enhancement of Yb³⁺/Er³⁺ Codoped KGdF₄ Upconversion Nanoparticles,” *optik*, vol. 227, pp. 166084, 2021.
- [46] D. Xu, L. Yao, H. Lin, S. Yang, Y. Zhang, “Crystal growth and upconversion luminescent properties of KLu₂F₇:Yb, Er nanocrystals” vol. 490, pp. 41–45, 2018.
- [47] X. Liang, J. Fan, Y. Zhao, R. Jin, “Synthesis of NaYF₄:Yb,Er upconversion nanoparticle-based optomagnetic multifunctional composite for drug delivery system” *Journal of Rare Earths*, 2020.
- [48] X. LIANG, F. Jun, W. Yongbo, Z. Yanyan, J. Ruyi, S. Tao, C. Min, W. Xuejun, “Synthesis of hollow and mesoporous structured NaYF₄:Yb,Er upconversion luminescent nanoparticles for targeted drug delivery”, *Journal of Rare Earths*, vol. 35, pp. 419–429, 2017.
- [49] V. M. Lojpur, P. S. Ahrenkiel, M. D. Dramićanin, “Color-tunable up-conversion emission in Y₂O₃:Yb³⁺, Er³⁺ nanoparticles prepared by polymer complex solution method,” *Nanoscale Research Letters*, vol. 8, pp. 1–6, 2013.
- [50] T. R. Corn, “Optical and Luminescence Properties of Erbium, Ytterbium and Terbium Doped in Aluminum Nitride”, 2010.

- [51] V. Đorđević, Ž. Antić, M. G. Nikolić, M. D. Dramićanin, “The concentration quenching of photoluminescence in Eu^{3+} -doped La_2O_3 ” *Journal of Research in Physics*, vol. 37, pp. 47–54, 2014.
- [52] A. M. Khachatouria, F. G. Fard, H. Sarpoolaky, C. Vogt, E. Vasileva, M. Mensi, S. Popov, M. S. Toprak, “Microwave synthesis of $\text{Y}_2\text{O}_3:\text{Eu}^{3+}$ nanophosphors: A study on the influence of dopant concentration and calcination temperature on structural and photoluminescence properties,” *Journal of Luminescence*, vol. 169, pp. 1–8, 2016.
- [53] R. Salhi, J. L. Deschanvres, “Efficient green and red up-conversion emissions in Er/Yb co-doped TiO_2 nanopowders prepared by hydrothermal-assisted sol–gel process,” *Journal of Luminescence*, vol. 176, pp. 250–259, 2016.
- [54] J. Oliva, C. R. Garci, L. A. D. Torres. C. CAMACHO, M. G-ROCHA, M. T. Romero, G. A. HIRATA, “Effect of the Er^{3+} codopant on the green upconversion emission of $\text{LaSr}_2\text{AlO}_5:\text{Yb}^{3+}$ phosphors,” *journal of electronic materials*, 2018.
- [55] J. Fu *et al.*, “Intense red–green up-conversion emission and their mechanisms of $\text{SrO}:\text{Er}^{3+}/\text{Yb}^{3+}$, Gd^{3+} , Lu^{3+} , Bi^{3+} ,” *Journal of Luminescence*, vol. 181, pp. 240–245, 2017.
- [56] C. Mi, J. Wu, Y. Yang, B. Han, and J. Wei, “Efficient upconversion luminescence from $\text{Ba}_5\text{Gd}_8\text{Zn}_4\text{O}_{21}:\text{Yb}^{3+}$, Er^{3+} based on a demonstrated cross-relaxation process,” *Scientific Reports*, vol. 6, pp. 1–11, 2016.
- [57] L. H. Slooff, M. J. A. De Dood, A. Van Blaaderen, A. Polman, “Effects of heat treatment and concentration on the luminescence properties of erbium-doped silica sol-gel films,” *Journal of Non-Crystalline Solids*, vol. 296, pp. 158–164, 2001.
- [58] R. Wang, X. Meng, F. Yin, Y. Feng, G. Qin, W. Qin, “Heavily erbium-doped low-hydroxyl fluorotellurite glasses for 27 μm laser applications,” *Optical Materials Express*, vol. 3, pp. 1127, 2013.
- [59] R. Arppe *et al.*, “Quenching of the upconversion luminescence of $\text{NaYF}_4:\text{Yb}^{3+},\text{Er}^{3+}$ and $\text{NaYF}_4:\text{Yb}^{3+},\text{Tm}^{3+}$ nanophosphors by water: The role of the sensitizer Yb^{3+} in non-radiative relaxation,” *Nanoscale*, vol. 7, pp. 11746–11757, 2015.
- [60] R. Lei *et al.*, “Influence of excitation power and doping concentration on the upconversion emission and optical temperature sensing behavior of $\text{Er}^{3+}:\text{BaGd}_2(\text{MoO}_4)_4$ phosphors,” *Optical Materials Express*, vol. 8, pp. 3023, 2018.
- [61] C. R. Kesavulu, K. Kiran Kumar, C. K. Jayasankar, “Upconversion properties of Er^{3+} -doped oxyfluoride glass-ceramics containing SrF_2 nanocrystals,” *Oxide-based Materials and Devices V*, vol. 8987, pp. 89871, 2014.
- [62] H. Sun *et al.*, “Single-band near-infrared upconversion emission and visible-light absorption in highly doped pseudo-perovskite oxides,” *Solar Energy Materials and Solar Cells*, vol. 205, pp. 110253, 2020.
- [63] A. Khare, “A critical review on the efficiency improvement of upconversion assisted solar cells,” *Journal of Alloys and Compounds*, vol. 821, pp. 153214, 2020.
- [64] S. P. Tiwari *et al.*, “Future prospects of fluoride based upconversion nanoparticles for emerging applications in biomedical and energy harvesting,” *journal of vacuum science and technology B*, vol. 37, pp. 028501, 2018.
- [65] J. Tang *et al.*, “Sol-gel prepared $\text{Yb}^{3+}/\text{Er}^{3+}$ co-doped RE_2O_3 (RE = La, Gd, Lu) nanocrystals: Structural characterization and temperature-dependent upconversion behavior,” *Journal of Alloys and Compounds*, vol. 740, pp. 229–236, 2018.
- [66] J. Shi, W. Ge, M. Xu, J. Zhu, “ $\text{Bi}_2\text{Ti}_2\text{O}_7$ nanoparticles: An oxide based upconversion

- luminescence host by a simple sol-gel route,” *Journal of Luminescence*, vol. 213, pp. 15–18, 2019.
- [67] D. A. H. Hanaor and C. C. Sorrell, “Review of the anatase to rutile phase transformation,” *Journal of Materials Science*, vol. 46, pp. 855–874, 2011.
- [68] U. of Colorado, “Mineral Structure and Property Data: TiO₂ Group.” .
- [69] A. A. Gribb and J. F. Banfield, “Particle size effects on transformation kinetics and phase stability in nanocrystalline TiO₂,” *American Mineralogist*, vol. 82, pp. 717–728, 1997.
- [70] H. Zhang and J. F. Banfield, “Thermodynamic analysis of phase stability of nanocrystalline titania,” *Journal of Materials Chemistry*, vol. 8, pp. 2073–2076, 1998.
- [71] M. R. Ranade *et al.*, “Energetics of nanocrystalline TiO₂” vol. 99, pp. 2–7, 2002.
- [72] S. J. Smith *et al.*, “Heat capacities and thermodynamic functions of TiO₂ anatase and rutile: Analysis of phase stability,” *american mineralogist*, vol. 91, pp. 91–91, 2009.
- [73] I. Cimieri, “Sol-gel preparation and characterization of titanium dioxide films for degradation of organic pollutants”, 2014.
- [74] Y. Wu *et al.*, “Efficient up-conversion red emission from TiO₂:Yb, Er nanocrystals,” *Optics Express*, vol. 25, pp. 22648, 2017.
- [75] Y. Bai, I. Mora-Seró, F. De Angelis, J. Bisquert, P. Wang, “Titanium dioxide nanomaterials for photovoltaic applications,” *Chemical Reviews*, vol. 114, pp. 10095–10130, 2014.
- [76] N. Sofyan, A. Ridhova, A. Yuwono, A. Udhiarto, “Fabriation of solar cells with TiO₂ nanoparticles sensitized using natural dyre extracted from mangosteen pericarps,” *International journal of technology*, vol. 6, pp. 1229-1238, 2017.
- [77] M. G. Wenwu Liu, Huanyu Zhanga, Hui-gang Wang, Mei Zhang, “Titanium mesh supported TiO₂ nanowire arrays/upconversion luminescence Er³⁺-Yb³⁺ codoped TiO₂ nanoparticles novel composites for flexible dye-sensitized solar cells,” *Applied Surface Science*, vol. 422, pp. 304–315, 2017.
- [78] C. H. Han, H. S. Lee, K. won Lee, S. Do Han, I. Singh, “Synthesis of amorphous Er³⁺-Yb³⁺ Co-doped TiO₂ and its application as a scattering layer for dye-sensitized solar cells,” *Bulletin of the Korean Chemical Society*, vol. 30, pp. 219–223, 2009.
- [79] X. Wanga *et al.*, “Enhanced Photovoltaic Performance of Perovskite Solar Cells Based on Er-Yb Co-doped TiO₂ Nanorod Arrays,” *Electrochimica Acta*, vol. 245, no. 1, pp. 839–845, 2017.
- [80] R. M. Gunji, G. R. S. Mattos, C. D. S. Bordon, L. A. Gómez-Malagón, and L. R. P. Kassab, “Efficiency enhancement of silicon solar cells covered by GeO₂-PbO glasses doped with Eu³⁺ and TiO₂ nanoparticles,” *Journal of Luminescence*, vol. 223, pp. 2–7, 2020.
- [81] K. Y. Jung, “Aerosol synthesis of TiO₂:Er³⁺/Yb³⁺ submicron-sized spherical particles and upconversion optimization for application as anti-counterfeiting materials”, *RSC Advances*, vol. 10, pp. 16323–16329, 2020.
- [82] C. S. T. Gonzalez Carreiiio, A. Mifsud, “Preparation of homogenous Zn/Co mixed oxides by spray pyrolysis” *Materials Chemistry and Physics*, vol. 27, pp. 287–296, 1991.
- [83] S. C. TSAI, Y. L. SONG, C. S. TSAI, C. C. YANG, W. Y. CHIU, H. M. LIN, “Ultrasonic spray pyrolysis for nanoparticles synthesis,” *journal of materials science*, vol. 40, pp. 50–62, 2004.
- [84] C. Li *et al.*, “Ultrasonic spray pyrolysis for nanoparticles synthesis”, *Journal of Materials Science*, vol. 9, pp. 3647–3657, 2004.

- [85] S. Yildirim, M. Yurddaskal, T. Dikici, I. Aritman, K. Ertekin, and E. Celik, "Structural and luminescence properties of undoped, Nd³⁺ and Er³⁺ doped TiO₂ nanoparticles synthesized by flame spray pyrolysis method," *Ceramics International*, vol. 42, pp. 10579–10586, 2016.
- [86] S. Thambidurai, P. Gowthaman, M. Venkatachalam, S. Suresh, and M. Kandasamy, "Morphology dependent photovoltaic performance of zinc oxide-cobalt oxide nanoparticle/nanorod composites synthesized by simple chemical co-precipitation method," *Journal of Alloys and Compounds*, vol. 852, pp. 156997, 2021.
- [87] M. Zikriya, Y. F. Nadaf, P. V. Bharathy, C. G. Renuka, "Luminescent characterization of rare earth Dy³⁺ ion doped TiO₂ prepared by simple chemical co-precipitation method," *Journal of Rare Earths*, vol. 37, pp. 24–31, 2019.
- [88] M. Thamima and S. Karuppuchamy, "Microwave assisted synthesis of Zinc oxide nanoparticles," *International Journal of ChemTech Research*, vol. 8, no. 11, pp. 250–256, 2015.
- [89] H. Q. Wang, T. Nann, "Monodisperse upconverting nanocrystals by Microwave-assisted synthesis," *ACS Nano*, vol. 3, pp. 3804–3808, 2009.
- [90] A. E. Danks, S. R. Hall, Z. Schnepf, "The evolution of 'sol-gel' chemistry as a technique for materials synthesis," *Materials Horizons*, vol. 3, pp. 91–112, 2016.
- [91] A. M. Alattar, "Design and manufacturing of supercritical drying autoclave for aerogel production," *Iraqi Journal of Physics (IJP)*, vol. 14, pp. 148–160, 2019.
- [92] M. Parashar, V. K. Shukla, R. Singh, "Metal oxides nanoparticles via solgel method: a review on synthesis, characterization and applications," *journal of materials science : materials in electronics*, 2020.
- [93] Q. Yang, J. Sha, X. Ma, and D. Yang, "Synthesis of NiO nanowires by a sol-gel process," *Materials Letters*, vol. 59, no. 14–15, pp. 1967–1970, 2005.
- [94] J. Jiang et al., "Sol-gel synthesis of K_{1.33}Mn₈O₁₆ nanorods and their applications for aqueous K-ion hybrid supercapacitors" *Materials Research Bulletin*, vol. 109, pp. 29–33, 2019.
- [95] R. Salhi, J. Deschanvres, "Efficient green and red up-conversion emissions in Er/Yb co-doped TiO₂ nanopowders prepared by hydrothermal-assisted sol-gel process," *Journal of Luminescence*, vol. 176, pp. 250–259, 2016.
- [96] J. Shi, W. Ge, M. Xu, and J. Zhu, "Bi₂Ti₂O₇ nanoparticles: An oxide based upconversion luminescence host by a simple sol-gel route," *Journal of Luminescence*, vol. 213, pp. 15–18, 2019.
- [97] J. Sun, Y. Lan, Z. Xia, H. Du, "Sol-gel synthesis and green upconversion luminescence in BaGd₂(MoO₄)₄:Yb³⁺, Er³⁺+phosphors," *Optical Materials*, vol. 33, pp. 576–581, 2011.
- [98] S. Pang, X. Li, Z. Shi, G. Yang, Z. Cui, "Preparation and characterization of sol-gel derived Er³⁺-Yb³⁺ codoped SiO₂/TiO₂ core-shell nanoparticles," *Materials Letters*, vol. 64, pp. 846–848, 2010.
- [99] E. M. Modan, A. G. Plaiasu, "Advantages and Disadvantages of Chemical Methods in the Elaboration of Nanomaterials" <https://doi.org/10.35219/mms.2020.1.08>.
- [100] I. Benammar, R. Salhi, J. Deschanvres, R. Maalej, "The Effect of Solvents and Rare-Earth Element (Er , Yb) Doping on Suspension Stability of Sol – Gel Titania Nanoparticles," *Journal of Luminescence*, pp. 718–726, 2017.

- [101] N. Hilal, V. M. Starov, P. Langston, “Interaction forces between colloidal particles in liquid: theory and experiment”, *advances in colloid and interface science*, vol. 134–135, pp. 151–166, 2007.
- [102] A. Lesaine, “structural and mechanical properties of dried colloidal silica layers” 2019.
- [103] N. M. Kovalchuk, V. M. Starov, “Aggregation in colloidal suspensions: Effect of colloidal forces and hydrodynamic interactions,” *Advances in Colloid and Interface Science*, vol. 179–182, pp. 99–106, 2012.
- [104] L. Sjogren, “Chapter 9: Colloidal suspensions” in *Stochastic Processes (Lecture Notes, Gothenburg)*, pp. 101–130, 1940.
- [105] H. Löwen, “Melting, freezing and colloidal suspensions,” *Physics Reports*, vol. 237, pp. 249–324, 1994.
- [106] E. Di Giuseppe *et al.*, “Rheological and mechanical properties of silica colloids : from Newtonian liquid to brittle behaviour” *Rheologica Acta*, vol. 51, pp. 451–465, 2012.
- [107] J. Widegren and L. Bergstro, “The effect of acids and bases on the dispersion and stabilization of ceramic particles in ethanol,” *Journal of the european ceramic society*, vol. 20, pp. 659–665, 2000.
- [108] Y. Wang *et al.*, “Fabrication of Cu₂SnS₃ thin films by ethanol-ammonium solution process by doctor-blade technique”, *Electronic Materials Letters*, vol. 13, pp. 478–482, 2017.
- [109] M. Asadzadeh, F. Tajabadi, D. Dastan, P. Sangpour, Z. Shi, N. Taghavinia, “Facile deposition of porous fluorine doped tin oxide by Dr. Blade method for capacitive applications,” *Ceramics International*, 2020.
- [110] A. Berni, M. Mennig, H. Schmidt, “Doctor Blade” in *Sol-Gel Technologies for Glass Producers and Users*, pp. 89-92, 2004.
- [111] <https://www.sciencedirect.com/topics/engineering/thin-film-processing-method>.
- [112] M. O’Kane, “Thin Film Coating Solution-Processing Techniques Compared”, *Ossila*: <https://www.ossila.com/pages/solution-processing-techniques-comparison>.
- [113] J. Puetz, M. A. Aegerter, “Dip Coating Technique,” *Sol-Gel Technologies for Glass Producers and Users*, pp. 37–48, 2004.
- [114] A. N. Ionela, A. I. Nicoara, O. R. Vasile, B. S. Vasile, “Chapter 9 - Inorganic micro- and nanostructured implants for tissue engineering” in *nanobimaterials in hard tissue engineering*, pp. 271–295, 2016.
- [115] “Solution-Processing Techniques: A Comparison.” *Ossila*.
- [116] J. F. Taylor, “Spin coating: An overview” *Finishing for electronics*, 2001 .
- [117] Z. Welchel, L. A. DeSilva, T. M. W. J. Banadara, “Properties of tris (8-hydroxyquinoline) aluminum thin films fabricated by spin coating from static and dynamic dispense methods,” *Optical Materials*, vol. 108, pp. 110447, 2020.
- [118] Advanced Lab course in Spin coating of thin polymer film and thickness determination by ellipsometry”, 2019.
- [119] Forge Nano, “What is ALD | Atomic Layer Deposition.”: <http://forgenano.com/uncategorized/atomic-layer-deposition/>.
- [120] C. Barbos *et al.*, “Characterization of Al₂O₃ Thin Films Prepared by Thermal ALD,” *Energy*

Procedia, vol. 77, pp. 558–564, 2015.

- [121] S. M. George, “Atomic Layer Deposition: An Overview,” *chemistry revision*, vol. 110, pp. 111–131, 2010.
- [122] H. C. M. Knoops, S. E. Potts, A. A. Bol, W. M. M. Kessels, “Atomic Layer Deposition,” *Handbook of Crystal Growth: Thin Films and Epitaxy: Second Edition*, vol. 3, pp. 1101–1134, 2015.
- [123] R. W. Johnson, A. Hultqvist, S. F. Bent, “A brief review of atomic layer deposition: From fundamentals to applications,” *Materials Today*, vol. 17, pp. 236–246, 2014.
- [124] L. A. Dobrzański, M. Szindler, M. M. Szindler, “Surface morphology and optical properties of Al₂O₃ thin films deposited by ALD method,” *archives of materials science and engineering*, vol. 73, pp. 18–24, 2015.
- [125] D. L. Caballero-Espitia, E. G. Lizarraga-Medina, H. A. Borbon-Nuñez, O. E. Contreras-Lopez, H. Tiznado, H. Marquez, “Study of Al₂O₃ thin films by ALD using H₂O and O₃ as oxygen source for waveguide applications,” *Optical Materials*, vol. 109, pp. 1–7, 2020.
- [126] A. Purniawan, P. J. French, G. Pandraud, P. M. Sarro, “TiO₂ ALD nanolayer as evanescent waveguide for biomedical sensor applications,” *Procedia Engineering*, vol. 5, pp. 1131–1135, 2010.
- [127] S. M. George, “Atomic layer deposition: An overview,” *Chemical Reviews*, vol. 110, pp. 111–131, 2010.
- [128] R. L. Puurunen, “Surface chemistry of atomic layer deposition: A case study for the trimethylaluminum/water process,” *Journal of Applied Physics*, vol. 97, 2005.
- [129] Z. Zhou *et al.*, “Performance improvement by alumina coatings on Y₃Al₅O₁₂:Ce³⁺ phosphor powder deposited using atomic layer deposition in a fluidized bed reactor,” *RSC Advances*, vol. 6, pp. 76454–76462, 2016.
- [130] D. Valdesueiro *et al.*, “Deposition Mechanism of Aluminum Oxide on Quantum Dot Films at Atmospheric Pressure and Room Temperature,” *Journal of Physical Chemistry C*, vol. 120, pp. 4266–4275, 2016.
- [131] X. Dong *et al.*, “Improvement of the humidity stability of organic-inorganic perovskite solar cells using ultrathin Al₂O₃ layers prepared by atomic layer deposition,” *Journal of Materials Chemistry A*, vol. 3, pp. 5360–5367, 2015.
- [132] W. Lu *et al.*, “Effective optimization of surface passivation on porous silicon carbide using atomic layer deposited Al₂O₃,” *RSC Advances*, vol. 7, pp. 8090–8097, 2017.
- [133] S. Swaminathan, Y. Sun, P. Pianetta, P. C. McIntyre, “Ultrathin ALD-Al₂O₃ layers for Ge(001) gate stacks: Local composition evolution and dielectric properties,” *Journal of Applied Physics*, vol. 110, p. 094105, 2011.
- [134] J. Hu, H. S. Philip Wong, “Effect of annealing ambient and temperature on the electrical characteristics of atomic layer deposition Al₂O₃/In_{0.53}Ga_{0.47}As metal-oxide-semiconductor capacitors and MOSFETs,” *Journal of Applied Physics*, vol. 111, pp. 0–8, 2012.
- [135] V. Djara *et al.*, “MOSFETs With an ALD Al₂O₃ Gate Dielectric,” vol. 59, pp. 1084–1090, 2012.
- [136] M. Schnabel *et al.*, “Hydrogen passivation of poly-Si/SiO_x contacts for Si solar cells using Al₂O₃ studied with deuterium,” *Applied Physics Letters*, vol. 112, pp. 1–10, 2018.
- [137] R. E. Rojas-Hernandez, N. P. Barradas, E. Alves, L. F. Santos, R. M. Almeida, “Up-conversion emission of aluminosilicate and titania films doped with Er³⁺/Yb³⁺ by ion implantation and sol-

- gel solution doping,” *Surface and Coatings Technology*, vol. 355, pp. 162–168, 2018.
- [138] X. Wang *et al.*, “Enhanced Photovoltaic Performance of Perovskite Solar Cells Based on Er-Yb Co-doped TiO₂ Nanorod Arrays,” *Electrochimica Acta*, vol. 245, pp. 839–845, 2017.
- [139] Z. Yang, K. Zhu, Z. Song, D. Zhou, Z. Yin, and J. Qiu, “Preparation and upconversion emission properties of TiO₂:Yb, Er inverse opals,” *Solid State Communications*, vol. 151, pp. 364–367, 2011.

Chapter II

Materials and methods

Introduction

In this work, a particular effort is made to propose an approach that does not involve sophisticated, costly devices and time consuming and complex experimental procedures.

This chapter concerns the synthesis of undoped and lanthanides codoped TiO₂ nanoparticles. During this step, we are interested in studying the synthesis parameters set. These parameters have an important impact on the morphological and structural and photoluminescence properties of the synthesized nanopowders. The second step concerns the optimization of the nanoparticles dispersions before their deposition on Si substrate. Finally, optimization of atomic layer deposition of Al₂O₃ parameters on Si substrate is performed.

This chapter will also describe the characterizing methods used in this work involving structural, thermal, chemical, optical and mechanical analysis. The described methods contribute to the bulk of the results that will be presented in the next chapters.

I. Low temperature procedure proposed in this study

I.1 Nanopowder synthesis using Sol-gel method

I.1.1 Hydrolysis

Hydrolysis of the precursors such as metal alkoxide takes place in water or alcohols as oxygen is necessary for the formation of metal oxide, which is provided by water or organic solvents (alcohols). If water is used as reaction medium, it is known as aqueous sol-gel method, and use of organic solvent lead to non-aqueous sol-gel route. In addition to water and alcohol, an acid or a base also helps in the hydrolysis of the precursors. The general chemical reaction for the hydrolysis process is given below:



Where M=metal, R=alkyl group (C_nH_{2n+1}). The amount of water strongly influences the gel formation, a higher water content facilitates the formation of a higher ratio of bridging.

I.1.2 Condensation

Condensation of adjacent molecules is produced, when water/alcohol are eliminated and metal oxide linkages are formed in the liquid state. Condensation occurs via two processes: olation is a process in which hydroxyl (-OH-) bridge is formed between two metal centers and oxolation in which an oxo (-O-) bridge is formed between two metal centers. The general chemical reaction for the condensation process is given below:



Condensation results in increasing the viscosity of the solvent that forms a porous structure maintaining a liquid phase called gel.

I.1.3 Aging

This step produces continuous changes in the structure and properties of the gel. During this step, polycondensation continues within the localized solution along with reprecipitation of the gel network.

I.1.4 Drying

This process is complicated because water and organic components are detached from the gel, which disturbs its structure. The encapsulated liquid can be removed from the gel by different drying processes as shown in **Figure II.1**: atmospheric/thermal drying (xerogel), supercritical drying (aerogel), and freeze-drying (cryogel), each one having different implications on the structure of the gel network.

- Xerogel is formed by the solvent evaporation from the wet gel under normal evaporation, resulting in collapse of the wet-gel structure. A high shrinkage of the gel is observed for this type of drying because of the strong capillary forces generated by the liquid, thereby a dense material is obtained. Xerogel has a relatively low surface area and pore volume and high shrinkage of the gel.
- Aerogels is resulted from supercritical drying of the wet gels in an autoclave under high temperature and pressure. Aerogels are nanoscale mesoporous materials of low density and high surface area. Zero capillary forces create an aerogel that nominally retains the low-density framework for the wet gel.
- Cryogel is formed by freezing the solvents at low temperature and pressure. The gel network shrinkage in cryogel is relatively lower than in xerogel. High levels of porosity can be achieved which is usually between xerogel and aerogel.

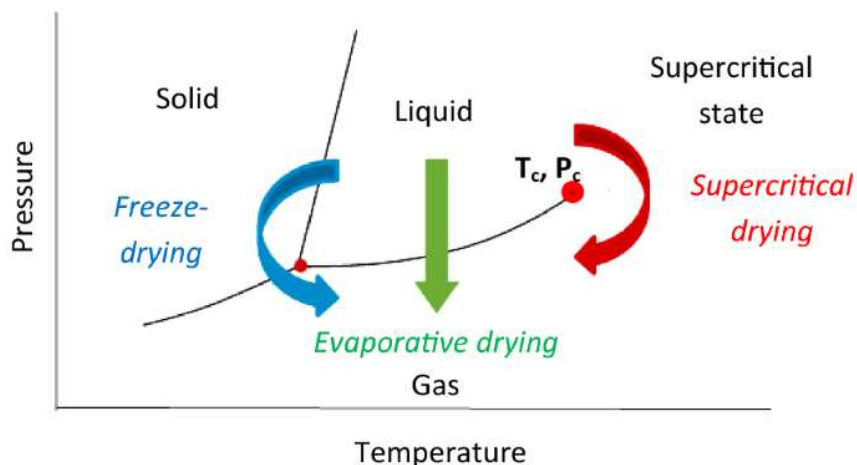


Figure II.1: Phase diagram of a pure substance presenting different thermal drying routes [1].

I.1.4.1 Supercritical drying

During this process, the liquid is evaporated in a precisely controlled way. As the substance in a liquid body crosses the boundary from liquid to the gas phase, the liquid changes into gas, while the liquid body's volume decreases. Therefore, the surface tensions in the liquid body pull against any solid and delicate structures of the gel. To overcome cracks, removing the solvent above its critical temperature and pressure without having to expose it to a vapour–liquid interface is the appropriate method [2]. This route from liquid to gas does not cross any phase boundary. Meanwhile, passing through the supercritical region the liquid and gaseous phases become indistinguishable. The surface tension disappears along with the capillary pressure gradient built up in the pore walls, avoiding the potential collapse of the pore volume due to the capillary force [3].

The solvent used for supercritical drying is a key factor with regard to chemical composition of aerogels. As illustrated in **Table II.1**, various substances are suitable for supercritical drying. In fact, when the original solvent in the gel is exchanged with another liquid, the gel may shrink [4], which is the case when using carbon dioxide. Aerogels elaborated using this solvent, due to its low critical temperature T_c (31.1°C) compared to other solvents, can undergo shrinkage up to 5% [5]. Therefore, a medium composed of a single phase (same solvent for hydrolysis and drying) can leave the porous texture of the wet gel intact. Supercritical drying batch autoclaving involves a minimum of four steps:

- Heating the autoclave, the pressure will increase steeply with temperature.
- Holding the chosen pressure and temperature above critical conditions.
- Venting of the gas phase.
- Cooling of the autoclave

Table II.1: Critical Points of Various Substances.

Substances	T _c (°C)	P _c (bar)
Ethanol	241	60.5
Methanol	239.5	79.7
Acetone	235.1	46.3
Hexane	234.6	29.8
Carbon dioxide	31.1	72.7

I.1.5 Thermal treatment

This final calcination step is performed to drive of the residues and water molecules out the desired powder. The calcination temperature is a very important parameter to control the pore size and the density of the material.

I.1.6 Parameters

Sol-gel chemistry is sensitive to the following parameters [6]:

- pH: it is directly connected to the hydrolysis step which is important in producing the gel network. Acidic pH speeds up hydrolysis and slows condensation, unlike basic pH. Under acid catalysis, which is the fastest synthesis route, the gel obtained is known as “polymer gel”: after gelling, an open structure is obtained. A low rate of hydrolysis under basic pH promotes nucleation and leads to formation of a colloidal solution where the size of the pores is controllable (unlike acid catalysis). The gel obtained is known as a "colloidal gel".
- Solvent: alkoxides are not miscible in water, so it is necessary to mix the precursors, water and optionally the catalyst, in a common solvent. It is required to use the alcohol corresponding to the ligand -OR of the alkoxide, in order to avoid possible reactions between the different components and prevent the modification of the kinetics reactions. For this reason, the starting sol should be an alcoholic solution.
- Temperature: this parameter plays a significant role in the formation of nanoparticles and it facilitates the nanoparticles undergoing into a gel network.
- Time: if a gel is formed slowly, it has usually a much more uniform structure.
- Agitation: mixing a sol during gelation process is important to control the uniform progress of chemical reactions in the solution.

- Alkoxide: the texture and crystallographic structure of titanium dioxide synthesized by sol-gel. Anatase phase with spherical shape can be obtained using titanium (IV) iso-propoxide (TTIP) precursor (with an appropriate pH and solvent).

Sol-gel process is heavily used and studied in our group [7-9]. Up to now, very wide ranges of materials are fabricated based on this method. They cover materials with optical, electronic and biomedical functions [10]. Advantages of sol-gel derived materials in these applications include low cost, simple and low temperature process that are capable of achieving pure and homogenous materials with interesting properties. In addition, it offers a careful control of many characteristics such as [11-13]:

- Particles size: size control on the nanometer scale.
- Surface area: increasing surface area is the most popular trend for improving the performance of the performance of several materials. Increasing the surface area of the material lead directly to the increasing of the reactivity.
- Shape: different morphologies.
- Crystalline structure and surface state on which their properties depend.

I.1.7 Synthesis of undoped and codoped TiO₂ nanopowders

Our TiO₂ nanopowders are prepared via two-step process. The first step is to prepare a solution of titanium oxide. In the second step, the drying under the supercritical conditions of ethanol of the titanium oxide solution in an autoclave is conducted.

For the undoped TiO₂ synthesis, alkoxide precursor titanium (IV) iso-propoxide (TTIP) - 30 ml with formula (Ti [OCH(CH₃)₂]₄) purchased from Sigma-Aldrich with purity of 98% is used. The titanium iso-propoxide is dissolved in a mixture of glacial acetic acid - 30 ml (CH₃COOH, ≥ 99.5%, CARLO-ERBA) and methanol- 30 ml (CH₃OH, 99.8%, Fisher chemical). Water for hydrolysis is slowly released from esterification reaction between acetic acid and methanol. The resultant sol is magnetically stirred for 15 min at room temperature in order to allow the dissolution of TTIP precursor and insure the homogenization of the reagents.

In order to prepare the codoped TiO₂ solution, we followed the same process used for the preparation of the undoped solution. Then, a specific percentage of erbium and ytterbium nitrate dissolved in ethanol is added leading to TiO₂ codoped 5 at.%Er - 5 at.%Yb. Erbium (III) nitrate pentahydrate (Er (NO₃)₃. 5H₂O, 99.9%, Sigma-Aldrich) and ytterbium nitrate pentahydrate (Yb (NO₃)₃. 5H₂O, 99.9%, Sigma-Aldrich) are used as the precursors for Erbium and Ytterbium

doping, respectively. The schematic presentation in **Figure II.2** illustrates the different steps for the preparation of the solution to produce the undoped and codoped TiO₂ nanopowders.

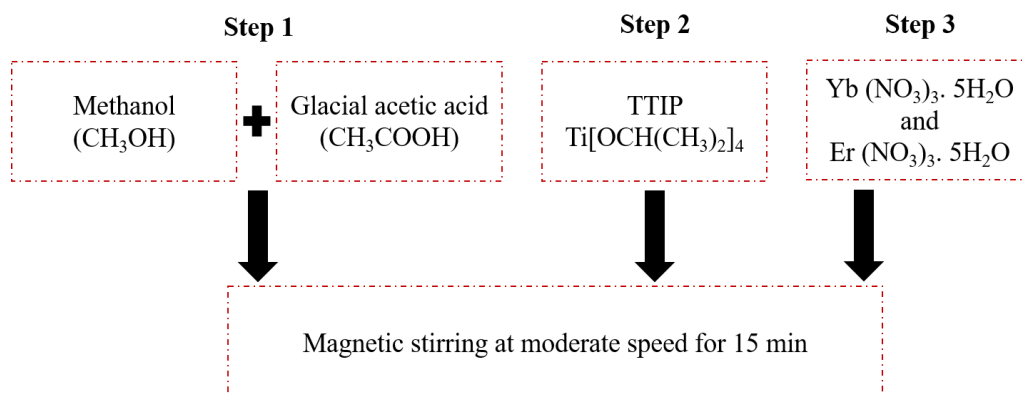


Figure II.2: Schematic illustration of the nanopowders synthesis procedure.

The autoclave used for the nanopowders synthesis is made of 316 stainless steel with capacity of 1L. The autoclave is equipped with a heating system and a pressure gauge to follow the evolution of the pressure as a function of the temperature set using a programmer. The maximum operating temperature and pressure are 350°C and 130 bar, respectively. It has a closure system consisting of two half-shells, a ring and compression screws. A safety device consisting of a rupture disc is also present in the system (**Figure II.3**).

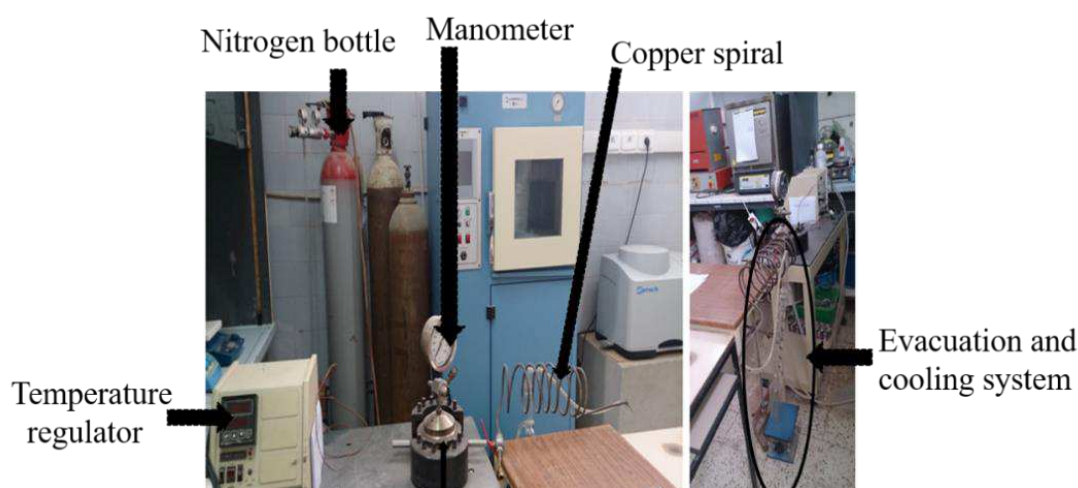


Figure II.3: Sol-gel under supercritical drying conditions equipment.

The solution is then located in the autoclave filled up with ethanol for drying under supercritical conditions. At T= 243°C and P= 63 bar, we are situated away from the critical point and we ensure that we are in the supercritical domain. After 3 hours of supercritical drying, a depressurization for 1 h down to room temperature is carried out. After that, nitrogen is injected under low flow for 5 min into the autoclave for better evacuation of the solvents. Finally, to

prevent the aerogel from cracking, the autoclave is opened after 24 h. Finally, the system is cooled to room temperature and at the end undoped and codoped TiO₂ aerogels (**Figure II.4**) are collected.

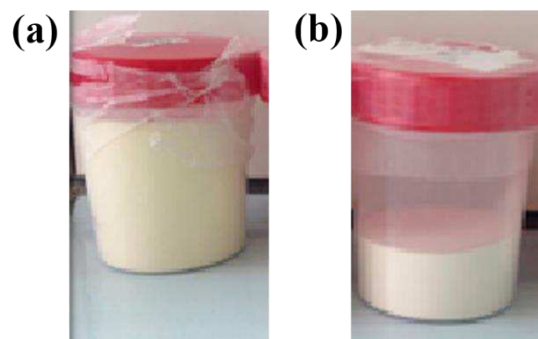


Figure II.4: The synthesized nanopowders: (a) undoped and (b) codoped TiO₂.

In order to improve the crystallographic and optical properties of the synthesized nanopowders, heat treatment is necessary. This treatment eliminates organic and hydroxyl contaminations within the matrices as well as structural defects. The temperature rise speed is 2.5° C/min and then it maintained at the desired temperature for 2 h.

I.2 Nanopowders dispersion

After the nanopowders synthesis, the second step is to study the colloidal behaviour of suspensions in order to obtain the optimum conditions for nanoparticles dispersion to deposit it on Si Substrate.

For nanopowders dispersion, absolute ethanol (99.99%, Sodipro) is chosen as a dilution medium because, compared to water, it allows the decrease of the surface tension of the liquid, resulting in better stability. In addition, it is reported in a previous study of our group that undoped and codoped TiO₂ nanopowders are well dispersed in ethanol compared to in water and methanol [14]. Moreover, its viscosity and its surface tension are decisive when spreading the solution with a view to obtaining nanometric thin films and avoiding dewetting phenomena during the deposition of the solution [15]. This solvent is non-aqueous polar solvent, offering a medium with a low dielectric constant and a low ionic concentration (**Table II.2**). Ethanol has also other advantages as good availability and low costs for mass production in up scaled processes.

Table II.2: Properties of ethanol.

	Dielectric constant	Viscosity (mPa.s)
ETOH	24.3	1.078

As colloid concentration plays an important role in the resulting deposition density of nanoparticles as the next step of our procedure, a concentrated solution $C = 0.24 \text{ M}$ is chosen based on previous study in our group on the concentration needed to have a full coverage of the substrate during spin-coating process. So, the process is carried out with 0.24 M concentration in absolute ethanol (99.99%, Sodipro) under magnetic stirring speed at 1000 rpm for 24 h, in order to improve the homogeneity of nanoparticles distribution in the solution and reach surface equilibrium [16]. The magnetic stirring of the solution induces a primary disintegration of the agglomerates formed during autoclaving. It is therefore preferable to add ultrasonic dispersion that is capable to produce more efficient fragmentation than that carried out by magnetic stirring. Therefore, 30 min of ultrasonication is applied to disperse particles. Finally, 1 min of magnetic stirring is additionally applied to insure solution homogeneity. This step allows to mix the TiO_2 particles and the solvent, thus resulting in a colloidal suspension of white color for undoped suspension and pink for the codoped suspension. The dispersion study is conducted under different operating conditions:

- Different types of sonicators (**Figure II.5**): bath (35 kHz, 30/240W) located in the platform at SIMaP or probe located at LEPMI (20 kHz, 500 W, pulses with a 40% amplitude and a continuous mode). In this work, low frequency is used in order to increase the dispersion rate by increasing the amplitude of the shock wave as explained in [17]. For the probe, the distance between the sonicator tip and beaker bottom-inner surface is maintained at 2 mm. Temperature evolution during sonication is monitored and the impact of changing the bath in order to avoid vaporization is also conducted. These effects will be explained in details in **chapter III**.

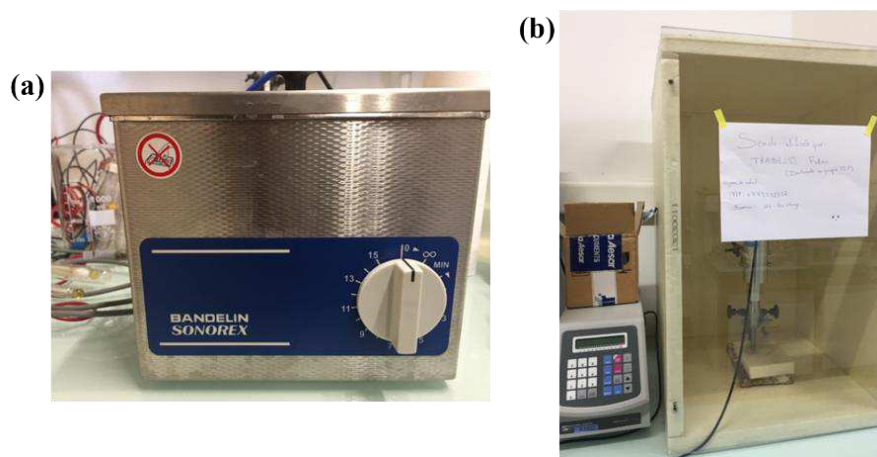


Figure II.5: The different sonicators used in this study (a) bath and (b) probe.

- pH of the solution: pH influences the surface charge and nanoparticles agglomeration behavior [28], its effect is investigated by adjusting the operational pH values from 3 to 10 with HCl / NaOH addition with different concentrations (0.1M, 0.01M and 0.001M). For pH variation in ethanol, the pH-meter (sensION+ PH3 basic pH benchtop meter) calibration is as follows: the Ag ± AgCl electrode is filled with an electrolyte consisting of 0.1 M LiCl in ethanol in the outer chamber and saturated LiCl in the inner chamber. The calibration is performed using ordinary water-based buffers resulting in an operational pH scale [29]. The equilibrium state is reached after 16 h in pure ethanol (operational pH= 7).
- Ultrasonication duration of the appropriate sonicator and doping impact.

I.3 Spin-coating

I.3.1 cleaning process

Prior to spin coating deposition, the silicon surface needs to be cleaned to remove all foreign matter prior to processing and to make it hydrophilic. There are two types of methods to make the surface hydrophilic: the first includes the chemical functionalization of the Si substrate with linker molecules by creating covalent bond (chemisorption). Numerous researches dealing with the functionalization of Si surface especially with amine-terminated silane (APTES) have shown that the silanization step is very sensitive toward experimental conditions. The final surface state of the modified substrate depends on temperature, water, concentration of APTES, and the duration of the substrate immersion [18-19]. The polymeric molecules used for the functionalization approach cannot be removed from the surface later, and will eventually affect the photoluminescence mechanisms.

The second approach is based on the activation of Si surface by electrostatic attraction (physisorption). In order to achieve the mechanism responsible for the attachment of nanoparticles to the Si surface without any linker molecules, it is necessary to investigate the surface and interface properties between Si and nanoparticles. S. Gorji al. [18] studied the immobilization of Au nanoparticles on Si substrate with the protonation of Si–OH groups created after RCA (Radio Corporation of America) cleaning process in presence of the low pH of Gold nanoparticles colloidal solution. The presented results prove that surface hydrophilicity can be obtained using RCA1-RCA2 or RCA1-HF-RCA2 treatments. The cleaning process is as follows:

- RCA 1 process consists of dipping the substrate in a hot alkaline solution (H₂O₂-NH₄OH-H₂O: organic decontamination) at 70 °C for 15 min, rinsed with deionized water.

- RCA 2 process consists of dipping the substrate in a hot acid solution (RCA2: H₂O₂-HCl-H₂O: inorganic decontamination) at 70 °C for 15 min, and rinsed again with deionized water.
 - Dipping the substrate in diluted HF solution (H₂O: HF with 50:1 volume ratio) for 2 min.
- Both RCA1 and RCA2 treated surfaces exhibited a wetting contact angle of 0. Etching Si surface by diluted HF (hydrofluoric acid) makes it relatively hydrophobic because the silicon native oxide is removed and the surface becomes H-terminated (**Figure II.6**).









	Surface wetting property	Contact angle (°)*		Surface energy (mJ/m ²)		Respective droplet image	
		n-Si	p-Si	n-Si	p-Si	n-Si	p-Si
Before RCA	Hydrophobic	78.98	72.67	36.12	40.06		
RCA1 + RCA2	Hydrophilic	-	-	-	-		
RCA1 + RCA2 + HF	Hydrophobic	73.71	64.56	39.41	45.06		
RCA1 + HF + RCA2	Hydrophilic	-	-	-	-		

Figure II.6: Surface wetting property of n-type and p-type Si before and after RCA process [18].

Therefore, our adapted approach is the simple, low cost one based on the formation of a pure native oxide at the final step of RCA cleaning process, which is rich in Si-OH groups. Then deposition of nanoparticles is conducted after the OH-termination stage by spin-coating technique. The n-type substrate is chosen because it previously demonstrated that it contains higher amount of OH-terminations than the p-type substrates after RCA process, which may affect the final density of nanoparticles on the surface [18,20]. The silicon substrate possesses an hydrophilic surface and is negatively charged after the RCA procedure. Adequate choice of nanoparticles surface, depend on their PIE in which no electrical charge exist on the surface, and pH lead to adhesion of nanoparticles onto Si surface. Silanol groups presented on Si surface present isoelectric point at pH=2.7 [20-21], which make it possible to control the charge (negatively or positively charged) under different pH of solution.

To choose between RCA1-RCA2 or RCA1-HF-RCA2 and the way that the cycles are deposited, a comparative study is performed. For the solution preparation, undoped TiO₂ suspension with 0.24 M concentration is magnetically stirred at 1000 rpm for 24h then

ultrasonicated for 30 min in a bath and further magnetically stirred for 1 min. The cleaning and deposition processes are as follows:

- RCA 1 process at 70 °C for 15 min, rinsed with deionized water.
- RCA 2 process) at 70 °C for 15 min, and rinsed again with deionized water.
- Dipping the substrate in diluted HF solution for 2 min.
- Drying the substrate after cleaning using spin-coating

For the deposition into Si surface, two cycles are deposited by spin-coating process (1000 rpm /60s, $V_{\text{solution}} = 200 \mu\text{l}$) either successively or separated by drying. For the drying step, the substrate is placed on a heating plate for 1 min at 140°C. The substrates are n-type (100) Si wafers (CZ, thickness 250-300 μm and resistivity 10-30 $\Omega\cdot\text{cm}$ from Sil'tronix ST) cut in 20 mm \times 20 mm pieces. Three substrates are prepared:

- S1: RCA1-RCA2 / cycle 1: nanoparticles deposition on Si / drying for 1 min at 140°C/ cycle 2: nanoparticles deposition on Si / drying for 1min at 140°C
- S2: RCA1-HF-RCA2 / cycle 1: nanoparticles deposition on Si / drying for 1 min at 140°C/ cycle 2: nanoparticles deposition on Si / drying for 1min at 140°C
- S3: RCA1-RCA2/ 2 successive cycles of nanoparticles deposition on Si/ drying for 1 min at 140°C

I.3.1.1 Microscopic observations

Figure II.7 shows the optical microscopic images of the different prepared substrates. It is shown for all substrates that the deposit is discontinuous and consists of very large particles (up to several hundred micrometers) whose sizes are highly polydisperse. The comparative study between S1 and S2 shows that RCA1-RCA2 processes lead to an homogenous distribution of the solution over the entire surface of the substrate. Almost the same coverage percent is presented in the center (33%) and border (35%). Unlike RCA1-HF-RCA2 treatment leads to higher density of particles in the border (46%) than the center of the substrate (36%) (**Table II.3**).

For the comparison conducted between S1 and S3, the deposition of the solution for second cycle after drying the previously deposited one provide the homogenous coverage in the two different areas for S1, unlike S3 where the solution tend to spread to the border of the substrate more than the center. It is also observed that the solvent doesn't evaporate at 140°C for 1 min (blue circles around the particles deposited), therefore increasing the drying temperature or time

is necessary. Our approach will be based on increasing the temperature of drying to 200°C while keeping the same duration (1 min).

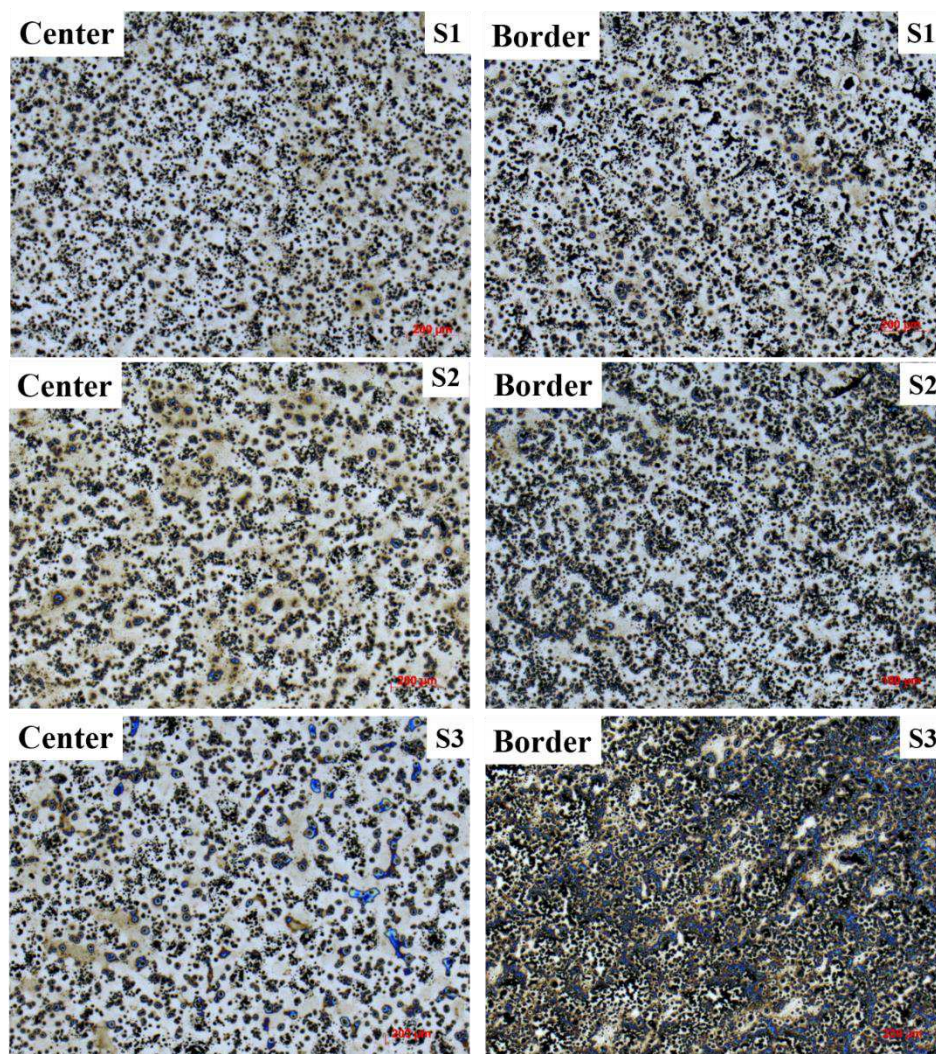


Figure II.7: Optical microscope observations of the different substrates S1, S2 and S3 in two areas (center and border).

Table II.3: Area coverage percents of the nanoparticles deposited on Si substrate deduced using ImageJ software.

	Center	Border
S1	33%	35%
S2	36%	46%
S3	33%	66%

The adopted cleaning process during this study is : a hot alkaline solution ($\text{H}_2\text{O}_2\text{-NH}_4\text{OH-H}_2\text{O}$: organic decontamination) at 70 °C for 15 min, rinsed with deionized water, followed by a dipping into a hot acid solution (RCA2: $\text{H}_2\text{O}_2\text{-HCl-H}_2\text{O}$: inorganic decontamination) at 70 °C

for 15 min, and rinsed again with DW (**Figure II.8**). The deposition of each new solution after drying for 1 min at 200°C the previously deposited one is adapted.

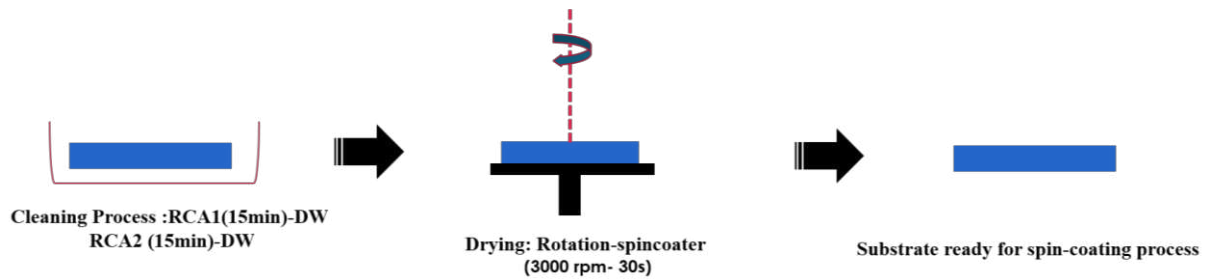


Figure II.8: Substrate cleaning process adapted in this study.

I.3.2 Influence of spin-coating operative parameters

Final film thickness and other properties will depend on the nature of the solution (viscosity, drying rate, surface tension, vapour pressure etc.) and the chosen parameters for the spin process. Parameters such as acceleration, rotational speed, rotational duration, drying and even the substrate itself influence the properties of coated films [22].

- **Viscosity:** On flat substrates, the coating thickness is determined by the centrifugal forces driving the liquid off the substrate and viscous resistance that acts in the opposite direction. As the viscosity increases at a constant spin speed, less material will flow off the sample, leaving a higher coating coverage [23]. On flat substrates, the coating thickness is determined by the centrifugal forces driving the liquid off the substrate and viscous resistance that acts in the opposite direction. Consistently to earlier report on CeO₂ suspensions in glycerol/water medium [24], higher coating are obtained with an increase of viscosity as a result of the largest viscous resistance of liquid solutions.
- **Surface Tension:** the surface tension of the coating must be matched with the substrate that is being coated upon. If surface tension mismatch occurs, the coating will not completely wet out leading to the formation of defects in the coating.
- **Volume of the solution:** the volume of the solution deposited on the substrate is an important factor that controls the coverage of the solution on the surface of substrate. It has a significant influence on the performance of the device.
- **Acceleration:** the acceleration of the substrate towards the desired spin speed can have an impact on the film properties. Since the deposited solution begins to dry during the first part of the spin cycle, it is important to properly control acceleration. It is reported that 50% of the solvent will be lost by evaporation in the first few seconds of the spin coating process.

- **Spin Speed:** the spin speed is one of the most important factors in spin coating process. The speed of the substrate (rpm) affects the degree of radial (centrifugal) force applied to spread the liquid over the substrate. As the substrate rotates at a higher spin speed around 3000 rpm, the rotational acceleration and the force on the liquid increases. Correspondingly, the amount of liquid forced from the sample is also increased, leaving a lower coating coverage or thin film. At this stage of high spin speed, minor variations of ± 50 rpm can cause result in a change of thickness by 10% [25]. Film thickness is a balance between the force applied to spread the solvent towards the edge of the substrate and the drying rate that affects the viscosity of the solvent. In general, relationship between the thickness of a spin-coated film and the spin speed is given below where t is the thickness and w is the angular velocity:

$$t \propto \frac{1}{\sqrt{w}} \text{ (Equation II.1)}$$

Previous work shows that thin film is obtained at higher rotational speed [26]. According to Ansari et al. [27], the size of grown Pd nanoparticles deposited on flat (Si and glass) substrates decreases with varying rotational speed from 1000 rpm to 4000 rpm.

- **Spin duration:** the spin time has an influence on the final coating coverage and substrate drying. As a sample rotates, the coating solution is removed from the surface of substrate. The effect of spin time on coating coverage is large for short time durations, but as the time increases a point of diminishing will occur, and the influence becomes minimal. The objective of this parameter is to keep the substrate spinning until the film is fully dry. This depends upon the boiling point and vapour pressure of the solvent and also on the temperature and humidity of the place where the spin process is performed. For most solvents like ethanol, methanol, water, acetone, a spin coating duration of 30 seconds is usually sufficient. Therefore these solvents are recommended [28].
- **Drying:** the drying rate of the deposited solution during the process is defined by the nature of the solution itself, volatility of the solvent used, as well as by the atmosphere surrounding the substrate. Therefore, a volatile solvent is recommended in order to evaporate it from the starting of the spin process. It is well known that factors as air temperature and humidity play a large role in determining coated film properties. It is also important that the air flow and associated turbulence above the substrate itself be minimized (or held constant). The slower rate of drying results in the increasing the uniformity of the film thickness across the substrates. As the solvent dries out while it moves toward the edge of the substrate, a radial thickness non-uniformities can occurs (since the solvent viscosity changes with distance).

Therefore, by slowing down the rate of drying, the viscosity will remain uniform across the substrate.

- **Substrate:** it is very important to verify that the disk which supports the substrate is horizontally levelled. The substrate must be wet by the depositing solution and presents an hydrophilic surface. Otherwise, due to the centrifugal force, the substrate cannot contain the solution properly which might go away from the substrate and results in no trace of material on the substrate. The substrate flatness and/or roughness factor could also influence the deposition method. The substrate has also to be perfectly cleaned [29].
- **Deceleration:** the deacceleration rate has the same potential as the acceleration rate to influence the coating properties. At this step, the amount of coating liquid remaining on the substrate is small and the impact of this change in spin speed is typically minimal.

Another important factor to investigate is the spin-coating number that influences drastically the thickness. The thickness of film increases as the number of spin-coating cycles increases. The most reported cycles in literature range from 1 to 12. However, it is worth noting that the thickness of film deposited by spin-coating may not show a linearity with cycle amount. Sadikin et al. [30] observed that 1, 2, 3 and 5 layers of TiO₂ particles deposited on ITO substrate by spin-coating present a thickness of 346, 1586, 2077 and 3841 nm respectively. Similar coatings of TiO₂ films deposited on TCO substrate reported by Pandiarajan et al. [31] present a thickness of about 360, 920 and 1000 nm for 4, 6 and 10 cycles, respectively. Cycle number variation for ZnO thin films from 4 to 12 leads to thickness of 225 and 530 nm [32].

This method has been widely used in the manufacture of integrated circuits, optical mirrors, color television screens and magnetic disk for data storage, and microelectronics [33-34]. Deposition of polymers, nanoparticles (CoFe₂O₄, ZnO, TiO₂) and biomaterials are commonly performed via spin coating [28], [35-38]. Most researches demonstrate a better uniformity and coverage of the solution using the spin-coating method among the other techniques [39].

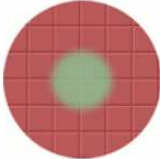

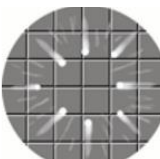
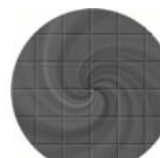
One of the most critical factors in spin coating process is repeatability. Few variations in the parameters that characterize the spin process can result in drastic variations in the deposited film. The spin-coating technique presents also other disadvantages.

- Waste of most of the solution during spinning [40]. Typical spin coating processes utilize only 2–5% of the material dispensed onto the substrate. It is effective for coating small substrates and is limited to batch processing.
- Possibility of the presence of contaminants (traces of solvent, humidity, etc.).

- Difficulty of accurately controlling the deposition (homogeneity, rugosity).

Some spin-coating troubles that may occur during deposition are illustrated in **Table II.4**

Table II.4: Spin Coating process troubleshooting [41].

Observations	Image	Reasons
Center circle (Chuck Mark)		-Problem due to the spin chuck (change it)
Uncoated Areas		-Low volume deposited
Comets, streaks or flares Fluid		-dispense rate is too high -Spin speed and acceleration settings are too high -Contaminations exist on substrate surface prior to dispense
Swirl pattern		-Spin speed and acceleration settings are too high -Spin time too short

As shown, there are several factors affecting the coating process. At the beginning of this thesis we faced some problems from the listed issues related to the adjustment of deposit conditions (**Figure II.9**). As an example, the photograph N°1 clearly shows a substrate with a circle in the middle and non-homogeneous deposit due to the use of a spin-coater jacket. We found necessary to remove the jacket to end up with the substrate N°2 and N°3 (same conditions). Unfortunately, for these samples there are still areas at the edge not well-coated, which can be explained by the use of a small chuck. So we have to change the chuck with a larger one to end up obtaining the substrate N°4.

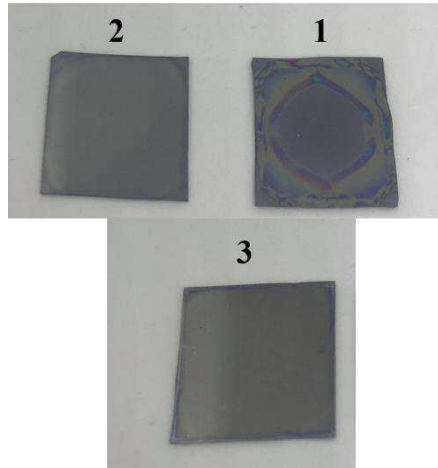


Figure II.9: Si/ codoped TiO₂ nanopowder under different operation parameter (1) using a spin-coater jacket, (2) without jacket and (3) without jacket changing the chuck.

In this study, one cycle of spin-coating process is based on two-steps: spinning the deposited solution in static mode and then, the fabricated film is pre-heated on a heating plate at 200°C for 1 min to evaporate the solvent (**Figure II.10**). The dispersions are added onto the substrate with a pipette without filtration. Based on literature, the quality of the spin coated films is influenced by three major factors: spinning speed, spinning time and volume. Therefore, Taguchi design of experiment (DOE) approach, more precisely the screening method or Plackett–Burman two level design, to optimize process conditions and get the important information with the minimum number of experiments is conducted and will be detailed in **chapter IV**.

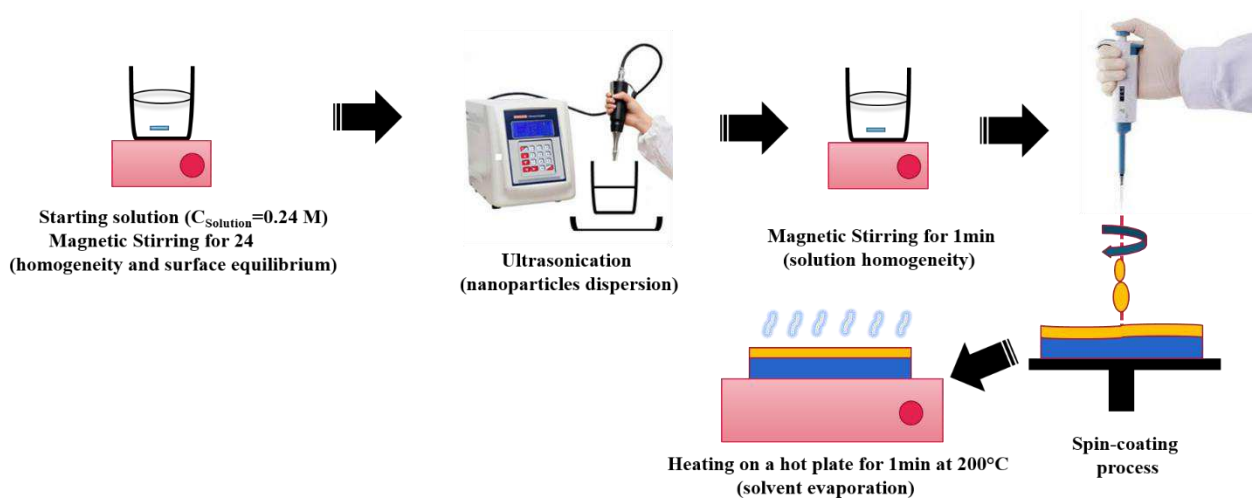
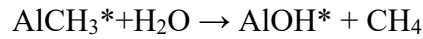
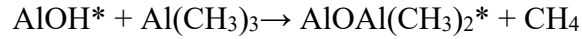


Figure II.10: Spin coating steps used in this study.

I.4 Al₂O₃-ALD coating on Si substrate

First, thermal Atomic layer deposition (T-ALD) of amorphous Al₂O₃ on Si substrate is performed on an home-made ALD reactor (ALD Nano 2), located in SiMaP, in order to set the ALD window and purge time of the TMA precursor. The TMA and H₂O yield to ALD- Al₂O₃ according to the following two reactions:



The asterisks (*) designate the surface species. In the first step, trimethylaluminum (TMA) molecules react with hydroxyl (OH) groups attached to the silicon substrate surface. Al atoms and methyl groups cover the surface and the remaining TMA molecules in the deposition chamber are no longer able to react with the surface. After purging the deposition chamber with nitrogen, water vapor is injected into the deposition chamber. The H₂O molecules act very fast with the Al-CH₃ complex attached to the surface. Hydrogen reacts with the methyl group to methane and oxygen reacts with aluminium to aluminium oxide.

II.4.1 ALD growth window

The deposition temperature is one of the most important parameter in the ALD process, as it controls the surface coverage. The film thickness is determined as a function of deposition temperatures ranging from 100 to 300°C, as shown in **Figure II.11**. The Al₂O₃ thin film is deposited by repeating the sequence of Al precursor exposure (1 s), N₂ gas purge (30 s), water exposure (1 s), and N₂ gas purge (60 s) for a fixed number of cycles (750 cycles). High purity nitrogen (N₂, 99.999%) is used as the carrier and purging gas during the entire deposition process with a flow rate of 100 sccm. Depositions are made on silicon substrates.

The film growth per cycle (GPC) is calculated by dividing the thickness measured by ellipsometry by the amount of deposition cycles. A constant GPC is observed between 150 and 250°C giving the growth rate of approximately 0.15 nm/cycle, which can be considered within its nominal reported value [42-43]. It describes the temperature range where the balance between chemical reactivity and physical desorption is stable, and then thickness of the layer does not depend on temperature. The growth rate decreases at high temperatures (above 250°C) and increases at low temperatures (below 150°C). GPC become slower at high substrate temperature most probably due to desorption or a loss of surface species required for further ALD nucleation, while it increases at low temperature which is attributed to the condensation of some precursors and co-reactants on the surface. In all other data that will be presented here,

Al₂O₃ is deposited at 200°C. It should be noted that the evolution of GPC at low temperatures (the observed decrease in GPC with temperature decreasing) is the reverse for what is known for the ALD-Al₂O₃ deposition using TMA and H₂O precursors (GPC drops with temperature decreasing).

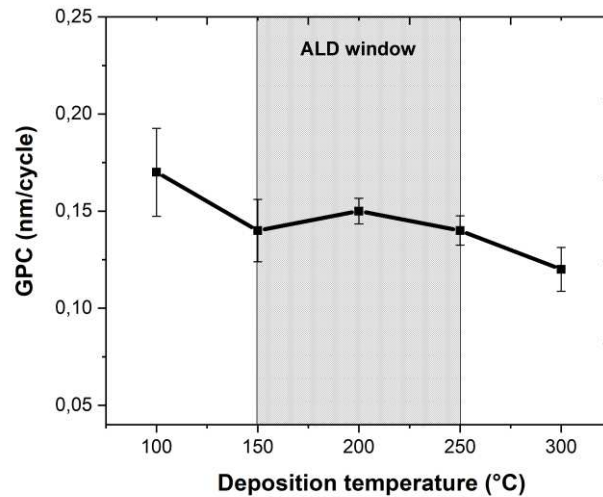


Figure II.11: The growth rate of ALD-Al₂O₃ deposited on silicon substrates as a function of deposition temperature.

II.4.2 Optimization of TMA pulse time

Figure II.12 presents the GPC as a function of TMA pulse time from 0.5s to 3s for deposition temperature of 200°C and 750 as number of cycles (N₂ gas purge (30 s), water exposure (1 s), and N₂ gas purge (60 s)). GPC increases gradually until saturation at 0.16 nm/cycle. The growth rate reached a self-limiting behavior when the TMA precursor pulse is ≥ 1.5 s. This indicates the saturating trend of the precursor adsorption, and an increase of the dose time can no more affect their density. These results confirms the deposition within ALD regime. Therefore, a 1.5s of TMA precursor pulse is implemented in other processes at 200°C.

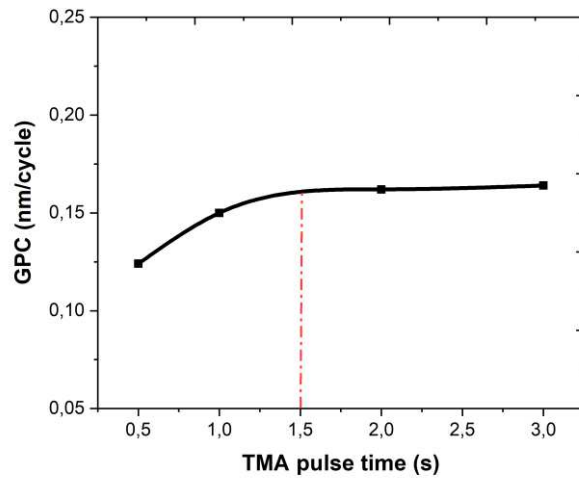


Figure II.12: The growth rate evolution as function of TMA pulse time.

II.4.3 Film thickness vs ALD cycle numbers

Figure II.13 shows the variation in the Al_2O_3 film thickness deposited on Si substrate with the number of cycles ranging from 50 to 1500 cycles by repeating the sequence of Al precursor exposure (1.5 s), N_2 gas purge (30 s), water exposure (1 s), and N_2 gas purge (60 s) at deposition temperature of 200°C . The film thickness increases regularly with the increase of ALD cycles. It confirms that the film grows in the ALD mode.

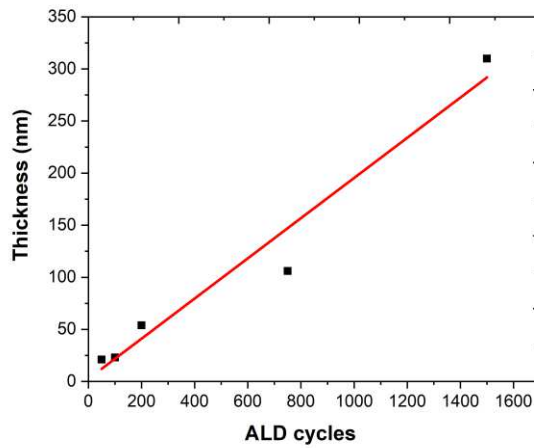


Figure II.13: Thickness evolution with ALD cycles.

II. Characterization

II.1 Structural Characterization

II.1.1 X-ray diffraction (XRD)

X-Ray diffraction is carried out on a BRUKER D8 Advanced diffractometer (SeriesII-2009) with Cu K α radiation ($\lambda=1.5418$ Å). The measurements are recorded in the 10-90° 2 θ range at room temperature with a step size of 0.05° using a counting time of one second per step.

II.1.2 BET analysis

Brunauer-Emmett-Teller (BET) theory is used to measure the surface area of solid or porous materials. The BET is based on two principle hypothesis. The adsorbent surface is assumed to be uniform and non-porous. The second assumption is that the gas molecules are adsorbed in the surface in a consecutive layer.

The Barrett, Joy and Halenda (BJH) theory enables to obtain specific surface area and pore size distribution. Its principle is based on the analysis of isotherms of adsorption and desorption of nitrogen at 77 K, showing a hysteresis loop. In this method, calculation of the specific surface area is done on the desorption part which is supposed to be the most representative of the equilibrium between gaseous nitrogen and condensed nitrogen by capillarity. Pores are considered to be filled at the equilibrium pressure for which a saturation plateau or an inflexion point can be seen. According to Brunauer classification, the shape of the hysteresis loop gives information on pore size and shape.

Surface area, average pore volume and average pore diameters of the nanoparticles are determined by physisorption of N₂ at 77 K by using Micrometrics Surface Area and porosity Analyzer: ASAP 2020. Before the measurement, the nanopowders are subjected to degassing operation at 150°C over night to remove residual moisture and adsorbed gases.

II.1.3 Electron microscopy

II.1.3.1 Scanning electron microscopy

Scanning Electron Microscopy (SEM) images are recorded with ZEISS Gemini SEM 500 type and JEOL IT500HR LV equipped of field emission microscope worked at 5 kV with the Inlens detector. For the ALD-Al₂O₃ coated sample, 1 nm of Au-Pd coating is performed prior to SEM imaging.

II.1.3.2 Transmission electron microscopy

The quality of nanoparticles to produce pure crystalline film at low temperature (phase, orientation, grain shape and size distribution) has been investigated using ACOM-TEM (Automated crystal phase and orientation mapping in TEM) and STEM-EDS (scanning transmission electron microscopy–energy-dispersive spectroscopy).

II.1.3.2.1 ACOM-TEM

This technique is also known as ASTAR™ (commercial counterpart provided by NanoMEGAS). In this approach, 2D diffraction patterns are systematically acquired with fast cameras while the focused probe is scanning the area of interest. This enables the reconstruction of 2D maps highlighting different crystalline phases, crystallographic orientation and/or local stress fields, and presence of amorphous areas in the matrix at the nanoscale with spatial resolution up to 1-3 nm in typical areas of several μm^2 .

For the ACOM-TEM experiments, a nanometric electron beam is scanned over the film surface and diffraction patterns produced at each scanned point are recorded. The DigiSTAR unit responsible for the scanning control is connected to the TEM deflection coils. Diffraction patterns are acquired with an external optical camera placed in the front of the TEM viewing screen. The algorithm used by ACOM-TEM for the automatic indexing of diffraction patterns is based on template matching: diffraction patterns are individually compared to series of templates that are computed for all possible crystal orientations of all expected phases. Indexing is performed by cross-correlating each acquired pattern with the templates [44]. The orientation defined by the template presenting the highest degree of matching is chosen (**Figure II.14**).

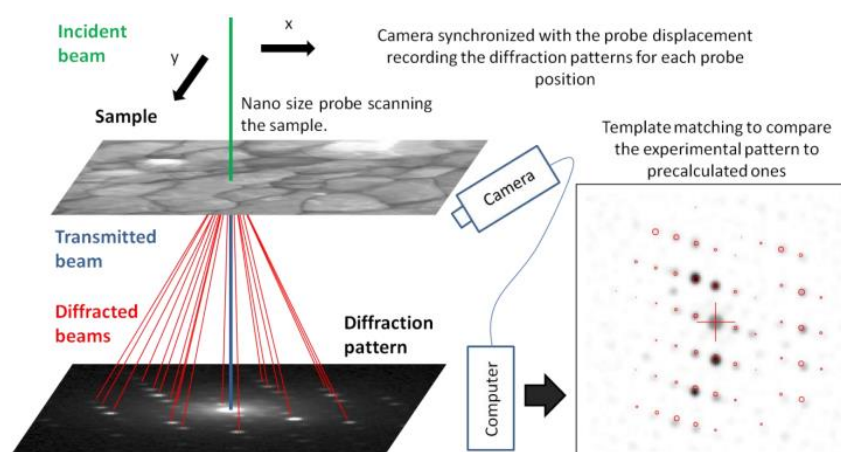


Figure II.14: Schematic representation of the ACOM-TEM method [45].

II.1.3.2.2 STEM-EDX

Elemental mapping at the atomic-scale by scanning transmission electron microscopy (STEM) using energy-dispersive X-ray spectroscopy (EDS) provides a powerful real-space approach to chemical characterization of material structures.

The data acquisition is carried out in a JEOL-2100F transmission electron microscope operated at 200 kV with a probe size around 1.5 nm. ACOM-TEM observations are conducted over dispersed nanopowders on a grid for 60 s in a solution under the optimized conditions: codoped TiO₂ suspension at operational pH = 3 (0.1 M of additives) and with 20 min as a suitable duration of a probe ultrasonication.

For the substrates coated with ALD-Al₂O₃ preparation for STEM-EDX and ACOM-TEM is conducted using focused ion beam lithography (FIB) technique. The cross sections preparation is done by Focused Ion Beam (FIB) milling operating at 30 kV, tilt angle -36° in a ZEISS Cross Beam NVISION 40.

II.1.4 Dynamic and electrophoretic light scattering

The particles dispersed in the liquid move randomly due to the collision with the surrounding solvent molecules, referred as Brownian motion. The particle size distribution can be determined using dynamic light scattering (DLS). The information about the nanoparticle surface charge can be obtained by zeta potential measurement using electrophoretic light scattering (ELS).

II.1.4.1 Dynamic light scattering

In DLS, when the particles are illuminated by a light source, the light is scattered in all directions. Then, the scattered light arrive to the detector. For the Brownian motion, the small particles move fast in a liquid, while the large particles move slowly. So the rates of intensity fluctuations are quicker for small particles than larger ones. The relationship between the size of a particle and its speed due to Brownian motion is defined in the Stokes-Einstein equation [46]:

$$D = \frac{T k_B}{6 \pi \eta R_H} \text{(Equation II.1)}$$

- D Translational diffusion coefficient [m²/s] – “speed of the particles”
 k_B Boltzmann constant (1.380×10^{-23} kg.m².s⁻².K⁻¹)
 T Temperature [K]

- h Viscosity of the medium [Pa.s]
 R_H Hydrodynamic radius [m]

The particle size measured with DLS is the diameter of the sphere that diffuses at the same speed as the particle being measured. The primary weighting model displayed in a DLS software show intensity-based results. The intensity of particles distribution can be recalculated to a volume and number. For this, the material refractive index and the absorbance of the measured sample at the laser wavelength need to be known. Intensity-based techniques present an attention on larger particles that diffuse more light than smaller particles. Meanwhile, volume and number distributions present a tendency to smaller particle fractions. The intensity-volume-number presentation of size distribution are just various representations of the same physical reality of differently sized particles distribution [46]. The initial results from a DLS measurement, representing the hydrodynamic diameter and the polydispersity index are related to the intensity weighted particle size distribution. Therefore, these values will not change, if different weighting models are selected.

The polydispersity index (PDI) is given in order to describe the broadness of the particle size distribution. However, the polydispersity index does not provide any information about the shape of the size distribution or the ratio between two particle fractions. The lower PDI value (0.5) shows larger polydisperse distribution.

Particle size distribution are measured with a Particle size analyzer VACSO ($\lambda= 657$ nm, Laser power 38%) utilizing dynamic light scattering (DLS). The temperature is set to 25°C. Before the measurements, suspensions are diluted to a concentration of $3.6 \cdot 10^{-4}$ M suitable for DLS measurements.

II.1.4.2 Electrophoretic light scattering

ELS or Zeta potential (ZP), also known as electrokinetic potential is measured in millivolts (mV). The particles dispersed in the liquid acquire surface charges due to the surface ions or the adsorption of the solvent ions. The ions carrying the opposite charge will be attracted strongly on the surface of the particles, forming the inner Stern layer. An outer, diffuse region where the ions are less attached is also formed, combined with the Stern layer creating a double electrical layer surrounding the particle [47]. **Figure II.15** presents the concept of zeta potential. The Smoluchowski equation linearly relates the electrophoretic mobility μ_e to the electrical potential at the shear plane (ζ , in V) and it is valid for dispersed particles of any shape and any concentration [48]:

$$\mu_e = \frac{\epsilon_0 \epsilon_r \zeta}{\eta} \text{ (Equation II.2)}$$

Where ϵ_r = relative permittivity/dielectric constant, ϵ_0 = permittivity of vacuum, ζ = ZP and η = viscosity at experimental temperature.

Due to the electric field, particles will move at different speeds which means that highly charged particles will move quickly than less charged ones. Particles that possess a zeta potential will migrate toward the opposite-charged electrode and the rate of migration is proportional to zeta potential.

As reported in literature, zeta potential values greater than the absolute value of ± 30 mV have high degrees of stability. Dispersions with less than the absolute value of ± 25 mV are relatively stable but will agglomerate due to Van Der Waals interparticle attractions [49-50]. The pH value at which the particle carries no electrical charge is known as the isoelectric point (pH_{iep}). The most important factor that affects zeta potential is the pH of the medium. Other factors include ionic strength, the concentration of any additives, and temperature

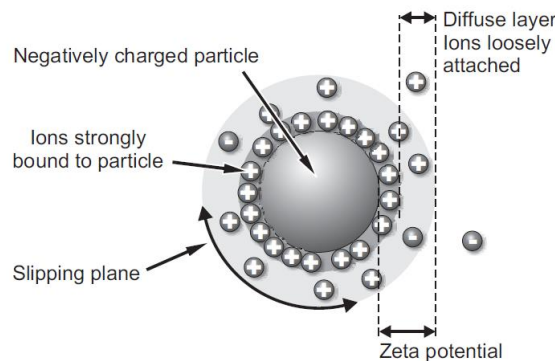


Figure II.15: Schematic diagram of the principle of the PZ technique [51].

Zeta potential measurements of the undoped and codoped TiO_2 suspensions are studied using a zeta potential analyzer DTS 1060 C model clear disposable zeta cell (Malvern Instruments). After magnetic agitation for 24 hours and ultrasonication for 20 min. Similarly, as DLS, before the measurements, suspensions are diluted to a concentration of 3.6×10^{-4} M.

II.1.2 Chemical characterization

II.1.2.1 Fourier-transform infrared spectroscopy

FT-IR spectra of the codoped TiO_2 nanopowders are performed using a Bio-Rad Infrared Fourier Transform spectrometer FTS165 with a resolution of 4 cm^{-1} to identify the functional groups present.

II.1.2.2 X-ray Photoelectron Spectroscopy

XPS also known as Electron Spectroscopy for Chemical Analysis (ESCA) reveals which chemical elements are present at the surface, and the nature of the chemical bond that exists between these elements. This technique has an information depth of 1–5 nm and therefore it is capable of examining only the outer layers or surfaces. It can detect all of the elements except hydrogen and helium.

In this study, XPS analysis is performed in a Vacuum Generator XR3E2 apparatus with a Mg K_{α} X-ray source at 15 kV, 20 mA to analyze the surface chemical compositions for the pure and codoped samples. Analyses are carried out at an angle of 90° between the sample surface and the hemispherical analyzer. Pressure in the chamber is lower than 10^{-8} Pa. The analyzed average area is about 40 mm²

II.1.3 Thermal analysis (TG-DTA)

The thermal properties of the as-prepared undoped and codoped nanopowders are carried out in a TGA (Thermogravimetric Analysis) apparatus (Setaram SETSYS Evolution 1750) using about 30 mg of powder in helium operated at an air flow of 40 ml/min when heating from 50 to 800 °C at a rate of 10 °C/min.

II.1.4 Optical analysis

II.1.4.1 Photoluminescence spectroscopy

In this work, the room temperature upconversion spectra at a wavelength (λ) of 980 nm are assessed in a Fluoromax 4P Horiba fluorimeter equipped with a 150 W xenon lamp as excitation source.

II.1.4.2 Spectroscopic ellipsometry

In this work, Spectroscopic Ellipsometry (SE) measurements are carried out with a Semilab SE-2000 using wavelengths in the range from 200.73 to 1596.86 nm at an incident angle of 75.06°. For fittings, simplex algorithm is used.

II.1.5 Mechanical analysis

II.1.5.1 Scratch Adhesion Test

Scratch test is performed to obtain the critical load as a useful adhesion coating parameter. A diamond indenter with a rounded tip (Rockwell) is pressed onto the surface under test. As the sample is moved underneath it at constant speed, the indenter leaves a scratch mark. The test force exerted by the indenter on the surface can either remain constant (Constant Load Scratch)

or be increased (Progressive Load Scratch). In most measurements, the progressive mode is used. Here, the force of the indenter is increased either stepwise or linearly until failure occurs at critical loads (L_c), Normal force (F_n) and frictional force (F_t) are recorded. At very low loads, the coating can resist to the indenter, but as the force increases, the material stress increases until a specific point when material failure sets in, the critical load L_c . Such critical loads (or critical failure point, L_c) is observed by subsequent optical microscopy, variations in frictional force (F_t), acoustic emission (AE) or changes in penetration depth (P_d).

In this study, the optical microscopy is used to estimate the minimum or critical load required to scribe away the film and leave behind a clear channel or visible substrate. In addition, the frictional force, F_t , is used as the force required to move the coating over the substrate.

II.5.2 Hardness

The hardness is the resistance of a coating to plastic deformation created by indentation. An indentation test consists in measuring the variation of an applied force (F_n) as a function of the imposed penetration. The nature and geometry of the indenter condition the mechanics of the test, therefore the exploitable values. In this work, the indenter used is of Berkovich type, which is a pyramidal tip with triangular base.

The hardness measurement from the force-penetration curve provided by the indentation test is given by the relation:

$$H = \frac{F_{max}}{A_c} \text{ (Equation II.3)}$$

Where F_{max} is the maximal force applied and A_c represents the contact area, which is the size of the impression left by an indenter or the depth of the indenter penetration.

References

- [1] T. Budtova, "Cellulose II aerogels: a review" *Cellulose*, vol. 26, pp. 81-121, 2019.
- [2] M. Mukhopadhyay, B. S. Rao, "Modeling of supercritical drying of ethanol-soaked silica aerogels with carbon dioxide" *Journal of Chemical Technology & Biotechnology*, vol. 83, pp. 1163–1169, 2008.
- [3] R. A. Laudise, D. W. Johnson, "Supercritical drying of gels" *Journal of Non-Crystalline Solids*, vol. 79, pp. 155–164, 1986.
- [4] J. Estella, J. C. Echeverría, M. Laguna, J. J. Garrido, "Effect of supercritical drying conditions in ethanol on the structural and textural properties of silica aerogels" *Journal of Porous Materials*, vol. 15, pp. 705–713, 2008.
- [5] S. Steiner, "Open source aerogel," 2014 : <http://www.aerogel.org/?p=345>.
- [6] FI. Benammar, "Synthèse par voie sol-gel et mise en suspension des nanoparticules dopées (Er, Yb) en vue d'application photovoltaïque," 2019.
- [7] I. Benammar, R. Salhi, J.-L. Deschanvres, R. Maalej, "The effect of rare earth element (Er, Yb) doping and heat treatment on suspension stability of Y₂O₃ nanoparticles elaborated by sol-gel method," *Journal of Materials Research and Technology*, vol. 9, pp. 12634–12642, 2020.
- [8] A. Zahrouni, A. Bendaoued, and R. Salhi, "Effect of sol-gel derived TiO₂ nanopowders on the mechanical and structural properties of a polymer matrix nanocomposites developed by vacuum-assisted resin transfer molding (VARTM)," *Ceramics International*, pp. 1–8, 2020.
- [9] M. Messaoud, F. Trabelsi, P. Kumari, A. Merenda, L. F. Dumée, "Recrystallization and coalescence kinetics of TiO₂ and ZnO nano-catalysts towards enhanced photocatalytic activity and colloidal stability within slurry reactors: Rationale nano-catalyst design for enhanced catalytic performance reactors," *Materials Chemistry and Physics*, vol. 252, 2020.
- [10] A. Dehghanghadikolaei, J. Ansary, and R. Ghoreishi, "Sol-gel process applications: A mini-review," *Proceedings of the Nature Research Society*, vol. 2, 2018.
- [11] Q. Shang et al., "Green and red up-conversion emissions of Er³⁺-Yb³⁺ Co-doped TiO₂ nanocrystals prepared by sol-gel method," *Journal of Luminescence*, vol. 128, pp. 1211–1216, 2008.
- [12] J. Reszczyńska, A. Iwulska, G. Sliwinski, A. Zaleska, "Characterization and photocatalytic activity of rare earth metal-doped titanium dioxide," *Physicochemical Problems of Mineral Processing*, vol. 48, pp. 201–208, 2012.
- [13] J. F. Conroy, M. E. Power, P. M. Norris, "Applications for Sol-Gel-Derived Materials in Medicine and Biology" *Journal of the Association for Laboratory Automation*, vol. 5, pp. 52–57, 2000.
- [14] I. Benammar, R. Salhi, J. Deschanvres, R. Maalej, "The Effect of Solvents and Rare-Earth Element (Er , Yb) Doping on Suspension Stability of Sol – Gel Titania Nanoparticles," *Journal of Luminescence*, pp. 718–726, 2017.
- [15] D. Riassetto, "Fonctionnalisation de surface par chimie douce en solution liquide. Nanoparticules métalliques (platine, or, argent) et revêtements TiO₂," 2010.

- [16] T. Moulina, R. Moreno, "Colloidal stability of gadolinium-doped ceria powder in aqueous and non-aqueous media," *Journal of the American ceramic society*, vol. 33, pp. 297–303, 2013.
- [17] S. Sumitomo, H. Koizumi, A. Uddin, Y. Kato, "Comparison of dispersion behavior of agglomerated particles in liquid between ultrasonic irradiation and mechanical stirring," *Ultrasonics - Sonochemistry*, vol. 40, pp. 822–831, 2018.
- [18] M. S. Gorji, K. A. Razak, K. Y. Cheong, "Gold nanoparticles deposited on linker-free silicon substrate and embedded in aluminum Schottky contact," *Journal of Colloid and Interface Science*, vol. 408, pp. 220–228, 2013.
- [19] M. Ben Haddada et al., "Optimizing the immobilization of gold nanoparticles on functionalized silicon surfaces: Amine- vs thiol-terminated silane" *Gold Bulletin*, vol. 46, pp. 335–341, 2013.
- [20] J. Cloarec, et al., "pH driven addressing of silicon nanowires onto pH driven addressing of silicon nanowires onto Si₃N₄ /SiO₂ micro-patterned surfaces" *Nanotechnology*, vol. 27, pp. 295602, 2016.
- [21] L. Dalstein, E. Potapova, E. Tyrode, "The elusive silica/water interface: Isolated silanols under water as revealed by vibrational sum frequency spectroscopy," *Physical Chemistry Chemical Physics*, vol. 19, no. 16, pp. 10343–10349, 2017.
- [22] V. Deepak Patil, S. Aravindan, P. Rao, "Nano-structure Formation by Annealing Ultrathin Polystyrene Film," in *Proceedings of 6th International & 27th All India Manufacturing Technology, Design and Research Conference College of Engineering, Pune, Maharashtra*, 2016.
- [23] J. F. Taylor, "Spin coating: An overview." *Finishing for electronics*.
- [24] R. Balzarotti, C. Cristiani, L. F. Francis, "Spin coating deposition on complex geometry substrates: Influence of operative parameters" *Surface & Coatings Technology*, 2017.
- [25] M. D. Tyona, "A theoretical study on spin coating technique" *Advances in materials Research*, vol. 2, pp. 195–208, 2013.
- [26] C.-M. Seaha, S.-P. Chai, S. Ichikawa, A. R. Mohamed, "Control of iron nanoparticle size by manipulating PEG–ethanol colloidal solutions and spin-coating parameters for the growth of single-walled carbon nanotubes" *particuology*, vol. 11, pp. 194–400, 2013.
- [27] A. A. Ansari and S. D. Sartale, "Effect of processing parameters on size, density and oxygen reduction reaction (ORR) activity of Pd nanoparticles grown by spin coating" *surface and coatings technology*, vol. 281, pp. 68–75, 2015.
- [28] "Spin Coating: Complete Guide to Theory and Techniques." *Osilla*.
- [29] M. M. Ferdaus et al., "Design and Fabrication of a Simple Cost Effective Spin Coater for Deposition of Thin Film" *Advances in environmental biology*, vol. 8, pp. 729–733, 2014.
- [30] S. N. Sadikin, M. Y. A. Rahman, A. A. Umar, M. M. Salleh, "Effect of spin-coating cycle on the properties of TiO₂ thin film and performance of DSSC," *International Journal of Electrochemical Science*, vol. 12, pp. 5529–5538, 2017.
- [31] P. Malliga, J. Pandiarajan, N. Prithivikumaran, K. Neyvasagam, "Influence of Film Thickness on Structural and Optical Properties of Sol – Gel Spin Coated TiO₂ Thin Film," *Journal of Applied Physics*, vol. 6, pp. 22–28, 2014.

- [32] H. S. Chin, L. S. Chao, K. S. Kao, “Study of structural and optical properties of ZnO thin films produced by sol-gel methods” *Sensors and Materials*, vol. 28, pp. 523–530, 2016.
- [33] N. Sahu, B. Parija, S. Panigrahi, “Fundamental understanding and modeling of spin coating process: A review” *Indian Journal of Physics*, vol. 83, pp. 493–502, 2009.
- [34] D. Verma, A. Ranga Rao, V. Dutta, “Surfactant-free CdTe nanoparticles mixed MEH-PPV hybrid solar cell deposited by spin coating technique,” *Solar Energy Materials and Solar Cells*, vol. 93, pp. 1482–1487, 2009.
- [35] X.J. Zhang, K. Hoshino, “Chapter 2 - Fundamentals of nano/microfabrication and scale effect,” in *Molecular Sensors and Nanodevices*, pp. 43–111, 2019.
- [36] R. Biswas, S. Chatterjee, “Effect of surface modification via sol-gel spin coating of ZnO nanoparticles on the performance of WO₃ photoanode based dye sensitized solar cells,” *Optik*, vol. 212, pp. 164142, 2020.
- [37] J. A. Ramos-Guivar, E. O. López, J. M. Greneche, F. Jochen Litterst, E. C. Passamani, “Effect of EDTA organic coating on the spin coating behavior of maghemite nanoparticles for lead (II) adsorption” *Applied Surface Science*, vol. 538, no. pp. 148021, 2021.
- [38] T. Komikado, A. Inoue, K. Masuda, T. Ando, and S. Umegaki, “Multi-layered mirrors fabricated by spin-coating organic polymers,” *Thin Solid Films*, vol. 515, pp. 3887–3892, 2007.
- [39] A. Boudrioua, M. Chakaroun, A. Fischer, “Organic Light-emitting Diodes,” in *organic lasers*, pp. 49–93, 2017.
- [40] K. Xiong et al., “From spin coating to doctor blading: A systematic study on the photovoltaic performance of an isoindigo-based polymer” *Solar Energy Materials and Solar Cells*, vol. 132, pp. 252–259, 2015.
- [41] “Spin Coat theory” UT Dallas:
<https://personal.utdallas.edu/~rar011300/CEEspinners/SpinTheory.pdf>
- [42] J. Koo, S. Kim, S. Jeon, H. Jeon, Y. Kim, Y. Won, “Characteristics of Al₂O₃ thin films deposited using dimethylaluminum isopropoxide and trimethylaluminum precursors by the plasma-enhanced atomic-layer deposition method,” *Journal of the Korean Physical Society*, vol. 48, pp. 131–136, 2006.
- [43] S. Gierałowska et al., “Properties and characterization of ALD grown dielectric oxides for MIS structures,” *Acta Physica Polonica A*, vol. 119, pp. 692–695, 2011.
- [44] A. Valery, “Caractérisation de microtextures par la technique ACOM-TEM dans le cadre du développement des technologies avancées en microélectronique,” 2017.
- [45] N. Sallel, “Recrystallization , abnormal grain growth and ultrafine microstructure of ODS ferritic steels,” 2015.
- [46] A. Paar, “The principles of dynamic light scattering,” <https://wiki.anton-paar.com/fr-fr/les-principes-de-la-diffusion-dynamique-de-la-lumiere/> .
- [47] S. JinPark, M-K. Seo, “Chapter 1 - Intermolecular Force,” in *Interface Science and Technology*, pp. 1–57, 2011.
- [48] F. Yang, W. Wu, S. Chena, W. Gan, “The ionic strength dependent zeta potential at the surface

- of hexadecane droplets in water and the corresponding interfacial adsorption of surfactants,” *Soft Matter*, vol. 13, pp. 638–646, 2017.
- [49] A. Kumar, C.K. Dixit, “Methods for characterization of nanoparticles,” *Advances in nanomedicine for the Delivery of therapeutic Nucleic Acid*, pp. 43–58, 2017.
- [50] N. Mandzy, E. Grulke, T. Druffel, “Breakage of TiO₂ agglomerates in electrostatically stabilized aqueous dispersions,” *Powder Technology*, vol. 160, pp. 121–126, 2005.
- [51] NanoComposix, “Zeta Potential Measurements,” <https://nanocomposix.com/pages/zeta-potential-measurements>.

Chapter III

Characterization of sol-gel nanopowders and suspensions optimization

Introduction

In this chapter, the structural and spectroscopic properties of undoped and codoped TiO₂ nanopowders using different characterization techniques are firstly presented (TG–DTA, XRD, FTIR, XPS, SEM, BET and TEM). Following this, the suspension optimization using various ways: electrostatic stabilization (pH, co-doping quantity) and physical dispersion (ultrasonication) process is monitored by measuring the zeta potential, and evaluating particle size distribution with SEM observations. Finally, deep investigation of the structure and composition of dispersed TiO₂ nanopowders under the optimized conditions is performed using scanning transmission electron microscopy–energy-dispersive spectroscopy (STEM-EDS) and automated crystal orientation mapping for transmission electron microscopy (ACOM-TEM).

I. Structural and spectroscopic studies of TiO₂ nanopowders

I.1 Thermal analysis (TG-DTA)

The thermal behavior and weight loss curves of as-prepared undoped and codoped TiO₂ nanopowders are investigated by the TG–DTA analysis recorded in the range of 50 - 800°C. From the TG curves presented in **Figure III.1**, two similar weight losses around 50 - 227°C and 227 - 800°C are shown for both nanopowders. The first weight loss can be attributed to the evaporation of physically adsorbed water, which is related to the significant endothermic peaks in the corresponding DTA curves. The second weight loss occurs at temperature from 227°C to 800°C, which could be assigned to the decomposition of various organic molecules, used during the preparation of nanopowders. In this region, two exothermic reactions are observed for both types of nanopowders as detected in the corresponding DTA curve. A larger exothermic peak at approximately 400°C could be probably assigned to the crystallization of a remaining amorphous portion toward anatase phase. In other reports, this transformation appears as a sharp peak if it is related to a total transformation from the amorphous to the crystalline phase [1][2], or to the decomposition of the rest of the organic residue [3]. The other smaller exothermic peak at approximately 300°C could be attributed to the combustion and the release of organic substances containing oxygen and carbon. Our TGA-DTA results have similarities with the literature although the reported peak positions are observed at different temperatures because of the use of different reagents in their synthesis [1], [4-6]. From the TG-DTA analysis, most of the organic contamination could be eliminated at temperature below 300°C.

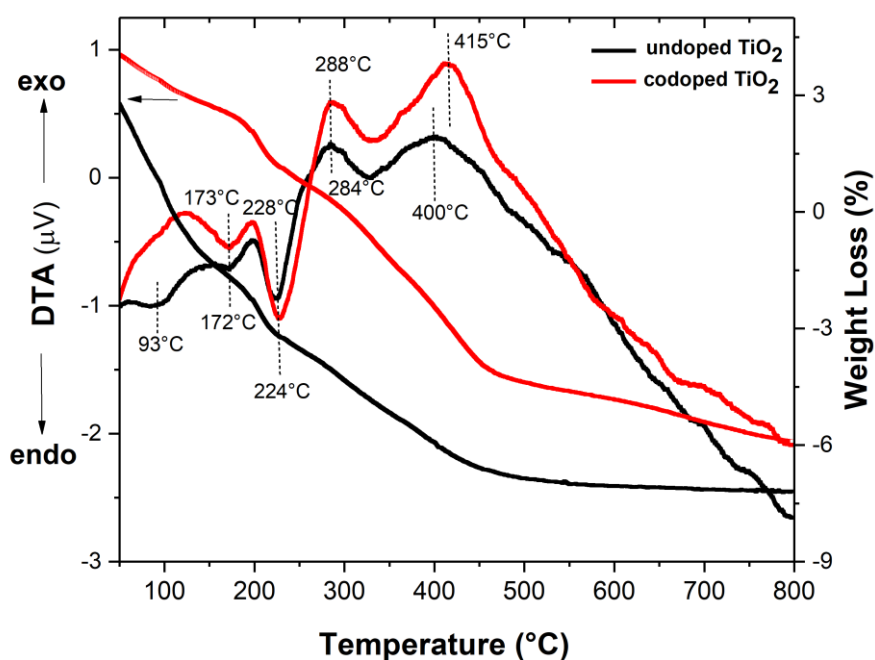


Figure III.1: TG-DTA curves of as-prepared undoped and codoped TiO₂ nanopowders.

Fourier transform infrared (FTIR) spectroscopy is used to identify the functional groups present in the as-prepared and calcined (at 300°C- 2 h) codoped TiO₂ nanopowders. As shown in **Figure III.2**, the FTIR absorbance spectra are composed of three different bands. In the low wavenumber range, the strong band between 900 and 400 cm⁻¹ is assigned to the Ti–O stretch [20]. In the medium wavenumber range, the stretching vibrations at 1560 and 1440 cm⁻¹ are attributed to C=O and C-O, corresponding to organic molecules [21]. In the high wavenumber range, the broad band between 3590 and 2750 cm⁻¹ is related to the stretching vibrations of hydroxyl group (O–H), indicating the presence of surface water as moisture on the surface [22-23]. After thermal treatment at 300°C, the intensity of hydroxyl and organic contamination bands disappears which is in a good agreement with the TG-ATD results.

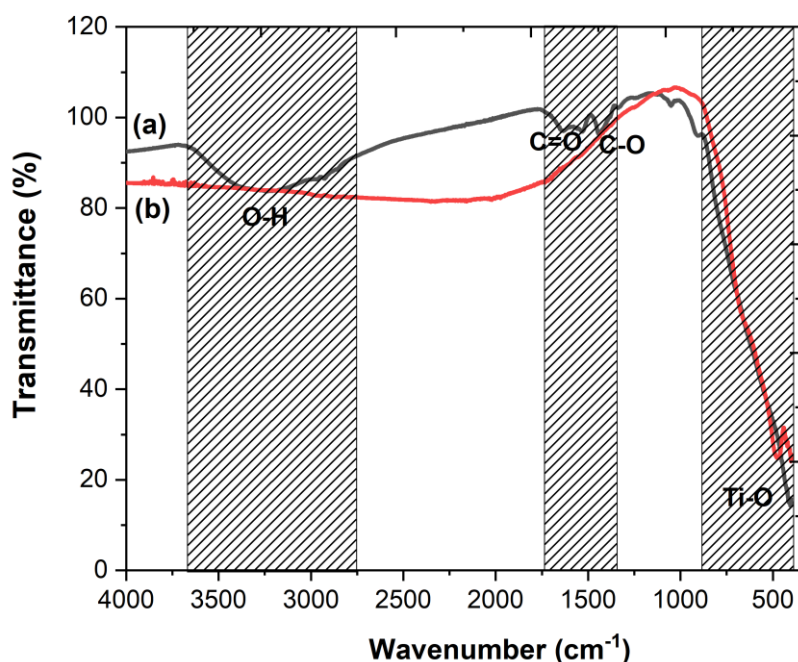


Figure III.2: FT-IR spectra of codoped TiO₂ nanopowders (a) as-prepared and (b) calcined at 300°C-2h.

Based on thermal and FTIR analysis, annealing temperature at a relatively low temperature of 300°C can enhance the crystallinity of the TiO₂ anatase structure and eliminate the hydroxyl and organic contaminations.

It is worth highlighting that these contaminations are reported to be unfavourable for photoluminescence properties [7]. For this reasons, this temperature of 300°C is used during this study. In the following, undoped and codoped TiO₂ nanopowder calcined at 300°C for 2 h are investigated.

I.2 Structural analysis

The crystal phase of undoped and codoped TiO₂ as-prepared and calcined at 300°C for 2 h are studied through X-ray powder diffraction. As illustrated in **Figure III.3**, all the diffraction peaks of the XRD patterns reveal the presence of pure TiO₂ in the anatase phase (System: Tetragonal, ICDD Card Number: 21-1272). From the XRD data, the crystallinity of nanopowders is demonstrated at the exit of the autoclave (T= 243°C, P= 64 bar) and the calcination at 300°C, further improves the crystallinity, which is in accordance with TG-DTA data. This result is interesting because it proves the effectiveness of the experimental used protocol during the formation of the sol and supercritical drying. Some studies report that a post heat treatment is essentially required to crystallize the amorphous particles and it is

recommended at temperatures above 500°C [5],[8-9]. Whereas, in our work, an annealing temperature of 300°C is sufficient to form the crystalline phase.

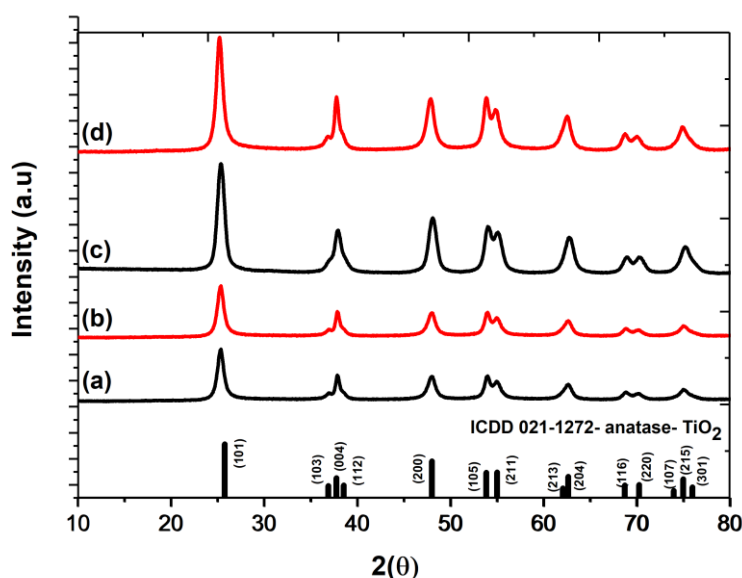


Figure III.3: XRD patterns of: (a, b) as-prepared undoped and codoped TiO₂, respectively and (c, d) undoped and codoped TiO₂, respectively calcined at 300°C- 2h.

Considering the codoping impact on structure, no other phase such as Er₂O₃, Yb₂O₃ is evidenced in the codoped nanopowder, proving the incorporation of Er³⁺ and Yb³⁺ ions into the TiO₂ matrix. Therefore, we can conclude that codoping has no impact on the structure. The mean crystallite size, *D*, is estimated using Debye-Sherrer equation for all the diffraction peaks:

$$D = \frac{K\lambda}{\beta_D \cos \theta} \quad (\text{Equation III.1})$$

Where *D* represents the crystallite size (Å), *K* the shape factor, λ is the wavelength of Cu K α radiation, θ the diffraction angle and β_D is the half-width of the diffraction peak (FWHM) in radians. The results of microstructural parameters of undoped and codoped TiO₂ as-prepared and calcined at 300°C for 2h are presented in **Table III.1**. The mean crystallite size remains almost the same after the calcination and with co-doping. However, there is a difference in the lattice parameters, which are slightly larger for the codoped sample than the undoped one (increase for the annealed samples by 0.16 % and 0.27 % for *a* and *c* parameters, respectively). That causes an anisotropic expansion of the TiO₂ unit cell volume by 0.40 %, indicating a distortion in the cell when the ions enter into TiO₂ structure [10]. Pérez and co-workers [11] indicates that cell parameter expansions could be attributed to the distortion caused by the substitution of Ti⁴⁺ by Er³⁺ ions.

The crystallite size and lattice distortion degree, η , are evaluated using the Williamson-Hall (W-H) method [12-14]. Details are given in Annex 1. All the diffraction peaks of undoped and codoped TiO₂ as-prepared and calcined at 300°C for 2 h are selected for carrying out the analysis. The results show positive strain values that reveal the presence of tensile strain for all the samples. As expected, the crystallite size estimated by Debye-Sherrer method differs from the ones calculated by the Williamson-Hall method due to the negligence of the lattice strain in the first method [15]. In our case, because of the presence of the tensile strain higher crystallite size are found with W-H method than with Debye-Sherrer. The lattice distortion remains almost the same after the calcination of the same sample but it increases after the codoping. This raise after the codoping can be explained by the large difference in the ionic radius between Er³⁺ (0.89 Å) and Yb³⁺ (0.86 Å) compared to Ti⁴⁺ (0.61 Å) which makes the replacement more difficult and leads to the distortion of the TiO₂ lattice [16-18].

These results illustrate that the calcination further enhance the crystallinity of the obtained phase without a remarkable increase in the size. That also confirms the incorporation of Er³⁺ and Yb³⁺ dopant ions in the host lattice without changing the crystalline phase nature.

Table III.1: Microstructural parameters of undoped and codoped TiO₂ as-prepared and calcined at 300°C for 2 h obtained from XRD patterns.

Sample	Mean crystallite size by Debye-Sherrer formula (nm)	Mean Crystallite Size by W-H plot (nm)	Lattice distortion η (%)	a (Å)	c (Å)	c/a ratio	Unit cell volume (Å ³)
undoped TiO ₂ as-prepared	10	12	0.08	3.7852	9.4901	2.5072	136
undoped TiO ₂ calcined	9	10	0.07	3.7862	9.4970	2.5083	136.14
codoped TiO ₂ as-prepared	11	16	0.32	3.7926	9.5051	2.5062	136.72
codoped TiO ₂ calcined	11	16	0.31	3.7923	9.5054	2.5064	136.69

I.3 Spectroscopic analysis

To identify the chemical valence states of Er and Yb elements in TiO₂ material, surface chemical compositions of undoped and codoped TiO₂ are performed using XPS analysis. The XPS spectra are recorded in the range of 0 - 900 eV. **Figure III.4a** shows the survey spectrum. The surface composition of nanoparticles is evaluated using the high-resolution (HR) Ti 2p, O

1s, C 1s, Yb 4d and Er 4d XPS spectra, respectively. As shown in **Figure III.4b**, the Ti 2p spectrum is characterized by a doublet composed of two symmetrical Ti 2p_{3/2} and Ti 2p_{1/2} peaks at binding energies of 458.8 eV, 464.5 eV and 458.7 eV, 464.4 eV for undoped and codoped TiO₂ respectively, generated from spin-orbit coupling and attributed to Ti⁴⁺ in TiO₂ anatase [24], [25]. Compared to undoped TiO₂, the Ti 2p peak for the codoped TiO₂ moves towards low binding energy, which is a direct measure of the lowering of valence state level of Ti⁴⁺ to Ti³⁺. Same observation is mentioned in other reports [26].

Figure III.4 e and **Figure III.4 f** present the Er 4d_{5/2} and Yb 4d_{5/2} spectra. Each peak could be deconvoluted into three peaks. First peaks are attributed to the Er-O and Yb-O bonds located at 168.7 eV and 184.9 eV [27]. Second peaks are related to the Er-OH and Yb-OH bonds located at 170.8 eV and 186.0 eV [28]. Additional peaks located at 167.6 eV and 183.4 eV could be attributed to metallic bonds more probably consisting of Er-Er and Yb-Yb, respectively. The presence of the mentioned peaks confirms the presence of Er³⁺ and Yb³⁺ ions.

Figure III.4c shows the O1s peak of the two samples, that can be deconvoluted into two peaks positioned at 530.0 eV, 531.5 eV and 529.9, 531.7 eV for undoped and codoped TiO₂ respectively. The peaks at lower binding energy are associated to surface lattice oxygen and the other peaks at higher binding energy are assigned to the H-O group from the absorbed H₂O on TiO₂ surface. The deconvolution of C 1s peak reveals three different types of bonds, the peak locating at 284.9 eV related to C-C, the other peak at 286.6 eV assigned to C-OH and peak at 288.6 eV associated C=O (**Figure III.4d**). The presence of carbonaceous species in XPS spectra could be attributed to the atmospheric gas adsorption due to the fact that powders remained in the bottles for a long time after elaboration before the analysis is made. For this reason, the nanopowders will be calcined one day prior to experiment and taken out of the oven the same day.

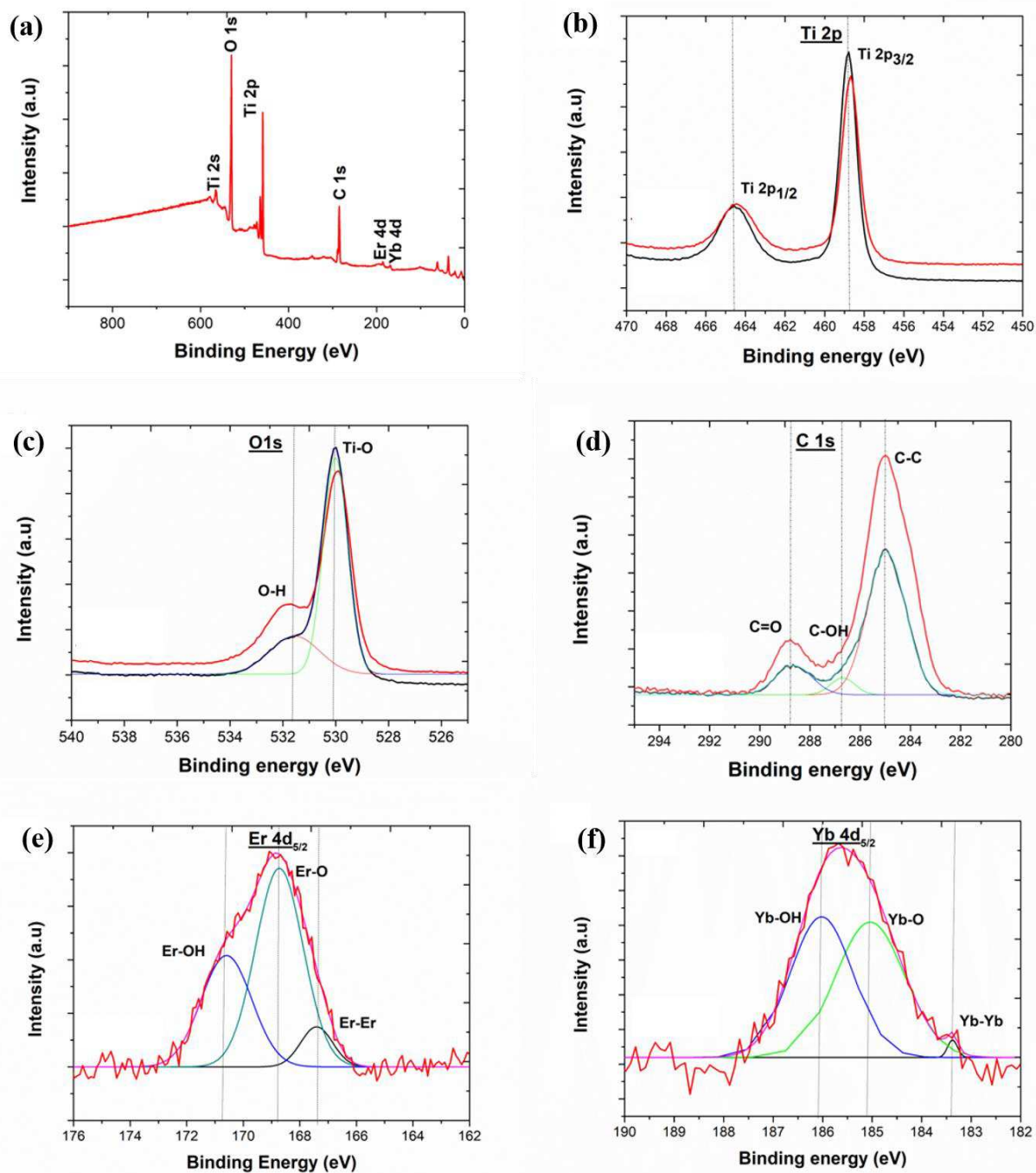


Figure III.4: XPS spectra of TiO_2 (a) Survey Scan, (b) $\text{Ti}2p$, (c) $\text{O}1s$ (d) $\text{C}1s$, (e) $\text{Er } 4d_{5/2}$ and (f) $\text{Yb } 4d_{5/2}$. Black line undoped TiO_2 and red line codoped nanoparticles calcined at 300°C - 2h.

I.4 Morphological and surface analysis

From SEM analysis, it is found that synthesized powders are made of spherical undoped and codoped TiO₂ aggregates with a diameter between 3 and 12 μm (**Figure III.5a, d**) consisting of large amounts of mono-dispersed particles below 50 nm in diameter (**Figure III.5b-f**). The codoping does not cause any change in the morphology. This observation is consistent with the XRD results. In fact, the fine nanoparticles prepared from the hydrolysis and condensation reactions have a high specific surface area and specific surface energy, which make the agglomeration with larger particle size easy to form, as observed [29]. The nanocrystallite aggregates present a porous structure arising from the nanometer sized crystallite units from which they are constructed.

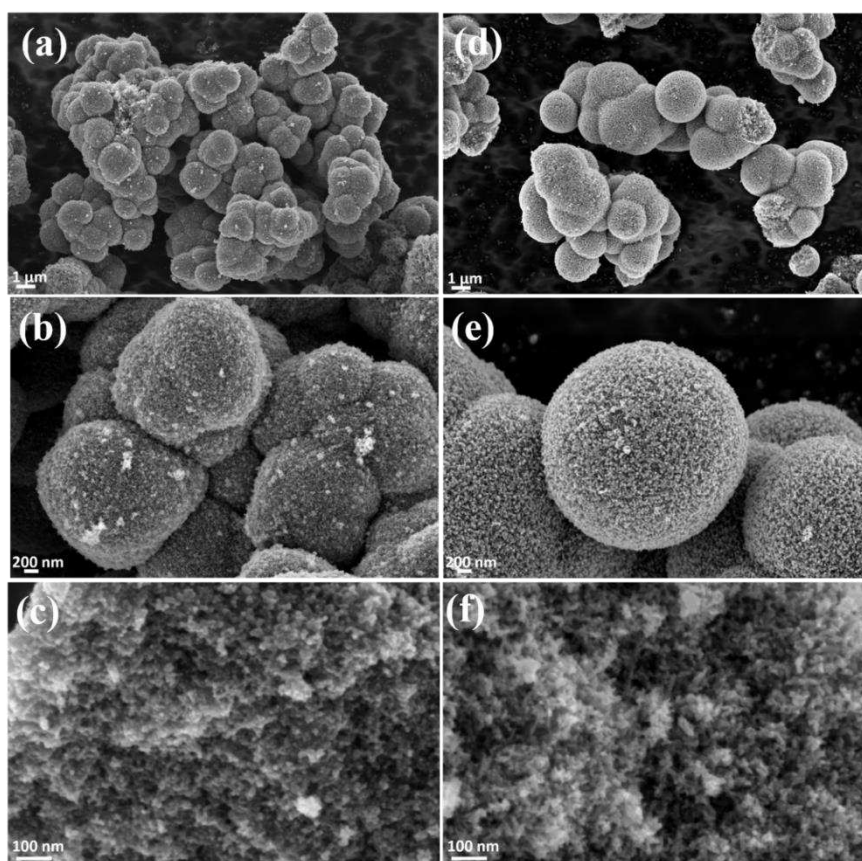


Figure III.5: SEM images of (a-c) undoped and (d-f) codoped TiO₂ nanopowders calcined at 300°C-2h at different magnifications.

Recently, spherical aggregates assembled from nanocrystallite have been reported to be able to overcome the drawbacks of the photoelectrodes based on nanoparticles and 1D nanostructure in solar energy conversion systems [30]. The spherical nanocrystallite aggregates have proved their ability to generate effective light scattering, comparable to the wavelengths of visible light, due to their sub-micrometer size. Unlike the large particle light scattering centers, the

nanocrystallite aggregates feature a highly porous structure arising from the nanometer sized crystallite building units from which they are constructed, therefore they allow a high internal surface area. In addition, to provide effective light scattering and large surface area, the nanocrystallite aggregates may offer better transport capacity for photogenerated electrons than that in a nanoparticle film, due to the compact structure inside the aggregates. Photoelectrodes derived from spherical nanocrystallite aggregates have demonstrated energy conversion efficiencies comparable or even higher than those made with TiO₂ nanoparticles, due to their above-mentioned multiple functions. Thus, the spherical aggregates are recognized as a promising class of material that may potentially lead to breakthroughs in improving the energy conversion efficiency, by further rational tailoring of the spherical aggregates with suitable morphology, size and porosity.

Since surface area is a crucial parameter for the use of the elaborated nanoparticles for many potential applications, further study of the specific surface area and pore-size distribution of the above-mentioned nanopowders is performed. According to the International Union of Pure and Applied Chemistry (IUPAC), adsorption isotherms can be classified as type-I to type-VI as illustrated in **Figure III.6**, which reflect the relationship between porous structures and their sorption type. The six isotherm types are characteristic of adsorbents that could be microporous (type I), nonporous or macroporous (types II, III, and VI), or mesoporous (types IV and V). The most characteristic feature of Type IV isotherm is the hysteresis loop that is associated with capillary condensation that takes place in mesoporous structure.

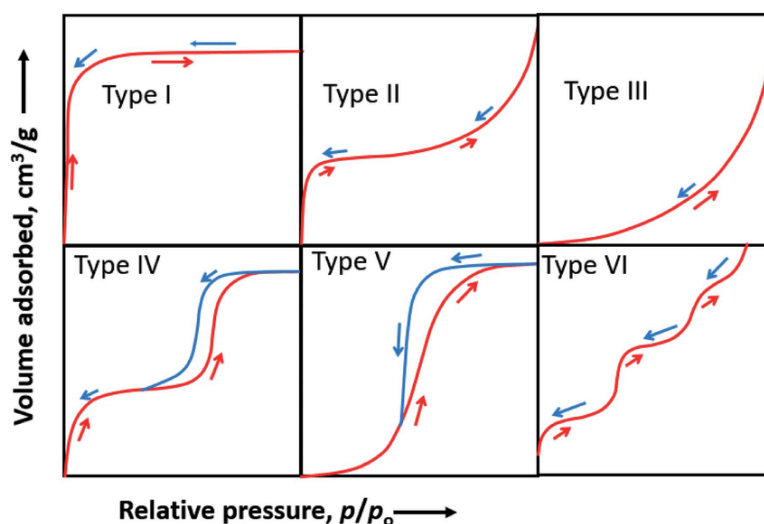


Figure III.6: Different types of adsorption isotherms as classified by IUPAC, showing both the adsorption and desorption pathways [31].

The adsorption-desorption isotherms of undoped and codoped TiO₂ shown in **Figure III.7a** belong to type IV, with a capillary condensation step at relative pressures of 0.79 to 0.96 and 0.66 to 0.92 for undoped and codoped nanopowders, respectively. The type IV behavior corresponds to the existence of ordered mesoporous structure [32-33].

The specific surface areas (S_{BET}) measured for the nanopowders elaborated via sol-gel method, are 125.7 m²/g and 140.6 m²/g for the undoped and codoped TiO₂, respectively. In general, in sol-gel synthesis, the nature of the gel is very important, as the pores in the gel are filled with ethanol. With a careful removal of the solvent under supercritical conditions, the porous structure remains undisturbed, which ultimately helps to increase the surface area of the samples compared to other methods such as co-precipitation and sol-gel with conventional rapid drying [34-37].

Moreover, codoping increases the specific surface area (S_{BET}) of TiO₂ nanopowders compared to the undoped ones, implying that the surface textural properties are improved in the presence of Er³⁺ and Yb³⁺ ions. Same observations have been reported in previous works [38-42], where it is demonstrated that the specific surface area of TiO₂ is largely related to the agglomeration degree. An increase in particles agglomeration is the major reason for the decrease in specific surface area. The codoping prevents the agglomeration of particles resulting in a high surface area.

Figure III.7b shows the pore-size distributions calculated from the N₂ adsorption isotherm because it gives a more realistic assessment of the pore size distribution and is proved to be in better qualitative agreement with SEM observations [43]. It is shown that the two samples contain mesoporous structure (dimensions in the range 2 - 50 nm) with a monomodal pore size distribution. The pore size distribution of the undoped TiO₂ exhibited a narrow pore size distribution centered at 34 nm with a total pore volume of 2.13 cm³/g. With the codoping, the pore size distribution is shifted to the smaller size positioned at 22 nm and the pore volume is decreased by 64%. The reason of this significant difference between the samples is due to the material compositions. As the surface area slightly increases with the codoping, a decrease in pore diameters is observed, which indicates the existence of finer particles. These results are in agreement with other reported observations [44].

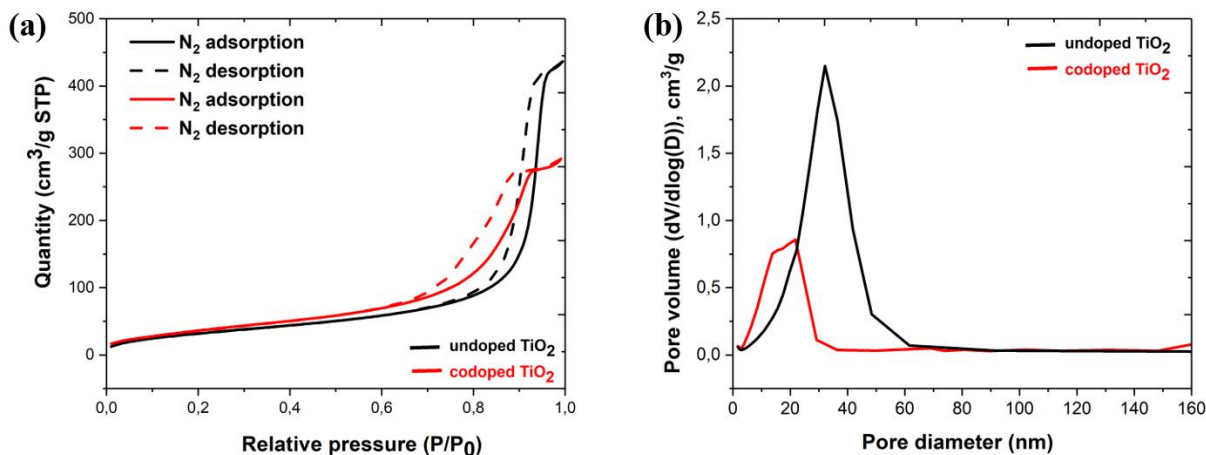


Figure III.7: (a) N₂ adsorption-desorption isotherms and (b) Barrett-Joyner-Halenda (BJH) pore size distributions as determined from the adsorption branch of the isotherm for N₂ gas on both undoped and codoped TiO₂ calcined at 300°C-2h.

The spherical shape and nanometer size of the particles with consequent high surface to volume ratio have an important impact on the photoluminescence properties. These characteristics are expected to lead to more light absorption from solar spectrum and enhancement of photonic devices performance [45-46].

Figure III.8 a and **Figure III.8 b** depict the TEM micrographs of codoped TiO₂ nanopowders. The micrograph proves that the nominal size of the nanoparticles is in the range of 10 – 20 nm and that the nanoparticles appear to be relatively homogeneous in size while fairly agglomerated. Furthermore, the local crystal structure of anatase is confirmed by selected area electron diffraction (SAED) technique; one SAED ring diffraction pattern with marked Miller indices of anatase TiO₂ nanopowder (ICDD Card Number: 21-1272). The diffraction rings clearly show the crystalline structure of the particles.

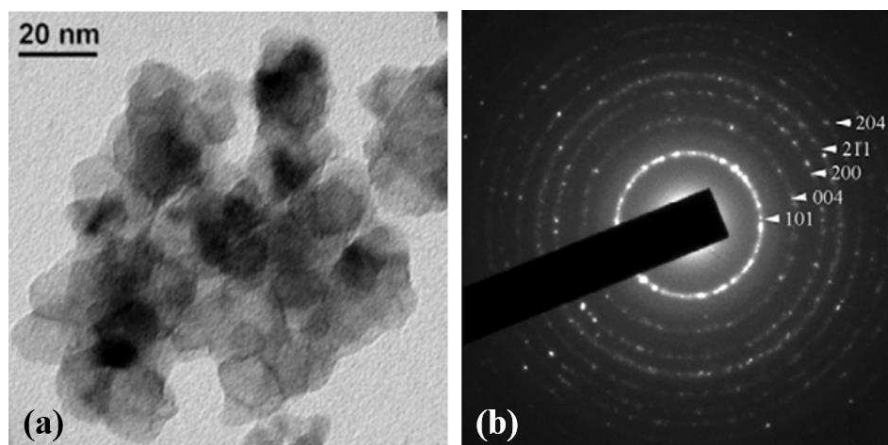


Figure III.8: (a) TEM image and (b) selected area electron diffraction patterns (SAED) where diffraction planes corresponding to anatase structure of co-doped TiO₂ nanoparticles.

We have found a good agreement between particles size measured by both structural and morphological characterization methods (XRD, SEM and TEM).

At the end of this section we clearly prove that we have synthesized particles with a controllable phase (anatase), size (diameter 10-20 nm), morphology (spherical shape), a good crystallinity, high surface area and doped with rare earth ions at low temperature ($T \leq 300^{\circ}\text{C}$).

II. Dispersion and stability optimization of TiO₂ nanoparticles in ethanol

The suspending is an important step for the photovoltaic application to fabricate nanostructured thin films. Indeed, the formation of a dense and homogeneous deposit of codoped TiO₂ nanopowders is possible only from a well-dispersed suspension. Important parameters governing the dispersion of nanoparticles are examined and discussed in this section. We will first describe differences for commonly used sonication methodologies to disperse particles. This will be followed by discussion of the electrostatic stabilization of nanoparticles. The effects of pH and additives concentration on nanoparticles size dispersion and surface charge are investigated. Then, the specific influence of probe sonication duration and codoping on the size distribution and sedimentation are examined.

II.1 Effect of the sonicator type

As shown in **Figure III.5**, the nanoparticles have a tendency to agglomerate with each other due to the van der Waals attractive forces. Therefore, ultrasonication is used as an external force to overcome the van der Waals attractions and dispersed nanoparticles. In this study, the impact of sonicator type on the temperature of the solution, under two different modes, and on the particle size of undoped TiO₂ dispersed in ethanol without pH variation are examined. Suspensions dispersion using either the bath or the probe sonicator is performed in order to

choose the most effective ultrasonication equipment for our study. For the probe sonicator, the distance between the tip and beaker bottom-inner surface is maintained at 2 mm.

In order to avoid solvent vaporization as well as a good breakage efficiency, two different modes of ultrasonication are studied for every sonicator, whilst maintaining a low constant temperature during the process. This can be explained by the fact that increasing the solvent temperature gives rise to its vapor pressure, so, more solvent vapor fills the cavitation bubbles, which tend to collapse less violently. Thereby, low sonication efficiency is expected [47]. The first mode consists of a continuous mode and the second one is based on the manual change of water bath every 5 min. The temperature evolution using bath and probe sonicators under these two modes are shown in **Figure III.9a** and **Figure III.9b**. The temperature difference at 0 min is related to the fact that the two experiments have been carried out on different days (not the same temperature). It is clearly seen that changing the water bath every 5 min leads to a decrease of the suspensions temperature in a constant way, especially when using the bath ($\sim 15^{\circ}\text{C}$) compared to the probe ($\sim 30^{\circ}\text{C}$). In order to obtain information about the particle size resulting from the dispersion, SEM observations after 10 min of ultrasonication of the dispersed particles on Si surface ($V_{\text{solution}} = 100 \mu\text{l}$ - 1000 rpm - 30 s) are presented from **Figure III.10a** to **Figure III.10d**. The SEM images of the dispersed particles show that the probe sonicator can drastically reduce the particle size. For the probe, it is noticeable that large particles are almost completely dispersed ($< 4 \mu\text{m}$) only after 10 min of ultrasonication treatment. For the bath, it seems obvious that the sonicator is almost ineffective in reducing the particle size. After 10 min of ultrasonication, the particle size is the same as the beginning (aggregates between 4 to 8 μm), whereas the probe sonicator is highly effective. These hard aggregates cannot be broken down into individual nanoparticles under the operating conditions of the bath, which gives too low energy. The vibrations created using bath sonicator (35 kHz, 240 W) induce low pressure waves that generates cavities. At this low pressure, the size of the cavities oscillates around a constant value (stable cavitation) and bubbles develop and burst at the surface of the liquid. At high pressure, which is the case of the probe (20 kHz, 500 W, amplitude 40 %), at high localized energy, the size of the cavities oscillates around an increasing value (transient cavitation), then cavities collapse violently producing intense stress and increase of the temperature of the suspension [48]. This induces stress which is strong enough to fragment particle agglomerates into smaller particles as shown in [49]. The effect of ultrasonic irradiation depends on the temperature, frequency, power and duration of the sonicator, as well as the material properties

and the solvent used. In conclusion, it has been found that samples prepared under high intensity of sonication are more dispersed after a short length of time (10 min).

These findings are in line with previous observations [50] and motivate the choice of probe sonication to prepare particle dispersions for this study. More details about the effect of ultrasonication duration of the chosen sonicator, pH of the solution and material composition (codoping) are examined in the next section.

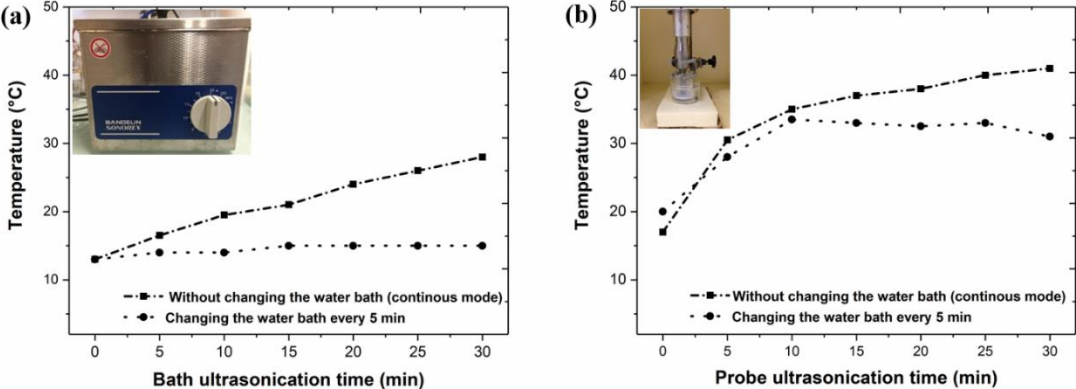


Figure III.9: (a, b) Examination of temperature evolution of pure TiO₂ suspensions in ethanol without adjusting pH of the solution using different ultrasonication methodologies under two different modes.

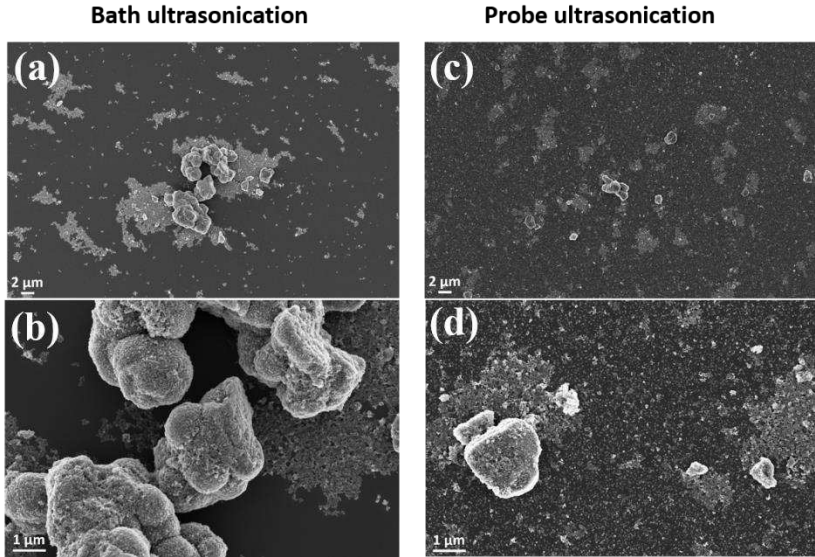


Figure III.10: SEM images of undoped TiO₂ suspensions after 10 min of ultrasonication with different magnifications using: (a-b) bath and (c-d) probe sonicators under the second mode (changing the water bath every 5 min).

II.2 Effect of pH

II.2.1 Fixed concentration of additives

Operational pH_{iep} (pH at isoelectric point) is defined as 3.8 for the undoped and codoped TiO_2 nanopowders in ethanol (**Figure III.11a**). This is located in the same range of isoelectric point of TiO_2 nanopowders in ethanol medium as found by Widegren et al. [51]. It should be noted that it is lower than the range determined in aqueous media ($\text{pH}_{\text{iep}}=5.5-7$) [52]. That indicates that the dispersion of nanoparticles in ethanol leads to an acidification of the medium [53].

Zeta potential data of undoped and codoped TiO_2 suspensions as a function of pH with additives concentration held constant for all dispersions at 0.1 M are shown in **Figure III.11a**. As presented, additives with 0.1 M cannot provide the stability of the pure and codoped suspensions since values higher than the absolute value of ± 25 mV cannot be obtained. Results show a decrease of the surface charge after an acid modification even lower than HCl with 0.1 M, which induce non-stability of nanoparticles. To provide additional information about the behavior of the dispersed nanoparticles, the evolution of these suspensions with time in the stationary state is also investigated (**Figure III.11b**). Undoped and codoped TiO_2 suspensions are settled within 1 hour for operational $\text{pH} = 5, 7, 8$ and 10 due to the low charge occurred on surface. For $\text{pH} 3$, zeta potential reaches approximatively the highest value (+14 mV), which provides a short time stability when looking to the sedimentation test. The codoped TiO_2 suspension remains stable after 2 hours while the pure TiO_2 suspension starts to sediment. Same results concerning the zeta potential and sedimentation time are found in other study [54]. The reason behind this difference is that these additives increase the ionic strength, thus compressing the ionic cloud, called electrical diffuse double layer composed by the nanoparticle surface charge and its counter ions, that surrounding the interacting nanoparticles [55]. This layer plays a fundamental role in the electrostatic stabilization because its compression can lead to more attractive van der Waals forces that cause coagulation as observed. However, the stability period of 2 hours is large enough to perform the next spin coating step (where the total duration is lower than 1 hour).

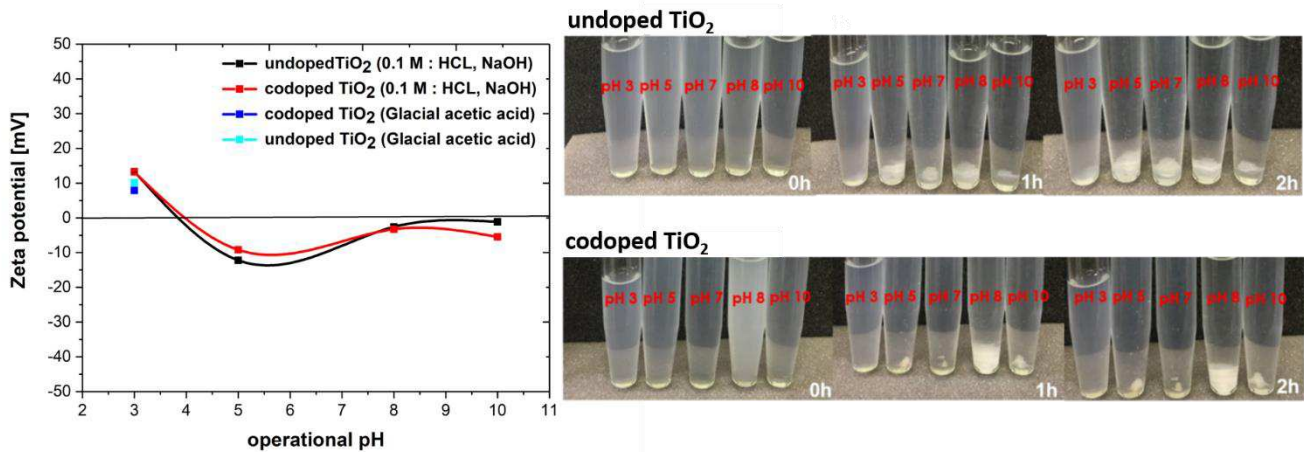


Figure III.11: Zeta potential as function of operational pH and evolution of suspensions with time in stationary state of undoped and codoped TiO₂.

II.2.2 Variation of additives concentration

In this section, we report the influence of HCl and NaOH concentration at various operational pH on undoped and codoped TiO₂ suspensions. **Figure III.12a** and **Figure III.12b** demonstrate the changes of the zeta potential values as a function of operational pH under different concentration of additives. The measured isoelectric points for pure and codoped suspensions are approximately between 3.8 and 5.6, which is consistent with the isoelectric point for TiO₂ reported in other studies [51], [53], [56].

The influence of additives concentration on the surface charge is found to be important. According to the results presented in **Figure III.12a** and **Figure III.12b**, the pH_{iep} of undoped and codoped suspensions increase with decreasing concentration of additives from 0.1 M to 0.001 M (HCl, NaOH). In addition, the surface charge considerably increases to achieve high zeta potential value > 30 mV when the concentration of additives is decreased to 0.001 M (HCl / NaOH). This suggests that the colloidal stability is sensitive to the concentration of additives. This effect can be related to the increase of the double layer surrounding the particles with decreasing the ionic concentration, thereby the ionic strength in the solution. As a result, the repulsive forces between particles become dominant over the attractive forces, which suppresses the agglomeration and lead to the formation of dispersed suspensions. The undoped TiO₂ suspensions show a stability with a high surface charge in the alkaline pH range between 8 and 10. This stability range is extended to the acidic medium at pH = 3 for the TiO₂ codoped suspensions.

In order to reach a better understanding of suspensions stability, sedimentation tests, based on visual observation, are carried out in order to validate the electrophoretic measurements.

Photographs of the evolution in time of undoped and codoped TiO₂ suspensions under 0.001 M of additives are taken after every 1 h. As it is shown in **Figure III.11a**, undoped TiO₂ suspension prepared at pH= 8 has a stability for 2 hours while suspensions at pH = 3, 5 and 10 that start to sediment rapidly and agglomeration is visually detected at the bottom in a short time. For the codoped TiO₂ (**Figure III.13b**), a high stability of the suspensions in both acid (Zeta potential = 28 mV/ pH = 3) and basic (Zeta potential = -35mV / pH = 8) medium is found. This result shows that with codoping a stable suspension can be prepared at pH acid or at pH basic, where absolute values of zeta potential are high enough to provide stability. At pH = 3 and 10 suspensions show a medium stability of two hours. On the other hand, codoped TiO₂ suspension made with pH value of 8 have shown almost no sedimentation in the first five hours after the preparation due the highest zeta potential that increases repulsive forces between particles and maintains it stable along a large period. In reason of hydrophilicity of the surface of substrate and the charge that occurs after the cleaning process that ensure the affinity between particles in solution and Silanol groups (negative charge - it will be explained in the next chapter) we choose pH = 3 (0.1 M additives) to proceed the other steps (stability for 1 hour). Similar studies performed with different additives concentration will belong to perspectives.

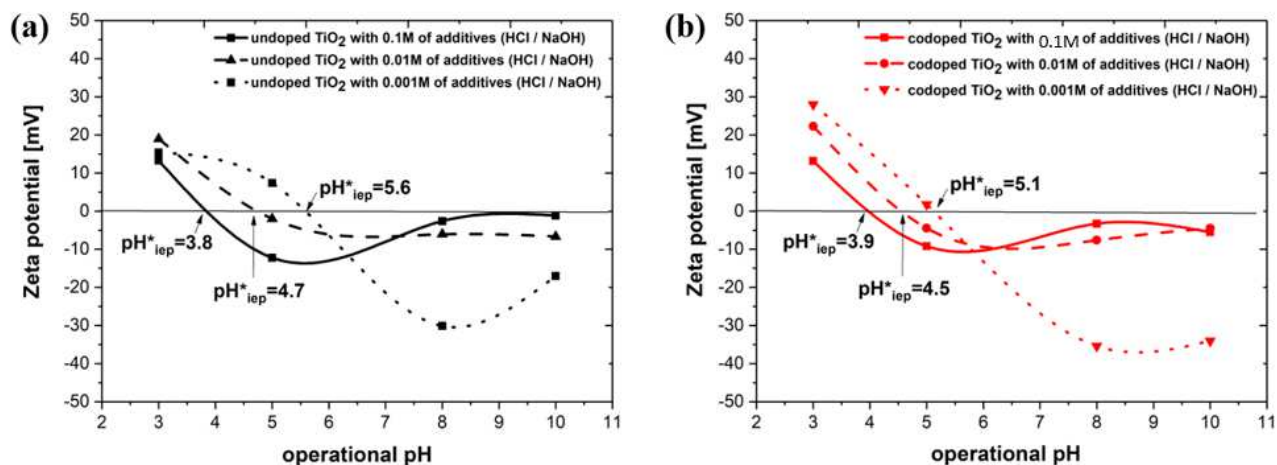


Figure III.12: (a, b) Zeta potential as function of operational pH and additives concentration of undoped and codoped TiO₂ suspensions.

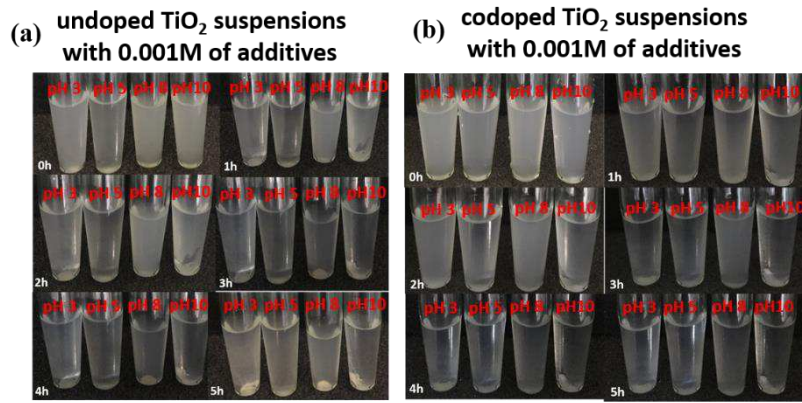


Figure III.13: evolution of suspensions with time in stationary state of (a) undoped and (b) codoped TiO_2 using 0.001 M of additives.

II.3 Ultrasonic duration and doping effect

Effect of ultrasonication (US) duration using probe on the average particle size is studied under various time: 0 min, 10 min, 20 min and 30 min, in order to achieve the maximum dispersion. From DLS results collected in **Figure III.14a** and **Figure III.14b**, undoped and codoped TiO_2 suspensions present different behavior. Undoped TiO_2 suspension is unstable and aggregation takes place. Also, different particle size distribution is obtained after each ultrasonication time. On the contrary, for the codoped TiO_2 a uniform size distribution is formed, 10 min of ultrasonication is enough to break the nanopowders apart and ensure incipient stability. Between 10 and 20 min, same size distribution is measured except for PDI. It is observed that 20 min has a low variation in size between the repeated measurements compared to 10 min and low density of agglomerated particles (see **Figure IV.1** chapter IV). For the codoped TiO_2 , the size is rapidly reduced with the increase of ultrasonication time to 20 min from 580 nm to 166 nm.

The occurrence can be explained by the acoustic cavitation phenomenon. Ultrasounds generate micro bubbles that collide with single particles. The micro bubbles collapse and generate large local energy due to the cavitation effects. The magnitude of the local energy intensity is proportional to the number of bubbles that collapse during cavitation and is equivalent to the sonication duration. The emission of cavitation energy produce shock waves that lead to particle breakages. Thereby, the prolonged application of ultrasonication will gradually degrade the particles into smaller size [57]. The differences in the decreasing rates between the present study and other studies can be attributed to the effect of the nanoparticle primary size, synthesis method and material types [58-59].

Chung et al.[60] studied the dispersion of two types of ZnO nanopowders produced by sol–gel and physical vapor synthesis that are purchased commercially. The first nanopowder is specified as 99.5 % pure ZnO with size of 20 nm and 50 m²/g specific surface area. The second nanopowder is specified as 99% pure ZnO with sizes ranging from 40 to 100 nm and a specific surface area of 10–25 m²/g. The two nanopowders consist of agglomerates ranging in size of 1 μm or larger. Probe ultrasonic agitation effectively reduces the mean particle size to 100 nm within 60 min for the first nanopowder, and within 20 min for the second nanopowder.

Mandzy and co-authors [61] show the dispersion behavior of three commercial nanopowders of TiO₂: anatase (5 nm-TEM), Degussa P25, which is a mixture of 90% anatase and 10% rutile (50 to 100 nm-TEM), and rutile (10 nm - TEM). Under the same ultrasonication conditions, DLS measurements show that the anatase (360 nm and 1530 nm) and rutile (70 and 1500 nm) phases have bimodal size distribution while Degussa present a monomodal size distribution (2760 nm). None of the powders are broken into their primary particle size even after 2h of mechanical breakage.

According to the results of Mahbubul et al. [62], the presence of agglomeration for commercial TiO₂-anatase nanoparticles, with an average particle size of 21 nm, is diminished significantly (to 167 nm- DLS) with increasing the ultrasonication time to 150 min.

Compared to their data, we have achieved almost the same size in a reduced duration (20 min). The different behavior depends on the nature of interparticle bonds. Even small adjustments to the manufacturing process result in considerable changes in particle properties and size distribution.

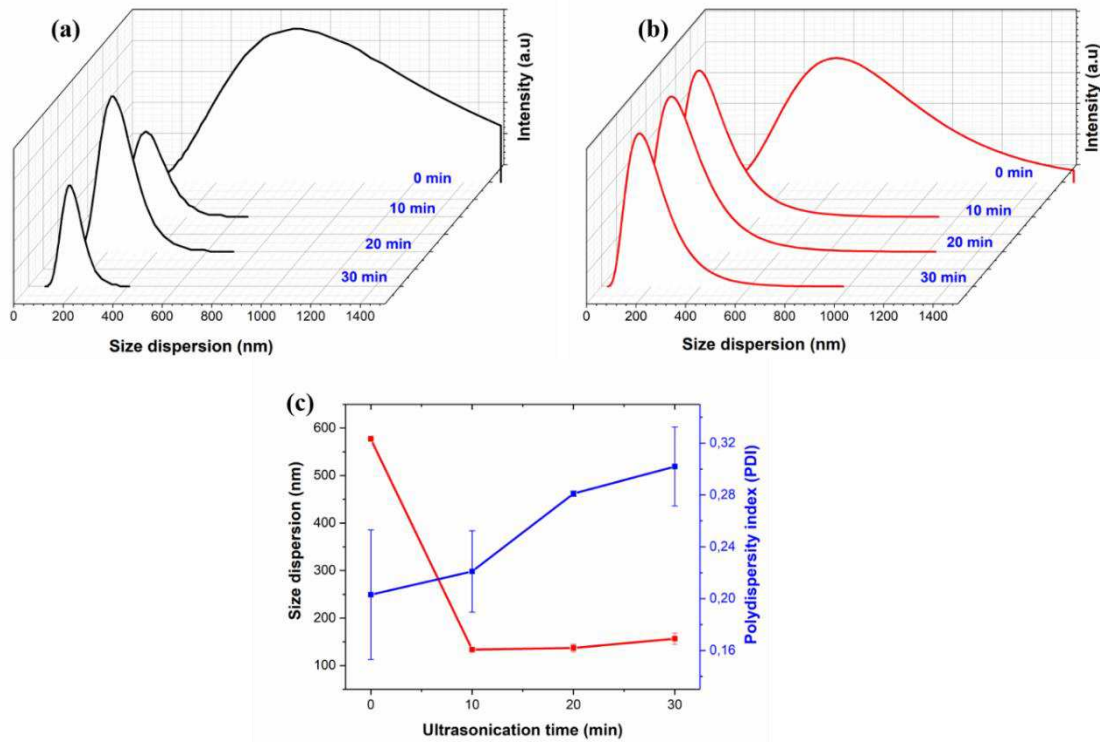


Figure III.14: Evolution of size dispersion of (a) undoped, (b) codoped TiO₂ nanopowders and (c) polydispersity index (PDI) of the codoped TiO₂ nanopowders in ethanol as a function of ultrasonication time (operational pH = 3 with 0.1M of additives, C_{solution} = 0.24 M, 24 h of magnetic stirring).

As it is found from DLS results, small size (below 200 nm) are obtained after 10 min to 20 min of ultrasonication. Above 20 min, an increase of the polydispersity index (PDI) due to the coalescence of the nanoparticles is notably observed (**Figure III.14c**). From the ultrasonication point of view, it is reported in literature that high power of ultrasonication could re-agglomerate the particles as a result of the increased collision of particles. Additionally, contamination of the suspension could take place [63-64]. It is reported that for prolonged ultrasonic duration (60 – 120 min), a dark sediment on the bottom of the ultrasonicated dispersions occurs. This sediment is due to an erosion of the ultrasonic probe. Thus, long ultrasonication times are not only inefficient but also result in the contamination of the suspension [61].

The improvement of the codoped TiO₂ dispersion with ultrasonication compared to the undoped TiO₂ can be attributed to the influence of Er³⁺ and Yb³⁺ ions that change the electronic structure, surface charge behavior and surface reactivity, which has been previously demonstrated through the increase in BET surface area and consequent high surface reactivity. Also, codoped TiO₂ result in a positive charge imbalance, therefore, active acidic sites will be formed, increasing the amount of hydroxyl groups absorbed [65]. Thereby, nanoparticles are expected

to be modified by the surface complexity which affects the intrinsic stability and provides agglomeration in agreement with [65-67]. In summary, 20 min of ultrasonication of the codoped nanoparticles is a suitable duration.

III. Deep investigation of structure and composition of the optimized dispersion of the codoped TiO₂

To provide additional information about the size distribution of the nanoparticles under the optimized conditions: codoped TiO₂ suspension at operational pH = 3 (0.1 M of additives) and with 20 min as a suitable duration of a probe ultrasonication, SEM observations are conducted over dispersed nanopowders on a TEM grid (Continuous ultrathin film on holey carbon). As shown in **Figure III.15a** to **Figure III.15c**, the entire grid is covered with nanoparticles, while slight agglomeration can also be noticed. A few number of agglomerates with a diameter range from 1 to 4 μm are observed. Their presence can be attributed to the low zeta potential (+14 mV) of suspension previously reported in **II.2.1**. For the codoped TiO₂ nanopowders, agglomerates from 3 to 12 μm range are shown (**Figure III.15d** and **Figure III.15e**). The ultrasonication causes the breakage of the agglomerates, but there are particles that reaggregate back to the 1 to 4 μm diameter due to the attractive forces among the dispersed particles that are stronger than repulsive forces [61].

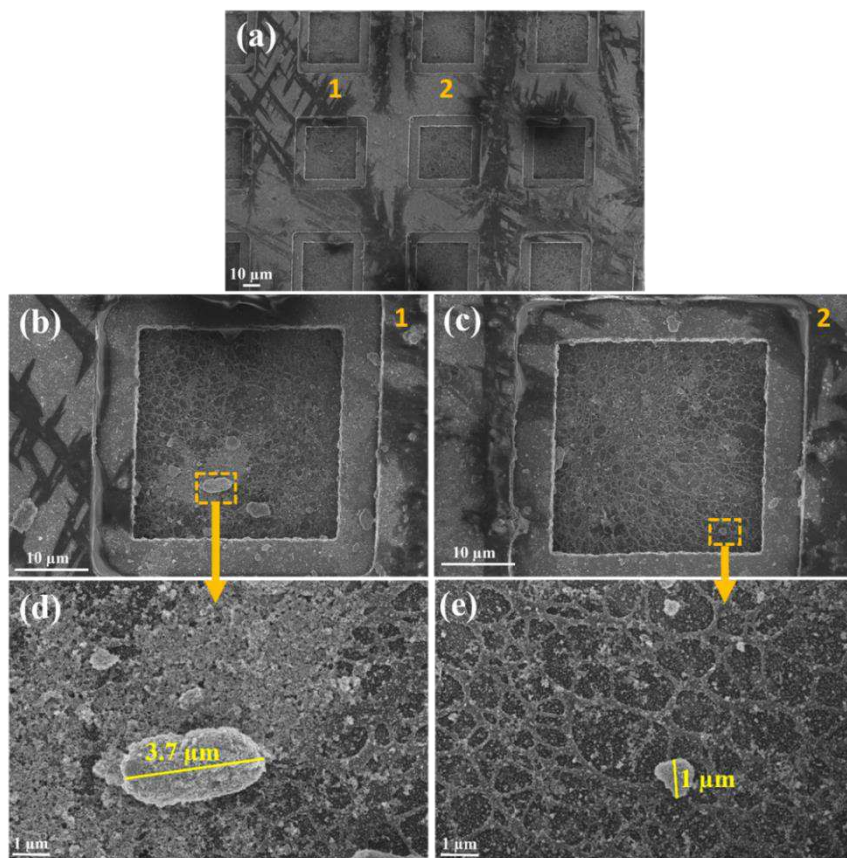


Figure III.15: SEM images of a grid after being soaked in the codoped TiO_2 suspension (operational $\text{pH} = 3$ with 0.1M of additives, $C_{\text{solution}} = 0.24 \text{ M}$, 24 h of magnetic stirring) for 60 s. (b, d) and (c, e) are the same image with different magnifications.

To gain deeper insight of nanoparticles size and crystallinity, the ACOM measurements are performed on dispersed nanopowders. **Figure III.16a** displays the index map, which is a plot of the matching index at every location [68]. It is clearly seen that every grain is indexed demonstrating the high crystallinity of nanopowders at low calcination temperature ($T = 300^\circ\text{C}$). The reconstructed orientation map along z-axis presented in **Figure III.16b** shows that the orientation of the grains varies randomly, each nanoparticle exhibits a single crystallographic orientation, which clearly proves the polycrystalline nature of the codoped TiO_2 . The spatial resolution of a few nanometers shows that no amorphous portion is detected. The validity of the indexing quality is ascertained in the phase reliability map with a reliability value equal to 15 (**Figure III.16c**). The dark areas are related to carbon and the indexed phase is shown in white proving the proposed unique phase.

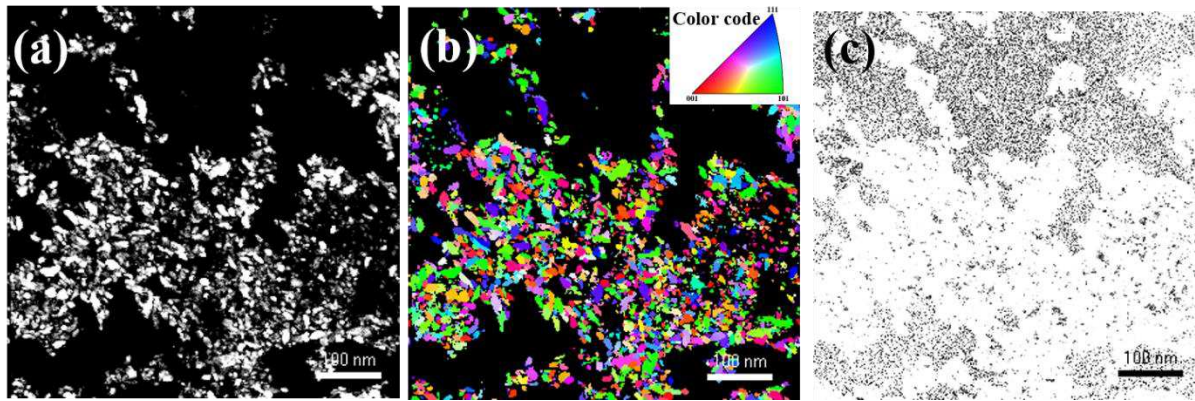


Figure III.16: ACOM-TEM on the codoped TiO_2 nanopowders: (a) orientation map along z-axis, (b) the matching index, (c) phase reliability.

To investigate the phase purity, phase maps by combining anatase and a generic of rutile, erbium and ytterbium oxides phases (**Figure III.17 a-c**) are constructed. No relevant signal for secondary phase is detected which confirms the purity of the presented phase. All the nanoparticles are well crystallized in the anatase phase, consistently with the corresponding XRD pattern. The few pixels located on the top left of the map are not significant, the presence of these phases cannot be considered depending on 3 pixels (each pixel is about 1.5 nm that mean only one mesh). It is clear from the index and phase maps that every grain is indexed for the anatase phase.

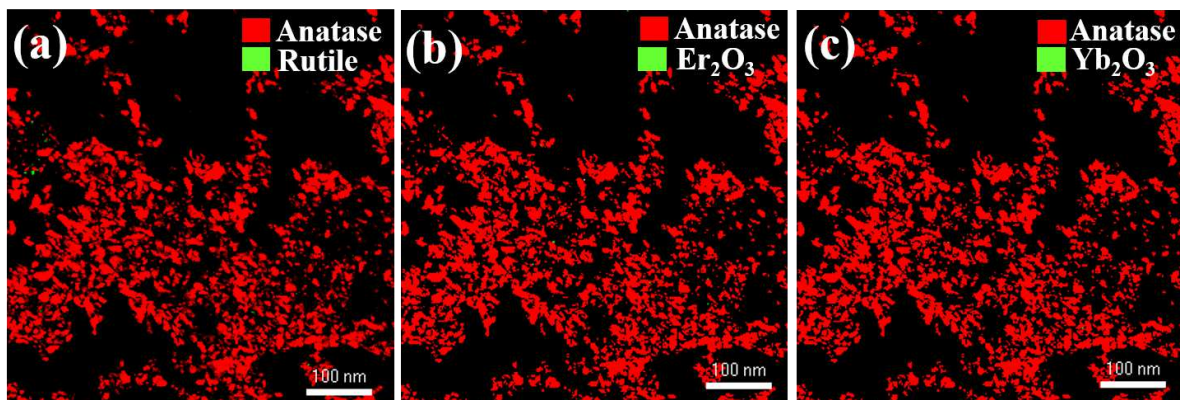


Figure III.17: a, b and c outputs of ACOM-TEM on the codoped TiO_2 nanopowders showing phase maps of anatase plotted with rutile, Er_2O_3 and Yb_2O_3 respectively.

Size distribution of nanomaterials is simple but relevant information. The particle size distribution histogram in **Figure III.18b** clearly indicates that the average particle size estimated from grain boundaries map (**Figure III.18a**) is ~ 9 nm, which agrees well with the calculated Scherrer size (**Table III.1**) and proves the effectiveness of the electrostatic stabilization (pH, co-doping) and physical dispersion (ultrasonication) processes used to get this particles size.

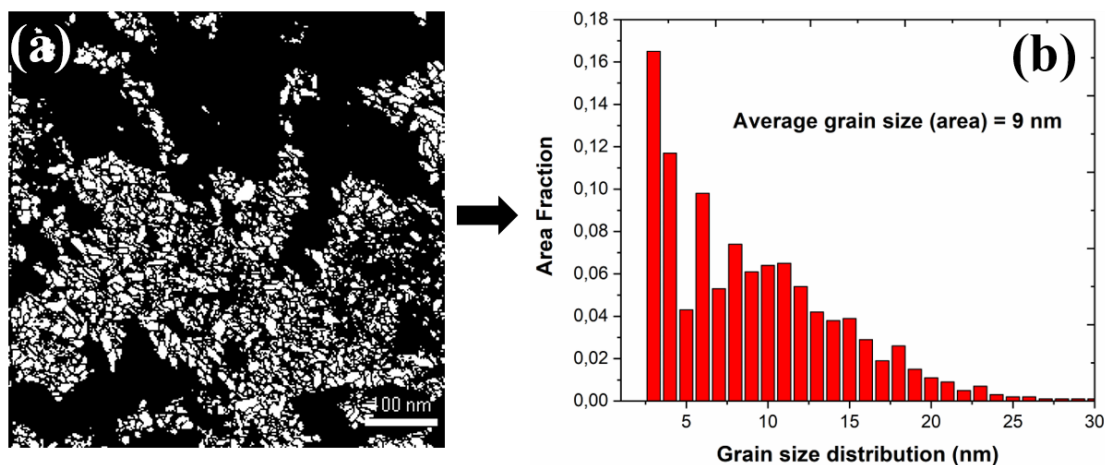


Figure III.18: outputs of ACOM-TEM on the codoped TiO₂ nanopowders showing (a) grain boundaries map and (b) grain size distribution deduced from (a).

In this section, the average nanoparticle size under the optimized conditions used is shown to be smaller than the starting material (3 μm – 12 μm), indicating the fragmentation of the agglomerates into smaller particles at the nanometer size which is beneficial for photoluminescence phenomena.

To verify the chemical composition and distribution inside the nanopowders, elemental mapping is carried out using STEM-EDS analysis. The High Angle Annular Dark Field (HAADF) image and line scanning profiles of the codoped TiO₂ are provided in **Figure III.19**. Results show the presence of all the elements: Ti, O, Er and Yb. It shows also that nanoparticles are nearly spherical in shape. The elemental mapping images clearly indicate the homogeneous and uniform distribution of the doping elements throughout the sample, which is considered to be one of the reasons for improved luminescence [69]. These results clearly confirm the successful incorporation of Er³⁺ and Yb³⁺ ions in TiO₂ host lattice without clear phase separation, which is in a good agreement with XRD results.

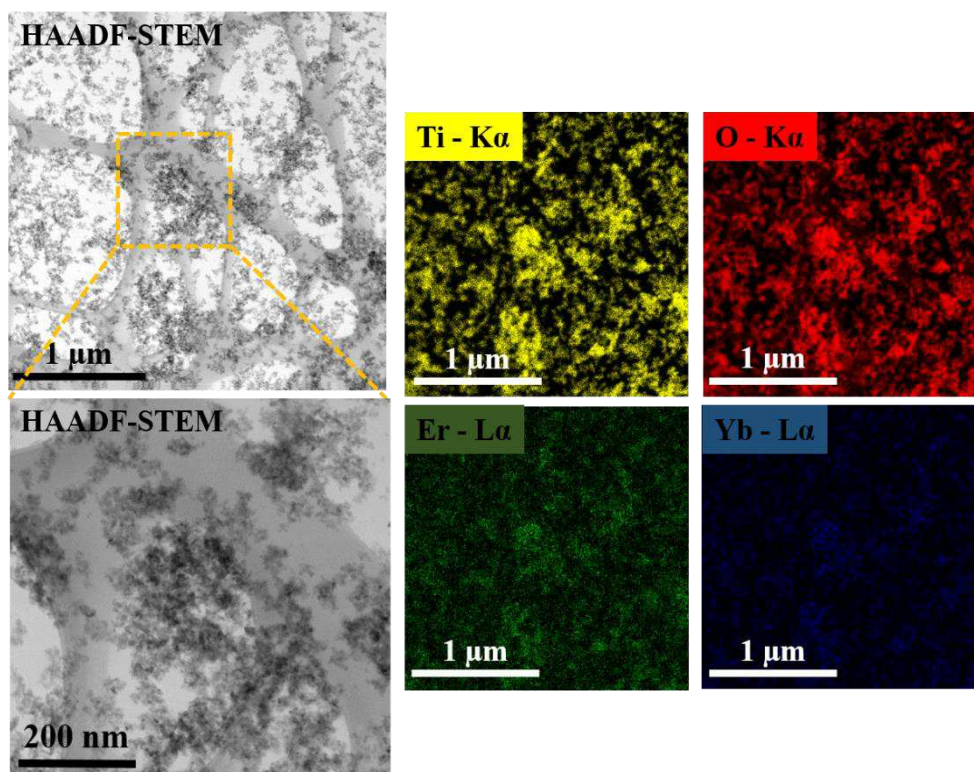


Figure III.19: HAADF-STEM image and representative STEM-EDS line scan profiles of the codoped TiO₂ nanopowders.

Chapter conclusion

Undoped and codoped TiO₂ nanopowders are successfully prepared by hydrothermal-assisted sol-gel method using supercritical drying of ethanol. These nanoparticles have an anatase structure and 10-20 nm size with high surface area (125.7 m²/g and 140.6 m²/g for the undoped and codoped TiO₂, respectively). Er and Yb ions are incorporated into the TiO₂ matrix. We observed that this doping does not influence the crystalline structure of TiO₂. The dispersion process shows that the use of powerful probe sonicator results in a greater size reduction for codoped TiO₂ at operational pH = 3 and with 20 min as a suitable duration of ultrasonication. The prepared codoped TiO₂ nanopowders present good crystallinity and high phase purity. After performing the dispersion process a significant size reducing is observed (~ 9 nm) with slight agglomeration (1 to 4 μm).

These nano-scaled particles with a large specific surface area will provide more active reaction sites and increase light absorption, which is advantageous for photovoltaic performance in order to address the issue of sub-bandgap loss (referred as transmission loss). Therefore, the next chapter objectives concern the formation of a film using spin-coating method from the

nanoparticles solution. In order to retain the luminescence efficiency, to protect the upconversion nanoparticles from the environment and to ensure the mechanical stability of the structure for photonic applications, the coating of an ultra-thin layer produced by ALD technique on the surface of the spin-coated nanoparticles material is performed.

References

- [1] A. Sadeghzadeh-Attar, "Photocatalytic degradation evaluation of N-Fe codoped aligned TiO₂ nanorods based on the effect of annealing temperature," *Journal of Advanced Ceramics*, vol. 9, pp. 107–122, 2020.
- [2] S. M. Ibrahim et al., "TiO₂ Transparent Thin Film for Eliminating Toluene", *Nanotechnology*, vol. 2012, pp. 1–9, 2012.
- [3] A. A. Kashale et al., "Biomediated green synthesis of TiO₂ nanoparticles for lithium ion battery application", *Composites Part B: Engineering*, vol. 99, pp. 297–304, 2016.
- [4] T. Kalaivani, P. Anilkumar, "Role of temperature on the phase modification of TiO₂ nanoparticles synthesized by the precipitation method," *Silicon*, vol. 10, pp. 1679–1686, 2018.
- [5] U. Nithiyantham, A. Ramadoss, S. R. Ede, S. Kundu, "DNA mediated wire-like clusters of self-assembled TiO₂ nanomaterials: Super capacitor and dye sensitized solar cell applications," *Nanoscale*, vol. 6, pp. 8010–8023, 2014.
- [6] X. Zhu et al., "The effect of heat treatment on the anatase-rutile phase transformation and photocatalytic activity of Sn-doped TiO₂ nanomaterials," *RSC Advances*, vol. 8, pp. 14249–14257, 2018.
- [7] T. Moon et al., "Hydroxyl-quenching effects on the photoluminescence properties of SnO₂:Eu³⁺ nanoparticles," *Journal of Physical Chemistry C*, vol. 111, pp. 4164–4167, 2007.
- [8] Mpanza P. Ntsikelelo, M. D. Thembinkosi, L. F. Koao, and M. E. T. Motloung V. Setumo, "Transformation from Anatase to Rutile Titania Using Hydrothermal Method: Investigation of Morphology and Thermal Stability," *sensors and materials*, vol. 4, pp. 1511–1522, 2020.
- [9] S. Phomma, T. Wutikhun, P. Kasamechonchung, T. Eksangsri, C. Sapcharoenkun, "Effect of Calcination Temperature on Photocatalytic Activity of Synthesized TiO₂ Nanoparticles via Wet Ball Milling Sol-Gel Method," *applied sciences*, vol. 4, pp. 64–75, 2020.
- [10] Y. Zhao, Y. Li, X. Ren, F. Gao, H. Zhao, "The Effect of Eu Doping on Microstructure, Morphology and Methanal-Sensing Performance of Highly Ordered SnO₂ Nanorods Array", *nanomaterials*, vol. 53, pp. 6677–6684, 2017.
- [11] B. J.A. Borrego Péreza et al., "Structural, optical, and photoluminescence properties of erbium doped TiO₂ films," *Vacuum*, vol. 169, p. 108873, 2019.
- [12] V. D. Mote, Y. Purushotham, and B. Dole, "Williamson-Hall analysis in estimation of lattice strain in nanometer-sized ZnO particles," *Journal of Theoretical and applied physics*, vol. 6, pp. 2251–2256, 2012.
- [13] Y. T. Prabhu, K. V. Rao, "X-Ray Analysis by Williamson-Hall and Size-Strain Plot Methods of ZnO Nanoparticles with Fuel Variation," *Scientific research*, pp. 21–28, 2014.
- [14] H. A. Yurtsever, M. Çiftçioğlu, "The effect of rare earth element doping on the microstructural evolution of sol-gel titania powders" *Journal of Alloys and Compounds*, vol. 695, pp. 1336–1353, 2017.

- [15] E. Emil, S. Gürmen, “Estimation of yttrium oxide microstructural parameters using the Williamson–Hall analysis”, *Materials Science and Technology*, vol. 34, pp. 1549–1557, 2018.
- [16] R. Zamiri, A. F. Lemos, A. Reblo, H. Abbastabar, “Effects of rare-earth (Er , La and Yb) doping on morphology and structure properties of ZnO nanostructures prepared by wet chemical method,” *Ceramics International*, vol. 40, pp. 1–7, 2013.
- [17] S. D. Senol, “Hydrothermal derived nanostructure rare earth (Er , Yb) -doped ZnO : structural , optical and electrical properties,” *Journal of Materials Science: Materials in Electronics*, vol. 27, pp. 7767–7775, 2016.
- [18] S. Horikoshi, Y. Minatodani, H. Tsutsumi, H. Uchida, “Influence of lattice distortion and oxygen vacancies on the UV- driven / microwave-assisted TiO₂ photocatalysis”, *Journal of Photochemistry & Photobiology, A: Chemistry*, vol. 265, pp. 20–28, 2013.
- [19] V. M. Vinosel, M. Asisi Janifer, S. Anand, S. Pauline, “Structural and Functional Group Characterization of Nanocomposite Fe₃O₄/TiO₂ and Its Magnetic Property ”, *Mechanics, Materials Science & Engineering*, pp. 2412–5954, 2017.
- [20] R. Salhi, J. Deschanvres, “Efficient green and red up-conversion emissions in Er/Yb co-doped TiO₂ nanopowders prepared by hydrothermal-assisted sol–gel process,” *Journal of Luminescence*, vol. 176, pp. 250–259, 2016.
- [21] S. H. Othman, S. Abdul Rashid, T. I. Mohd Ghazi, N. Abdullah, “Dispersion and stabilization of photocatalytic TiO₂ nanoparticles in aqueous suspension for coatings applications,” *Journal of Nanomaterials*, vol. 2012, 2012.
- [22] S. El-Sherbiny, F. Morsy, M. Samir, O. A. Fouad, “Synthesis, characterization and application of TiO₂ nanopowders as special paper coating pigment,” *Applied Nanoscience*, vol. 4, pp. 305–313, 2014.
- [23] A. K. Bordbar, A. A. Rastegari, R. Amiri, E. Ranjbakhsh, M. Abbasi, A. R. Khosropour, “Characterization of Modified Magnetite Nanoparticles for Albumin Immobilization,” *Biotechnology Research International*, vol. 2014, pp. 1–6, 2014.
- [24] T. Pan, P. Liao, K. Chang, L. Chi, “Structural and sensing characteristics of Gd₂Ti₂O₇ , Er₂TiO₅ and Lu₂Ti₂O₇ sensing membrane electrolyte – insulator – semiconductor for bio-sensing applications,” *Electrochimica Acta*, vol. 89, pp. 798–806, 2013.
- [25] J. Yang, Y. Hu, C. Jin, L. Zhuge, X. Wu, “Structural and optical properties of Er-doped TiO₂ thin films prepared by dual-frequency magnetron co-sputtering,” *Thin Solid Films*, vol. 637, pp. 9–13, 2017.
- [26] Z. Rao et al., “Defect Chemistry of Er -Doped TiO₂ and Its Photocatalytic Activity for the Degradation of Flowing Gas Phase VOCs,” *The Journal of Physical Chemistry*, vol. 123, pp. 12321–12334, 2019.
- [27] F. Chen, J. Her, Y. Shao, Y. H. Matsuda, T. Pan, “Structural and electrical characteristics of high- κ Er₂O₃ and Er₂TiO₅ gate dielectrics for a-IGZO thin-film transistors”, *Nanoscale Research letters*, pp. 3–8, 2013.
- [28] X. Wang et al., “Enhanced Photovoltaic Performance of Perovskite Solar Cells Based on Er-Yb Co-doped TiO₂ Nanorod Arrays,” *Electrochimica Acta*, vol. 245, pp. 839–845, 2017.

- [29] A. Kocjan, M. Logar, Z. Shen, “The agglomeration, coalescence and sliding of nanoparticles, leading to the rapid sintering of zirconia nanoceramics,” *Scientific Reports*, vol. 7, pp. 1–8, 2017.
- [30] R. Salhi, H. Roussel, P. Chaudouët, R. Maalej, M. Fourati, J. Deschanvres, “Effect of Humidity and UV Assistance on the Properties of Erbium Doped Yttrium Oxide Films Prepared by Aerosol-MOCVD,” *Chemical vapor deposition*, vol. 17, pp. 93–97, 2011.
- [31] K. V. Kumar et al., “Characterization of the adsorption site energies and heterogeneous surfaces of porous materials,” *Journal of Materials Chemistry A*, vol. 7, p. 10104, 2019.
- [32] A. Modwi, A. Imam, M. Ibn, O. Islamic, “Fe-Cu-ZnO nanocomposite as novel adsorbent: characterizations and indigo carmine dye removal,” *Journal of Optoelectronics and Biomedical Materials*, vol. 10, pp. 55–61, 2018.
- [33] M. A. Wahab, F. Darain, M. A. Karim, and J. N. Beltramini, “Nano-confined synthesis of highly ordered mesoporous carbon and its performance as electrode material for electrochemical behavior of riboflavin (vitamin B2) and dopamine,” *International Journal of Electrochemical Science*, vol. 10, pp. 7732–7742, 2015.
- [34] R. Moussaoui, K. Elghniji, M. ben Mosbah, E. Elaloui, and Y. Moussaoui, “Sol–gel synthesis of highly TiO₂ aerogel photocatalyst via high temperature supercritical drying,” *Journal of Saudi Chemical Society*, vol. 21, pp. 751–760, 2017.
- [35] S. Sert Çok, F. Koç, F. Balkan, N. Gizli, “Revealing the pore characteristics and physicochemical properties of silica ionogels based on different sol-gel drying strategies,” *Journal of Solid State Chemistry*, vol. 278, 2019.
- [36] M. A. Valenzuela, P. Bosch, G. Aguilar-Rios, A. Montoya, and I. Schifter, “Comparison between sol-gel, coprecipitation and wet mixing synthesis of ZnAl₂O₄,” *Journal of sol-gel science and technology*, vol. 8, pp. 107–110, 1997.
- [37] A. F. Bedilo, K. J. Klabunde, “Synthesis of high surface area zirconia aerogels using high temperature supercritical drying,” *nanostructured materials*, vol. 8, pp. 119–135, 1997.
- [38] N. N. Binita, Z. Yaakob, R. Resmi, “Influence of synthesis methods on zirconium doped titania photocatalysts,” *Central European Journal of Chemistry*, vol. 8, pp. 182–187, 2010.
- [39] D. V. Dao, M. van den Brecht, Z. Koeller, T. K. Le, “Effect of metal ion doping on the optical properties and the deactivation of photocatalytic activity of ZnO nanopowder for application in sunscreens,” *Powder Technology*, vol. 288, pp. 366–370, 2016.
- [40] K. Kalantari, M. Kalbasi, M. Sohrabi, S. J. Royaei, “Enhancing the photocatalytic oxidation of dibenzothiophene using visible light responsive Fe and N co-doped TiO₂ nanoparticles,” *Ceramics International*, vol. 43, pp. 973–981, 2017.
- [41] S. M. Adyani and M. Ghorbani, “A comparative study of physicochemical and photocatalytic properties of visible light responsive Fe, Gd and P single and tri-doped TiO₂ nanomaterials,” *Journal of Rare Earths*, vol. 36, pp. 72–85, 2018.
- [42] X. Zhu et al., “Effects of Ag⁰-modification and Fe³⁺-doping on the structural, optical and photocatalytic properties of TiO₂” *RSC Advances*, vol. 9, pp. 40003–40012, 2019.
- [43] Y. H. Tan, J. A. Davis, K. Fujikawa, N. V. Ganesh, A. V. Demchenko, K. J. Stine, “Surface area and pore size characteristics of nanoporous gold subjected to thermal, mechanical, or surface

modification studied using gas adsorption isotherms, cyclic voltammetry, thermogravimetric analysis, and scanning electron microscopy”, *Journal of Materials Chemistry*, vol. 22, pp. 6733–6745, 2012.

[44] A. Shrikant P. Takle, Sonali D. Naik, Supriya. K. Khore, Siddhanath A. Ohwal, B. B. K. Namdev M. Bhujbal, Sukeshani L. Landge, R. S. Sonawane, “Photodegradation of spent wash, a sugar industry waste, using vanadium-doped TiO₂ nanoparticles” *Royal Society of chemistry advances*, vol. 66, pp. 37–39, 2012.

[45] G. Arroyos and R. C. G. Frem, “Luminescent spherical particles of lanthanide-based infinite coordination polymers with tailorable sizes”, *CrystEngComm*, vol. 22, pp. 2439–2446, 2020.

[46] A. Van Dijken, J. Makkinje, A. Meijerink, “The influence of particle size on the luminescence quantum efficiency of nanocrystalline ZnO particles”, *Journal of Luminescence*, vol. 92, pp. 323–328, 2001.

[47] H. M. Santos, C. Lodeiro, J.-L. C. Martinez, “the power of ultrasound,” 2554.

[48] Hielcher ultrasound Technology, “Probe-Type Sonication vs. Ultrasonic Bath: An Efficiency Comparison.”

[49] S. J. Chung et al., “Characterization of ZnO nanoparticle suspension in water: Effectiveness of ultrasonic dispersion”, *Powder Technology*, vol. 194, pp. 75–80, 2009.

[50] L. I. N. Hai, Z. Guo, X. I. E. Fei, “Influence of Sonication on the Stability and Thermal Properties of Al₂O₃ Nanofluids,” *nanomaterials*, vol. 23, no. 3, pp. 3–6, 2014.

[51] J. Widegren, “Electrostatic Stabilization of Ultrafine Titania in Ethanol”, *J.Am.Ceram.Soc.*, vol. 28, pp. 523–528, 2002.

[52] G. A. Parks, “The isoelectric points of solid oxides, solid hydroxides, and aqueous hydroxo complex systems,” *Chemical Reviews*, vol. 65, pp. 177–198, 1964.

[53] J. Widegren and L. Bergstro, “The effect of acids and bases on the dispersion and stabilization of ceramic particles in ethanol”, *Journal of the European ceramic society*, vol. 20, pp. 659–665, 2000.

[54] W. Science, J. Qi, Y. Ye, H. Wang, “Dispersion and stability of titanium dioxide nanoparticles in aqueous suspension : Effects of ultrasonication and concentration”, *Water Science and technology*, vol. 67, pp. 147–151, 2013.

[55] M.-K. S. Soo-Jin Park, “Chapter 10- Comprehension of nanocomposites” in *Interface Science and Technology*, vol. 18, pp. 777–819, 2011.

[56] J. O. Carneiro et al., “Synthesis of iron-doped TiO₂ nanoparticles by ball-milling process: The influence of process parameters on the structural, optical, magnetic, and photocatalytic properties” *Journal of Materials Science*, vol. 49, pp. 7476–7488, 2014.

[57] L. Ye, X. Zhu, and Y. Liu, “Numerical study on dual-frequency ultrasonic enhancing cavitation effect based on bubble dynamic evolution,” *Ultrasonics-Sonochemistry*, vol. 59, pp. 104744, 2019.

[58] K. Sato, J. Li, and H. Kamiya, “Ultrasonic Dispersion of TiO₂ Nanoparticles in Aqueous Suspension,” *Journal of the American ceramic society*, vol. 2487, pp. 2–8, 2008.

- [59] I. M. Mahbubul, E. Begum, R. Saidur, and M. A. Amalina, "Optimization of ultrasonication period for better dispersion and stability of TiO₂ – water nanofluid," *Ultrasonics - Sonochemistry*, vol. 37, pp. 360–367, 2017.
- [60] S. J. Chung et al., "Characterization of ZnO nanoparticle suspension in water: Effectiveness of ultrasonic dispersion," *Powder Technology*, vol. 194, pp. 75–80, 2009.
- [61] N. Mandzy, E. Grulke, and T. Druffel, "Breakage of TiO₂ agglomerates in electrostatically stabilized aqueous dispersions", *Powder technology*, vol. 160, pp. 121–126, 2005.
- [62] I. M. Mahbubul, E. B. Elcioglu, R. Saidur, M. A. Amalina, "Optimization of ultrasonication period for better dispersion and stability of TiO₂–water nanofluid," *Ultrasonics Sonochemistry*, vol. 37, pp. 360–367, 2017.
- [63] D. Uskokovic and M. Mitric, "Ultrasonic de-agglomeration of barium titanate powder" *Ultrasonics Sonochemistry*, vol. 15, pp. 16–20, 2008.
- [64] J. K. Kozo Tanabe, Takashi Sumiyoshi, Katsue Shibata, Tadamistu Kiyoura, "A new hypothesis regarding the surface acidity of binary metal oxides," *bulletin of chemical society of japan*, vol. 47, pp. 1064–1066, 1974.
- [65] K. Suttiponparnit, V. Tiwari, M. Sahu, and P. Biswas, "Effect of Pt or Pd doping on stability of TiO₂ nanoparticle suspension in water", *Journal of Industrial and Engineering Chemistry*, vol. 19, pp. 150–156, 2013.
- [66] Y. Zhang, H. Zhang, Y. Xu, and Y. Wang, "Significant effect of lanthanide doping on the texture and properties of nanocrystalline mesoporous TiO₂" *Journal of Solid State Chemistry*, vol. 177, pp. 3490–3498, 2004.
- [67] S. Manoranjan, S. Komkrit, S. Sirikalaya, C. Tawatchai, and B. Pratim, "Characterization of doped TiO₂ nanoparticle dispersions" *Chemical engineering science*, vol. 66, pp. 3482–3490, 2011.
- [68] E. F. Rauch, M. Véron, "Automated crystal orientation and phase mapping in TEM" , *materials characterization*, vol. 98, pp. 1–9, 2014.
- [69] W. N. Wang, W. Widiyastuti, T. Ogi, I. W. Lenggoro, K. Okuyama, "Correlations between crystallite/particle size and photoluminescence properties of submicrometer phosphors", *Chemistry of Materials*, vol. 19, pp. 1723–1730, 2007.

Chapter IV

Codoped TiO₂ nanopowder deposited as thin films and ALD coated with Al₂O₃

Introduction

In this chapter, the codoped TiO₂ UC nanopowder is dispersed on a n-type (100) silicon substrate and then is coated with an amorphous Al₂O₃ using atomic layer deposition technique (ALD).

The first part of this chapter concerns the presentation of a DOE approach with the Hadamard matrix of order 4 conducted for the spin coating step in order to optimize the deposition conditions with a minimum number of experiments. Following this, the impact of spin coating cycles on PL response is studied. The second part treats the impact of different ALD-Al₂O₃ thicknesses and FGA treatment on the structural and compositional properties of codoped TiO₂ nanopowders assembled on n-type (100) Si. For that purpose, various analysis approaches involving XRD, SEM, automated crystal phase and orientation mapping in TEM (ACOM-TEM) and scanning transmission electron microscopy–energy-dispersive spectroscopy (STEM-EDS) are performed.

I. Deposition of dispersed nanopowders on Si wafer

I.1 Deposition quality and adhesion tests

First of all, in order to verify the results illustrated by DLS measurements in **chapter III**, the deposits quality with varying the ultrasonication duration is shown in **Figure IV.1**. The SEM micrographs are in a good agreement with DLS measurements concerning the effect of ultrasonication duration. It is observed that the highest density of deposited nanopowder increases with increasing ultrasonication time. In addition, it shows the enhancement of the film quality (minimum number of huge particles from the top view) deposited using codoped TiO₂ compared to undoped TiO₂.

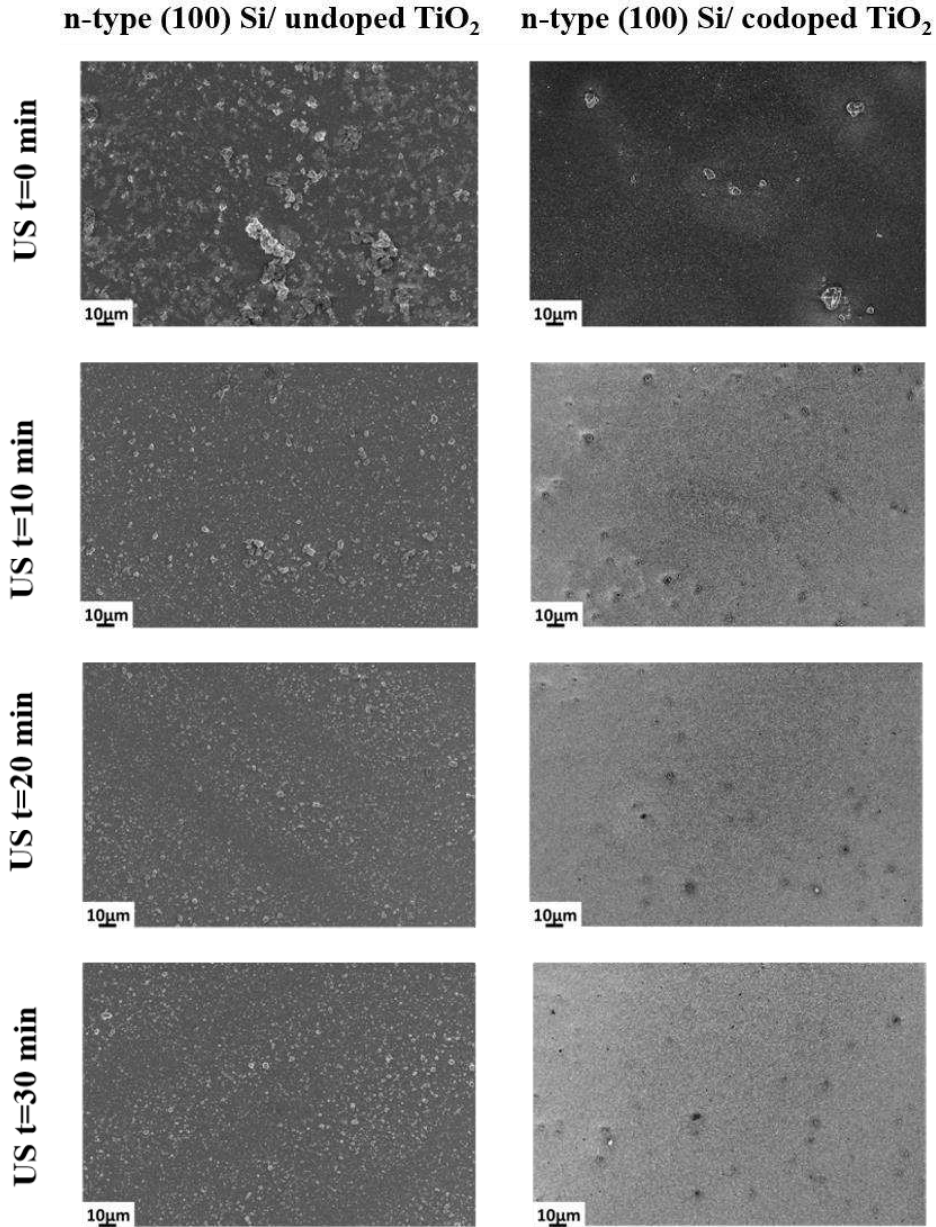


Figure IV.1 : SEM images of deposited colloidal suspension of undoped and codoped TiO₂ under different time of ultrasonication (t = 0 min, 10 min, 20 min and 30 min) on n-type (100) Si wafer using a spin coating process (depositing phase: 1000 rpm - 30 s and drying phase: 1 min at 200°C on a hotplate).

The performance of this step depends on the ability of nanoparticles to adhere to substrate. The silicon substrate possesses an hydrophilic surface and it is negatively charged after the RCA1-RCA2 procedure [1]. Since the nanoparticles are positively charged at operational pH= 3, a good adhesion between the substrate and the nanoparticles is expected [2]. Two different tests are conducted to evaluate the adhesion of codoped TiO₂ nanopowders on substrate: the first one by rinsing the substrate with water and the second by blowing it with a nitrogen gas gun as

shown. The SEM images in **Figure IV.2**, show effectively a total coverage of substrate after these two tests indicating a good adhesion between the codoped nanopowders and the substrate.

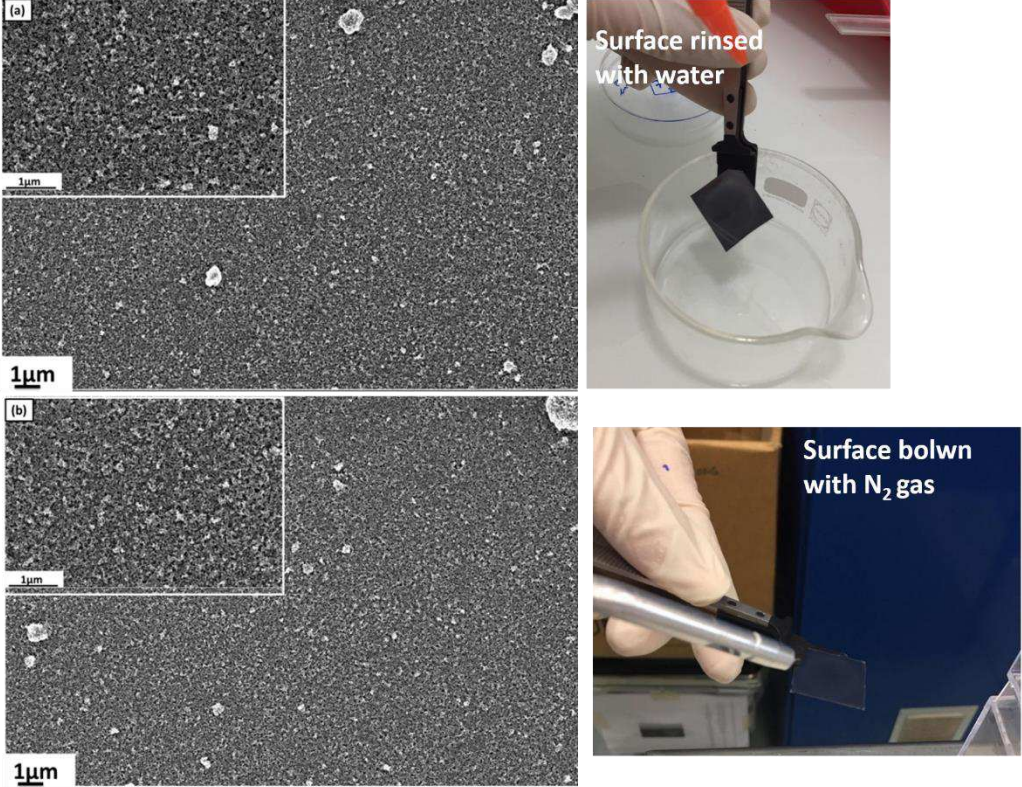


Figure IV.2: SEM images of adhesion tests: (a) rinsed with water and (b) blown with N₂ gas of codoped TiO₂ film deposited on n-type (100) Si wafer using a spin coating process (depositing phase: 1000 rpm – 30 s, US = 20 min and drying phase: 200°C - 1 min on a hotplate).

I.2 Spin-coating

The mean idea of the DOE method, specifically the screening method or Plackett–Burman two level design, is to vary all the factors (inputs) simultaneously over a set of planned experiments and, after that, measure the responses (outputs) as shown in **Figure IV.3**.

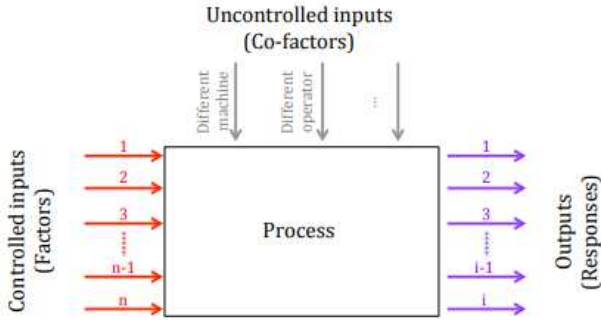


Figure IV.3: Schematic view of the process as reported in [3].

It consists of varying all the process parameters at each experiment according to a Hadamard matrix of order 4 (Figure IV.4).

$$H_4 = \begin{pmatrix} 1 & 1 & 1 & 1 \\ 1 & -1 & 1 & -1 \\ 1 & 1 & -1 & -1 \\ 1 & -1 & -1 & 1 \end{pmatrix}$$

Figure IV.4: Hadamard matrix H4.

The method consists of four experimental steps:

- Repeating three times the same experiment on central points with fixed 3 parameters to quantify the error on the responses
- Running 4 experiments following levels indicated by an Hadamard matrix of order 4 for each parameter and measuring the responses
- One experiment with all the parameters in a -1 of Hadamard matrix to assess the robustness of the simple linear model obtained.
- Finally, the experiment on central point is done one more time. It allows to evaluate some drift in the process

I.2.1 Study of optimization conditions for spin-coating process

The DOE method is used to extract the influence of the spin-coating process parameters around a central point [3-4]. Three parameters are chosen for this work, which are: the volume of the colloidal suspension, spinning time and spinning speed as illustrated in Table IV.1. For the desired response, the target is the minimum number of huge particles with minimum size of 400 nm on the surface of Si.

Table IV.1: Levels of the factors used in the experimental design following Hadamard matrix of order 4.

Factor	Level (-1)	Central working recipe (0)	Level (+1)
P1: Spinning speed (rpm)	1000	2000	3000
P2: Spinning time (s)	30	45	60
P3: Volume (μL)	200	300	400

The deposition is conducted immediately after the substrate cleaning. The solution is dropped into the center of the substrate using a micropipette (100 μ L -1000 μ L). In total, nine SEM pictures are taken on each sample, starting from center and moving towards the border of the substrate.

Table IV.2 summarizes the set of experiments performed in this study with the corresponding values of the parameters. Experiments from 1 to 3, are processed according to the central working recipe, experiments from 4 to 7 follow the Hadamard matrix, experiment 8 and 9 are out of Hadamard matrix (-1) and central points, respectively.

Table IV.2: Experiments designed by the DOE approach following Hadamard matrix of order 4

	P1	P2	P3
DOE1 : central points 1	0	0	0
DOE2 : central points 2	0	0	0
DOE3 : central points 3	0	0	0
DOE4 : Hadamard 1	1	1	1
DOE5 : Hadamard 2	-1	1	-1
DOE6 : Hadamard 3	1	-1	-1
DOE7 : Hadamard 4	-1	-1	1
DOE8 : out of Hadamard matrix	-1	-1	-1
DOE9 : central points 4	0	0	0
	P1	P2	P3
DOE1 : central points 1	2000 rpm	45s	300 μ l
DOE2 : central points 2	2000 rpm	45s	300 μ l
DOE3 : central points 3	2000 rpm	45s	300 μ l
DOE4 : Hadamard 1	3000 rpm	60s	400 μ l
DOE5 : Hadamard 2	1000 rpm	60s	200 μ l
DOE6 : Hadamard 3	3000 rpm	30s	200 μ l
DOE7 : Hadamard 4	1000 rpm	30s	400 μ l
DOE8 : out of Hadamard matrix	1000 rpm	30s	200 μ l
DOE9 : central points 4	2000 rpm	45s	300 μ l

The number of huge particles is measured in 3 different areas (**Figure IV.5**). SEM micrographs are taken in three different areas: center (C: 10 mm), intermediate (I: 5 mm) and border (B: 2 mm). In every area three images are taken randomly to check the homogeneity in every point. All images are taken in black and white to separate background from the particles of interest to facilitate their treatment with the public domain program ImageJ [5-6], in order to facilitate the count of the number of huge particles. First, SEM image is converted to 8-bit and then the scale is calibrated pixels/ μm . Image is duplicated to work on the copy. Adjust threshold is set to make sure of the dark background, default mode is used. Then, the entire image is selected as the area of interest ($56.82 \times 37.88 \mu\text{m} - 1020 \times 680$). Finally, particles analyzing is run and before that “display results”, “Clear results”, “Summarize”, and “Exclude on edges” are selected. The results displayed the number of particles that fit the parameters within the image and is used as the total count.

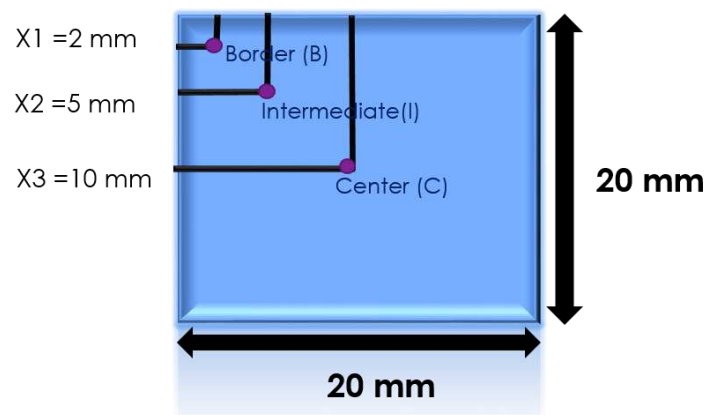


Figure IV.5: The three different areas of SEM observations for DOE

SEM images are taken at 2000x magnification (**Figure IV.6**). All experiments and characterization are performed in a limited period (3 weeks).

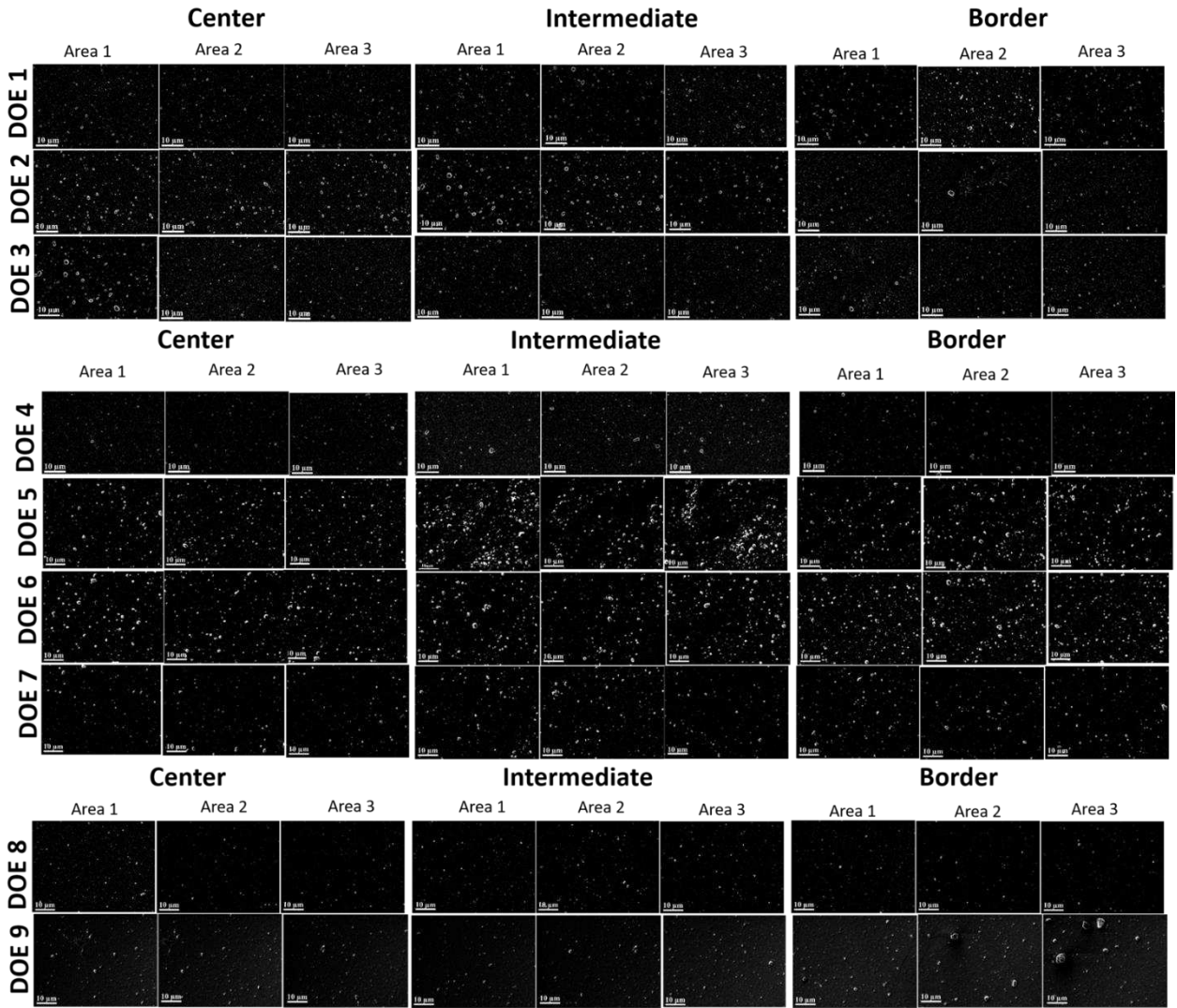


Figure IV.6: SEM top view images of the DOE experiments in every area.

The GNU Octave 5.1.0 program is used to determine the optimum deposition conditions. As a response, getting the minimum number of huge particles on the surface is the goal. The screening method allows us to deduce the polynomial coefficients of a linear relationship between each output and the 3 varying parameters:

$$R_k = A_{k,0} + \sum_{n=1}^3 A_{k,n} P_n \text{ (Equation IV.1)}$$

Where R_k is the response value number k , n is a parameter number and P a parameter level (± 1). $A_{k,0}$ is the mean value of the response number k . To assess the influence of a parameter on a response, the weight A associated to a parameter P is compared to 2 times the standard deviation (2σ) of the response evaluated with the four central working points (average of response of DOE 1, 2, 3 and 9). A weight below this limit has no statistical significance: the associated parameter does not play any significant role on the measured response within a 95% confidence interval [4].

Figure IV.7 and **Table IV.3** present the parameter weight of each parameter on the response, which is $A_{k,n}$. In **Table IV.3**, the influence of each parameter is given by levels. – or + presents a negative or positive influence of the parameter on the value (not on the desirability) of the response, while (\pm) shows an influence above 2σ (certain). Based on the *Equation IV.1*, the desired response is to minimize the number of huge particles which mean a negative response. $A_{k,n}$ is negative for all the three parameters that means we should put all the studied parameters P_n in +1 level to get the desired response.

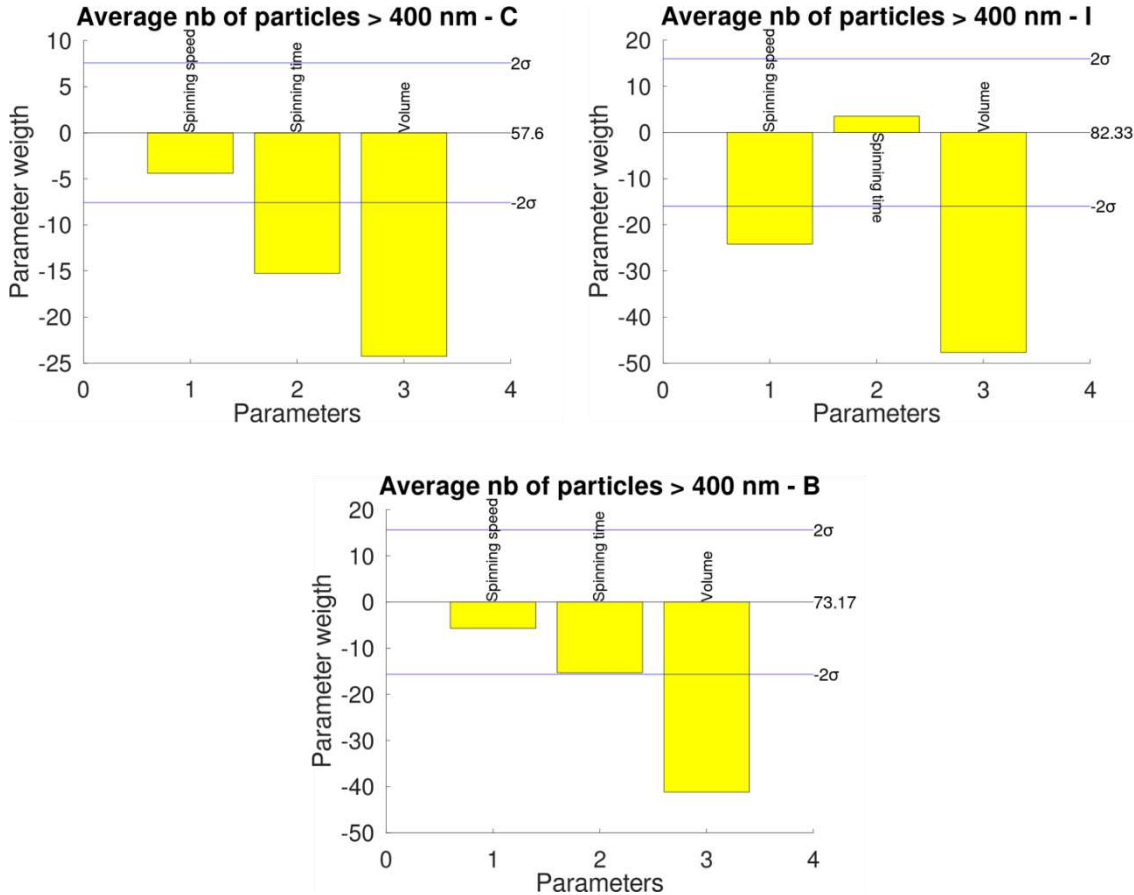


Figure IV.7: Level of impact of parameters on responses.

As a result, the best condition for spin-coating is to dispense 400 μ L of the colloidal suspension on Si substrate at the spin speed of 3000 rpm for 60s in order to obtain the minimum of huge particles on Si surface.

Table IV.3: Level of impact of parameters on responses.

Factor	Spinning speed	Spinning time	Volume
Center	no effect	+	+
Intermediate	+	no effect	+
Border	no effect	no effect	+

I.2.2 Spin coating cycles influence on PL response

An important target for investigation is to maintain the UC luminescence response of nanoparticles after the spin-coating deposition. The crucial factor that controls this emission is the coating cycles amount [7]. For that purpose, the number of spin coating cycles is varied between 2 and 8. Between 2 cycles, the wafer containing nanopowders is heated at 200°C for 1 min. As it can be seen from the SEM micrographs presented in **Figure IV.8**, the total surface of the substrate is well covered with nanoparticles as the cycle number increases up to 8. **Figure IV.9** shows the evolution of the film thickness versus the number of cycles. As estimated from cross sectional SEM measurements, more coating cycles can result in a larger film thickness which are found to be between 265 ± 21 nm, 326 ± 44 nm and 713 ± 89 nm for 2, 4 and 8 cycles respectively. The measured thicknesses are the average values of three thicknesses in three different areas. It is worth mentioning that from this work and the literature data, the thickness deposited with spin coating process cannot be perfectly controlled through varying cycle numbers as illustrated in **Figure IV.9**. In addition, it is interesting to note that during the preparation of the cross-section samples, the nanoparticles based films detached from the substrate (white arrow in **Figure IV.9**). Based on the comparison between measured thicknesses in this study and other reports, it can be concluded that the thicknesses are in the same order with other reports. In fact, increasing cycle numbers gives a compact film with a total coverage as observed in **Figure IV.8** and **Figure IV.9**. It also provides a relatively larger amount of fluorescent sites that is beneficial and leads to the increase of PL intensities [7]. Therefore, adjusting the number of spin-coated layers to 8 is optimum for preparing an upconversion film of codoped TiO₂ nanopowder while getting an optical response as the powder phase with full coverage of the substrate and compact film. This result is in good agreement with the literature: Srinatha et al reported the deposition of Al-doped ZnO nanoparticles on glass substrate (2.54×2.54 cm²) using sol-gel spin coating (3000 rpm- 60 s-10 cycles) with thicknesses between 400 and 500 nm. The higher intensity of PL emission is shown with the thicker film [8]. Another paper mentioned that spin coating of TiO₂ film (3000 rpm-15 s) on TCO substrate (2.5×2.5 cm²), with a thickness of about 0.92 μm (8 cycles) and 1.07 μm (10 cycles), have a higher PL emission than 4 and 6 cycles [9]. In addition, it is found that increasing thickness above 2.9 μm decreases the performance of nanoparticles (Cu₂SnSe₃) which are deposited by drop casting into FTO substrate due to more defects in thicker films [10].

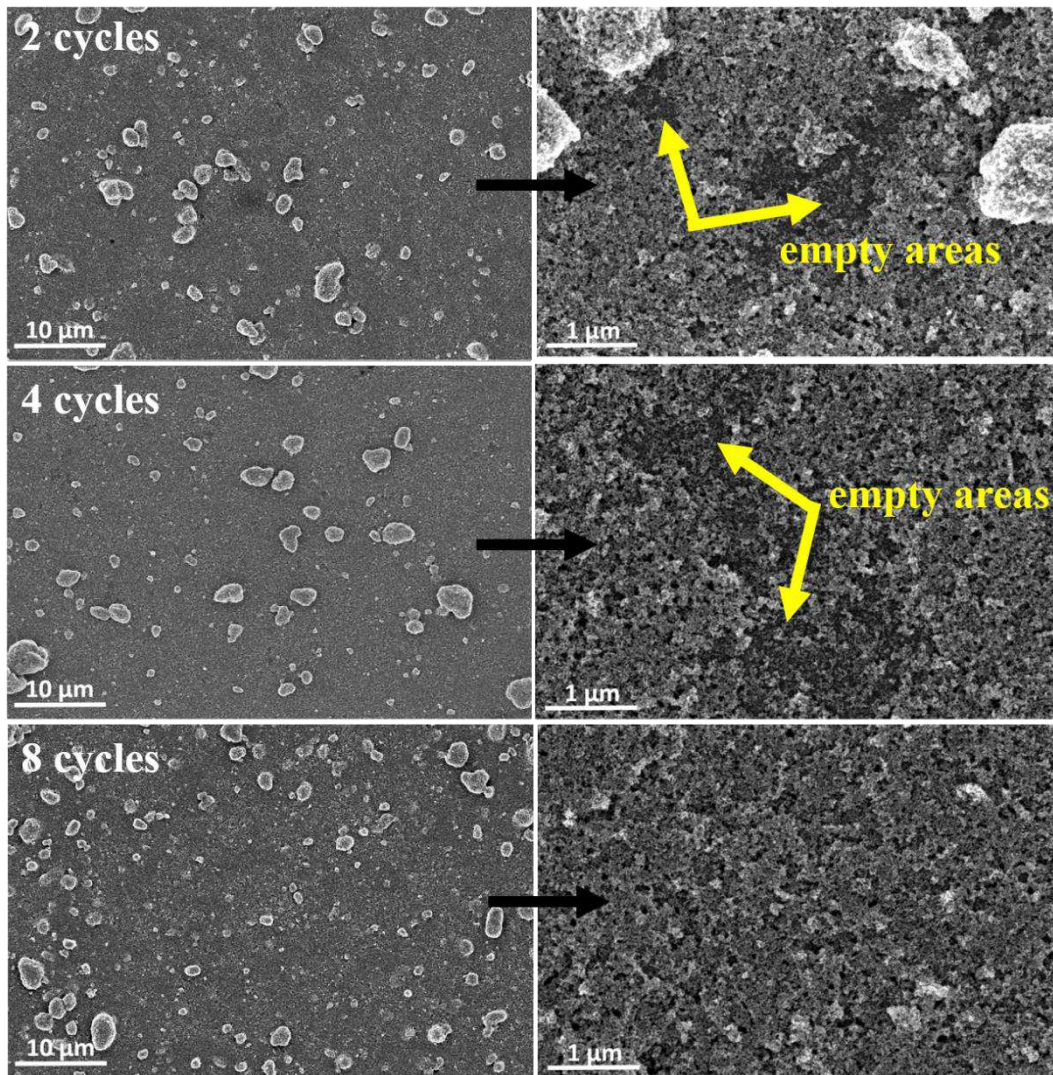


Figure IV.8: SEM Top view images of Si/ codoped TiO₂ nanopowder with different spin-coating cycle numbers (2, 4 and 8).

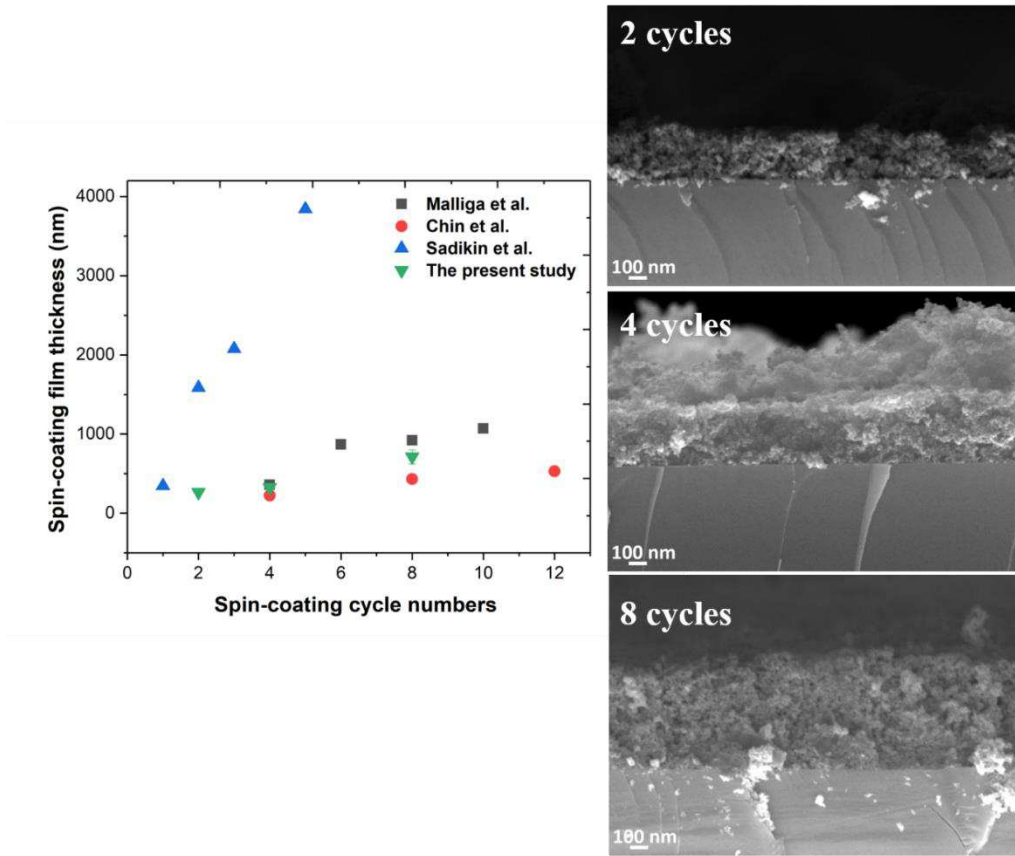


Figure IV.9: Thickness comparison with other reports and cross-sectional SEM images of Si/codoped TiO₂ nanopowder with different spin-coating cycle numbers (2, 4 and 8), (bar errors are included in the dot size).

PL emission of the films composed of assembled nanoparticles with different cycle numbers at room temperature under 514 nm excitation is performed. The spin-coating cycle amount of 2, 4 and 8 are selected since they are the most reported cycles for spin coating in literature [9], [11-12]. **Figure IV.11** shows the evolution PL spectra from powder phase to deposited codoped TiO₂ nanopowder on Si substrate with various number of cycles. In order to distinguish between Er³⁺ ion emission and TiO₂ Raman peaks, superposition of PL spectra of undoped and codoped TiO₂ nanopowders is performed. From **Figure IV.10**, four characteristic Raman active modes of anatase TiO₂ with symmetries E_g, B_{1g}, A_{1g} and E_g are clearly seen at 519, 526, 530 and 533 nm, respectively [13-14]. Therefore, other peaks than these ones can be assigned to Er³⁺ emissions. The downshift of Raman modes in codoped TiO₂ nanopowder compared to undoped nanopowder could be assigned to the lattice deformation caused by using elements with different radii, which is in line with the XRD analysis [15-16].

The Er³⁺ emission in TiO₂ can be associated with two main emissions. Green emission corresponding to the ²H_{11/2} + ⁴S_{3/2} → ⁴I_{15/2} transition and red emission attributed to ⁴F_{9/2} → ⁴I_{15/2} transition can be observed (**Figure IV.11 a**). The green emissions between 521-523 nm and

548-565 nm are strong while the red emissions located between 647 nm and 686 nm are weak. Similar observation is reported by Kifle and co-workers under the same excitation wavelength ($\lambda=514$ nm) for Er^{3+} [17]. For the various number of cycles, as expected, the emission intensity increases when going from the low to the high number of cycles (**Figure IV.11 b**).

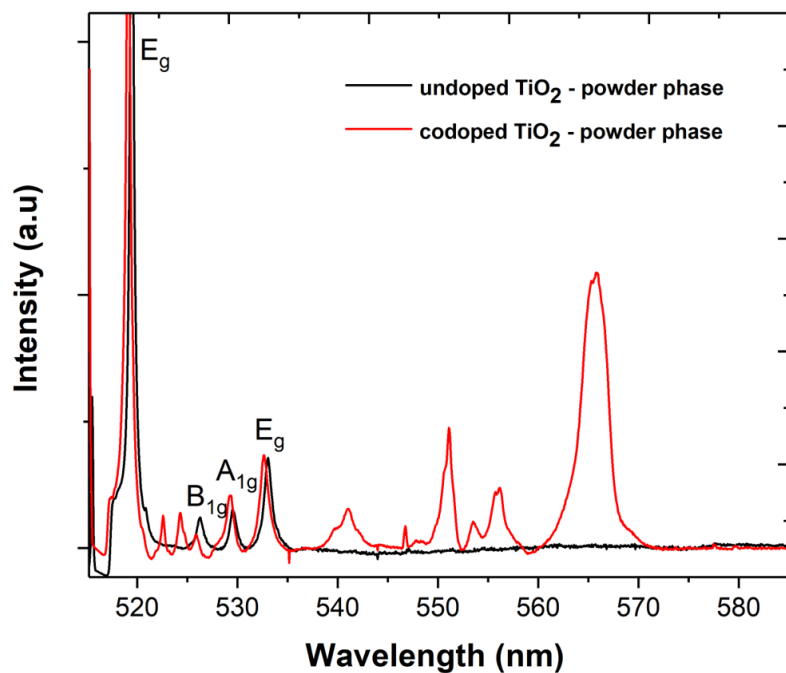


Figure IV.10: Identification Raman peaks from PL emissions of Er^{3+} under excitation wavelength $\lambda=514$ nm of undoped and codoped TiO_2 nanopowders.

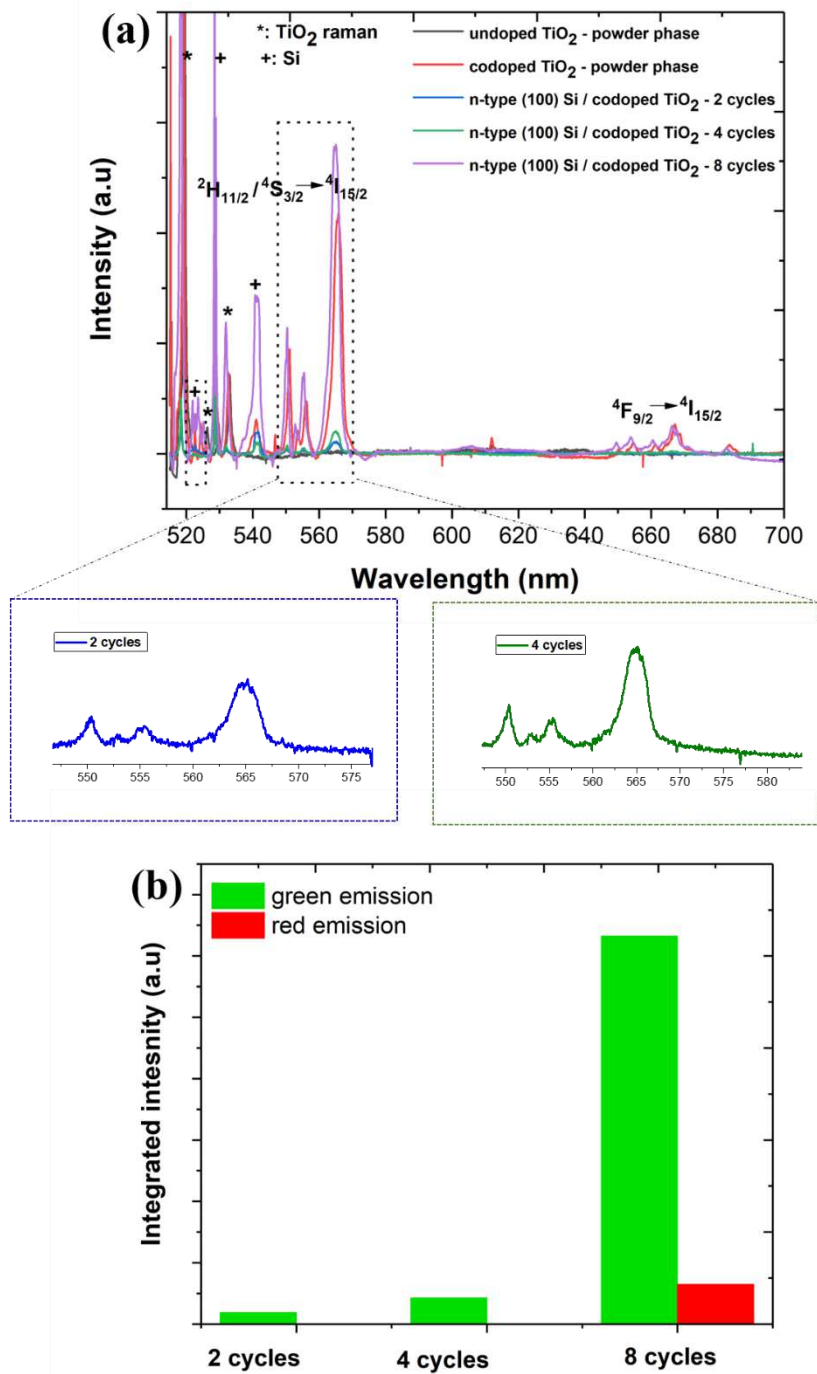


Figure IV.11: (a) PL emission under excitation wavelength $\lambda=514$ nm of all the different samples from powder to film and (b) the corresponding integrated intensity of the peaks. The green emissions are shown in dotted rectangle.

In addition to the luminescence enhancement with increasing the cycle numbers, a slight blue shift of peak positions of the deposited codoped TiO₂ nanopowder (2, 4 and 8 cycles) with respect to its position for the codoped nanopowder can be noticed (**Figure IV.12**). The peak positions remain unaffected when the cycle amount undergoes from 2 to 8 cycles. Based on

previous reports [18-19], two possible reasons are the decrease of particles size after the dispersion step (ultrasonication), which is consistent with DLS and SEM analysis and the local strain on nanopowder induced by the Si substrate (interaction of nanopowder with the substrate interface). Rodriguez et al. [20] reported a blue shift in 1554 nm emission intensity for the Si nanocrystals embedded in a silica matrix with higher Er^{3+} concentrations that is attributed to the decrease in the nanocrystals size.

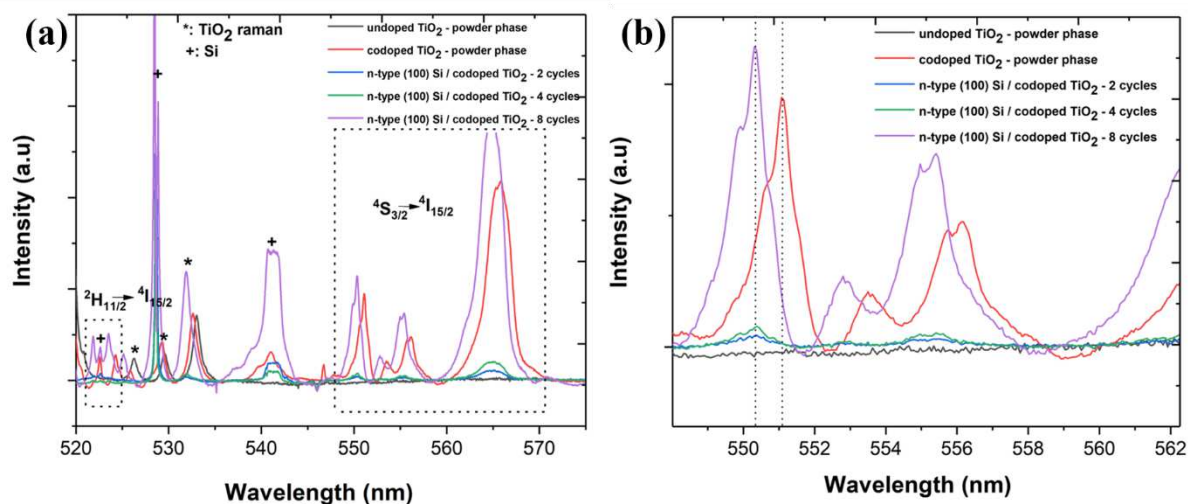


Figure IV.12: PL emission of different samples under excitation wavelength $\lambda=514$ nm (a) green emissions of Er^{3+} ($^2\text{H}_{11/2} + ^4\text{S}_{3/2} \rightarrow ^4\text{I}_{15/2}$) enlarged and presented in order to get a clear view and (b) blue shift of the peaks

II. ALD- Al_2O_3 coating on codoped TiO_2 nanopowder deposited on Si wafer

II.1 Morphological analysis

ALD- Al_2O_3 on UC nanopowder deposited on Si is performed on an home-made ALD reactor (ALD Nano 2), located in SIMaP. TMA and H_2O water are used as the precursor and oxidant, respectively. The reactor temperature is set to 200 °C during deposition. Nitrogen is used as the purge and the carrier gas with a flow rate of 100 sccm. Each cycle consists of a 1.5 s of TMA with a 30 s purge time, followed by a 1 s pulse of H_2O with a 60 s purge time. From calculation of saturation dose (Annex 2), 1.5s is sufficient to saturate the nanopowder based thin film. The ALD- Al_2O_3 deposition is followed by the FGA treatment. To the end of this section, the samples will be labelled as presented in **Table IV.4**.

Table IV.4: Films attribution name.

Abbreviation	Film Attribution
<i>Np</i>	Si/ 5% (Er ³⁺ -Yb ³⁺) codoped TiO ₂ nanopowder (8 cycles) calcined at 300°C
<i>Np/62</i>	Si/ 5% (Er ³⁺ -Yb ³⁺) codoped TiO ₂ nanopowder (8 cycles) calcined at 300°C/ 62 cycles of ALD-Al ₂ O ₃ (deposition at 200°C for 4 hours)
<i>Np/62+FGA</i>	Si/ 5% (Er ³⁺ -Yb ³⁺) codoped TiO ₂ nanopowder (8 cycles) calcined at 300°C/ 62 cycles of ALD-Al ₂ O ₃ (deposition at 200°C for 4 hours) + FGA (N ₂ :H ₂ - 95%:5%) at 430°C for 30min
<i>Np/620</i>	Si/ 5% (Er ³⁺ -Yb ³⁺) codoped TiO ₂ nanopowder (8 cycles) calcined at 300°C/ 620 cycles of ALD-Al ₂ O ₃ (deposition at 200°C for 17 hours)
<i>Np/620+FGA</i>	Si/ 5% (Er ³⁺ -Yb ³⁺) codoped TiO ₂ nanopowder (8 cycles) calcined at 300°C/ 620 cycles of ALD-Al ₂ O ₃ (deposition at 200°C for 4 hours) + FGA (N ₂ :H ₂ - 95%:5%) at 430°C for 30min
<i>62</i>	Si/ 62 cycles of ALD-Al ₂ O ₃ (deposition at 200°C for 4 hours)
<i>620</i>	Si/ 620 cycles of ALD-Al ₂ O ₃ (deposition at 200°C for 4 hours)

Figure IV.13 and **Figure IV.14** show the top views of the different films before and after FGA. The presence of aggregates on the surface of the films is clearly seen as discussed previously in **chapter III**. The ALD-Al₂O₃ present a granular morphology. The entire surface of the nanopowder based thin film is covered with Al₂O₃ with a thin microstructure for the thin layer and large grains for the thickest sample. Conformal and full surface coverage of ALD-Al₂O₃ layer onto the exposed surface of nanopowder is achieved. The oxide coating could observed around each huge particle.

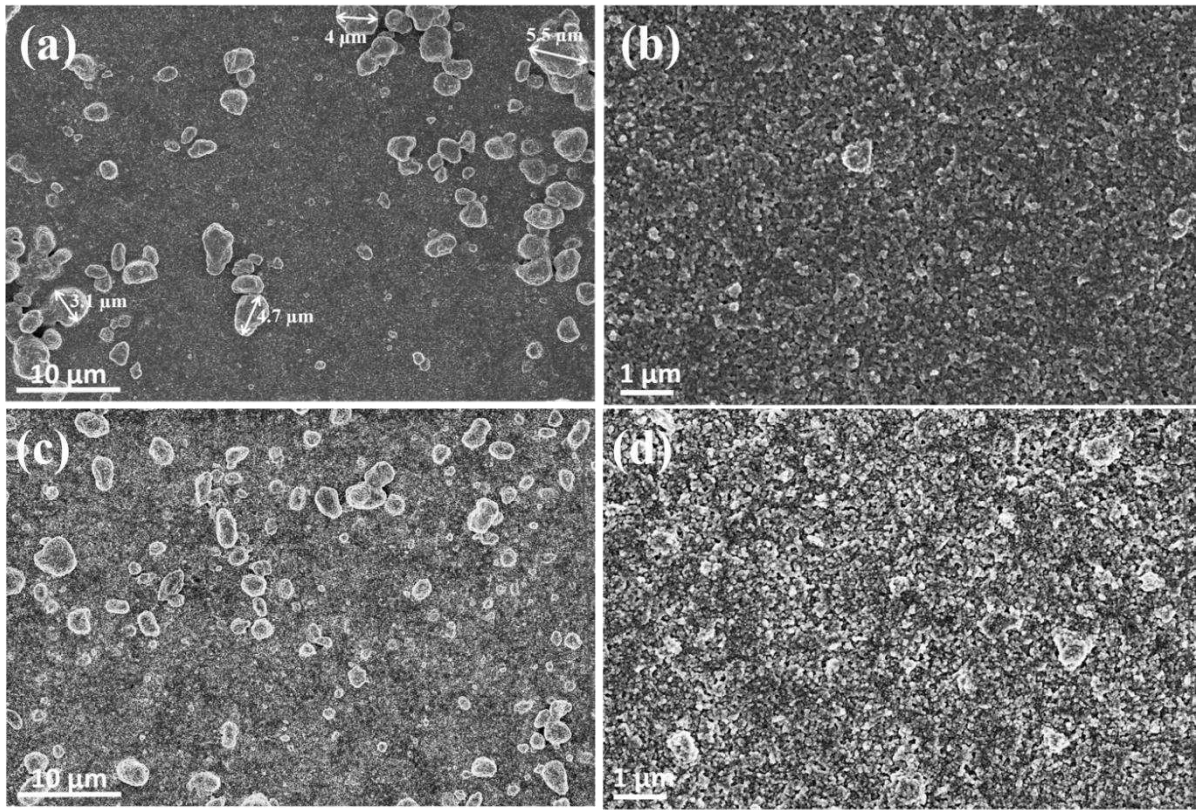


Figure IV.13: SEM top view images of (a-b) Np/62 and (c-d) Np/62+ FGA.

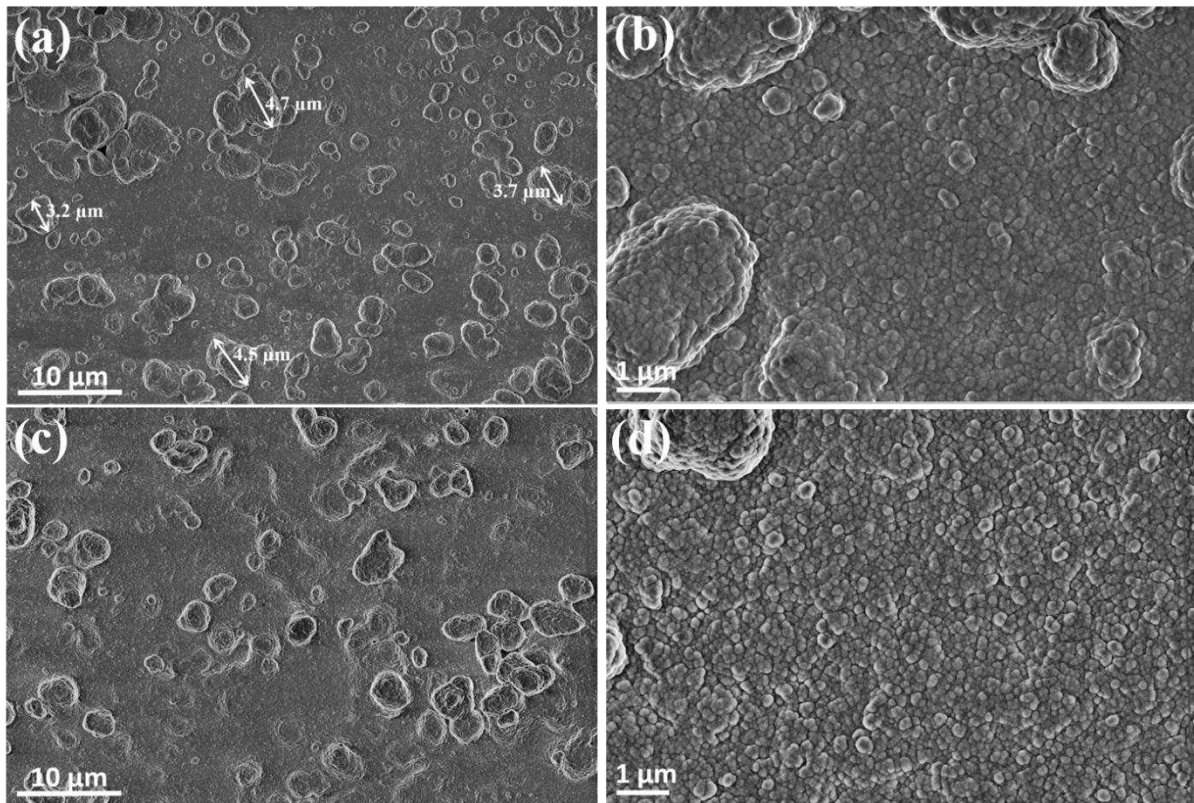


Figure IV.14: SEM top view images of (a-b) Np/620 and (c-d) Np/620+ FGA.

Figure IV.15 shows more clearly the conformality of the coating. The SEM images indicate that ALD- Al_2O_3 coating infiltrates and conformally coats the pores which is typically the role of ALD technique [21]. This infiltration behavior of ALD on porous structure is commonly reported [21-22]. We may assume that with a physical type technique the deposition process mainly occurs on the exposed surface of nanopowder while during the ALD process, molecules of precursors penetrate into the holes forming the layer of Al_2O_3 inside the holes [23] leading to deposition both on the surface and inside the nanoporous material. With increasing the ALD cycle numbers (from 62 to 620 cycles), the pores will become smaller and will gradually close.

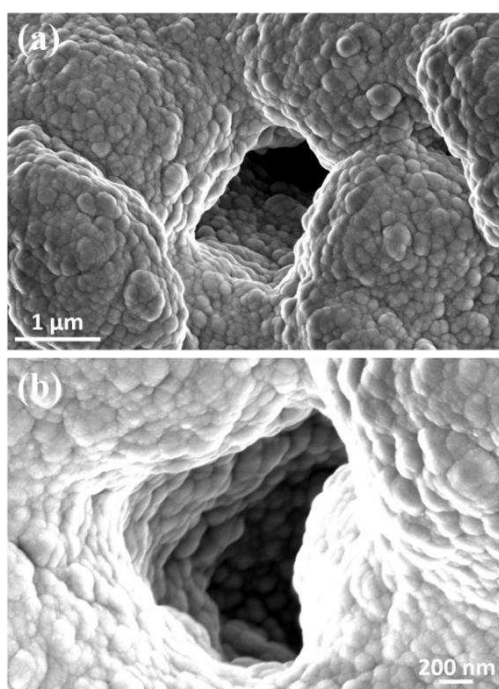


Figure IV.15: SEM images of a pore on the surface of Np/620 +FGA film.

The resulting films are cleaved and examined by SEM. According to the cross sectional SEM images (**Figure IV.17** and **Figure IV.18**), the films are composed of a dense arrangement of nanoparticles, the thickness of the films ranging between 650 and 950 nm with a porous microstructure. Typical columnar structure of ALD- Al_2O_3 is observed for Np/620 film. **Figure IV.19** depicts the HR-TEM images, it can be seen that different measured thicknesses ranging from 19-21 nm and 100-130 nm are found for the Np/62+FGA and Np/620+FGA, respectively. It is difficult to measure exactly the film thickness. This thickness scattering can be explained by the roughness of the nanopowder that composes the porous film [24-25]. Additional information is given with ACOM-TEM measurements (it is explained in details in the second

section of this chapter). **Figure IV.19 e** reveals that TiO_2 nanoparticles are embedded in Al_2O_3 film, which can explain the difficulty of thickness measurements.

It is clearly observed in **Figure IV.17 e** and **Figure IV.18 d** that FGA induces densification, better interconnection between the codoped TiO_2 nanopowder grains and better interface between nanoparticles and Al_2O_3 which is clearly observed for the thicker layer. Before FGA treatment, the codoped TiO_2 nanopowder is observed as distinct individual particles, while after conducting the annealing process, the particles are assembled. It becomes difficult to differentiate between the ALD- Al_2O_3 layer and particles, suggesting the infiltration of ALD- Al_2O_3 into the film, which could consequently improve the adhesion of films to the substrate. This observation is in agreement with the study conducted by Yuelong Li et al. [26] that shows a thin ALD- TiO_2 layer deposited on TiO_2 host particles serves as binding layer to enhance the interconnection of TiO_2 nanoparticles of photoelectrode (**Figure IV.16**). It worth mentioning that our film does not contain as much as voids as presented in **Figure IV.16** but it is only an approximate representation of enhanced interparticle connections.

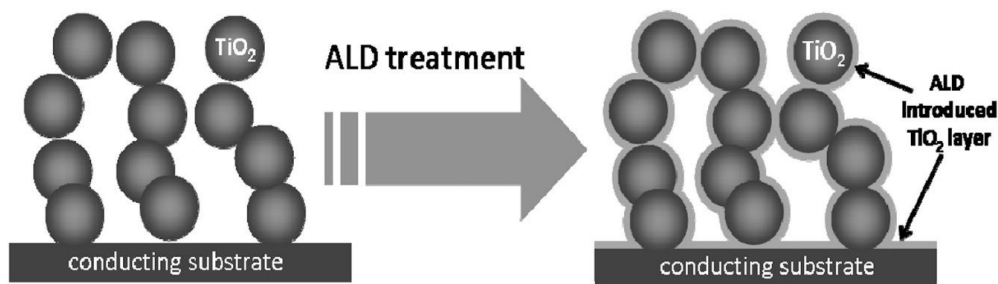


Figure IV.16: ALD- TiO_2 layer on TiO_2 nanoparticles to enhance interparticles connection as reported in [26].

The ALD- Al_2O_3 thickness variation along the film can be explained by the initial porous microstructure of the codoped TiO_2 nanopowder and surface roughness of the fabricated film [22]. For this reason, it is suggested that the infiltration of ALD- Al_2O_3 layer inside the porous film may cause thickness variation along the sample.

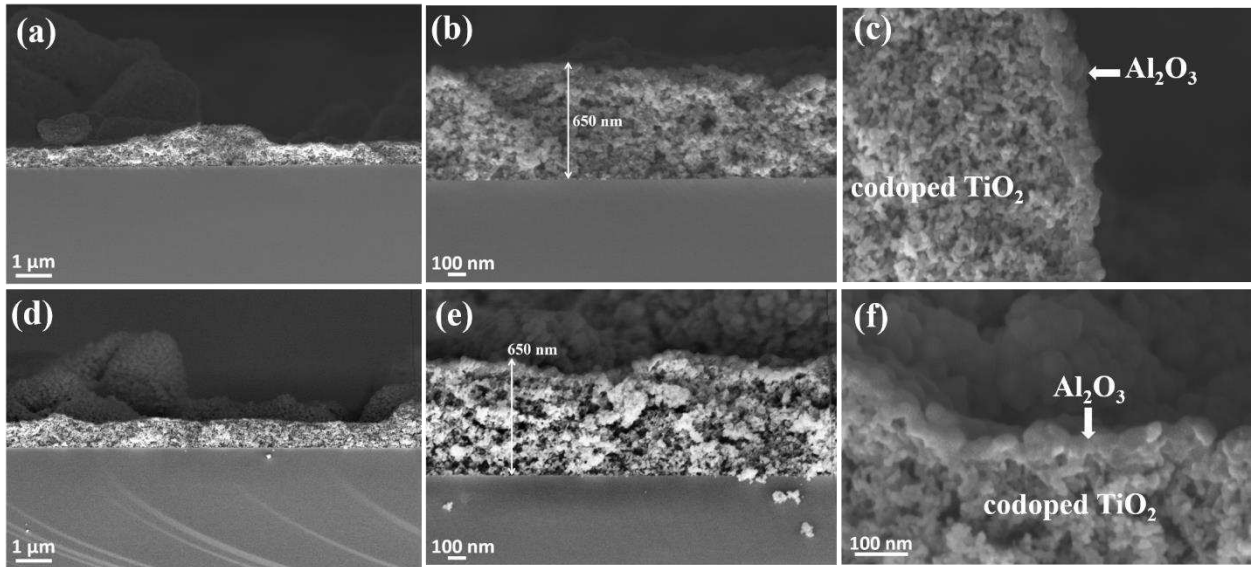


Figure IV.17: Cross-sectional SEM images of (a-c) Np/62, (d-f) Np/62 + FGA films.

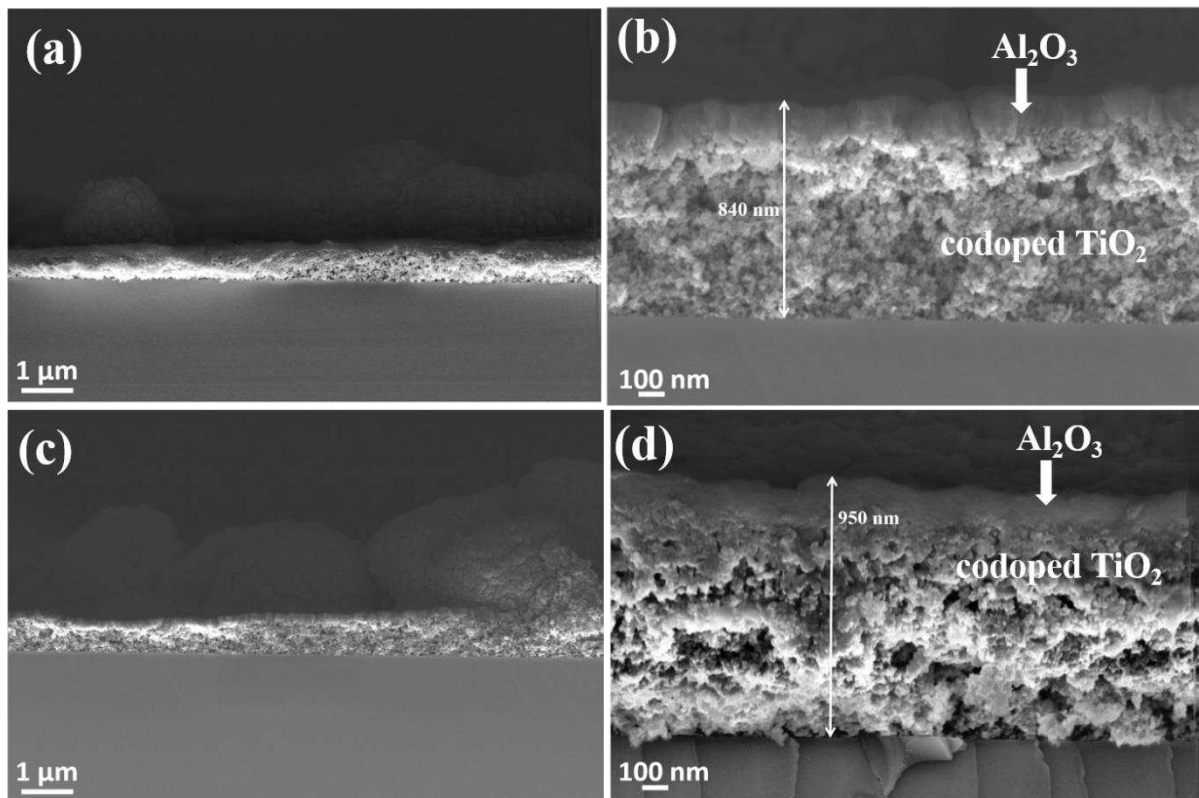


Figure IV.18: Cross-sectional SEM images of (a-b) Np/620, (c-d) Np/620+FGA films.

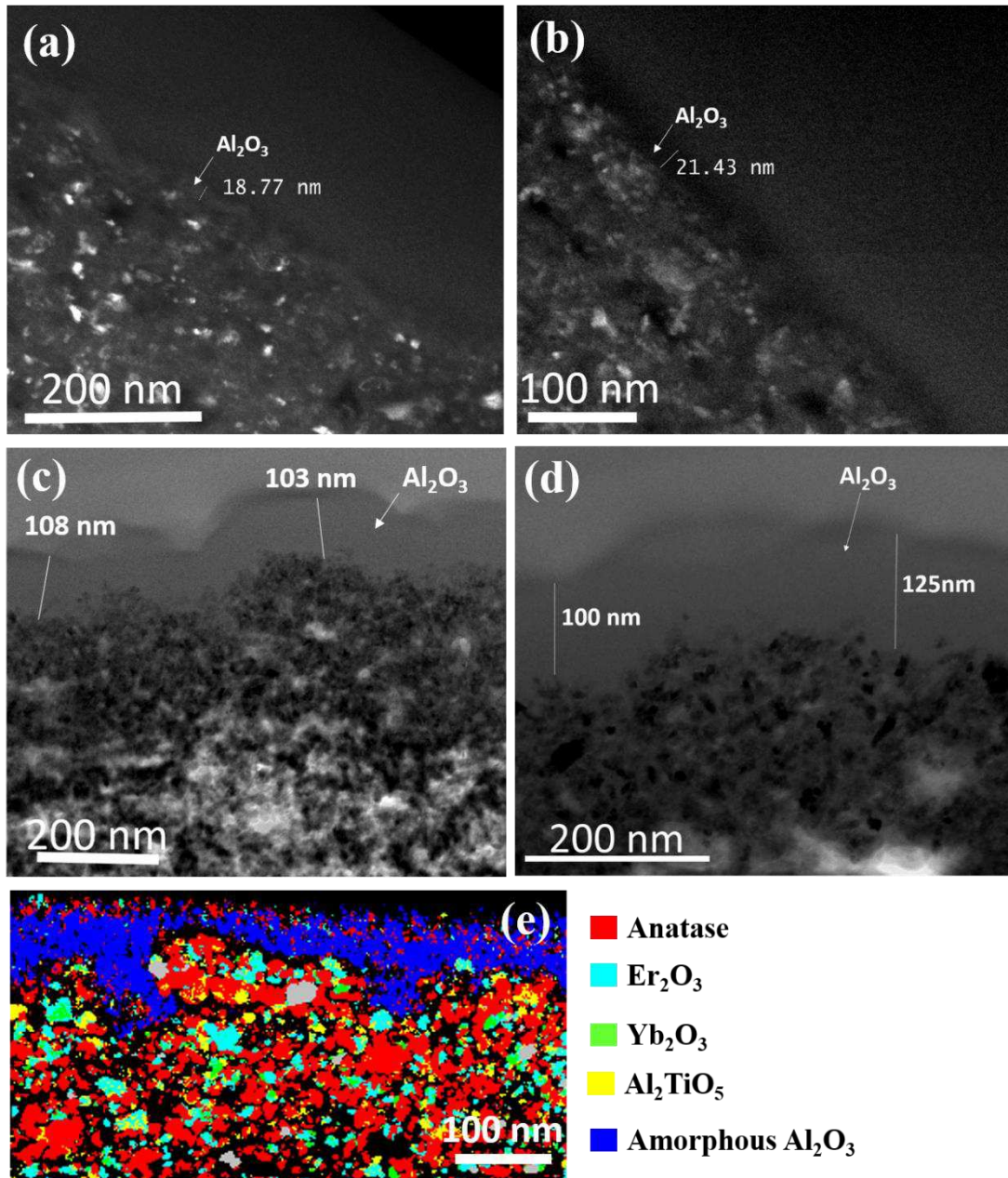


Figure IV.19: HR-TEM images showing the thickness of (a, b) Np/62+FGA, (c, d) Np/620 +FGA films and (e) ACOM-TEM on the Np/ 62 film showing phase map of anatase plotted with Er₂O₃, Yb₂O₃, Al₂TiO₅ and amorphous Al₂O₃ respectively.

II.2 Compositional investigations of ALD-Al₂O₃ coating on codoped TiO₂ nanopowder deposited on Si

The infiltration or diffusion is dependent on several factors such as the chemical and physical nature of the materials, the annealing temperature and duration [27]. Elemental mapping is performed using STEM-EDS analysis in order to prove and estimate the depth of the infiltration of ALD-Al₂O₃ over the nanopowder film after the conducted procedure. The EDS mapping of the cross sectional films with 62 and 620 cycles of ALD-Al₂O₃ provided in **Figure IV.20** and

Figure IV.21 clearly reveal the presence of all the elements: Ti, O and Al. The elemental mapping images for 620 cycles of ALD- Al_2O_3 indicate the Al accumulation on the top of the films, which confirms the existence of Al_2O_3 coating layer on sample surface. For the 62 cycles, the formation of the film is not clearly observed on the top because the thickness is very low to be detected. The films seem also to be consist of a large number of pores in a random manner. The images also prove that there is a slight diffusion of ALD- Al_2O_3 through the film for the sample before FGA treatment, which is related to the diffusion of precursor molecules during the deposition process. The surface of the nanopowder that composes the porous film shows an ability to retain Al containing gaseous species due to the functional groups that exhibits on surface (hydroxyl groups). Meanwhile, this diffusion seems to be improved after the FGA treatment with the Al and O elements densities decreasing gradually from top to bottom (near to Si surface substrate) of the film, a gradient between the top and bottom of the structure can be observed.

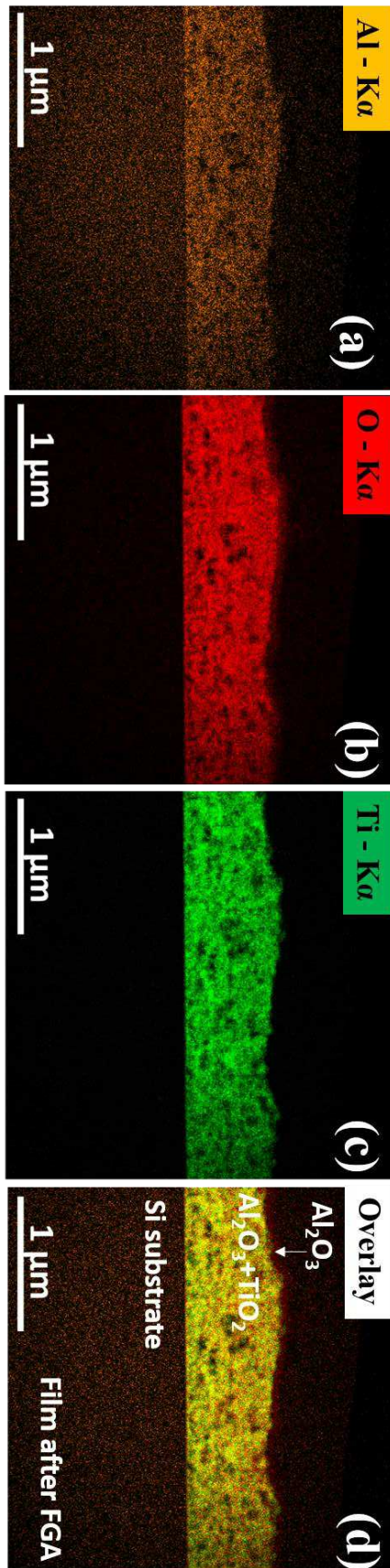


Figure IV.20: STEM-EDS elemental mapping of Np/ 62+ FGA film.

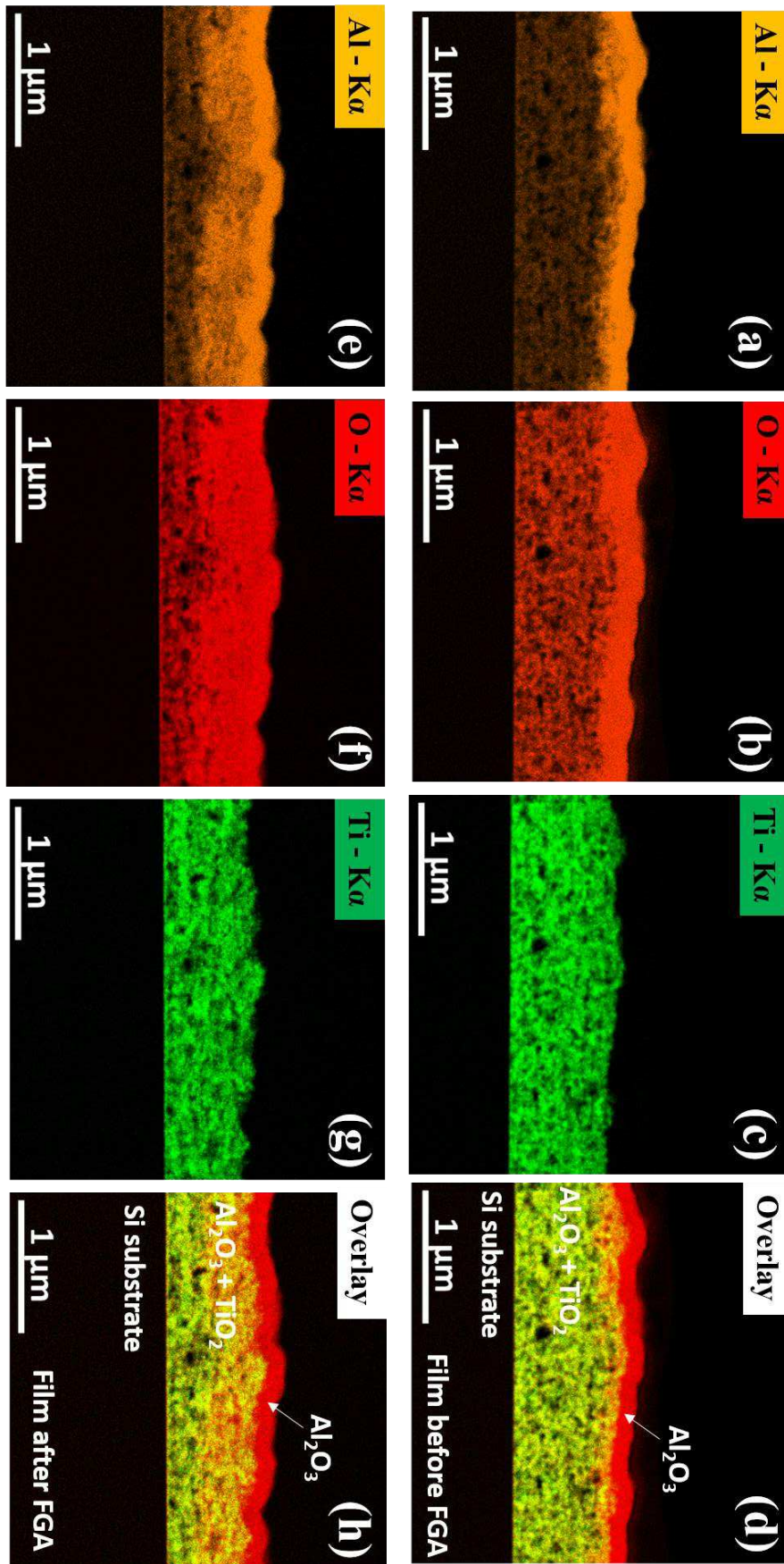


Figure IV.21: STEM-EDS elemental mapping of (a-d) Np/620 and (e-h) Np/620+FGA.

With the STEM-EDS line scan profiles (**Figure IV.22**), information on the ALD- Al_2O_3 diffusion is acquired by comparing the samples with different thicknesses before and after the FGA treatment. The results illustrate that the diffusion is more pronounced when a post heat treatment is applied, Al and O elements expand significantly into the interior of the film. The Al diffusion for Np/620 film into the porous matrix is limited to a depth of 136 nm before annealing, while a much deeper and stable penetration over 250 nm is observed then it decreases gradually with a depth of 140 nm after annealing. In total, the existence of Al is about 450 nm in depth over the film. Such evolution provides direct evidence for atomic interdiffusion across the films upon annealing. These results confirm that the coated films composed of assembled nanopowders contains Al_2O_3 not only on the top of the film but also within the porous matrix to form a composite. From Oxygen elemental mapping it is obvious that the infiltration of O element is similar to Al (**Figure IV.21 e** and **Figure IV.21 f**), which can also confirmed by the depth profile presented in **Figure IV.22 b** and **Figure IV.22 c**. For the post heat-treated film the evolution of O and Al amount are similar, and O amount remains high compared to Ti when compare it with the untreated layer. Therefore, it can be concluded that the infiltration of both constituents occur simultaneously.

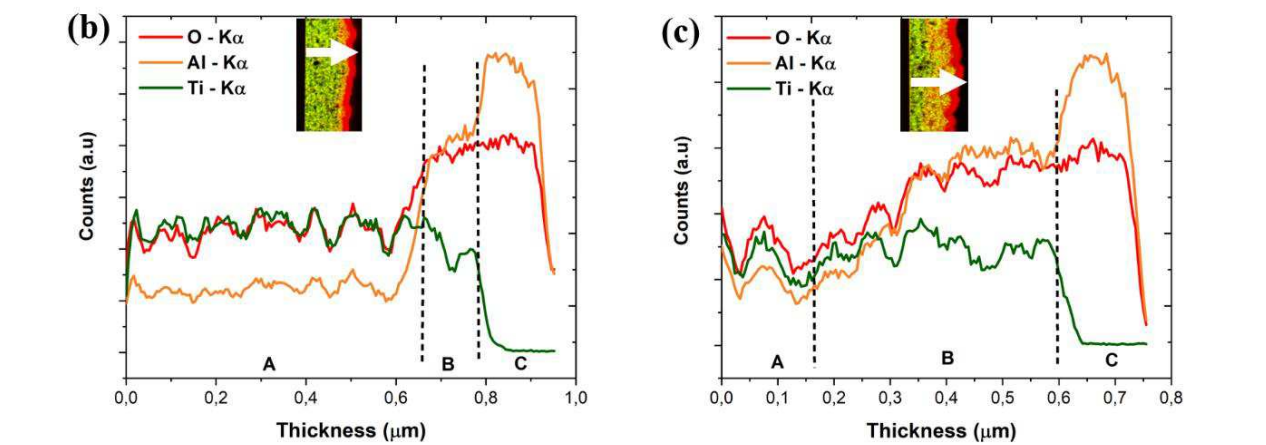
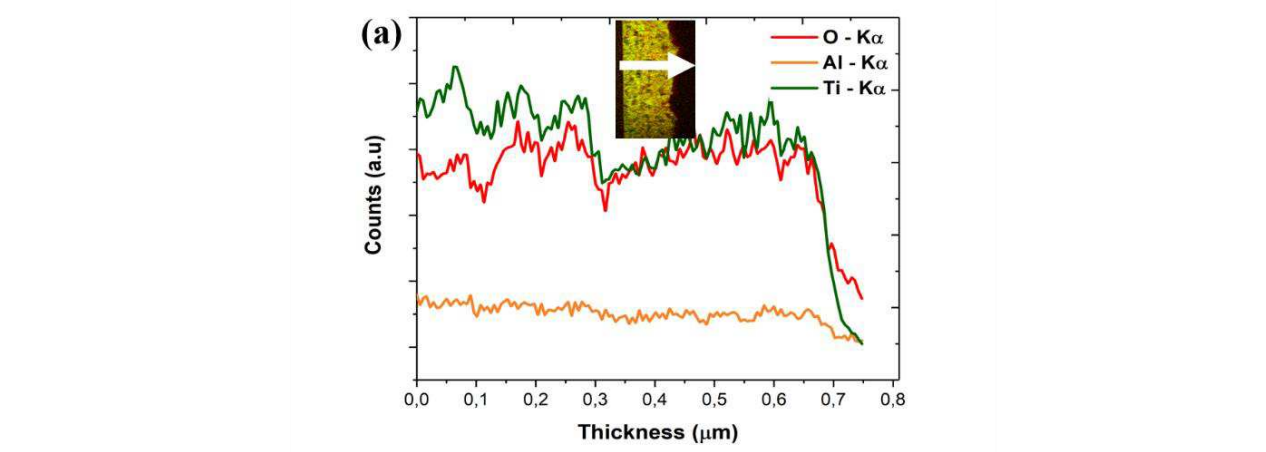


Figure IV.22: Depth profile of the different elements for (a) Np/ 62+FGA, (b) Np/ 620 and (c) Np/ 620 + FGA. The white arrows give the direction of the scan, from the tail (0 μm) to the head (between 0.7 and 0.95 μm)

This result suggests that an effective interparticle bonding is resulted by this diffusion within the codoped TiO_2 nanopowder. The penetration of an element is determined by the porous skeleton of the matrix. Therefore, the size and shape of pores are very important factors [28]. For the precursors diffusion during the deposition process, the pores play a key role to promote the facile diffusion of precursors along the film. During the film annealing, densification as observed in SEM images may occurs by dehydration of the residual hydroxyl groups [29], which causes a decrease in the film porosity and rearrangement of pores. This densification results from the minimization of the surface energy by replacing the solid-gas interfaces by grain boundaries [30]. So, the increasing of grain boundaries at the grain contact can be a fast path for mass transport (**Figure IV.23**), especially when enhanced by a stress gradient created by the deposition of ALD- Al_2O_3 on the surface in our case. Thereby, the grain boundaries diffusion being orders of magnitude faster than volume diffusion can play a key role in material

rearrangement particularly at low temperatures ($\leq 0.6 T_{\text{melting}}$) [31-32]. Therefore, Al and O can migrate through the film along the grain boundaries created between adjacent particles.

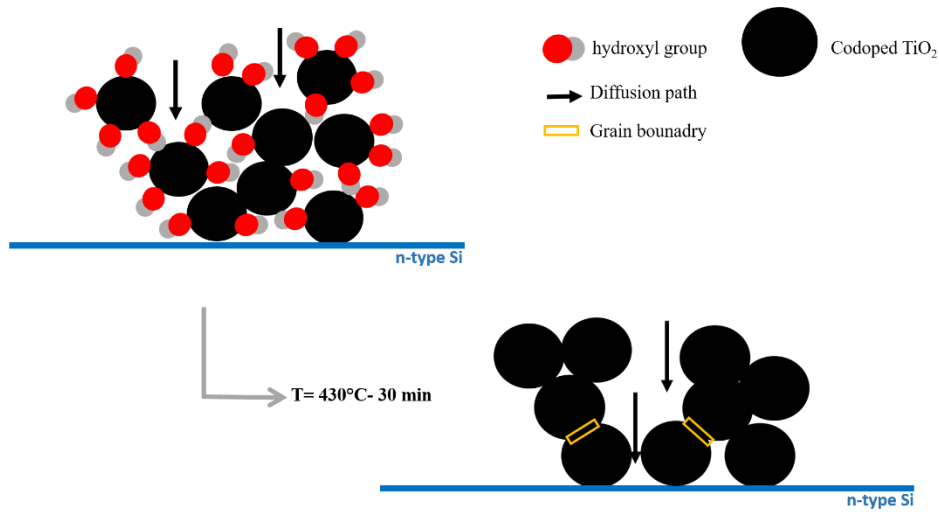


Figure IV.23: The possible explanation for Al and O elements diffusion after FGA.

Similar behaviour is observed by Chen et al., who reported the fast diffusion of Ti from $\text{Li}(\text{Ni}_{0.4}\text{Co}_{0.2}\text{Mn}_{0.4})_{1-x}\text{Ti}_x\text{O}_2$ to $\text{LiNi}_{0.8}\text{Co}_{0.1}\text{Mn}_{0.1}\text{O}_2$ particles due to higher diffusion coefficient along grain boundary after calcination at 400°C- 4h and sintering of the cathode at 800°C-10h. Cheng and co-workers [33] show also the important step of annealing (600°C-2h in air) of Li_3PO_4 coating deposited by ALD on nickel-rich layered-oxide cathode material for lithium ion batteries in order to fill the grain boundaries, improve the cycle stability and suppress cracking issue by diffusion of P.

Al diffusivity into the porous film composed of codoped TiO₂ nanopowder is related to the diffusion length according to the following formula:

$$L = \sqrt{D_{\text{Al}} \times t} \quad (\text{Equation IV.2})$$

Where L is diffusion length, D_{Al} is the diffusivity (m^2/s) of Al in the porous film and t the duration of heat treatment (s). Knowing the diffusion length from penetration depth profile deduced from STEM-EDS analysis after ALD and FGA (450 nm) and t (1050 min), the estimated D_{Al} is about $10^{-17} \text{ m}^2/\text{s}$. For the 62 cycles of ALD- Al_2O_3 , it is clearly seen the existence of Al in constant amount from the top to bottom of the film.

Tang and co-workers [34] present a density-functional-theory (DFT) study of aluminum intercalation into the two polymorphs of TiO₂ (anatase and rutile) material as an electrode for aluminum-ion batteries. The diffusion coefficient of Al^{3+} is calculated to be $10^{-24} \text{ m}^2/\text{s}$, indicating a poor mobility of aluminium ions in bulk anatase. Therefore, the apparent diffusion

coefficient we measure (10^{-16} m²/s) is probably due to fast diffusion in grain boundaries rather than in the bulk of nanoparticles.

In spite of the fact that many studies have been done on the ALD–Al₂O₃ deposited on powders, there is no study, known to us, which attempted to study of the infiltration of ALD-Al₂O₃ followed by FGA into a porous film composed of upconversion nanopowder. A unique study on the distribution of 150 cycles of ALD- Al₂O₃ grown at 300°C and coated on porous structure (porous silicon) without further post deposition heat treatment has been conducted by Iatsunskiy et al. [29] showing the depth penetration profile of ALD-Al₂O₃ layer into the film.

In this section, we prove the diffusion of ALD precursors during deposition process into the porous film as a result of diffusion through the pores. Then the improvement of this diffusion by post heat treatment can be explained by Al and O migration through the film along the grain boundaries.

II.3 Structural investigation of ALD-Al₂O₃ coating on codoped TiO₂ nanopowder deposited on Si

The influence of the ALD-Al₂O₃ coating on crystal structure of the different films is performed. The XRD patterns of Si/ codoped TiO₂ nanopowder coated with different thicknesses of ALD-Al₂O₃ layer followed by FGA treatment are given in **Figure IV.24**. Each pattern peaks are indexed for the anatase phase by comparison with the ICDD card number: 21-1272, indicating that all samples are constituted by a single crystalline anatase phase. No other phases such as rutile, Er₂O₃, Yb₂O₃ is evidenced, suggesting that anatase phase is unaffected by the ALD deposition step and the subsequent FGA step. For the ALD-Al₂O₃ layer, it is demonstrated in literature that deposition in the temperature range of 200°C-500°C and film thickness up to 200 nm, leads to the formation of an amorphous structure of Al₂O₃ [23].

Crystallite size of the deposited nanopowders on Si substrate and coated with different thickness of ALD –Al₂O₃ followed by FGA treatment is calculated using Debye Sherrer and Williamson-Hall methods, as previously detailed in **chapter III** (details are given in Annex 1), for the three diffraction detected planes (101), (004) and (200). The results of microstructural parameters of the samples are presented in **Table IV.5**. The mean crystallite size remains almost the same until the end of the procedure. The ALD –Al₂O₃ layer acts as a buffer layer to suppress the growth of particles, which results in the same crystallite size [35]. The results show that the lattice strain decreases as its value remains positive for Np and Np/62+FGA films and reveals the presence of tensile strain. However, it is interesting to note that increasing of the thickness

of ALD-Al₂O₃ layer (up to 620 cycles) alter the lattice strain from positive to negative, the developed strain is compressive in nature. A decrease in lattice parameter “c” is noticed which demonstrates the development of external compressive strain. Possible explanation is linked to the resultant forces from the surface to the volume of the deposited 620 cycles of ALD-Al₂O₃ thick layer.

These results confirm that until the end of the procedure no remarkable increase in the crystallite size is observed. The procedure proposed in the present study is efficient compared to the work conducted by Yogita et al. [36] that shows an increase of the crystallite size of pure TiO₂ nanoparticles synthesized by sol-gel method by 111% upon an annealing at 500°C-1h.

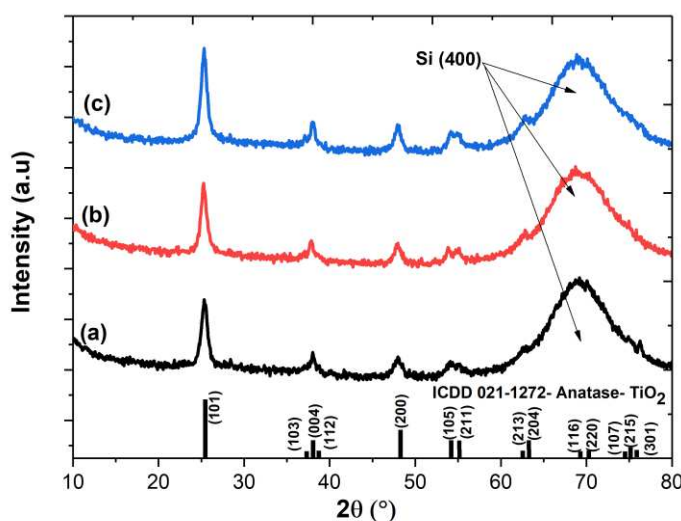


Figure IV.24: XRD patterns of: (a) Np, (b) Np/ 62 +FGA and (c) Np/620+FGA films.

Table IV.5: Microstructural parameters of the films uncoated and coated with different thickness of ALD-Al₂O₃ layer from XRD patterns.

Sample	Mean crystallite size by Debye-Sherrer formula (nm)	Mean Crystallite Size by W-H plot (nm)	Lattice distortion η (%)	a (Å)	c (Å)	c/a ratio	Unit cell volume (Å ³)
Np	11	16	0.37	3.7911	9.4638	2.4963	136.02
Np/62+FGA	11	11	0.004	3.7901	9.5076	2.5085	136.58
Np/620 + FGA	12	11	- 0.13	3.7911	9.4638	2.4963	136.02

To get an insight into the phase purity, the ACOM measurements are performed on different structures. Phase maps by combining anatase and a generic of rutile, aluminium titanate (Al_2TiO_5), pyrochlore ($\text{Er}/\text{Yb}_2\text{Ti}_2\text{O}_7$) erbium and ytterbium oxides (Er_2O_3 and Yb_2O_3) phases are constructed. No rutile and pyrochlore phases are detected. From the results presented from **Figure IV.26** to **Figure IV.28**, it is clearly seen from the phase map combined with index that every grain is indexed. It reveals the coexistence of aluminium titanate and erbium and/ytterbium oxides for the Np/62, Np/620 and Np/620+FGA films. These phases are still present even when combining reliability with index and phase maps. Since Al_2TiO_5 and erbium /ytterbium oxides are detected in Np/62, Np/620 and Np/620+FGA films, it is indicated that these phases have appeared during the ALD process at low temperature (200°C) for the different number of cycles with different duration of process (for 62 cycles, the process takes 4 hours while it is 17 hours for 620 cycles). We cannot differentiate between erbium and ytterbium oxides because of the similarity in crystallographic response (same crystal system (cubic), space group (Ia-3)) as shown in **Figure IV.25** and the small crystallites size of these phases (~ 10 nm). The reliability factor, which measures the ratio between the correlation indexes related to the two solutions has a poor value (<15).

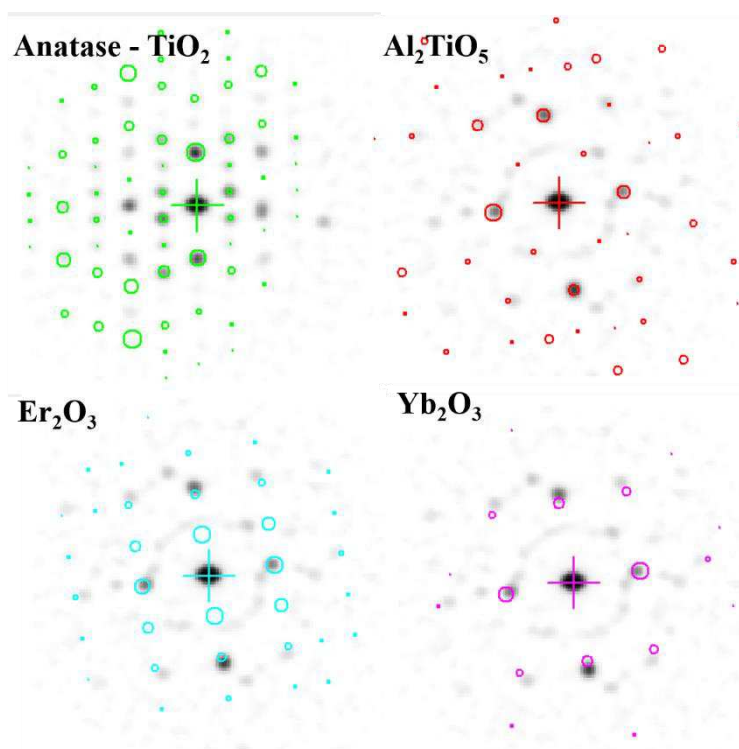


Figure IV.25: Acquired pattern fitted with anatase, Al_2TiO_5 , Er_2O_3 and Yb_2O_3 templates.

The observation for the Np/620+FGA film is not in agreement with the corresponding XRD pattern, which proves that these secondary phases have small concentrations and sizes that are below the level of detection of the XRD instrument [37].

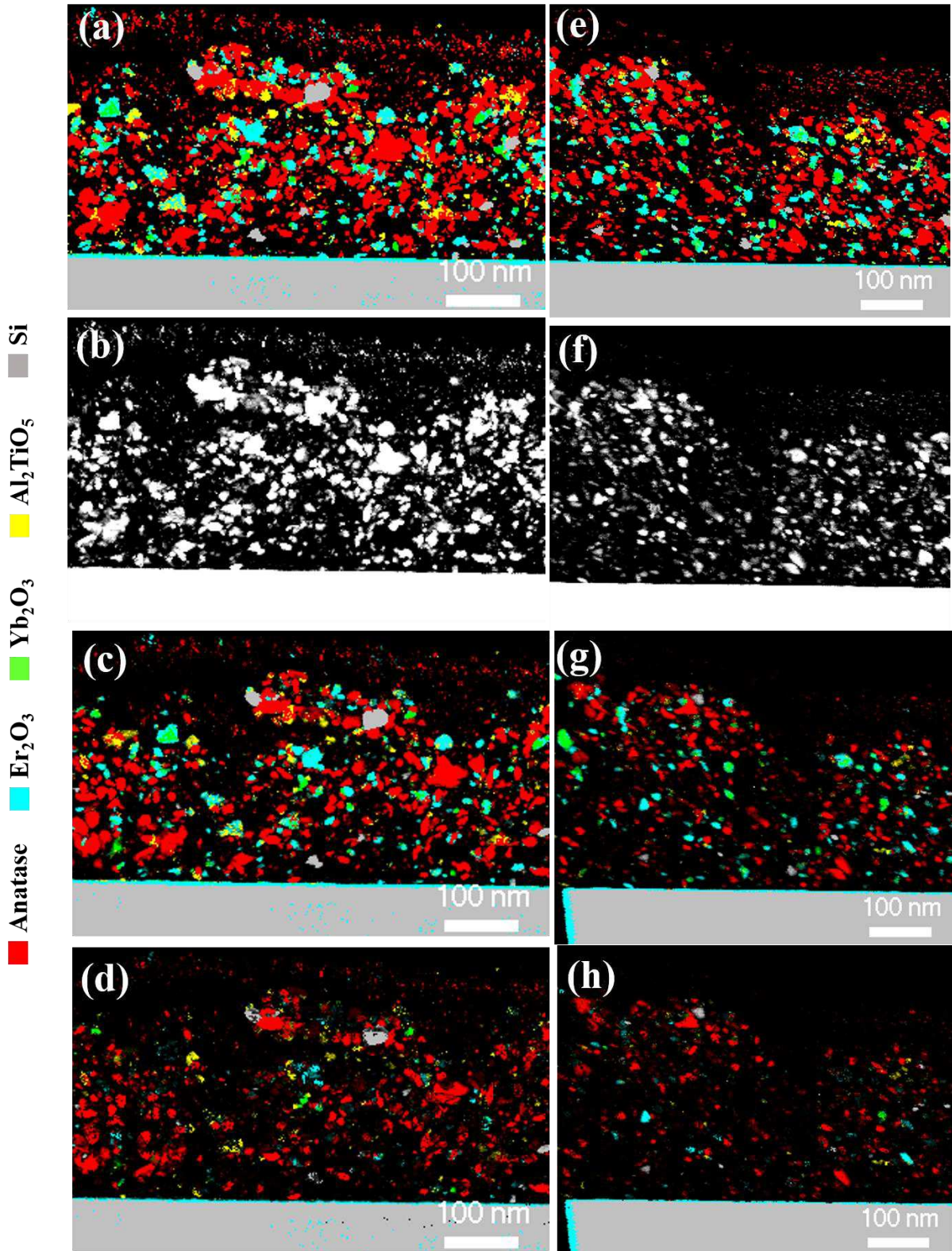


Figure IV.26: ACOM-TEM on the Np/ 62 exhibited on two different areas showing phase maps of anatase plotted with Er_2O_3 , Yb_2O_3 and Al_2TiO_5 respectively: (a, e) phase map, (b, f) the matching index, (c, g) combined phase-index maps and (d, h) combined phase-index-reliability.

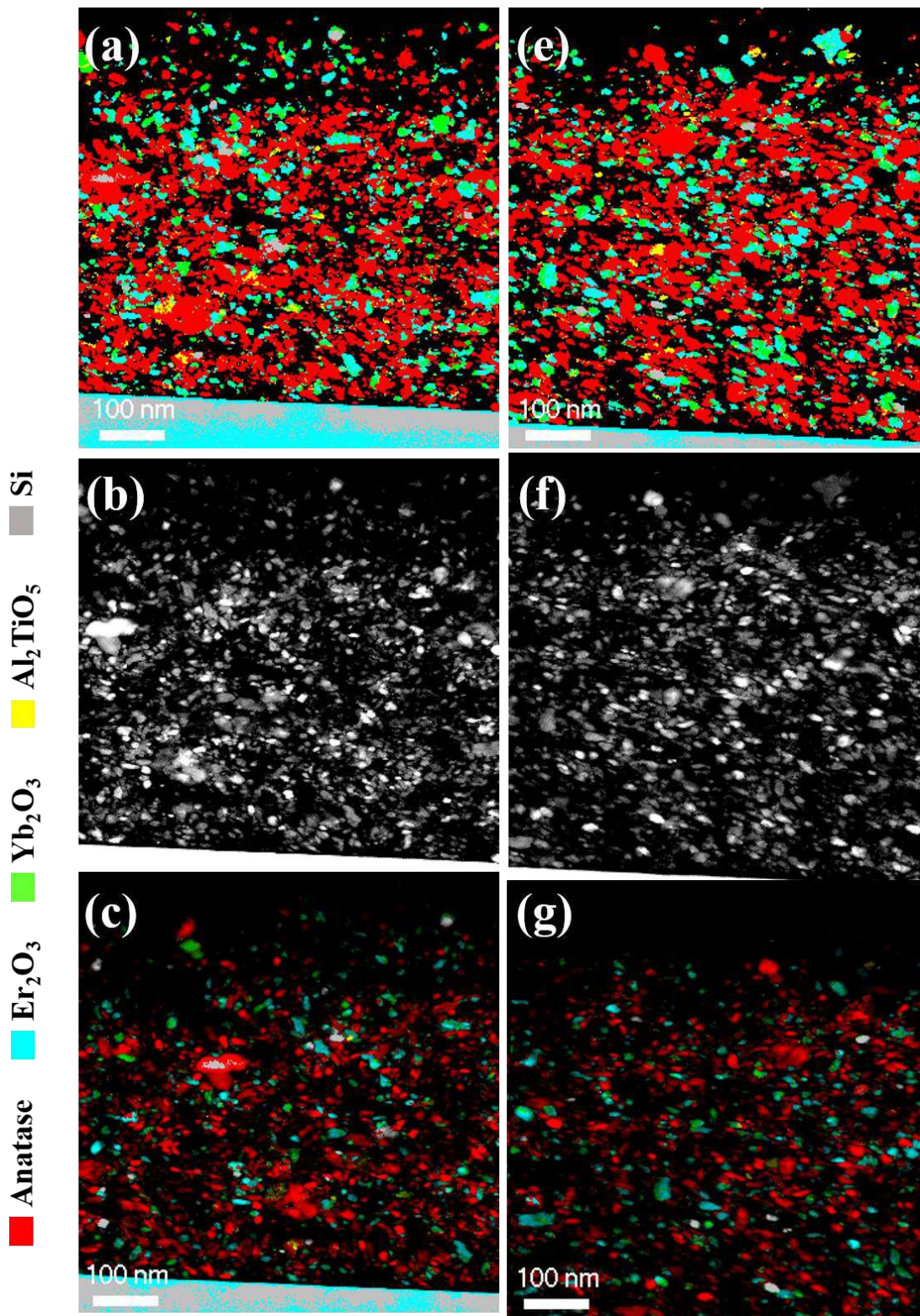


Figure IV.27: ACOM-TEM on the Np/ 620 exhibited on two different areas showing phase maps of anatase plotted with Er_2O_3 , Yb_2O_3 and Al_2TiO_5 respectively: (a, e) phase map, (b, f) the matching index, (c, g) combined phase-index maps and (d, h) combined phase-index-reliability.

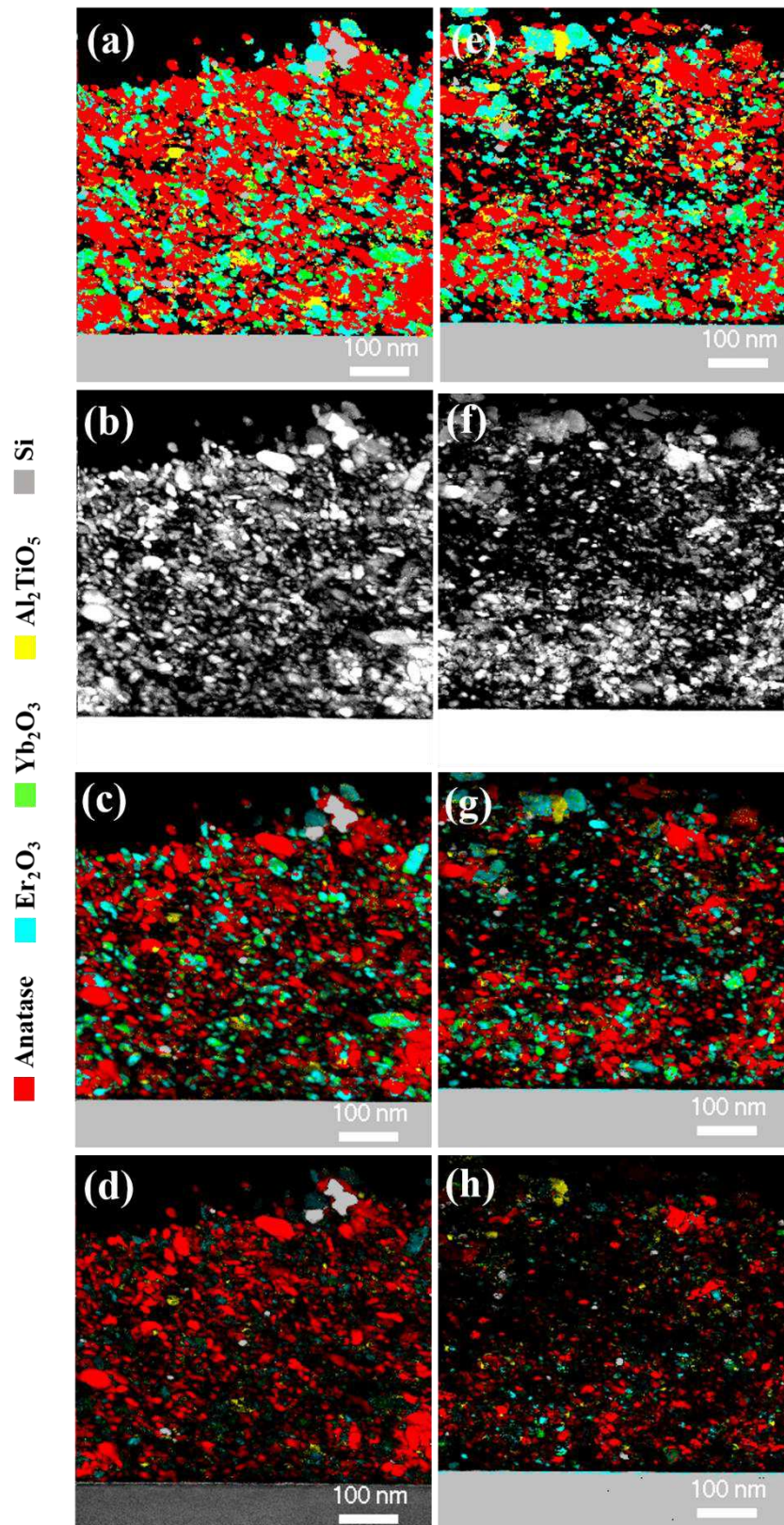


Figure IV.28: ACOM-TEM on the Np/ 620 + FGA exhibited on two different areas showing phase maps of anatase plotted with Er_2O_3 , Yb_2O_3 and Al_2TiO_5 respectively: (a, e) phase map, (b, f) the matching index, (c, g) combined phase-index maps and (d, h) combined phase-index-reliability.

The formation of Al_2TiO_5 , crystallizing in the orthorhombic system with the space group Cmcm and the following lattice parameters $a = 3.591\text{\AA}$, $b = 9.429\text{\AA}$ and $c = 9.636\text{\AA}$, may be explained by the substitution of Er^{3+} or Yb^{3+} sites by Al^{3+} in the TiO_2 lattice. Due to its smaller ionic radius (0.535\AA), Al^{3+} can be inserted into anatase. Here, we present a possible diffusion into the volume. For the codoped TiO_2 , as the dopants (Er^{3+} and Yb^{3+}) present a different charge than Ti^{4+} , oxygen vacancies can be created to compensate the missing charges. These defects can influence the diffusion rate. More vacancies makes it easier for ions to move [38]. The ability of diffusion of Al^{3+} interstitially in TiO_2 anatase have been reported in literature [39-43]. Usually, the Al_2TiO_5 formation occurs at high temperature of sintering ($>1200^\circ\text{C}$) of TiO_2 - Al_2O_3 . Its appearance at low temperature, as the present study (200°C), can be explained by the reactivity of the nano-scale material. Meanwhile, further investigation are required to understand the mechanism in details.

In this section, we prove the major presence of the anatase phase with minor secondary phases that could be identified as Al_2TiO_5 , Er_2O_3 and/ Yb_2O_3 in the Si/ codoped TiO_2 nanopowder/ALD- Al_2O_3 . We prove by using ACOM technique that these phases are formed during the ALD step despite the low thermal budget ($T = 200^\circ\text{C}$ - 4 hours) used in the present study. These secondary phases cannot be quantified due to their low amount and low crystallites size. A volume diffusion is suggested during this diffusion, and for the preferential sites that can be occupied by aluminum into codoped TiO_2 , theoretical calculations are required.

Chapter conclusion

This chapter investigates the optimization of spin-coating parameters influence on the deposition of codoped TiO_2 deposition on Si wafer with a minimum number of huge particles using DOE approach with the Hadamard matrix of order 4. It is demonstrated that increasing spinning time, speed and volume lead to decreasing number of huge particles on the surface of Si substrate. In addition, the luminescence has been optimized separately and 8 cycles of spin coating with a thickness between 650-750 nm are found to be sufficient to get a luminescence response similar to powder.

For the ALD part, different thicknesses of amorphous Al_2O_3 layer are deposited into the surface of codoped TiO_2 nanopowder spin-coated on n-type (100) Si wafer. The compositional analysis reveals that for the thicker layer of ALD- Al_2O_3 followed by FGA treatment, the improvement of the infiltration of Al and O elements in the porous film composed of codoped TiO_2 nanopowder is clearly observed. This infiltration can occur through the change in pores

distribution in the film after the densification and the increasing of the grain boundaries densities leading to the formation of composite. Deep investigation of the films structure by ACOM-TEM reveals the majority presence of anatase phase with other minority secondary phases ($\text{Al}_2\text{TiO}_5 + \text{Er/Yb}_2\text{O}_3$) resulting from the diffusion of Al^{3+} into the TiO_2 lattice by replacing Er^{3+} or Yb^{3+} sites. These results are promising with the increase of adhesion of nanopowder to the substrate. Therefore, the next chapter objectives are to investigate mechanical properties and upconversion luminescence efficiency of the different coated nanopowder based thin films.

References

- [1] J. Cloarec, C. Chevalier, J. Genest, “pH driven addressing of silicon nanowires onto pH driven addressing of silicon nanowires onto Si₃N₄/SiO₂ micro-patterned surfaces,” *Nanotechnology*, vol. 27, pp. 295–602, 2016.
- [2] N. B. Ghomrasni, C. Chivas-joly, L. Devoille, N. Feltin, “Challenges in sample preparation for measuring nanoparticles size by scanning electron microscopy from suspensions, powder form and complex media,” *Powder Technology*, vol. 359, pp. 226–237, 2019.
- [3] C. Pierre, “thesis-CHAPTER III: Spin coating and experimental design.”, 2011
- [4] R. Boichot et al., “Epitaxial growth of AlN on (0001) sapphire: Assessment of HVPE process by a design of experiments approach,” *Coatings*, vol. 7, pp. 136, 2017.
- [5] N. Stolze, C. Bader, C. Henning, J. Mastin, A. E. Holmes, A. L. Sutlief, “Automated image analysis with ImageJ of yeast colony forming units from cannabis flowers,” *Journal of Microbiological Methods*, vol. 164, 2019.
- [6] M. Đuriš, Z. Arsenijević, D. Jaćimovski, T. Kaluđerović Radoičić, “Optimal pixel resolution for sand particles size and shape analysis,” *Powder Technology*, vol. 302, pp. 177–186, 2016.
- [7] A. Rodriguez-Gómez, A. García-Valenzuela, E. Haro-Poniatowski, J. C. Alonso-Huitrón, “Effect of thickness on the photoluminescence of silicon quantum dots embedded in silicon nitride films,” *Journal of Applied Physics*, vol. 113, 2013.
- [8] N. Srinatha, P. Raghu, H. M. Mahesh, B. Angadi, “Spin-coated Al-doped ZnO thin films for optical applications: Structural, micro-structural, optical and luminescence studies,” *Journal of Alloys and Compounds*, vol. 722, pp. 888–895, 2017.
- [9] P. Malliga, J. Pandiarajan, N. Prithivikumaran, K. Neyvasagam, “Influence of Film Thickness on Structural and Optical Properties of Sol – Gel Spin Coated TiO₂ Thin Film,” *Journal of Applied Physics*, vol. 6, pp. 22–28, 2014.
- [10] C. B. Song, Y. L. Zhao, D. M. Sogn, L. Zhu, X. Q. Gu, and Y. H. Qiang, “Dye-sensitized solar cells based on TiO₂ nanotube/nanoparticle composite as photoanode and Cu₂SnSe₃ as counter electrode,” *International Journal of Electrochemical Science*, vol. 9, pp. 3158–3165, 2014.
- [11] S. N. Sadikin, M. Y. A. Rahman, A. A. Umar, and M. M. Salleh, “Effect of spin-coating cycle on the properties of TiO₂ thin film and performance of DSSC,” *International Journal of Electrochemical Science*, vol. 12, pp. 5529–5538, 2017.
- [12] H. S. Chin, L. S. Chao, and K. S. Kao, “Study of structural and optical properties of ZnO thin films produced by sol-gel methods,” *Sensors and Materials*, vol. 28, pp. 523–530, 2016.
- [13] S. Challagulla, K. Tarafder, R. Ganesan, S. Roy, “Structure sensitive photocatalytic reduction of nitroarenes over TiO₂,” *scientific reports*, vol. 7, p. 8783, 2017.
- [14] R. K. T. Appadurai, Chandrasekar M Subramaniam, B. S. Smagul Karazhanov, “Electrochemical Performance of Nitrogen-Doped TiO₂ Nanotubes as Electrode Material for Supercapacitor and Li-Ion Battery,” *molecules*, vol. 24, p. 2952, 2019.
- [15] R. T. Sataloff, M. M. Johns, K. M. Kost, “Signature of strong ferromagnetism and optical properties of Co doped TiO₂ nanoparticles” *Journal of applied physics*, vol. 110, p. 114322, 2011.
- [16] C. Stella, N. Soundararajan, K. Ramachandran, “Structural, optical, dielectric and magnetic properties of Mn_{1-x}CoxO₂ nanowires,” *Superlattices and Microstructures*, vol. 71, pp. 203–210, 2014.
- [17] E. Kifle et al., “Fs-laser-written erbium-doped double tungstate waveguide laser,” *Optics express*, vol. 26, p. 30826, 2018.

- [18] X. Luo et al., “photoluminescence blue shift of CdSe nanoparticles caused by exchange of surface capping layer,” *The journal of physical chemistry C*, vol. 115, pp. 20817–20823, 2011.
- [19] A. Pérez et al., “size dependent absolute quantum yields for size separated colloiddally stable silicon nanocrystals,” *American chemical society*, vol. 12, pp. 337–342, 2012.
- [20] Jose Rodríguez, J. G. C. Veinot, “Realization of sensitized erbium luminescence in Si–nanocrystal composites obtained from solution processable sol–gel derived materials,”
- [21] I. Brytavskiy et al., “Effect of porous silicon substrate on structural, mechanical and optical properties of MOCVD and ALD ruthenium oxide nanolayers,” *Applied Surface Science*, vol. 471, pp. 686–693, 2019.
- [22] O. Tiurin, N. Solomatin, M. Auinat, Y. Ein-Eli, “Atomic layer deposition (ALD) of lithium fluoride (LiF) protective film on Li-ion battery $\text{LiMn}_{1.5}\text{Ni}_{0.5}\text{O}_4$ cathode powder material,” *Journal of power sources*, vol. 448, p. 227373, 2020.
- [23] I. Iatsunskiy, M. K., M. Jancelewicz, K. Załęski, S. Jurga, V. Smyntyna, “Structural and XPS characterization of ALD Al_2O_3 coated porous silicon,” *Vaccum*, vol. 113, pp. 52–58, 2015.
- [24] T. Keuter, N. H. Menzler, G. Mauer, F. Vondahlen, R. Vaßen, H. P. Buchkremer, “Modeling precursor diffusion and reaction of atomic layer deposition in porous structures,” *Journal of vacuum science and technology A*, vol. 33, 2014.
- [25] J. Guo, H. van Bui, D. Valdesueiro, S. Yuan, B. Liang, and J. R. van Ommen, “Suppressing the photocatalytic activity of TiO_2 nanoparticles by extremely thin Al_2O_3 films grown by gas-phase deposition at ambient conditions,” *Nanomaterials*, vol. 8, 2018.
- [26] Y. Li, L. Ma, Y. Yoo, G. Wang, X. Zhang, M. J. Ko, “Atomic layer deposition: A versatile method to enhance TiO_2 nanoparticles interconnection of dye-sensitized solar cell at low temperature,” *Journal of Industrial and Engineering Chemistry*, vol. 73, pp. 351–356, 2019.
- [27] M. Knez, “Diffusion phenomena in atomic layer deposition,” *semiconductor science and technology*, vol. 27, pp. 074001, 2012.
- [28] RK. Konopka, M. Szafran, “Fabrication of Al_2O_3 -Al composites by infiltration method and their characteristic” *Journal of materials processing technology*, vol. 175, pp. 266-270, 2006.
- [29] I. Iatsunskiy, M. Kempinski, V. Smyntyna, “Structural and XPS characterization of ALD Al_2O_3 coated porous silicon,” *Vaccum*, vol. 113, pp. 52–58, 2015.
- [30] A-K. Mohamed, “Ceramics: sintering and microstructure”, TP sintering.
- [31] A. Atkinson, “Grain boundary diffusion-structural effects and mechanisms.” *Journal de physique*, 1985.
- [32] “Investigation of grain boundary self-diffusion at low temperature in polycrystalline aluminium by means of the dislocation spreading method” *Acta. Metall. Mater*, vol. 139, pp. 1953-1958, 1991.
- [33] I. ben Ammar, “synthèse par voie sol-gel et mise en suspension des nanoparticules dopées (Er-Yb) en vue d’application photovoltaïque” 2019.
- [34] B. J.A. Borrego Péreza et al., “Structural, optical, and photoluminescence properties of erbium doped TiO_2 films,” *Vacuum*, vol. 169, p. 108873, 2019.
- [35] S. Li et al., “Effective atomic interface engineering in $\text{Bi}_2\text{Te}_{2.7}\text{Se}_{0.3}$ thermoelectric material by atomic-layer-deposition approach” *Nano Energy*, vol. 49, pp. 257-266, 2018.

- [36] Y. Kumari, L. K. Jangir, A. Kumar, M. K. A, K. Awasthi, “Luminescent and structural behaviour of Tb^{3+} ions doped TiO_2 nanoparticles synthesized by facile sol-gel method,” *Physica B: Physics of Condensed Matter*, vol. 602, p. 412465, 2021.
- [37] Paweł Mazierskia et al., “On the excitation mechanism of visible responsible Er- TiO_2 system proved by experimental and theoretical investigations for boosting photocatalytic activity,” *Applied Surface Science*, vol. 527, p. 146815, 2020.
- [38] J. Zheng, X. Hu, Z. Ren, X. Xue, K. Chou, “Solid-state reaction studies in Al_2O_3 - TiO_2 system by diffusion couple method” *ISIJ International*, vol. 57, pp. 1762–1766, 2017.
- [39] B. Zhao et al., “The application of Al_2TiO_5 at the TiO_2 /perovskite interface to decrease carrier losses in solar cells,” *Journal of materials chemistry A*, vol. 5, pp. 3691-3698, 2017.
- [40] T. Koketsu et al., “Reversible magnesium and aluminum ions insertion in cation -deficient anatase TiO_2 ” *nature materials*, 2017.
- [41] S. Liu et al., “Aluminum storage behavior of anatase TiO_2 nanotube arrays in aqueous solution for aluminum ion batteries” *Energy and Environmental Science*, vol. 5, pp. 9743, 2012.
- [42] M. Sobhani, T. Ebadzadeh, M. R. Rahimipour “Formation and densification behavior of reaction sintered alumina–20 wt.% aluminium titanate nano-composites,” *International Journal of Refractory Metals and Hard Materials*, vol. 47, pp. 49-53, 2014.
- [43] M. Singh, I.M. Low, “Depth-profiling of phase composition and preferred orientation in a graded alumina/mullite/aluminium-titanate hybrid using X-ray and synchrotron radiation diffraction” *Materials Research Bulletin*, vol. 37, pp. 1279–1291, 2002.

Chapter V

Luminescence and mechanical properties of the coated nanopowder based thin films

Introduction

In this chapter, the codoped TiO₂ nanopowder is firstly dispersed on a n-type (100) silicon substrate. Then, it is coated with amorphous Al₂O₃ using atomic layer deposition technique (ALD) followed by FGA treatment at 430°C for 30 min as the optimized conditions for ALD-Al₂O₃ passivation layer based on literature as an effective way to activate the passivation layer. Understanding the impact of different ALD-Al₂O₃ thicknesses and FGA step on the UC luminescence (in terms of strong response) and mechanical (best adhesion and hardness) and properties of the codoped TiO₂ nanopowder assembled on n-type Si (100) substrate is conducted. For that purpose, various analysis approaches including photoluminescence, high-resolution TEM (HR-TEM), scratch test and nanoindentation are performed to understand the role of the final structure on the luminescent and mechanical properties.

I. UC luminescence study

The UC luminescence properties of the uncoated and coated codoped TiO₂ nanopowder are studied in order to understand the influence of ALD-Al₂O₃ coating thickness and post heat treatment, which are necessary steps towards the improvement of the efficiency of Si based solar cells.

Figure V.1a displays the UC luminescence spectra at room temperature under 980 nm excitation of the codoped TiO₂ nanopowder on powder phase, Np, Np/ 62, Np/62+FGA, Np/620 and Np/620+FGA (see **Table IV.4 - chapter IV**). It should be noted that the recorded spectra of the different films (uncoated and coated) are conducted after 6 months of their fabrication. Before measurements are performed, calcination on a hotplate at 200°C for 1 min, is conducted in order to evaporate the adsorbed H₂O molecules on surface. The powder phase spectra is recorded only after one month of being synthesized due the non-availability of spectrophotometer (collaboration with physics department, Faculty of sciences of Sfax). So, the presented comparison in this section can further prove the durability of UC luminescence. In addition the acquisition PL response for Np and Np/62+FGA films is not completed until the IR region due to the technical problem.

It can be seen that the same UC emissions regions for the all the samples are observed proving that the basic optical behavior of the material has not been changed by the coating and FGA treatment. Three emission regions can be distinguished. The emissions centered at 544 nm (green region), 584 nm (green region), 620-686 nm (red region) are originated from ${}^2\text{H}_{11/2} \rightarrow {}^4\text{I}_{15/2}$, ${}^4\text{S}_{3/2} \rightarrow {}^4\text{I}_{15/2}$ and ${}^4\text{F}_{9/2} \rightarrow {}^4\text{I}_{15/2}$ transitions, respectively as have already been reported by

many studies [1-2]. In addition, the NIR emission band centered at 840 nm can probably be originated from $^4I_{9/2} \rightarrow ^4I_{13/2}$ transitions [3-4]. The presence of f-f transitions of Er^{3+} and the strong absorption of Yb^{3+} ($^4F_{7/2} + h\nu_{980nm} \rightarrow ^4F_{5/2}$) sustains the effective incorporation of the lanthanide dopants into TiO_2 lattice.

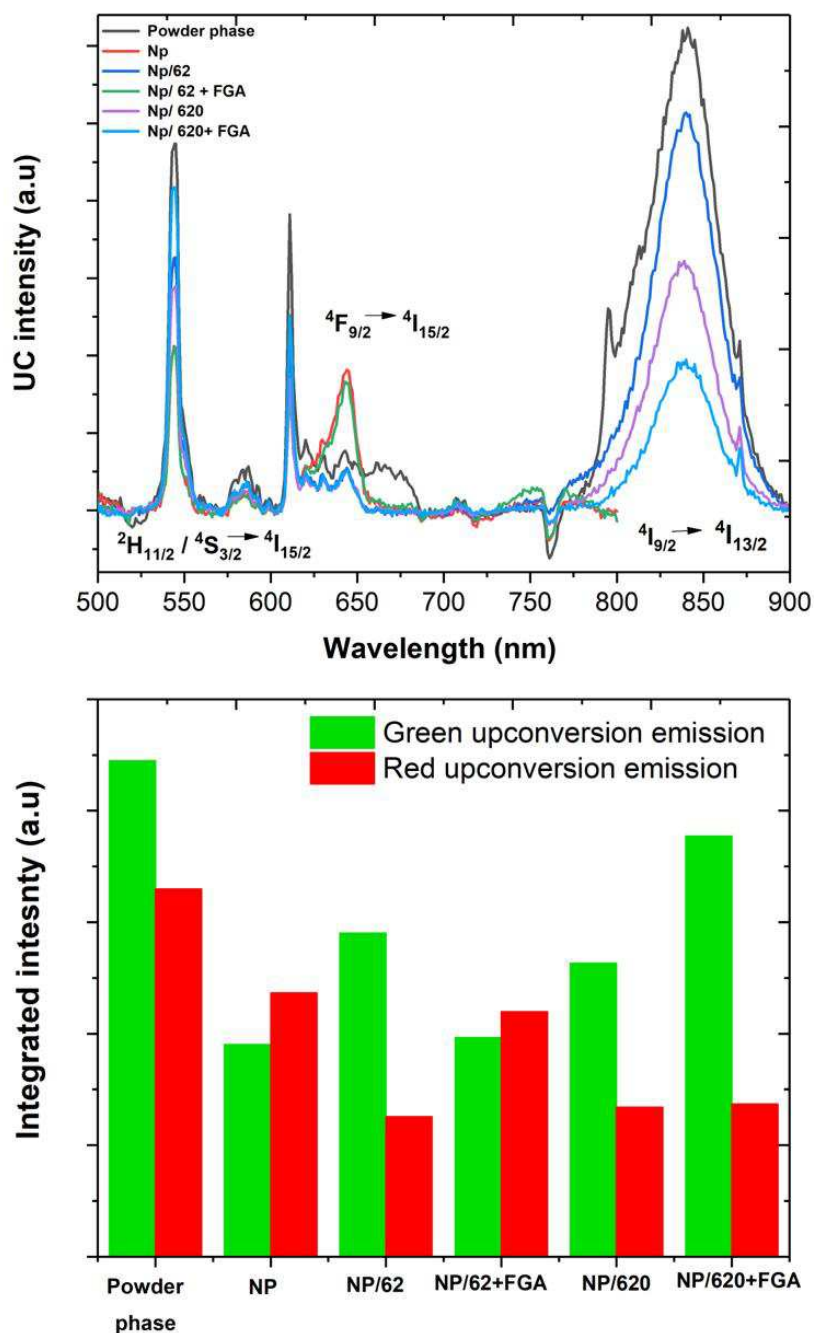


Figure V.1: UC luminescence spectra and histogram from the integrated intensities from powder phase to coated nanopowder based films.

The proposed mechanism of UC emission have been widely discussed previously in the literature and it is originated from two-photon UC process (**Figure V.2**): The ${}^2F_{5/2}$ (Yb^{3+}) and ${}^4I_{11/2}$ (Er^{3+}) levels are in energetic resonance. Since the absorption cross-section of the ${}^2F_{7/2} \rightarrow {}^2F_{5/2}$ transition of Yb^{3+} ion, corresponding to IR absorption at 980 nm, is much larger than that of the ${}^4I_{15/2} \rightarrow {}^4I_{11/2}$ transition of Er^{3+} ion, the ETU mechanism is the most dominant process. Therefore, upon 980 nm laser excitation, Yb^{3+} ions can efficiently transfer their energy to Er^{3+} populating the ${}^4I_{11/2}$ excited state of neighboring Er^{3+} and then relax to the ground state ${}^2F_{7/2}$. Then the Er^{3+} ion populated in ${}^4I_{11/2}$ captured the photon from second surrounding Yb^{3+} ion and jumped to ${}^4F_{7/2}$ higher energy level through ESA. However, due to the short life time of the ${}^4F_{7/2}$ level in Er^{3+} , non-radiative multiphonon process to the lower ${}^2H_{11/2}$ and ${}^4S_{3/2}$ levels takes place due to the small energy distance between them. Then a relaxation of the populated levels to the ground state ${}^4I_{15/2}$, resulting in the green emission.

The observed red emission is generated from non-radiative relaxation from the ${}^4S_{3/2}$ to ${}^4F_{9/2}$ level and cross relaxation process (CR): $(\text{Er}^{3+}) {}^4F_{7/2} + (\text{Er}^{3+}) {}^4I_{11/2} \rightarrow (\text{Er}^{3+}) {}^4F_{9/2}$. The powerful NIR emission (840 nm) is produced by non-radiative transition of ${}^4F_{9/2}$ (Er^{3+}) \rightarrow ${}^4I_{9/2}$ (Er^{3+}). The intensity of the red emission is lower than that in green. It can be explained by the weak absorption cross relaxation [5-6]. No apparent modification on peak positions (similar emission bands) after the deposition, coating and post heat treatment steps can be observed except increment in their intensities, which suggests that that the mechanism is not changed.

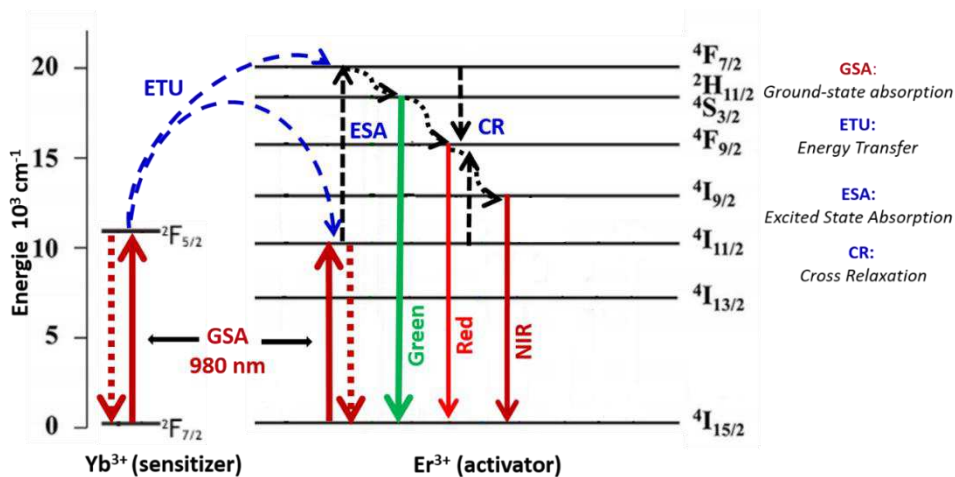


Figure V.2: Schematic energy level diagram of Er^{3+} and Yb^{3+} showing the possible mechanism.

Meanwhile, the change in intensity from powder phase to deposited and coated films could be related to the change of the environment when particles are connected to n-type (100) Si surface. In addition, the amount of particles deposited on the surface of silicon substrate that lead to layer with 650-750 nm thick with porosity is not the same as a compact pellet (powder phase).

Moreover, the change observed in the red emission profile can be related to surface defect assigned to OH group presence on the surface of nanopowder. It is a well-known fact that with substitution of Ti^{4+} with trivalent Lanthanide, the most probable defect generated is the oxygen vacancy to compensate for the introduced negative charges. Oxygen vacancies in the surface are shown to dissociate H_2O through the transfer of one proton to a nearby oxygen atom, forming two hydroxyl groups for every vacancy. Due to the small size of the nanocrystalline host, a large portion of the dopant ions are typically exposed to the surroundings. Therefore, OH group quenches the luminescence of lanthanide-doped nanocrystals as a consequence of high energy vibrational modes of OH-group ($3200\text{--}3600\text{ cm}^{-1}$) that lead to the increase of non-radiative relaxation of the excited states.

For Er^{3+} doped materials, the OH-groups quench the luminescence of Er^{3+} ions by facilitating non radiative multiphonon relaxation of the ${}^4\text{I}_{11/2} \rightarrow {}^4\text{I}_{13/2}$ and ${}^2\text{H}_{11/2}/{}^4\text{S}_{3/2} \rightarrow {}^4\text{F}_{9/2}$ transitions. Both relaxation pathways favor the population of the ${}^4\text{F}_{9/2}$ state from which the red emission occurs at the expense of the green luminescence. In addition, the absorption of 980 nm excitation light by Yb^{3+} overlaps with the absorption band of water, which can also lead to the decrease of luminescence intensity. Therefore, it can be concluded that codoped TiO_2 nanopowder is not very stable because of the large sensitive surface area that causes the degradation of UC luminescence.

The intensity of UC luminescence bands (green, red and NIR) show significant difference when comparing the uncoated (Np) and coated films: Np/62 and Np/620 (**Figure V.1 a**). The intensity increases with increasing ALD- Al_2O_3 cycle numbers up to 62 cycles. Then, for 620 cycles, the intensity slightly decreases (green by 9%, red by 1% and NIR by 32%) compared to Np/62 film but it still much higher than the uncoated film (Np). The increasing when applying ALD- Al_2O_3 layer on nanoparticles based thin films suggesting a positive effect of ALD- Al_2O_3 on UC luminescence as a consequence of the improved absorption of NIR photons. It can be explained by the reduction of the number of surface defects assigned to OH group. TMA precursor reacts readily with the surface hydroxyl species on during the first cycle of ALD process [7] and then the layer deposited act as a barrier preventing the nanopowder surface from the surrounding environment which lead to the observed enhancement as illustrated in **Figure V.3**. This isolation behavior from the environment improve immediately the optical performance stability of the particles. Wang et al. [8] demonstrate that by covering the $\text{NaGdF}_4:\text{Yb}^{3+}, \text{Tm}^{3+}$ core with a thin inactive NaGdF_4 shell, the quenching effect related to water largely decreased compared with the core material. It is also reported that the emission intensity of 10 nm UC nanoparticles

could be increased by 450 times upon coating a thin surface protection layer [9]. Other report mentions that even an ALD- Al_2O_3 film with a thickness of only 5 nm on a SiN film with a thickness of 100 nm reduced the water vapor transmission rate from 710^{-3} to 510^{-5} g/m^2 day at 38 °C and relative humidity 85% [10].

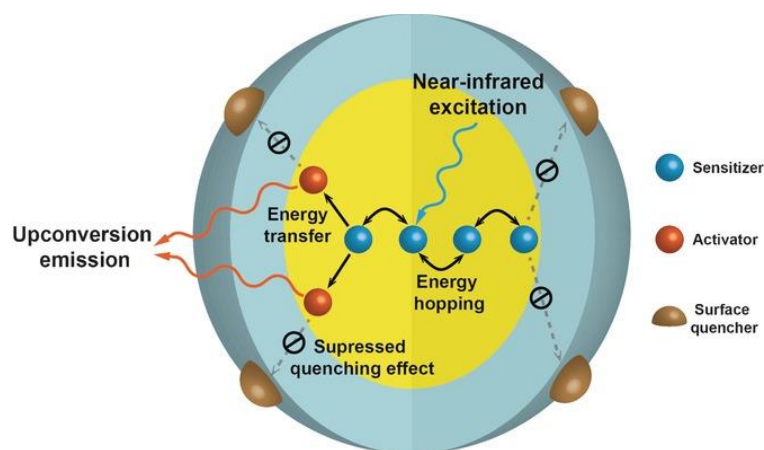


Figure V.3: Protection behavior of the coating of luminescent nanoparticles from OH group to insure better luminescence response as reported in [11].

When the cycle numbers went to 620, the incident illumination and the emitted light can be slightly obstructed by the over protective covering, thus the intensity of UC emissions decreased. 62 and 620 cycles have the same emission profile in the red, which shows that for Np film the high intensity of the red emission can be surely linked to OH group on the surface of the film. Similar observation is provided by and Zhou co-workers [12] which demonstrates that increasing the thickness of ALD- Al_2O_3 when increasing the cycle numbers from 15 to 40 cycles light absorption as well as light emission are decreased as high amount of Al_2O_3 . ALD- Al_2O_3 coating found to hamper the light absorption as well as the light emission.

Another possible explanation related to the enhancement of UC luminescence after the deposition of ALD- Al_2O_3 can be assigned to the surrounding coordination environment around Er^{3+} ions. Tailoring the local crystal field around lanthanide is an effective approach to modify the UC luminescence. In this study, the distortion of the host environment around Er^{3+} occupies sites belonging to Ti^{4+} , replacing Ti^{4+} by small trivalent aluminium Al^{3+} (0.535 Å) could strength the emission efficiency due to asymmetric field around the lanthanide ion [13]. Both local symmetry and the phonon energies influence the radiative and non-radiative processes which changes the emission intensity. Xu and co-workers [14] show an improvement of green emissions from $\text{CaWO}_4: \text{Er}^{3+}\text{-Yb}^{3+}$ by introducing Cr^{3+} ions as a result of the distortion of

crystal structure. The distortion lead to lower symmetry around Er^{3+} which improve the 4f-4f transitions.

Therefore, ALD- Al_2O_3 layer can benefit the luminescence properties, but a too thick coating will slightly decrease the UC luminescence. It should be pointed that the formation of secondary phases as previously discussed in **chapter IV** according to ACOM-TEM results, can not have a drastic influence on the improvement of UC luminescence due to the low amount of these phases that could not be detected by XRD or quantified by ACOM-TEM. Otherwise, concerning these phases, Al_2TiO_5 will not have influence on the UC properties because it absorb in UV region (under 400 nm). For Yb_2O_3 , it absorbs and emits at 980 nm, the emitted photons can probably be reabsorbed after that by codoped TiO_2 or even by Er_2O_3 . For Er_2O_3 , the Er^{3+} ion alone can achieve luminescence without the requirement of a sensitizer that means no ETU process is presented (weak efficiency compared to when using a sensitizer) [15]. The energy of the 980 nm matches the absorption energy level between $^4\text{I}_{15/2}$ ground state and $^4\text{I}_{11/2}$ excitation state of Er^{3+} . Under 980 nm pumping laser, the $^4\text{I}_{15/2}$ electrons of Er^{3+} at ground state are excited onto $^4\text{F}_{7/2}$ excitation state through a resonant energy transfer process: $2 ^4\text{I}_{11/2} \rightarrow ^4\text{F}_{7/2} + ^4\text{I}_{15/2}$. $^4\text{F}_{7/2}$ level decay onto $^2\text{H}_{11/2}$ and $^4\text{S}_{3/2}$ and then from $^4\text{S}_{3/2}$ to $^4\text{S}_{9/2}$ level via the nonradioactive relaxation, and then fall back to $^4\text{I}_{15/2}$ ground state to result in green and red emissions.

It is worth highlighting that the step of annealing is highly required for the activation of ALD- Al_2O_3 layer for the improvement of electrical properties as detailed in **chapter I**. After FGA, it can be clearly seen that UC luminescence of Np/62+FGA and Np/620+FGA decreases when compared to Np/62 and Np/620 respectively. It is reported that under hydrogen treatment H atoms can interact with lattice oxygen of TiO_2 presented on the surface. In fact, for temperature range from 300°C up to 450°C (FGA= 430°C), it is demonstrated that the formation of Ti^{3+} defects as the electrons of the H atoms are transferred to the Ti^{4+} . In addition, electrons are transferred from hydrogen to the oxygen atoms in the lattice of TiO_2 . Then, the lattice oxygen is abstracted from the surface by which the O atom leaves with the H atom to form H_2O [16]. The generation of oxygen vacancies that can be formed adjacently to lanthanides ions can cause the reduction of Er^{3+} to Er^{2+} which change the emission peaks [17]. Furthermore, as water molecule vibration is a luminescence quencher it can be the cause of the decrease in UC intensities of the different bands for 62 and 620 cycles upon FGA [18]. For the thinner film of ALD- Al_2O_3 (Np/62), the H atom and H_2O (formed by dehydroxylation from the aluminol groups Al-OH, as previously explained in **chapter I**) can diffuse through the thin Al_2O_3 layer

(19-21 nm) to the interface to react immediately with TiO_2 [19]. Whereas, using thicker layer of Al_2O_3 (100-125 nm), release of H atoms and H_2O also occurs but this thick layer practically prevent their diffusion to the interface of the Al_2O_3 with codoped TiO_2 nanopowder. H_2O located in the ALD- Al_2O_3 layer can absorb the excitation wavelength photons leading to the decrease of the number of photons that could be absorbed by Yb^{3+} ions. Interestingly, for Np/620+FGA, the red and NIR are weakened while the green emission peak intensity is drastically enhanced by about 98% compared to Np film.

Same observation is reported elsewhere with the increasing of annealing temperature of the nanopowder, which is explained by the change in the crystalline field at the optical centers [20]. In this study, this change is caused by the intrinsic point defects within the electronic band gap generated in Al_2O_3 layer during ALD process. As reported in [21-25], amorphous Al_2O_3 layer grown by ALD process contains: interstitial oxygen (O_i)/aluminium (Al_i), vacancies of oxygen (V_O)/aluminium (V_Al), and also interstitial hydrogen (H_i) point defects, that occupied energy levels in the band gap amorphous Al_2O_3 . After annealing of the layer, it is assumed that interstitial oxygen (O_i) and aluminium vacancies (V_Al) are predominantly presented, which cause the negative charging of amorphous Al_2O_3 film used for the passivation of Si solar cells. Their energy levels are located near to the valence band. So, the underlying reason for UC enhancement may be caused from these defects. As shown **Figure V.4 a**, Al_2O_3 layer is fully coated around the particles and diffused along the whole film. The defects present in this layer will make from this latter an absorption center that ensure an additional energy transfer to Er^{3+} ions after being excited with 980 nm (**Figure V.4 b**). Subsequently, UC nanopowder emitted an intense green emission after a combination of a direct (from Yb^{3+}) and indirect (from Al_2O_3) excitation.

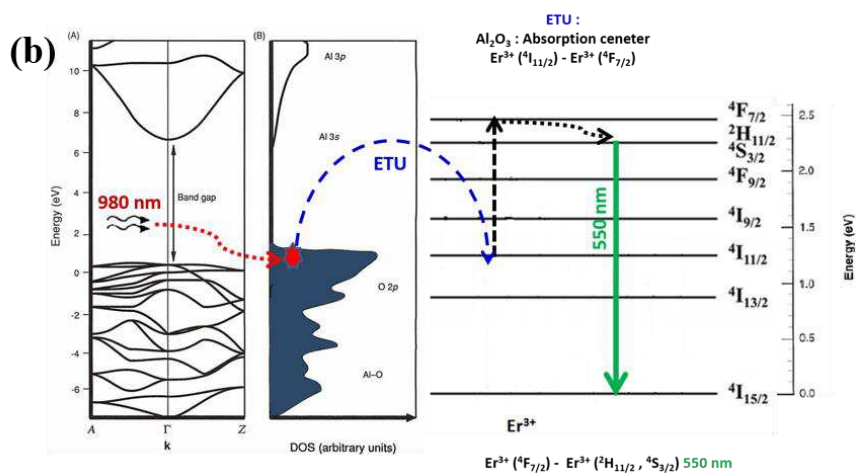
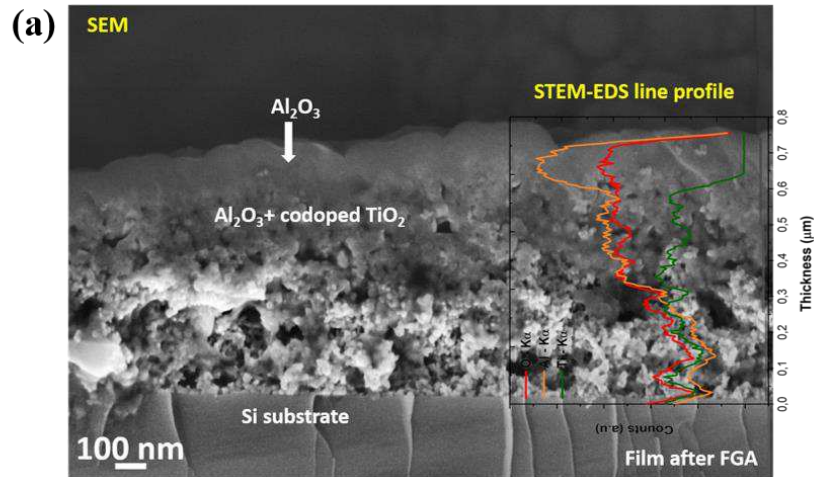


Figure V.4: (a) SEM image of Np/620 +FGA combined with line profile graph for Al and O elements presence along the film and (b) The probably mechanism for the indirect excitation of Er³⁺ ions by ALD-Al₂O₃ layer.

This section reveals the effective maintaining of UC phenomenon during the proposed procedure when passing from powder phase to deposited nanopowder on Si substrate and after that when coated with ALD layer followed by FGA treatment. Selective enhancement of UC luminescence can be ensured by applying ALD-Al₂O₃ layer and annealing treatment. Increasing the thickness layer with increasing the cycle numbers of ALD-Al₂O₃ up to 620 with further annealing in forming gas could strength the green UC emission.

II. Mechanical properties

II.1. Adhesion measurements

Depending on the application, the film can be exposed to different external environmental factors that may damage its surface, which can result in the decrease of the device efficiency. For this reason, a practical coating must be adherent and able to resist to corrosive environment. Among different studied ALD materials (TiO_2 , Al_2O_3 , SiO_2 and ZnO), Al_2O_3 provides the best mechanical reinforcement. Here we investigate the effect of ALD coating and thermal treatment on adhesion of the coated nanopowder based films.

Scratch testing is probably the most popular and widely used test for assessing coating-substrate adhesion properties. The scratch adhesion test is frequently viewed as a simple way of introducing a quantity of mechanical energy sufficient to detach the coating from the substrate. Scratch test are performed on a Micro Combi Tester (MCT³, Anton Paar). Here, all sensor signals (friction force, penetration depth and acoustic emission) are given with the whole scratch image in focus. Thus, the critical loads (see next paragraph) are identified by observing the synchronized optical and signal recording. During our tests, a continuously increasing load is applied on the coating surface with a diamond indenter (Rockwell of radius 100 μm) and drawn across the surface of the samples (4 mm) under a progressive mode. The reproducibility of the above scratch test is confirmed by testing several times, 10 scratch tests are done on each sample, with adjacent tracks separated by 200 μm . There is a pre-scan, which measure a topographic profile of the sample surface before the scratch test measurement. No post-scan step is performed. To compare the adhesion behavior of samples at the same scratching conditions, a scratch test with a load is progressively increased from 10 mN to reach 10 N with speed 1000 mN/s and approach speed of 0.05 mm/s.

Choice of indicators: In order to compare samples, two indicators (named in the following Lc1 and Lc 2) corresponding to two possible critical loads are chosen for each samples based on the analysis of the scratch damage features. Generally, the Lc for surface coatings is defined according to the crack generation and delamination criteria as described in [26]. Lc1 and Lc2 are defined as the failure occurring in the coating and the silicon substrate, respectively. Lc1 is adapted for each samples since the failure mode can be different for each samples (for films attribution see **Table IV.2 - chapter IV**):

- For Np film, the failure point Lc1 is designated as the Si substrate exposure by the detachment of the film composed of nanopowder from the substrate. No failure is found in the substrate due to the low normal force applied to the sample (30 mN).
- For 62 and 620 films, Lc1 is considered as continuous cracking until the fracture (Lc2) (**Figure V.6 a** and **Figure V.6 b**).
- For Np/62 and Np/62+FGA films, Lc1 is assigned to continuous delamination until the fracture (Lc2) (**Figure V.6 c** and **Figure V.8 a**).
- For Np/620 and Np/620+FGA films, the failure is attributed to continuous Si exposure (Lc1) until the fracture (Lc2) (**Figure V.6 d** and **Figure V.8 b**).

The presented values of Lc1 and Lc2 are the average of the 10 scratch tests performed.

Results: Without any ALD coating (**Figure V.5**) a sudden opening of a large flat at the bottom groove occurs at $18 \text{ mN} \pm 0.82$ and $1.62 \pm 0.17 \text{ mm}$. It indicates a complete detachment of the film from the substrate. This film show a mechanical fragility due to the weak cohesive strength between particles and the weak adhesion of nanopowder thin film to the substrate.

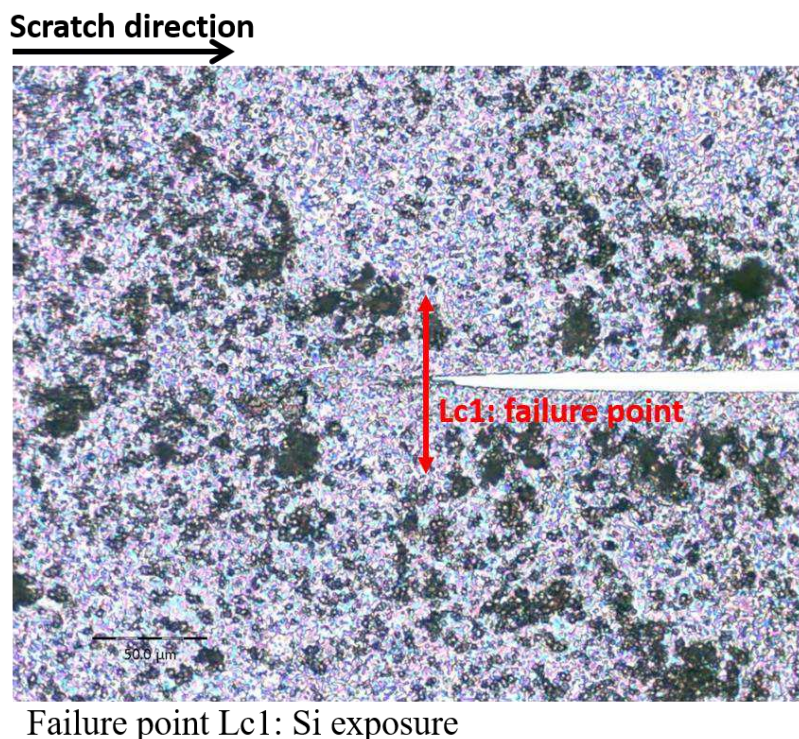


Figure V.5: Optical images of the resulting scratch channel after the test being applied on Np.

We first studied the influence of ALD- Al_2O_3 layer thickness on the adhesion properties of the film. A drastic increase of L_c1 is observed when passing from Np to coated nanopowder based films (**Figure V.9**). With only 62 cycles of ALD- Al_2O_3 the critical failure, L_c1 is 300 times higher (from 18 mN to 6 N). Interestingly, the critical loads L_c1 and L_c2 for coated nanopowder based films are of the same order of magnitude or even higher than those for the pure ALD- Al_2O_3 films. It possibly indicates that the critical loads are limited by the cohesion in the alumina itself and not at the interface between Al_2O_3 and TiO_2 nanoparticles, suggesting a strong interfacial bonding between nanoparticles and the alumina matrix. Increasing the thickness of ALD coating does not significantly increase the appearance of the critical failures. L_c1 and L_c2 slightly increase (respectively 19% and 4%). This behaviour is also visible on 62 and 620 samples (without nanoparticles) where only a 6 % and 4% increasing is respectively obtained for L_c1 and L_c2 . From our observations, it can be concluded that even a thin layer of ALD- Al_2O_3 can improve significantly the adhesion of nanopowder to substrate. The improvement of mechanical stability with few ALD cycles has also been observed by Riley et al. [27] in the case of nano- MoO_3 electrode composites. Also, since the higher the normal force to appear the first failure point (L_c1), the better adhesion of the film to substrate, which mean that the thicker untreated film protect better the Si substrate.

Then, the influence of the post heat treatment step of ALD- Al_2O_3 layer of the same thickness on the adhesion properties of the film is studied. From **Figure V.9**, it can be observed that L_c1 increases slightly by 4% and much higher by 18% with a shift to high position in L_c1 appearance for Np/62 and Np/620, respectively after FGA treatment. This reveals the positive impact of heat treatment on the adhesion properties. For L_c2 , it seems to always decrease after the application of FGA treatment. It appears that for Np/620 film before and after the FGA treatment, the fracture is not always achieved, which demonstrate the protection of Si substrate by the coated nanopowder based thin film as shown in **Figure V.7**.

Figure V.10 depicts the F_t at L_c1 for every film (62 and 620 cycles) before and after FGA treatment. For 620 cycles, it is normal that the F_t decreases while the F_n increases. What can be compared is L_c1 of 62 cycles because they have almost the same F_n . It is observed that after annealing F_t decreases, which means that the sliding movement is reduced. This is related to the increase in the density, bending strength as the number of pores decreased and densification of the coated nanoparticles based films took place [28].

In conclusion, it is clearly demonstrated that both annealing treatment and thicker layer of ALD- Al_2O_3 coating resulted in a substantial enhancement of the adhesion properties of nanopowder based thin films. The films can be classified as follows depending on their adhesion: Np/ 620 + FGA > Np/ 620 > Np/ 62 + FGA > Np/ 62 > Np.

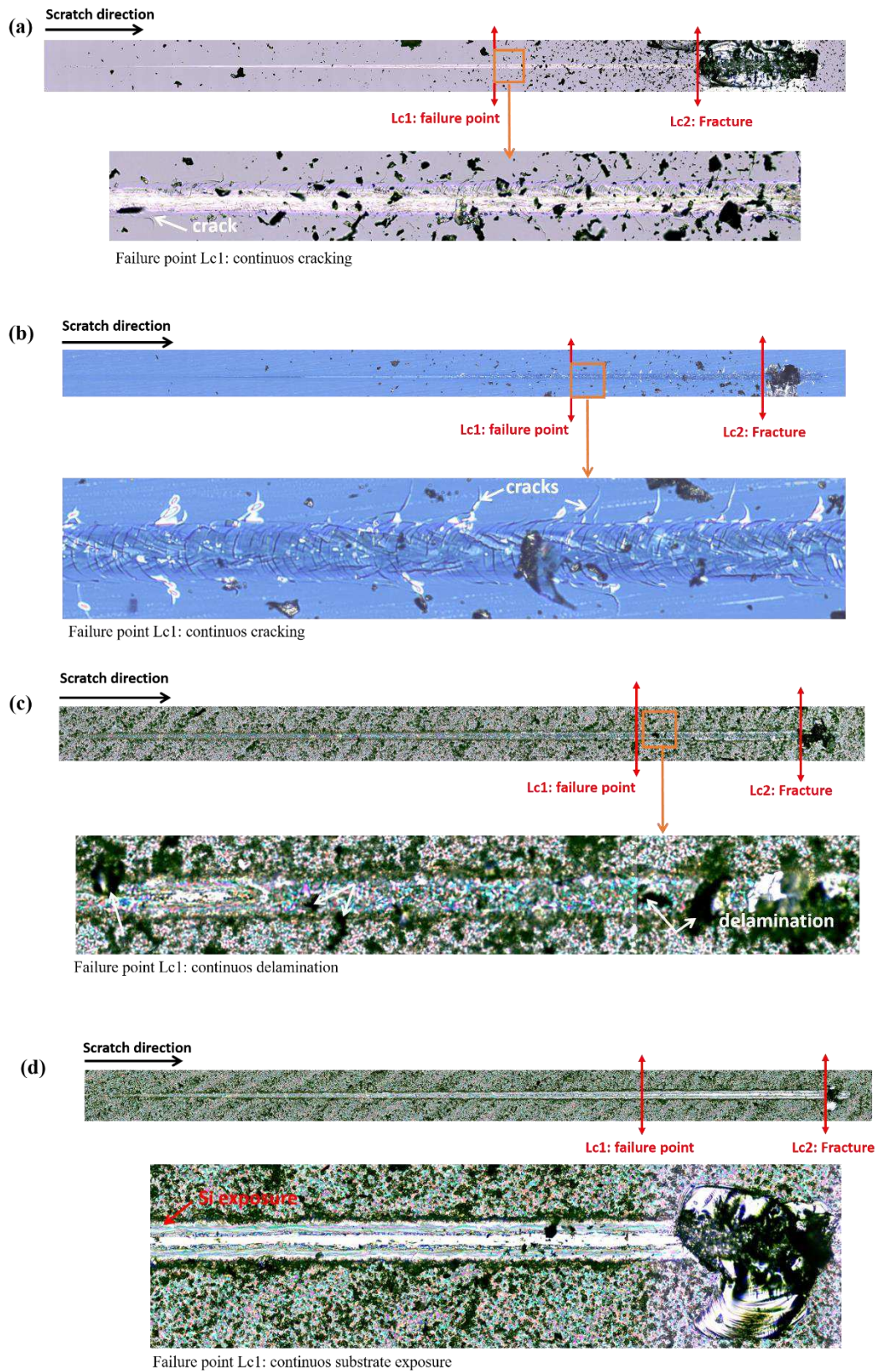


Figure V.6: Optical images of the resulting scratch channel after the test being applied on (a) 62, (b) 620, (c) Np / 62 and (d) Np/ 620.

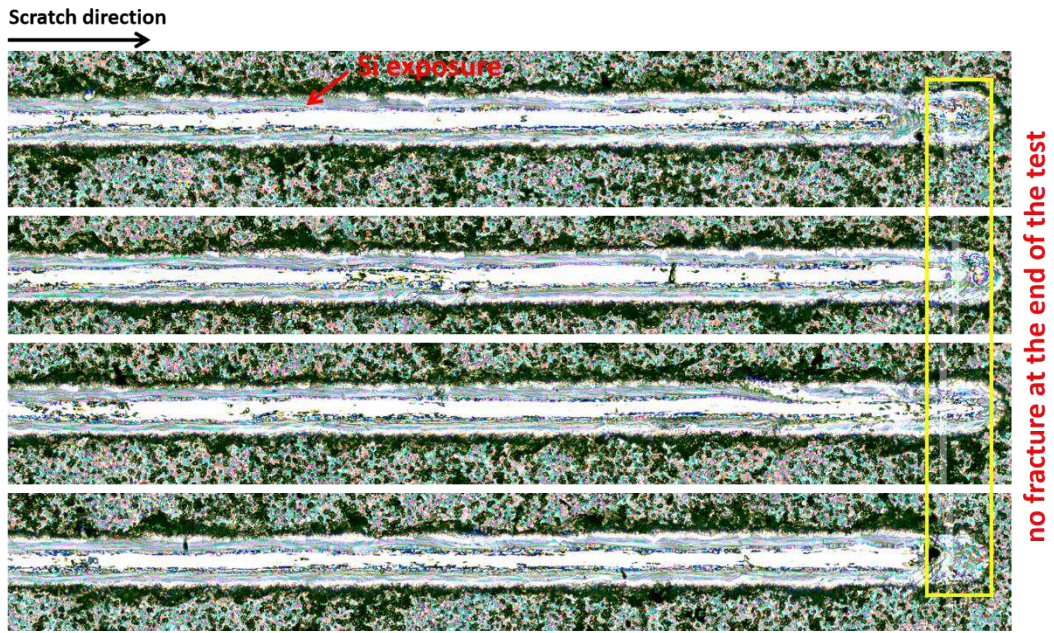


Figure V.7: Optical images of the resulting scratch channel after the test being applied Np/620+FGA.

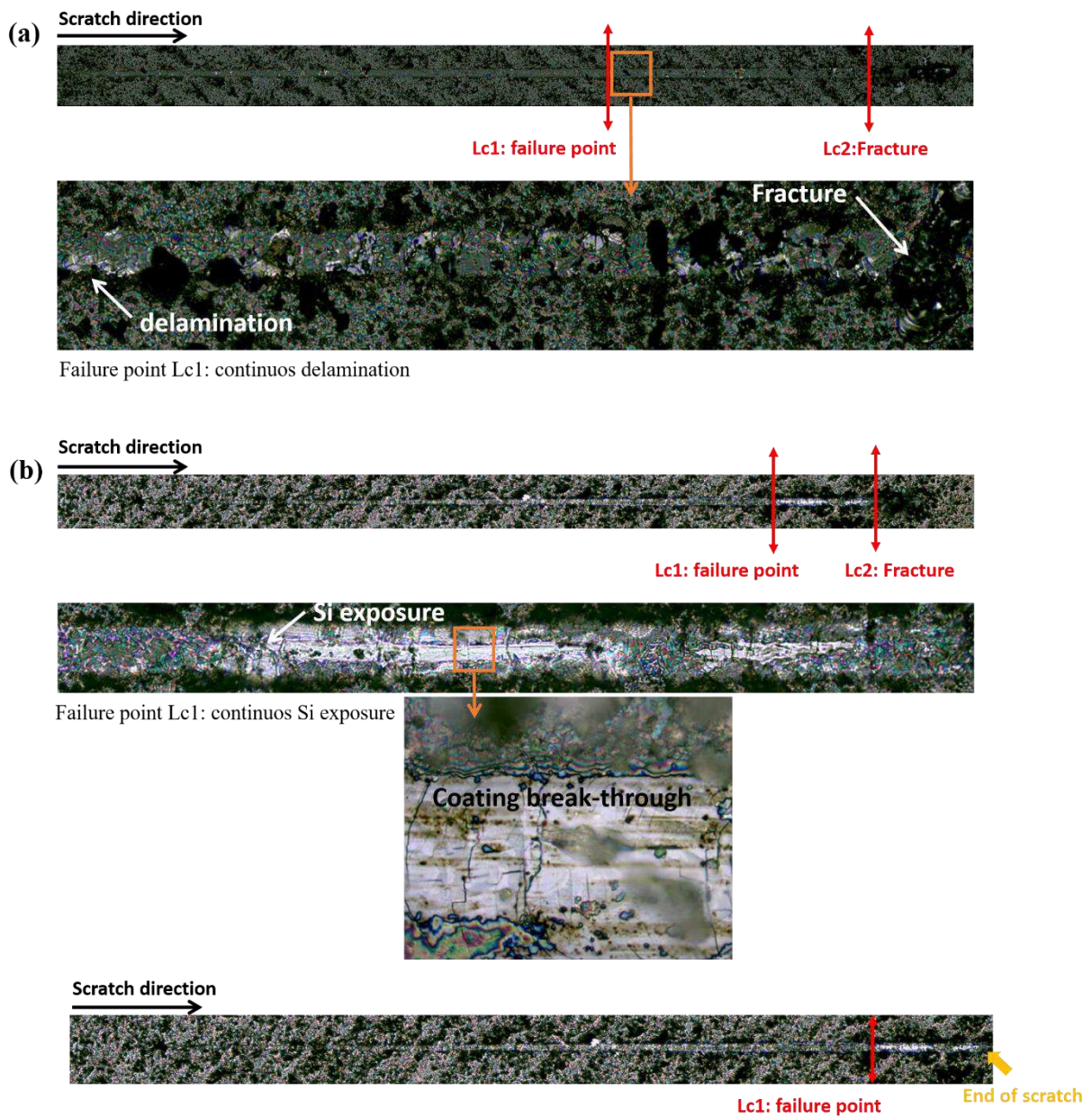


Figure V.8: Optical images of the resulting scratch channel after the test being applied on (a) Np /62 +FGA and (b) Np/620+FGA.

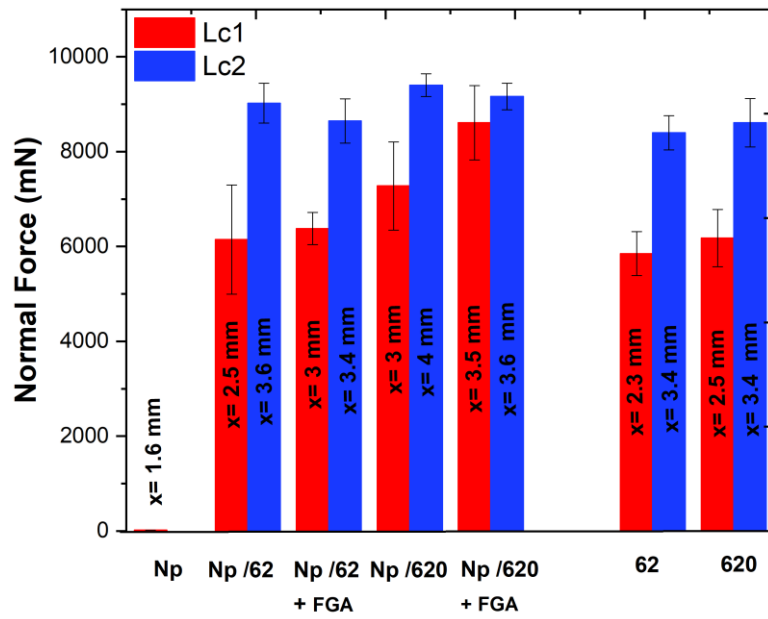


Figure V.9: The critical loads Lc1 and Lc2 of different films as average value of 10 measurements.

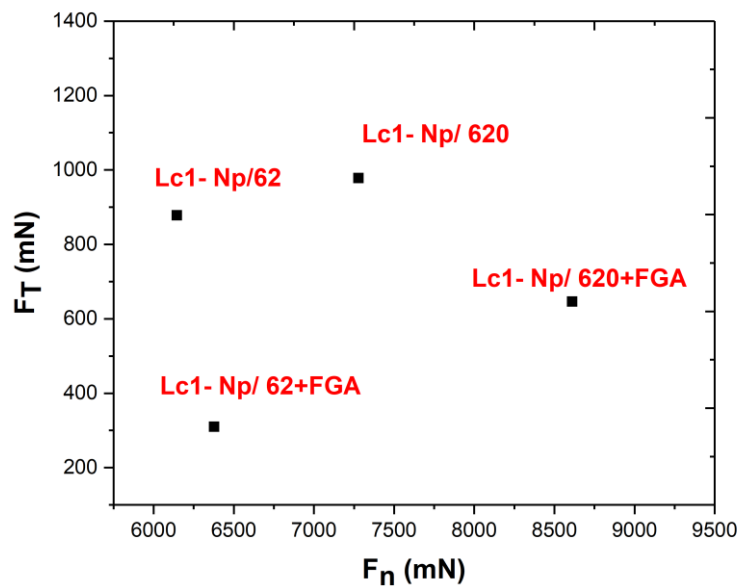


Figure V.10: Frictional force (F_T) evolution with the detected normal force (F_n) at the failure point of Np/ 62 and Np/ 620 before and after the FGA treatment.

II.2 Hardness

In this section, we explore ALD as a layer to reinforce nanopowder based thin films. Hardness of the 620, Np/620 and NP/620+FGA are investigated using nanoindentation. The hardness of the Np/62 film is not measured due to the too thin layer (19 - 21 nm). Several indentations at different places of the coating are made to ensure statistically relevant data set/significant results. For the 620, a set of 25 indents are performed in a two-dimensional array (x- and y-spacing of 10 μm) with a normal force (F_n) varying from 0.5 to 75 mN is conducted using a Berkovich indenter. In addition, for the deposited layer of ALD on nanopowder, a series of 5 indents separated with a distance of 20 μm is with a normal force (F_n) varying from 0.5 to 75 mN is performed using a Berkovich indenter. The estimation of hardness values is based on Oliver and Pharr approximation method. The results of examined films are summarized in **Table V.1**.

Table V.1: Hardness values of different films.

Samples	Hardness (GPa)
620	15 ± 2
Np/ 620	1.6 ± 0.6
Np/ 620 + FGA	6.5 ± 5.1

The Berkovich hardness calculated for 620 is about 15 ± 2 GPa which is the same value (14.57 ± 0.96) reported of 100 nm ALD- Al_2O_3 on copper at 200°C [29]. The obtained hardness values for Np/620 before and after FGA show a hardness ranging from 1.6 ± 0.6 to 6 ± 5.1 GPa. Np/620 that did not undergo annealing process displays a lower hardness value than the annealed film, which demonstrates that annealing treatment can remarkably improve the mechanical properties of the obtained heterostructure, which is in line with scratch test results.

Comparing the hardness values presented in this study with the values of TiO_2 uncoated films as reported in literature, it seems that ALD- Al_2O_3 layer and annealing improve the hardness. Yaghoubi and co-workers [30] present a close study to our work about the deposition of 330 nm thick of anatase- TiO_2 granular film (average grain size 13 nm) on soda lime glass by dip-coating and annealed at 300°C . The film hardness (Berkovich tip) achieved is 0.69 GPa. Hafedh and co-workers [31] also present a hardness value of 1 GPa for TiO_2 nanopowder (Degussa P25) composed of 30% rutile and 70% anatase with average particle size of 21 nm deposited on stainless steel 316L using electrophoretic deposition method.

The high error bar could be explained by the macroscopic heterogeneities of the film. This can be clearly seen from the optical images presented in **Figure V.13**, showing the difference in the print of tip in each area. Three scenarios should be taken into account: pore filled with ALD- Al_2O_3 (high hardness due to Al_2O_3) (**Figure V.11** and **Figure 12**), huge particle coated with ALD- Al_2O_3 or immediately dense film composed of nanopowder coated with ALD- Al_2O_3 zones can form underneath the indenter during indentation.

Existing literature reports extensively the hardness of TiO_2 nanotube arrays. The mechanical properties depend on the phase. Amorphous TiO_2 shows a hardness of about 0.1 GPa. Anatase presents low hardness due to its smaller density as compared to rutile structure with values ranging from 94 MPa to 3.5 GPa are reported [32-33]. These variation of values could be attributed to different indenter tips that can be used (Vickers tips for microhardness, Berkovitch tips for nanohardness, cube corner tips for nanohardness, etc.) which entails different hardness values. It has been demonstrated that materials with nano-sized grains exhibit different mechanical properties, compared to the polycrystalline materials with grain sizes of micrometer size. In addition, here the formation of secondary phases influence cannot be taken into account because the two films have the same phase composition.

The improvement of hardness with ALD- Al_2O_3 coating is reported in literature. Similar observation is presented by Zhang et al. [34] which report the deposition of ALD- Al_2O_3 with a thickness about 0.5-2 nm on TiO_2 nanoparticles thin film (thickness ~ 700 nm) with a porosity of 40%. As the ALD thickness increases, the porosity decreases (to 29%) and the hardness increase drastically of about 13.1% for TiO_2 nanoparticles (average size of 21 nm) after being coated with ALD- Al_2O_3 . Another study show that ALD- Al_2O_3 coating with a thickness of 42 nm resulted in a substantial enhancement of the mechanical properties of rutile- TiO_2 nanotube layer with thickness of 20 μm . Hardness investigated by nanoindentation significantly increased to 23 GPa compared to uncoated nanotube (4 GPa) [35].

Therefore, improvement of the hardness after annealing can be attributed to the infiltration of Al_2O_3 layer within the porous matrix, which lead to the formation of a dense and compact film. As a result, an effective interparticle bonding and pores filling are accomplished that lead to increasing the hardness of the film. Moreover, the possible increases of the density of grain boundaries after annealing may help to constrain the movement of defects such as dislocations and cracks, so their propagation is diminished. The phase transformation (secondary phases

detected by ACOM-TEM) should be also taken into consideration because it can lead to a significant change in the mechanical properties.

These results demonstrate that thick layer of Al₂O₃-ALD and annealing step provide the best mechanical reinforcement for nanoparticle based thin films.

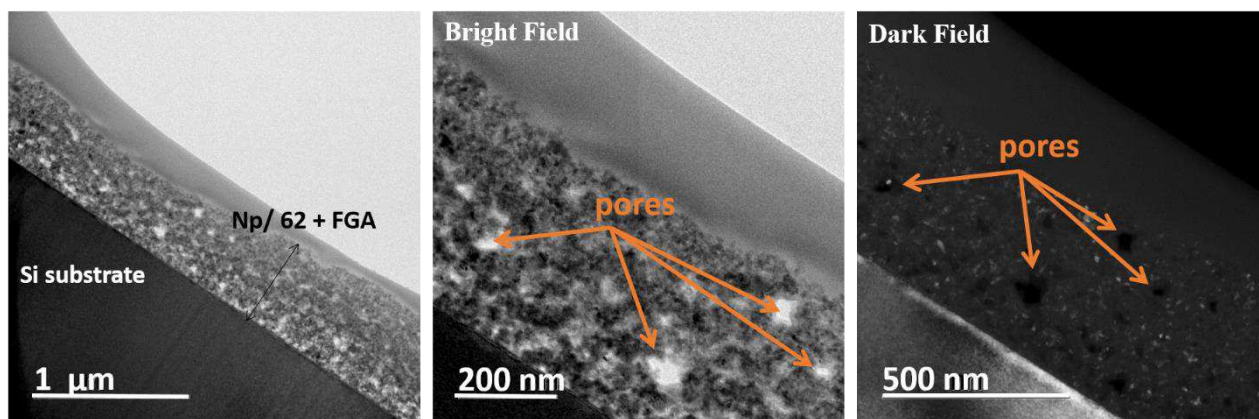


Figure V.11: HR-TEM images of Np/62+FGA showing the porosities among the film.

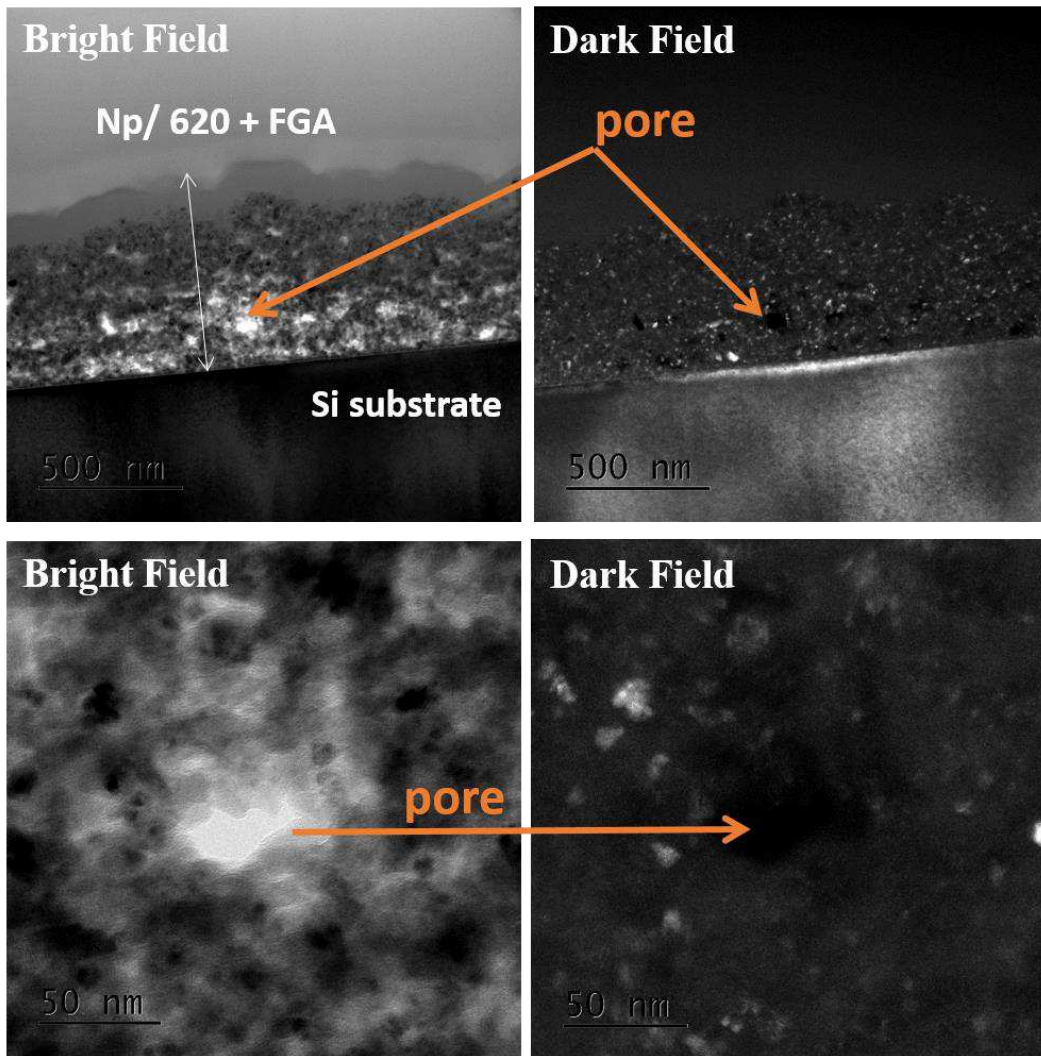


Figure V.12: HR-TEM images of Np/620+FGA showing the porosities among the film.

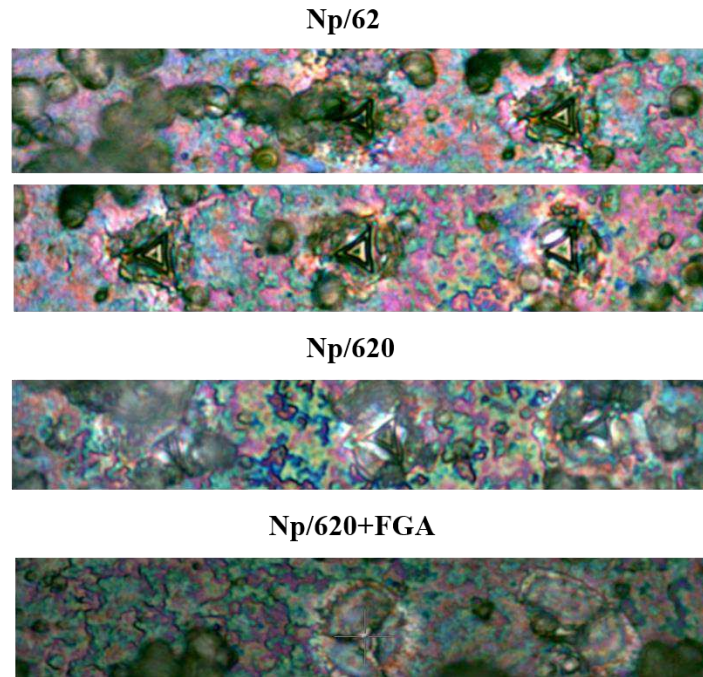


Figure V.13: Optical images of Berkovich indent print on different films.

Chapter Conclusion

In this chapter, we report the influence of 62 and 620 cycles of amorphous ALD- Al_2O_3 and FGA step on the UC luminescence and mechanical properties of codoped TiO_2 nanopowder assembled on n-type Si (100) substrate. In summary, the results indicate that introducing of ALD- Al_2O_3 layer into the surface of codoped TiO_2 nanopowder could improve drastically the UC luminescence. Regulating the color output can be achieved by controlling the thickness and heat treatment step. This study reveals that selective UC luminescence can be assured by controlling the thickness of ALD- Al_2O_3 layer and the post heat treatment step.

Based on Scratch test and hardness measurements, the resulting thick layer of ALD- Al_2O_3 annealed heterostructure shows significant improvement of adhesion and hardness properties than the uncoated and coated with thin layer ALD- Al_2O_3 due to enhanced interparticle bonding and filling of the pores. It can be concluded that both the annealing treatment and the ALD- Al_2O_3 coating resulted in a substantial enhancement of the mechanical properties of codoped TiO_2 nanopowder film deposited on Si substrate. Most importantly, the ALD reinforced nanopowder thin films retained the original functionality of the nanopowder i.e: is UC phenomenon.

Such investigation provides valuable approach to improve the emission efficiency of UC nanomaterials combined with great mechanical properties, which makes it promising for industrial and commercial applications.

References

- [1] Y. Ledemi et al., “White light and multicolor emission tuning in triply doped $\text{Yb}^{3+}/\text{Tm}^{3+}/\text{Er}^{3+}$ novel fluoro-phosphate transparent glass-ceramics” *Journal of Materials Chemistry C*, vol. 2, pp. 5046–5056, 2014.
- [2] S. Krause, M. Koerstz, R. Arppe-Tabbara, T. Soukka, and T. Vosch, “NIR induced modulation of the red emission from erbium ions for selective lanthanide imaging” *Methods and Applications in Fluorescence*, vol. 6, pp. 044001, 2018.
- [3] M. Xin, “High luminescent $\text{TiO}_2\text{-Yb}_2\text{O}_3\text{: Er, Li}$ complex nano spherical upconversion phosphor prepared by a hydrothermally treatment” *Journal of Luminescence*, vol. 213, pp. 415–420, 2019.
- [4] W.A.Pisarski, J.Pisarska, R.Lisiecki, W.R-Romanowskib, “Erbium-doped lead silicate glass for near-infrared emission and temperature-dependent up-conversion applications,” *Opto-electronics review*, vol. 4, pp. 57–71, 2017.
- [5] R. Salhi and J. Deschanvres, “Efficient green and red up-conversion emissions in Er / Yb co-doped TiO_2 nanopowders prepared by hydrothermal-assisted sol–gel process,” *Journal of Luminescence*, vol. 176, pp. 250–259, 2016.
- [6] W. Bian, M. Zhou, G. Chen, X. Yu, M. Pokhrel, Y. Mao, “Upconversion luminescence of ytterbium and erbium co-doped gadolinium oxysulfate hollow nanoparticles,” *Applied Materials Today*, vol. 13, pp. 381–386, 2018.
- [7] J.D. Ferguson, A.W Weimer, S.M. George, “Atomic layer deposition of Al_2O_3 films on polyethylene particles,” *Chemistry of materials*, vol. 16, pp. 5602–5609, 2004.
- [8] J. Wang et al., “Spectral engineering of lanthanide-doped upconversion nanoparticles and their biosensing applications” *materials chemistry frontiers*, vol. 5, pp. 1743-1770, 2021.
- [9] F. Wang, J. Wang, X. Liu, “Direct Evidence of a Surface Quenching Effect on Size Dependent Luminescence of Upconversion Nanoparticles,” *Angewandte Chemie International Edition*, vol. 49, pp. 7456–7460, 2010.
- [10] L. Helmich et al., “Atomic layer deposited Al_2O_3 as effective barrier against the diffusion of hydrogen from $\text{SiN}_x\text{:H}$ layers into crystalline silicon during rapid thermal annealing” *Physica status solidi*, pp. 2000367, 2020.
- [11] L. Liang, X. Qin, K. Zheng, and X. Liu, “Energy Flux Manipulation in Upconversion Nanosystems” *Accounts of Chemical Research*, vol. 52, pp. 228–236, 2019.
- [12] Z. Zhou et al., “Performance improvement by alumina coatings on $\text{Y}_3\text{Al}_5\text{O}_{12}\text{:Ce}^{3+}$ phosphor powder deposited using atomic layer deposition in a fluidized bed reactor,” *RSC advances*, vol. 6, pp. 55–76454, 2016.
- [13] N. Rakov, R. B. Guimarães, G. S. Maciel, “Thermometric analysis of the near-infrared emission from Er^{3+} in yttrium silicate powders containing Mg^{2+} ” *Journal of Alloys and Compounds*, vol. 735, pp. 1629–1636, 2018.

- [14] W. Xu, Y. Hu, L. Zheng, Z. Zhang, W. Cao, "Improved green upconversion emissions from $\text{CaWO}_4: \text{Er}^{3+}\text{-Yb}^{3+}$ by Cr^{3+} codoping for optical thermometry," *Journal of Luminescence*, vol. 215, pp. 116617, 2019.
- [15] S. Mingyi et al., "Effect of Yb^{3+} concentration on upconversion luminescence of AlON: Er^{3+} phosphors" *Journal of rare earths*, vol. 33, pp. 227, 2014.
- [16] X. Pan, M. Q. Yang, X. Fu, N. Zhang, Y. J. Xu, "Defective TiO_2 with oxygen vacancies: Synthesis, properties and photocatalytic applications," *Nanoscale*, vol. 5, pp. 3601–3614, 2013.
- [17] W. Ji et al., "Role of oxygen vacancy on the photoluminescence of $\text{BaMgSiO}_4:\text{Eu}$ phosphors: Experimental and theoretical analysis," *Inorganic Chemistry*, vol. 54, , pp. 1556–1562, 2015.
- [18] T. Potlog, P. Dumitriu, M. Dobromir, A. Manole, D. Luca, "Nb-doped TiO_2 thin films for photovoltaic applications," *Materials and Design*, vol. 85, pp. 558–563, 2015.
- [19] F. Lebreton, "Silicon surface passivation properties of aluminum oxide grown by atomic layer deposition for low temperature solar cells processes" 2018.
- [20] V. G. Ilves et al., "Multimodal upconversion $\text{CaF}_2: \text{Mn} / \text{Yb} / \text{Er} / \text{Si}$ nanoparticles" *Journal of fluorine chemistry*, vol. 231, pp. 109457, 2020.
- [21] K. Henkel, M. Kot, and D. Schmeißer, "Localized defect states and charge trapping in atomic layer deposited- Al_2O_3 films" *Journal of Vacuum Science & Technology A*, vol. 35, pp. 01B125-1, 2017.
- [22] T. V. Perevalov et al., "Oxygen deficiency defects in amorphous Al_2O_3 " *Journal of Applied Physics*, vol. 108, pp. 013501, 2010.
- [23] O. A. Dicks, J. Cottom, A. L. Shluger, V. V. Afanas, "The origin of negative charging in amorphous Al_2O_3 films: The role of native defects" *Nanotechnology*, vol. 30, pp. 205201, 2019.
- [24] Y. Gandhi, M. V. R. Rao, C. S. Rao, I. V. Kityk, a N. Veeraiah, "Role of Al_2O_3 in upconversion and NIR emission in Tm^{3+} and Er^{3+} codoped calcium fluoro phosphorous silicate glass system" *Journal of Luminescence*, vol. 131, no. 7, pp. 1443–1452, 2011.
- [25] B. D. Evans, "A review of the optical properties of anion lattice vacancies, and electrical conduction in $\alpha\text{-Al}_2\text{O}_3$: their relation to radiation-induced electrical degradation" *Journal of Nuclear Materials*, vol. 219, pp. 202–223, 1995.
- [26] R. M. E. Ylivaara et al., "Aluminium oxide from Trimethylaluminium and water by atomic layer deposition: the temperature dependence of residual stress, elastic modulus, hardness and adhesion", *Thin solid films*, vol. 552, pp. 124-135, 2014.
- [27] L. A. Riley, A. S. Cavanagh, S. M. George, S.-H. Lee, A. C. Dillon, "Improved Mechanical Integrity of ALD-Coated Composite Electrodes for Li-Ion Batteries" *Electrochemical and Solid-State Letters*, vol. 14, pp. A29–A31, 2011.
- [28] Q. Wu, W. S. Miao, Y. Du Zhang, H. J. Gao, D. Hui, "Mechanical properties of nanomaterials: A review," *Nanotechnology Reviews*, vol. 9, pp. 259–273, 2020.

- [29] M. L. Chang, L. C. Wang, H. C. Lin, M. J. Chen, K. M. Lin, "Investigation of defects in ultra-thin Al₂O₃ films deposited on pure copper by the atomic layer deposition technique" *Applied Surface Science*, vol. 359, pp. 533–542, 2015.
- [30] H. Yaghoubi, N. Taghavinia, E. K. Alamdari, and A. A. Volinsky, "Nanomechanical properties of TiO₂ granular thin films" *ACS Applied Materials and Interfaces*, vol. 2, pp. 2629–2636, 2010.
- [31] D. Hafedh, K. Kaouther, B. C. L. Ahmed, "Multi-property improvement of TiO₂-WO₃ mixed oxide films deposited on 316L stainless steel by electrophoretic method" *Surface and Coatings Technology*, vol. 326, pp. 45–52, 2017.
- [32] "Hardness of nanocrystalline TiO₂ thin films" *Nano research*, vol. 18–19, pp. 195–200, 2012.
- [33] F. Schmidt-Stein, S. Thiemann, S. Berger, R. Hahn, P. Schmuki, "Mechanical properties of anatase and semi-metallic TiO₂ nanotubes" *Acta Materialia*, vol. 58, pp. 6317–6323, 2010.
- [34] L. Zhang, J. H. Prosser, G. Feng, D. Lee, "Mechanical properties of atomic layer deposition-reinforced nanoparticle thin films" *Nanoscale*, vol. 4, pp. 6543–6552, 2012.
- [35] R. Zazpe et al., "Atomic Layer Deposition Al₂O₃ Coatings Significantly Improve Thermal, Chemical, and Mechanical Stability of Anodic TiO₂ Nanotube Layers" *Langmuir*, vol. 33, pp. 3208–3216, 2017.

General conclusion and perspectives

Lanthanide-doped UC nanomaterials are of particular interest for the research community due to their ability to shape light by UC and their promising optical properties that can result by the precise engineering of surface. As well-known due to the large surface area-to-volume ratio of nanomaterials with size reduction compared to their bulk, the luminescence is typically suppressed by surface quenching attributed to the increase of surface defects. Here, we demonstrate a procedure that exploits surface quenching processes to improve the luminescence of our lanthanide-doped UC nanomaterials, through adding a coating around the codoped nanopowder with lanthanides ions. This coating will further have an impact on the mechanical properties of nanoparticles based thin films.

The main objective of the present study is the preparation of films with an efficient green and red UC luminescence at temperature below 500°C. As the film acquired luminescence response any mechanical damages to the film would compromise its optical property. For this reason, adhesion and hardness are investigated. The application of the proposed structure is to be integrated in Si based solar cells as an approach to improve their efficiency and durability.

The proposed hybrid approach consists first on the synthesis of lanthanides (Er^{3+} and Yb^{3+}) codoped TiO_2 nanopowder synthesized by hydrothermal-assisted sol-gel method under supercritical conditions of ethanol ($T= 263^\circ\text{C}$, $P= 65$ bar) followed by calcination at 300°C . Then, the nanopowder is dispersed at the surface of Si substrate using a spin-coating process (200°C). Finally, the assembled Er^{3+} - Yb^{3+} codoped TiO_2 UC nanopowder film is coated with an amorphous Al_2O_3 layer using ALD technique as a unique approach for surface passivation and to reinforce mechanical properties at a relatively low temperature ($T= 200^\circ\text{C}$) followed by annealing in forming gas composed of $\text{N}_2:\text{H}_2$ at 430°C .

Investigation of the calcination and codoping impact on the structure is firstly performed on the nanopowders. It is demonstrated the crystallinity of nanopowders (undoped and codoped) at the exit of the autoclave which is further improved after the calcination without an increase in crystallite size demonstrating the effectiveness of the method used for elaboration. Codoping the TiO_2 nanopowder with lanthanides induces an anisotropic expansion of the TiO_2 unit cell volume by 0.40 %, indicating a distortion of the cell. Strain measurement using Williamson-Hall method shows that tensile strain increased after codoping. It is observed that the doping

does not influence the crystalline structure of TiO₂; only anatase phase is detected. Therefore, it can be concluded that Er³⁺ and Yb³⁺ ions are incorporated into the TiO₂ matrix. These dopants introduction into the TiO₂ lattice does not cause any change in the morphology of spherical particles but it slightly increases the specific surface area of TiO₂ nanopowder from 125.7 m²/g to 140.6 m²/g.

For the next step referred to the dispersion of nanopowders, suspension optimization based on electrostatic stabilization (pH, co-doping quantity) and physical dispersion (ultrasonication) process is monitored. It is proved that the use of powerful probe sonicator instead of bath sonicator, results in a greater size reduction for codoped TiO₂ at operational pH = 3 adjusted with 0.1 HCl and with 20 min as a suitable duration of ultrasonication. The enhancement of the codoped TiO₂ dispersion with ultrasonication compared to the undoped TiO₂ can be explained by the influence of Er³⁺ and Yb³⁺ ions on the electronic structure, surface charge behavior and surface reactivity. After codoping, a positive charge imbalance is generated that means the formation of active acidic sites, increasing the amount of hydroxyl groups absorbed which affects the intrinsic stability and provides agglomeration. After performing the dispersion process, a significant size reduction is observed (~ 9 nm) with slight agglomeration (1 to 4 μm). The agglomerates presence can be attributed to the low zeta potential (+14 mV) which provides a short time stability and causes the number of desagglomerated particles that reaggregate back to the 1 to 4 μm diameter as a result of the attractive forces among the dispersed particles, stronger than repulsive forces.

For nanopowder based thin film, a DOE approach with the Hadamard matrix of order 4 is performed in order to deposit codoped TiO₂ nanopowder on Si substrate. The increase of the three main parameters of spin-coating (time, speed and solution volume) led to the decrease of huge particles on the substrate surface. Different thicknesses of amorphous ALD-Al₂O₃ layer are deposited into the surface of codoped TiO₂ nanopowder followed by a FGA annealing at 430°C for 30 min. ALD precursors show a diffusion during deposition process into the porous film as a result of diffusion through the pores. Then, further improvement of this diffusion is found after annealing that can be explained by Al and O migration through the film along the grain boundaries. This diffusion resulted in a formation of secondary phases (Al₂TiO₅, Er₂O₃ and/ Yb₂O₃) with small amount into the film which further demonstrates volume diffusion of Al³⁺ into the codoped TiO₂ structure.

For luminescence investigation, the coated nanoparticles based thin film, composed of a thick layer of ALD-Al₂O₃, as a passivation layer, led to significant enhancement of green UC

luminescence (by 98%) compared to other emissions (red and NIR) that decreased in comparison with the uncoated film which is helpful to improve PV cells efficiency. Such unexpected behavior can be attributed the intrinsic defects within the electronic band gap and charge transfer defect states generated within ALD- Al_2O_3 deposition. The Al_2O_3 , an absorption center that ensure an additional energy transfer to Er^{3+} ions upon IR excitation (980 nm), will be made from the defects. This selective enhancement allowed us to design nanoparticles with a surface quenching-assisted mechanism for bright NIR to green UC with a distinctive efficiency peak with a specific thickness.

The NIR to green UC nanopowder based thin film ($5\%\text{Er}^{3+}$ - $5\%\text{Yb}^{3+}$) coated with 620 cycles of ALD- Al_2O_3 and annealed further provides the best hardness and adhesion properties due to the formation of a bonded, dense and compact structure made from the latter a promising composite material in variety of fields involving bioimaging, since, 980 nm is within the transparent biological window (650-1350 nm) and can offer deep tissue penetration. It is interesting to note that until the end of the procedure no remarkable increase in crystallite size is observed. The discussion and results in this thesis demonstrate the efficiency of the low temperature hybrid synthesis approach that combined sol-gel and ALD techniques to prepare a composite with attractive functions.

Further studies are clearly needed to understand the reason behind the UC green enhancement. This can be achieved by quantification measurements (internal quantum efficiency measurements) of luminescence to accurately compare the optical properties with those reported in literature, since the study presented in this thesis is purely qualitative.

Conducting a study on the impact of different annealing temperatures and different atmospheres (N_2 , O_2) on UC luminescence and the structure of the material holds significant potential by this way we can combine between the best electrical properties and good optical and mechanical properties of the device based on the recipe selected for Si-based solar cells passivation (ALD- Al_2O_3 + annealing). In addition, it is essential to perform an electrical measurement on the proposed structure to evaluate its efficiency.

The dispersion process, also aligned with $\text{pH}= 8$, should be optimized when depositing the solution on Si substrate in order to get a good adhesion, by increasing the affinity between the surface of the substrate and nanoparticles surface. It is also interesting to conduct another study with changing the dopants percents ($13\%\text{Er}^{3+}$ - $5\%\text{Yb}^{3+}$) or changing the host matrix to Al_2O_3 while keeping the same percents of dopants to get the best material and percents for dispersion.

Following this, investigation of the effect of the intrinsic properties of nanopowder based thin film in determining the final properties of the ALD-Al₂O₃ reinforced thin films and compositional matching between ALD and nanopowders can be interesting. Other suggestion is the deposition of ALD-Al₂O₃ immediately on nanoparticles using fluidized bed reactor to form core-shell structure.

Annex 1: Williamson –Hall method for crystallite size and strain calculation

For Williamson-Hall method, it is assumed that size and strain broadening are additive components of the total broadening of a Bragg peak. The contributions of crystallite size (β_D) and lattice strain (β_s) to total peak broadening are described as:

$$\beta_{hkl} = \beta_D + \beta_s \text{ (Equation A.1.1)}$$

The strain induced in powders due to imperfection and distortion can be calculated using the formula:

$$\eta \approx \frac{\beta_s}{\tan \theta} \text{ (Equation A.1.2)}$$

Debye–Scherrer formula can be rearranged with Equation (A.1.2):

$$D = \frac{K\lambda}{\beta_D \cos \theta} \text{ (Equation A.1.3)}$$

$$\beta_{hkl} = \frac{K\lambda}{D \cos \theta} + (4\eta \tan \theta) \text{ (Equation A.1.4)}$$

Rearranging Equation (A.1.4) leads to:

$$\beta_{hkl} \cos \theta = \frac{K\lambda}{D} + 4\eta \sin \theta \text{ (Equation A.1.5)}$$

This equation represents the uniform deformation model (UDM), where the lattice distortion is uniform in all crystallographic directions that considering the isotropic nature of the crystal. ($\beta_{hkl} \cos \theta$) is plotted with respect to ($4 \sin \theta$). As a result, the crystallite size can be estimated from the y-intercept, and the lattice distortion degree η , from the slope of the linear fit of the data. As reported, a negative slope in the Williamson-Hall plot indicates the presence of compressive strain, while a positive slope indicates the presence of tensile strain [1-2].

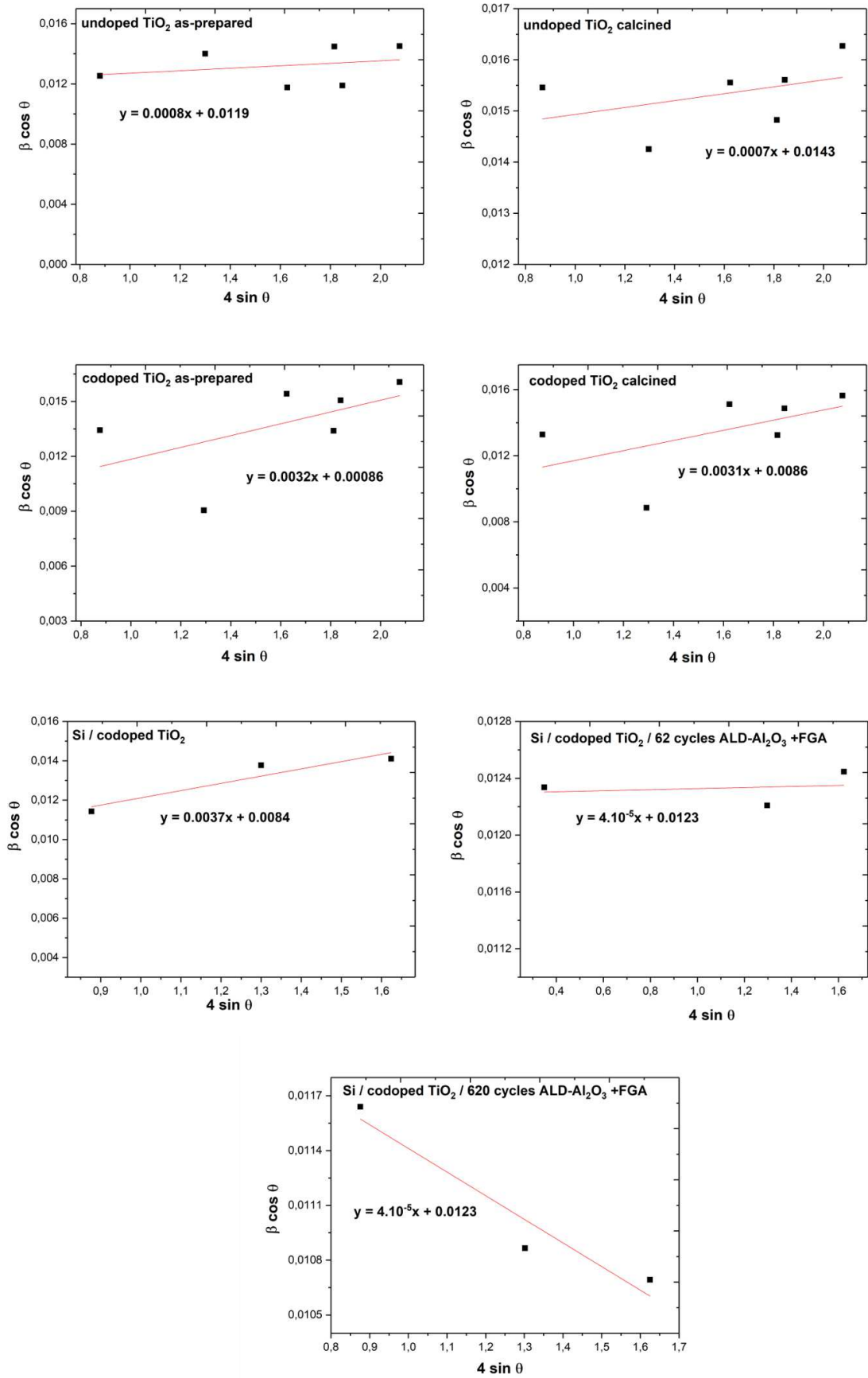


Figure A.1.1: Williamson-Hall plot of $\beta_{hkl} \cos \theta$ vs $4 \sin \theta$.

The generalized Hook's law refers to the strain, keeping the linear proportionality between the stress and distortion:

$$\sigma = \eta Y \text{ (Equation A.1.6)}$$

The stress is proportional to the distortion, with the constant of proportionality being the modulus of elasticity or Young's modulus (Y). Y_{hkl} is Young's modulus in the direction perpendicular to the set of the crystal plane (hkl). For a given tetragonal system, Young's modulus is described by the following equation:

$$\frac{1}{Y_{hkl}} = \frac{S_{11}(h^4 + k^4) + (2S_{12} + S_{66})h^2 k^2 + (2S_{13} + S_{44})(h^2 + k^2)l^2 + S_{33} l^4}{(h^2 + k^2 + l^2)^2} \text{ (Equation A.1.7)}$$

Where S_{11} , S_{12} , S_{13} , S_{33} , S_{44} , and S_{66} are the elastic compliances of TiO_2 . **Table A.1.1** summarize the elastic compliances for both anatase and rutile phases.

Table A.1.1: Elastic compliances values of anatase and rutile phases.

Elastic compliances	Values for anatase (Pa ⁻¹)	Values for rutile (Pa ⁻¹)
S_{11}	$5.1 \cdot 10^{-12}$	$6.8 \cdot 10^{-12}$
S_{12}	$-8 \cdot 10^{-13}$	$-4 \cdot 10^{-12}$
S_{13}	$-3.3 \cdot 10^{-12}$	$-0.85 \cdot 10^{-12}$
S_{33}	$1.07 \cdot 10^{-11}$	$2.6 \cdot 10^{-12}$
S_{44}	$1.85 \cdot 10^{-11}$	$8.06 \cdot 10^{-12}$
S_{66}	$1.67 \cdot 10^{-11}$	$5.21 \cdot 10^{-12}$

The stress calculated for each plane (hkl) for all the samples is illustrated in **Table A.1.2**. It is shown that for the undoped TiO_2 the stress is around 1-75 MPa while for the codoped TiO_2 is between 4 and 299 MPa. These values demonstrate a higher stress for (004) and (101) planes than for the others.

Table A.1.2: The stress calculated for each plane (hkl) of the four samples.

	σ (MPa) (101)	σ (MPa) (004)	σ (MPa) (200)	σ (MPa) (105)	σ (MPa) (211)	σ (MPa) (204)
Undoped as- prepared	40,7	74.8	9,80	2,56	3,87	0.94
Undoped calcined	35.6	65.4	8,58	2,24	3,38	0.82
Codoped as- prepared	163	299	39.2	10.2	15.5	3,76
Codoped calcined	158	290	38	9,92	15	3,65

References

- [1] E. Emil, S. Gürmen, “Estimation of yttrium oxide microstructural parameters using the Williamson–Hall analysis,” *Materials Science and Technology (United Kingdom)*, vol. 34, pp. 1549–1557, 2018.
- [2] B. Bharti, P. B. Barman, R. Kumar, “XRD analysis of undoped and Fe doped TiO₂ nanoparticles by Williamson Hall method,” *AIP Conference Proceedings*, vol. 1675, pp. 3–7, 2015.

Annex 2: Comparison between the TMA amounts injected to the exposed surface of nanoparticles based film

What amount do I deliver during one cycle of ALD into the film? We can verify if the TMA exposure time employed during ALD is suitable to treat the porous film. This section investigates the amount of TMA dose injected during one cycle of ALD process and the surface of TiO₂ nanopowder needed to be covered.

First, it is necessary to calculate the amount of nanopowder deposited on Si substrate that will be covered. The first step is to calculate the mass of TiO₂ nanopowder deposited on Si substrate ($m_{TiO_2/si}$):

$$m_{TiO_2/si} (kg) = t (m) \times d(m^2) \times \rho(kg.m^{-3}) \quad (Equation A.2.8)$$

Where t the thickness of the film, we will take the high thickness deposited by spin-coating method, which is $8.50 \cdot 10^{-7}$ m, d the Si dimensions (0.02×0.02 m²) and ρ the density of TiO₂ (4230 kg/m³). Equation gives a value for $m_{TiO_2/si}$ of $1.44 \cdot 10^{-6}$ kg. The surface of TiO₂ nanopowder on Si substrate ($S_{TiO_2/si}$) can be then calculated as shown in equation:

$$S_{TiO_2/si} (m^2) = S_{BET} (m^2.kg^{-1}) \times m_{TiO_2/si} (kg) \quad (Equation A.2.9)$$

Where S_{BET} is the specific surface area is found with BET method (140000 m²/kg). Steric hindrance is used to define the saturation in the reaction of TMA precursor with a value corresponding to 10^{-6} mole/m². Thereby, for 1 cycle we can calculate the surface of nanopowder to be covered which we can get it by multiplication of $S_{TiO_2/si}$ and the adsorption of TMA on surface. The amount per cycle needed for TiO₂ nanopowder deposited on Si (0.02×0.02 m²) to form a film with a thickness of about 850 nm is equal to $2.7 \cdot 10^{-7}$ mole.

For the measurement of the amount of TMA injected per cycle during our process, we need to know first the saturation vapor pressure (P_{sat}), the pressure at which the gas phase of TMA is in equilibrium with its liquid phase. P_{sat} can be calculated as follows using Antoine law:

$$P_{sat} = 10^{A - \frac{B}{C+T}} \quad (Equation A.2.10)$$

Where A, B and C are Antoine parameters and T is the temperature in Kelvin. Then calculation of the flux (J) can be conducted as follows:

$$J (mole.m^{-2}.s^{-1}) = \frac{P_{sat}(Pa)}{\sqrt{2\pi R(J.mole^{-1}K^{-1})T(K)}} \quad (Equation A.2.11)$$

As the P_{sat} is 12 mbar and T is equal to 293 K, J is equal to $9.8 \text{ mole}\cdot\text{m}^{-2}\cdot\text{s}^{-1}$. To access to the amount the J should be multiplied with the surface of TMA bubbler (10^{-4} m^2) and the injection time of TMA precursor during one cycle (1.5 s). The result is $4.6 \cdot 10^{-3}$ mole of TMA per cycle. Comparing the amount injected of TMA per cycle and the surface of TiO_2 nanopowder to be covered, we believe that applied ALD parameters are sufficient to treat the whole film since it is in saturation regime.

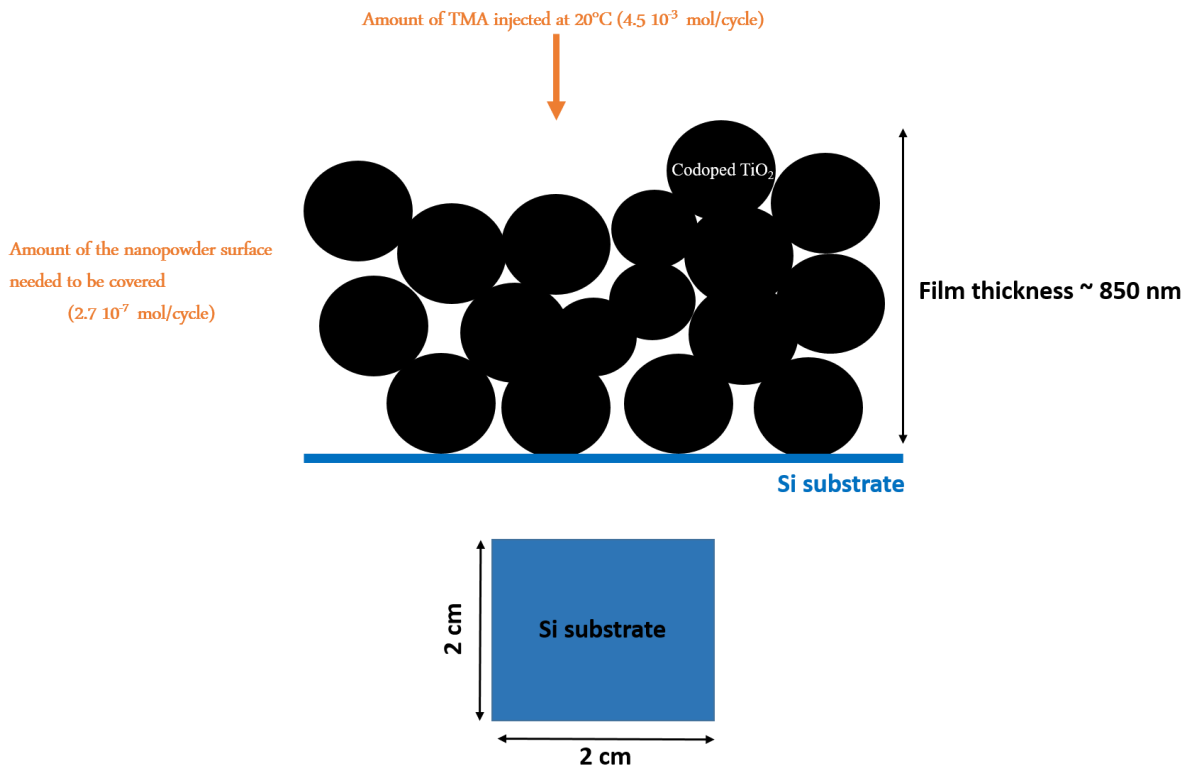


Figure A.2.2: Schematic representation of the amount of TMA precursor injected and the exposed surface of nanopowders.

If we take the example of mini-Si solar cell with dimensions $40 \times 46 \text{ cm}^2$ and try deposit a film of nanoparticles with thickness of 850 nm, the surface to be covered will be $9.2 \cdot 10^{-5}$ mol per cycle, and TMA pulse with 1.5 s is always sufficient to cover the whole exposed surface.